Optimal control for studying wave energy in hydraulic systems

A dissertation submitted for the degree of
Doctor of Philosophy

Alia Al Ghosoun

Supervised by
DR. MOHAMMED SEAID

Department of Engineering, Durham University
UK

January 13, 2021

Dedication

To the greatest father and mother, to my parents, whose love for me knew no bounds.

To my outstanding supervisor, who was the guiding light for every step of the way.

To my supportive husband (Mustafa), and lovely daughter (Tala), whose support for me has no bounds.

To my precious brothers (Abdallah and Abdelbaset) and sisters (Rayah, haya and hebah), for continuous support and love.

To all of my friends and family.

Acknowledgements

I would like to express my deepest appreciation and respect to those who have contributed to this thesis.

I would like first, to express my deepest appreciation and respect to my outstanding supervisor Dr. Mohammed Seaid for giving me the opportunity to do this PhD study under his invaluable supervision, advise, guidance and encouragement throughout the course of the study. I am indept to the support, enthusiasm, insight and assistance. I have been extremely lucky to have a supervisor who cared so much about my work and its daily basis from the start of the project till date. Under his guidance I successfully overcame many difficulties and learned a lot. His own zeal of perfection, passion and encouragement has always inspired me to do more. His constant support and push to attend conferences and pursue collaboration with other researchers is greatly appreciated. Thank you very much for every friendly discussion, for being endless patient, without that this thesis not have been achieved and I am very proud for being one of your PhD students.

I would like to extend my thanks for my second supervisor Dr. Ashraf Osman, for his valuable advice, discussions and investigations which lead to the successful completion of this work.

I am highly indepted and gratefully appreciate and acknowledge the support received from Dr. Nabil El Mocayd, for his generous help, encouragements, valuable guidance and suggestions through this research.

My special thanks to all of my friends for their wishes and prayers. Special thanks for Mr. Jaafar Albadr and Mr. Hamed Khaki for being there whenever I need a support.

Finally, I would like to owe thanks to my family: my beloved mom and dad for their great support, I am specially grateful for your emotional support. Great thanks for my husband for his continued love, support and understanding during my pursuit of PhD degree that made the completion of this thesis possible. He was always around and helped to keep things in perspective. I gratefully value his contribution and deeply appreciate his believe in me. I appreciate my little girl Tala for the patience she showed during my thesis writing, and her big support specially in tidying up. I am very lucky to have such a great family. Mom and dad, my brothers and sisters, lovely husband and beautiful daughter, I sincerely thank you.

Declaration

I hereby confirm that all of the result described in this thesis is the original work of mine. Any published ideas or techniques from the others are fully acknowledged in accordance with the standard referencing practices.

List of publications

- **Published papers:**
  - **Alia Al Ghosoun**, Ashraf Osman, and Mohammed Seaid. **Hybrid finite volume/finite element simulations of wave runup by static deformation on seabeds.** *Engineering computations*, **Accepted**.
  - **Alia Al Ghosoun**, Ashraf Osman, and Mohammed Seaid. **A computational model for simulation of shallow water waves by elastic deformations in the topography.** *Communications in computational physics,* **Accepted**.
  - Nabil El Mocayd, **Alia Al Ghosoun**, Driss Ouazar, and Mohammed Seaid. **Uncertainty quantification of bathymetric effects in a two-layer shallow water model: case of the Gibraltar strait.** *Advances in Hydroinformatics*, 53:779-791, 2020. *doi.org*/10.1007/978 − 981 − 15 − 5436 − 061.
  - **Alia Al Ghosoun**, Nabil El Mocayd, and Mohammed Seaid. **An optimal control method for reconstruction of topography in dam-breaks flows.** *International Journal of mechanical and mechatronics engineering*, 14:250-262, 2020.
  - **Alia Al Ghosoun**, Ashraf Osman, and Mohammed Seaid. **A finite element/finite volume method for dam-break flows over deformable beds**. *International Journal of bioengineering and life sciences*, 12:395-399, 2018. *doi.org*/10.5281/*zenodo*.1474968.
  - **Alia Al Ghosoun**, Michael Herty, and Mohammed Seaid. **A new numerical treatment of moving wet/dry fronts in dam-break flows**. *J. Appl. Math. Comput*, 59:489-516, 2018. *doi.org*/10.1007/*s*12190 − 018 − 1189 − 5.
  - **Alia Al Ghosoun**, Michael Herty, and Mohammed Seaid. **Numerical Modeling of wave Run-up in shallow water flows using moving wet/dry treatment**. *International Journal of mechanical and mechatronics engineering*, 11:1757-1761, 2017. *doi.org*/10.5281/*zenodo*.1340496.
- **Submitted papers:**
  - **Alia Al Ghosoun**, Nabil El Mocayd, and Mohammed Seaid. **Uncertainty quantification related to numerical methods in hydraulic computations.** *Submitted to Journal of computational physics.*

- **Alia Al Ghosoun**, Nabil El Mocayd, and Mohammed Seaid. **Efficient quantification of uncertainties in multilayer shallow water flows with mass exchange.** *Submitted to International Journal for uncertainty quantification.*

- **Attended Conferences:**

Parts of this thesis have been presented in the following conferences:

- **International conference on mechanical engineering and applied mechanics**, London (United Kingdom), April 23-24, 2020.

- **International conference on mathematical and computational modelling**, Granada (Spain), September 9-11, 2019.

- **20th International conference on computational engineering and application**, Istanbul (Turkey), October 22-23, 2018. (Best paper award).

- **19th International conference on computational fluid dynamics** , London, United Kingdom,October 19-20, 2017. (Best presentation award).

Abstract

A class of novel models for water waves induced by elastic deformation in the topography is developed and analyzed. The depth-averaged shallow water equations including friction terms for the water free-surface and the well-known second-order elastostatic formulation for the bed deformation have been implemented. Friction forces and water hydrostatic pressure distribution are also accounted for in this model. At the interface between the water flow and the bed topography, transfer conditions are implemented. Furthermore, a hybrid finite element/finite volume method for solving free-surface run-up flow problems over deformable beds has been proposed. The deformations in the topography have been generated by a localized force which causes propagations of the water waves with different amplitudes and frequencies. Two different methods have been proposed for the transfer of informations through the interface. The first one is the two-mesh procedure; in this method a proper interpolation has been implemented to transfer the data between the surface nodes and the control volumes using uniform finite volume meshes. In the second method, and to avoid the interpolation at the interface, a finite volume method using non-uniform meshes has been implemented. When the shallow water waves approach the coastline they begin to transform as they enter shallow water regime. As each wave begins to experience the seabed, both run-up and overtopping occur. To solve for this, a class of stable, accurate and simple numerical model for moving wet/dry fronts in shallow water equations using the parametrization concept and the point-wise Riemann solver has been proposed.

Many parameters of shallow water equations are subject to uncertainties to the inherit randomness of natural processes. To incorporate uncertain parameters into the stochastic shallow water equations, the stochastic properties of different parameters that are considered uncertain, namely inflow boundary condition, the bed friction coefficients and the domain topography are added to the system. Development of accurate and efficient tools for uncertainty quantification in shallow water flows has been proposed and carefully examined for single-layer, two-layer finite volume models. To further quantify the uncertainty in shallow water flows the proposed methods have been extended to multi-layer shallow water flows with mass exchange terms subject to stochastic topography, uncertain friction and viscosity coefficients. Several test examples and well-established benchmark problems have been used to assess the numerical performance of the proposed models and methods. Comparisons to experimental measurements have also been carried out in this thesis. Finally, an optimal control technique for bed reconstruction has been presented as in many engineering applications this information is not entirely provided.

Keywords: Shallow water equations, Finite volume method, Finite element method, Uncertainty quantifications, Multi-layer shallow water, Optimal control.

Contents

List of Figures

List of Tables

Nomenclature

Symbols	Description
z	Bed topography function $[m]$
h	Water height $[m]$
t	Time $[s]$
T	Simulation time $[s]$
g	Acceleration of gravity $[m/s^2]$
$\mathbf{n}$	Unit normal
u	Flow velocity $[m/s]$
x_0	Initial location of dam-break $[m]$
h_0	Initial water depth $[m]$
u_0	Initial flow velocity $[m/s]$
$\mathbf{s}$	Shallow water wave speed $[m/s]$
Q	Shallow water flow discharge $[m^3/s]$
Y	Departure point in FVC $[m]$
n_b, M_b	Manning Coefficient $[m/s^{\frac{1}{3}}]$
f_x	External forces in x-direction $[N]$
f_z	External forces in z-direction $[N]$
$\mathbf{K}$	Stiffness matrix
R	Pipe radius $[m]$
E	Young's modulus $[MPa]$
M	Number of shallow water layers
l	Relevant size of the shallow water layer
v	Kinematic viscosity m^2/s
w	Wind velocity m/s

Greek symbols

ζ	Location of wet/dry interface $[m]$
η	Free-surface elevation $[m]$
λ	Shallow water system eigenvalues
τ_f	Bed friction force $[N]$
ρ	Water density $[kg/m^3]$
ρ_a	Air density $[kg/m^3]$
σ_x	Normal stress component in x direction $[kg/m.s^2]$
σ_z	Normal stress component in z direction $[kg/m.s^2]$
τ_{xz}	Shear stress $[kg/m.s^2]$
ϵ	Strain tensor $[kg/m.s^2]$
σ_v	Fixed stresses $[kg/m.s^2]$
Ω	Interior domain $[m]$
α, β	Bed inclination angles
τ_i	Interface boundary
ν	Poisson ratio

Acronyms

CFD	Computational fluid dynamics
CFL	Courant-Friedrichs-Lewy
FVC	Finite volume method of characteristics
FVM	Finite volume method
FDM	Finite difference method
FEM	Finite element method
1D	One-dimension
2D	Two-dimension
C-property	Conservation property
HLL	Harten-Lax-van Leer
HLLC	Harten-Lax-van Leer-Contact
TVD	Total Variation Disminishing
LS	Least Square minimization
LOO	Leave-one-out
SVD	Singular value decomposition
IC	Interval of confidence
PDF	Probability density function
PCE	Polynomial chaos expansion
POD	Proper orthogonal decomposition
KL	Karunen-Loève expansion

Chapter 1

Introduction

1.1 Project background

Dam-breaks, flooding, and tsunamis are some of the most destructive natural disasters globally, without doubt in coastal areas. The risk and impact of floods in both rural and urban areas have increased in recent decades, as a result of urbanization and population growth. Moreover, an increasing amount of people and property are being concentrated in coastal zones and on floodplains [228]. Thus, the robustness of dams is of paramount importance. Dam-breaks has devastating consequences, such as the Teton failure of 1976, which rendered 25,000 homeless, caused eleven deaths, and accrued damage to a total of 400 million US dollars [215]. Tsunamis also pose significant danger. Characterized by large waves, tsunamis carry enormous energy; their vastly increasing amplitudes destroy vulnerable populations and structures. They are caused by the sudden displacement of a large mass of water [129]. Large earthquakes, with epicentres near an ocean basin, are the most common cause of such displacements, though tsunamis are also caused by volcanic eruptions and landslides, either above or below water [241]. Killing almost 20,000 people, the 2011 Tohuku Tsunami in Japan caused mass destruction on the North shore of Honshu, including a major nuclear disaster at the Fukushima-Daichi power plant [110]. Implementing shallow water systems, which mitigate the effects of tsunamis, dam-breaks, and other flooding, are an essential part of effective emergency planning. By producing a design solution that unifies various subfields, mechatronics aims to enhance understandings of the shallow water phenomena, given that real-time field measurements are challenging to conduct. Thus, mechatronics is a systematic approach, optimizing methods and tools.

Strategic development of coastal and river systems minimizes risks, whilst allowing maximum use of their boundaries [125]. Techniques such as sea walls, diversion spillways, and bank reinforcement are just a few of the methods employed to mitigate danger [176]. Crucially, these methods are dependent on a comprehensive understanding of the interaction between water and soil. As computer technology advances, scientists continually attempt to use numerical modelling to better predict a growing number of high-impact geophysical events. Coastal hazards have became an increasing concern as the worlds population continues to grow. Much of this growth occurs in coastal areas, with 44 percent of the global population living within 150 kilometres of the coastline, including eight of the worlds largest cities [103]. Consequently, natural disasters are causing more death and destruction than ever before. Unfortunately, human activities, such as urbanization and deforestation, contribute to the frequency of these events. As a result, establishing important tools and techniques to predict the likelihood of

these disasters is crucial. The insight and information gained from prediction tools can be utilized in numerous ways, whether for the drafting of maps, risk assessments, development and evacuation planning, the education of local inhabitants [118]. In order to develop these prediction tools, physical (experimental) or mathematical (computational) models can be used. However, experiments can be costly, time consuming and difficult to be reused in different scenarios [134]. Many institutions around the world are working to develop complete systems for generation, propagation, and inundation, with the goal of producing and transmitting life-saving information; so important are accurate models, which must protect coastal populations, whilst minimizing the expense and danger of false alarms.

Nowadays computational resources offer new simulation possibilities. Mathematical models can faithfully predict physical problems in many engineering disciplines [137]. Mathematical modelling attempts to simulate the real world by providing insight into incomplete data. One of the most commonly used models in shallow water is a set of partial differential equations, known by the shallow water equations (depth-averaged Navier-Stokes equations). Shallow water equations (SWEs) are a sub-discipline of computational fluid dynamics, focusing on the mathematical description and numerical approximation of different flow types. These equations address the kind of computational challenges related to fluid flows, bathymetry disturbances, as well as the coupling between them [117]. These are, from a mathematical point of view, conservation of mass and conservation of momentum equations [244], also known as Saint Venant equations [84]. They are typically used to model free-surface flows, river and lake hydrodynamics, long wave run-up, as well as flows in open channels. One-dimensional, shallow water equations represent most of the system characteristics and are used extensively in computer models such as SWMM5, MIKE11, and SOBEK1D [8]. The solutions of these hyperbolic systems of partial differential equations (PDEs) are dependent on time, as well as one or more spatial variables. In shallow water equations, pressure is assumed to be hydrostatically distributed due to gravity. Currently, shallow water systems are able to solve different shallow water flows with different initial and boundary conditions. The focus of current research is the creation of a fast and modular method for solving more complex problems and which might be easily extrapolated to other dimensions and domains.

1.2 Modelling shallow water systems

Water is one of the most important natural resources in human history. Open channel hydraulics have been a great interest to researchers and engineers. Moreover, free-surface flows in rivers, estuaries, and oceans are complex phenomena [8]. Although great steps have been made in the numerical modelling of open channel hydraulics, the automatic, physical description of open channel flow remains difficult [25]. Analytical solutions of open channel flow equations are not generally available, except in the most simple cases [163]. Thus, numerical solutions for open channels flow are of great significance to researchers and engineers. Devised by Claude Navier in 1812, before being adapted by George Stokes in 1845, Navier-Stokes equations govern the behaviour of three-dimensional (3D), viscous fluids in shallow areas. The shallow water equations (SWEs) and the Navier stokes equations are set of hyperbolic partial differential equations, which have numerous applications; they are typically used to model free-surface flows, rivers, lake hydrodynamics, long wave run-up, and flows in open channels [206]. The equations were derived from the depth-averaged Navier-Stokes equations where the horizontal

length is much more greater than the vertical water depth [192]. The one-dimensional (1D) shallow water equations represent most of the system characterestics and it is used extensively in computer models, hence its integral much easier than the two-dimensional (2D) system [266].

Most recently, research has been devoted to the development of nonlinear shallow water equations, which study the physical flow processes [159]. Numerical models provide approximate solutions for different types of flow, making them suitable for practical applications as predictive tools [257]. The governing equations of flow are the conservation of mass and momentum [19]. In real terms, flow rate and water depth are sufficient to describe the flow characteristics [169]. The conservation of mass and momentum equations which called the Saint-Venant equations are used to model the one-dimensional open channel flow problem with some conditions are made; the cross-section of the channel is rectangular, bed slope is small, the pressure distribution assumed to be hydrostatic and the water density is constant[247].

Recently, many investigations and numerical modelling techniques have been developed to solve SWEs, with each method having its own benefits and drawbacks. Generally, these can be divided into three main categories: Finite difference(FD), Finite element(FE), and Finite volume(FV) methods . The FDM, proposed by Richardson in 1910 [204], is the oldest of these numerical methods; it discretizes the PDEs defined on a certain domain, then differentiates them using Taylor series expansion. After this, it solves the equations at each node and applies the boundary conditions [53]. A finite difference method for solving initial boundary value problem for the one-dimensional nonlinear system of differential equations describing shallow water flows in a class of discontinuous functions is suggested in [152]. This method considered to be direct and easy to implement. However, the drawback of this method is that it is restricted to a very simple grid, as it suffers from lack of flexibility from the geometric point of view. In addition to that, the mass and momentum are not conserved using this method.

The FEM was developed in the 1970s [76] and is well-known in solving hyperbolic equations. It involves the discretization of the system into a series of sub-domains, called finite elements, which are connected at a discrete number of nodal points. Triangular and Lagrangian isoparametric finite elements are generally used [207]. Attention has been paid by coastal and ocean researchers to the accuracy of the integral invariants [181]. A selective lumping FEM for shallow water flows was examined by researchers in [132]. Accuracy estimates for FEMs applied to hyperbolic partial differential equations have been extensively studied; for example, a Fourier analysis for evaluation the accuracy of finite element methods for the linearized shallow water equations was investigated in [147]. The computational cost of the finite element methods were considered in [67], concluding that the finite element methods are computationally more expensive than the finite difference methods. Some of the reasons behind the success of this method include its ability to increase the order of the elements [52], locally refine the mesh when needed and its suitability to combine different functions on the same element [2]. The method is also known for its suitability in handling the irregular and curved geometries in the solution. The limitation of this method is the mathematic in this method advanced and more complex compared to FDM and FVM. This always results in increased time for efficient computations.

When dealing with flow discontinuities, volume conservation becomes an important issue for schemes based on non-conservative differential form of the nonlinear shallow water equations. Finite volume method, however, has the advantage of solving the integral form of the nonlin-

ear equations as fully conservative form [269]. Finite volume method was used in the 1950's [242], in this method the domain is discretized into a group of finite volumes. The integral equations are then calculated for each of these volumes to calculate the solution. The main feature of the finite volume method is the flux estimation at each cell interface, where the fluxes are evaluated for each cell boundary on the left and right sides [69]. Different schemes are available to estimate the fluxes some of them are first-order accuracy and some are second order. Lax-Friedrich method is an example of the first-order schemes, as it approximates the space using a central difference approach using all neighbouring values to predict forward in time. The approximations made by this scheme normally smooth and diffusive [224]. Unlike the Lax-Friedrich scheme, the Lax-wendroff scheme is second order accuracy with regards both space and time. Many approximate solvers now exist to evaluate the fluxes, most of these solvers have the capability of hydraulic shock capturing with a high level of accuracy using structured and unstructered meshes [54]. In [182], researchers investigate one-dimensional wave run-up, overtopping and regeneration problems using a Roe-type Riemann solver and resolved the moving shoreline problem by imposing a minimum water depth. A similar scheme was presented by [258] but used the characterestic method to track the shoreline. The main advantage of FVM is that it combines the simplicity of the FDM and the geometrical flexibility of the FEM. Furthermore, the finite volume method also guarantees the conservation of mass and momentum during the simulations [255, 211], and it is able to solve problems in large domains, turbulent flows and higher speed flows. In addition to its power in solving the nonlinear problems.

In recent years, finite volume methods have attracted wide attention and achieved good results in the numerical simulations of different real life hydrodynamic problems, such as free-surface flows in shallow lakes, dam-breaks, floods and coastal indudations [255]. Due to initial conditions and a consequence of the fluid motion, the thickness of the layer vanishes inside the calculation domain. A similar difficulty appears in two-layer fluids when the thickness of at least one of the layers vanishes [56]. Depending on the flow conditions, some of the cells of the domain can pass from dry state to wet state or conversely according to the complexity of the topography. Steep slopes can indeed create wet/dry interfaces, forming discontinuities which may cause numerical instabilities. These can manifest in unrealistic water depths (infinite or negative) and generate spurious oscillations . As a consequence, the resulting scheme may be non-conservative or unstable [268]. Most of the numerical methods in solving wet/dry flows simulation are of two general types:

- **Moving grid methods:** This class of solutions includes any technique that involves continious mesh updating such that a set of nodes is permenantly located on the moving boundary as the solution evolves. These methods rely on the Lagrangian kinematic description. The boundary nodes are moved with the fluid velocity. The water front in this method can be tracked by updating the velocity of the moving front, then defining the moving shoreline position. The grid is then continuously moved to match the moving fronts. This approach appeared in the late sixties [202]. A 2D approach was proposed in [88] where only the boundary elements are moved. This method encounter serious problems related to the mesh distortion so that moving grid methods often used the Largrangian approach [89, 21]. This class of equations defines an additional equation related to the mesh velocity. The remeshing or mesh adaptation operations required to cope with the computational domain variations are presented by researchers in [21,

232]. Recently, researchers in [158] proposed a Lagrangian formulation for solving the shallow water equations using the natural elements method and a continuous remeshing algorithm. However, this method considered to be complicated to be implemented in solving real-life hydraulic problems where an area has alternate wet/dry states, and it required large time computations.

- **Fixed grid methods:** These problems solve the wet/dry state in a fixed computational domain eventually larger than the initially occupied by a fluid. The domain can contain small islands that could be inudated. Some of the first wet/dry treatments over fixed grids were proposed by researchers in [36]. Then a finite difference method in solving wet/dry treatment is presented by some researchers as in [119]. The model presented by the researchers in [135] used a thin layer of water everywhere in the domain, but this does not conserve mass and momentum and may become unstable when dry zones appear within the computational domain. Some researchers tolerate negative water depths when treating adverse slopes to control the mass conservation. Negative depths correspond to dry areas and positive depth to wet ones. Despite the lack of meaning of negative depths, conservation is not completely satisfied in general situations. To solve this problem a water tolerance is define above which the water level is considered to be dry, but this model still sensitive to the value of the tolerance. Even more, the smaller tolerance the more accurate is the model, but this could generate spurious oscillations at the wet/dry fronts in the domain. A reasonable value has to be choosen to satisfy both accuracy and stability. Instead, it has been noted that under a certain limit of bed slope for a supercritical flow a negative water depth is still generated [35]. To solve this problem some researchers aim to remove the added amount of water from the neighbouring cell, see for example [18], or remove it form all the cells after each time step as in [183]. Different techniques to tackle this problem where implemented by researchers, for example researchers in [47] proposed a velocity extrapolation technique to reduce the errors produces from the momentum equations in the partially wet cells. For all techniques decribed in the literature a specific discretization shoud be imlplemented to cope the problem of well-balancing in the presence of the wet/dry fronts [155]. It can be concluded that the major difficulty in this approach lies in the accurate calculation of the flow field as on a partially wet/cell due to unrealistic high oscillations when the water depth tends towards zero.

It is notable in the literature that, despite the moving grid accuracy in tracking waterfront position, this method is difficult to implement for complex topographies, especially when dry zones appear within the computational domain. Hence, the fixed grid method is most used in practice, though specific issues relevant to wet/dry treatment are still under investigation, such as the well-balancing of the flux and the source term, the conservation of mass and momentum during simulations. These properties should be verified in all situations including the transient flows experiencing flooding and drying over real complex topographies. Wetting and drying modelling must include a suitable numerical treatment of the source terms and wet/dry interfaces in accordance with the principle of conservation. In fact, the topography source term contains the bathymetry gradient, and sharp slopes due to abrupt variations in the irregular bathymetries and a very small water depth close to the wet/dry fronts are known to be responsible for numerical instabilities. Moreover during wetting and drying processes, the water depth becomes very small near the wet/dry interfaces which causes several instabilities. Particular attention should be paid to the bathymetry source term to simulate flows over non-flat beds [167].

To overcome these challenges, conventional shallow water equations were reformulated in a moving coordinates system. The computational domain changes over time are calculated only for the wet areas, before an efficient FVM is applied to solve SWEs in moving domains. The developed method satisfies the conservation property, offering a solution free from spurious oscillations in the moving wet/dry fronts. Not only a robust simulator of slowly varying wet/dry interfaces, this method is also suitable for rapidly varying ones, even those containing shocks or discontinuities.

1.2.1 Shallow water flow over deformable bed

Modelling of wave-seabed interaction is one of the longest standing challenges with which geotechnical engineers are faced; it is a key consideration in the design of offshore structures like pipelines and breakwaters. In addition to the floating/sinking objects on the seabed, such as mines or shipwrecks, the design of offshore structures for different environmental conditions has become an important enterprise [73]. Most shallow flow studies are carried out over fixed beds and few over mobile ones. Over the past decades, the development of efficient and accurate numerical models of nonlinear SWEs over variable beds has been an increasing focus of scientist and coastal engineers, due to their practical importance [17]. Researchers are currently working on developing an efficient and accurate approach to model the flows. This represents a great challenge due to the time and special scales the abrupt changes took places versus the evolution of the water free-surface [171]. One of the most important examples of this type of movement is the tsunami. Tsunamis are long-period sea waves, caused by the displacement of large bodies of water, such as in sudden depressions or uplifts of the seafloor, landslides, underwater volcanic eruptions, or earthquakes. In the latter event, large-scale elastic deformation, brought on by the earthquake rupturing process, provokes a spike in the potential energy of the oceans water column [256]. The power associated with these waves is devastating, which makes the predictions of these waves very important in effected areas. Modelling coastal morphology, however, is not straightforward, requiring the accurate representation of physical processes and the ability to propagate changes in bathymetry over broad time and vast spaces [230]. Wave-seabed interaction has been extensively examined by marine geotechnical engineers in recent years. One of the reasons for this growing interest is that a number of marine installations have been damaged by seabed-instability induced waves. The majority of existing studies are either uncoupled or involve only one-way coupling, which may not represent the real process in marine environments. Therefore, a coupling model is needed to supplement understanding of wave-seabed response. These efforts broadly comprise of two main methodologies:

- **Experimental techniques:** have been employed to assess these waves; very early experiments were carried out in 1844 by [193], who used a sinking box to generate waves. Later researchers in [229] hydraulically drive a vertical rectangular wall to transfer momentum into the water column and create waves. A comparison between numerical, analytical, and experimental data is conducted by researchers in [237], deducing that the nonlinear SWEs successfully reproduce the experimental results. A new hydraulic approach is introduced by researchers in [114] for movable bed wave generation. However, this model is unsuitable for modelling waves near coastlines [107]. In experimental modelling, the ability to generate different types of waves is valuable, as the data of

the generated waves are vital for the validation and calibration of the numerical models. Experimental methods are commonly expensive, lack reproducibility, and require large spaces to run.

- **Numerical techniques:** are contemporarily popular and a common means of determining bathymetric changes. Nonlinear SWEs, nonlinear Boussinesq models, and fully nonlinear potential models are the most commonly used. Adapted versions, which encompass the effects of turbulence, are also quite widespread. Given that water is an incompressible, inviscid fluid, with irrotational motion, the governing equations for water-wave motion are referred to as the fully nonlinear potential model and are utilized to model strongly nonlinear waves, also imposing appropriate boundary conditions on the free-surfaces [230]. Mathematical models are considered to be one of the best methods in understanding the dynamics of shallow water flows based on a sudden bed changes. In recent times, numerical solutions, including finite difference, finite element, and finite volume techniques, have mainly concentrated on fixed beds. Nevertheless, in order to reflect geomorphological changes, a fully coupled system must be devised. Researchers in [102] present a theoretical analysis of the Riemann problem for a free-surface flow over a movable bed. In their study, they devoted their attention to reciprocal interactions between the current and the bed in highly transient conditions. A fully coupled model, where mass and momentum exchanges, the result of sediment fluxes, are taken into account, is utilized. Numerical techniques provide more accurate results of wave-seabed interaction when compared to experimental data. However, a special source discretization, the selection of appropriate flux discretization, and time-stepping are crucial to the accuracy of these techniques and to avoid spurious oscillations at the interface and conserve the mass and momentum [29].

The research presented in this thesis is considered to be a step forward in the analysis of shallow water flows over deformable beds which are under the effect of localized force. A coupled finite element method/finite volume method has been investigated, the system is fully coupled at the interface, where the data is transferred. This method has several advantages. Firstly, it applies to steady flows over irregular beds. Secondly, it does not require either the nonlinear solution of algebraic equations or special front tracking. The model is accurate, stable, and preserves all flow features, including shocks and discontinuities, with a special treatment of the interface.

1.2.2 Uncertainty quantification for numerical simulation of free-surface flows

The input conditions of different shallow water applications involve a certain degree of uncertainty and, in most cases, follow some form of statistical distributions. Apart from being able to model these extreme flood events, the capability of accounting for the variability of the input parameters is an important element of hazard assessment [122]. Uncertainty in coastal and offshore engineering are either related to weather conditions, structural or bathymetry factors. In the first case, weather conditions are grouped into a number of parameters, according to probability distributions associated with wave, wind, and sea levels. Other elements are the density ratio of layers, friction coefficient, and fault deformation in the event of tsunamis [58].

These parameters are modelled statistically or experimentally, where measurement is a source of uncertainty.

Many parameters of shallow water equations are uncertain, due to the inherent randomness of natural processes and humankind's incomplete knowledge of them. These unknowns include initial and boundary conditions, data and coefficients determining wind stress, bed friction coefficients, such as Mannings, and the turbulent viscosity coefficient. To incorporate uncertain parameters into stochastic SWEs, the stochastic properties of different parameters that are considered uncertain, namely inflow boundary conditions, bed friction coefficient, and domain topography, are added to the system. Various parametrizations have been practised in flood modelling with these equations. Many researchers highlight the same, uncertain parameters in SWEs, with some of them treating the uncertain parameters in a probabilistic manner. As aforementioned, managing variables is essential to flood modelling practice. The uncertainty of SWE-based flood modelling derives from difficulties in obtaining precise knowledge of topography or inflow discharge data, to name only two examples. Minor uncertainties can have an amplified impact and allowing catastrophic events to occur unexpectedly. Thus, all uncertainties must be quantified, allowing their effects on the model results to be accounted for.

Most of the latest researches in shallow water models involve numerical schemes with deterministic input conditions for precisely defined topographies. However, little attention has been given to propagation uncertainty throughout the modelling process to the provision of risk-based approaches for different shallow water flows hazard assessments. Although various remedies to modelling input uncertainty exist, the most popular frameworks input uncertainty statistically, in the form of random parameters. The resulting equations are stochastic (random) partial differential equations. The solution must be sought in a stochastic sense and statistical quantities, such as the mean, variance, higher moments, confidence of intervals, and probability distribution function, are the objects of interest. The modelling and computation of solution statistics are highly nontrivial. Difficulties include the potentially large numbers of random variables to parametrize and the computational challenge of evaluating statistical moments which may need numerous PDEs solvers. Nevertheless, several numerical methods have been developed for uncertainty quantification in hyperbolic partial differential equations. In general, these methods come under three main categories:

- **Stochastic Galerkin method:** these are based on polynomial chaos expansion, expanding the sought of solution random field in terms of basis functions, orthogonal with respect to the underlying probability distribution. Projecting the resulting expansion into this orthonormal basis yields a system of partial differential equations for the underlying coefficients, which has the potential to be very large [58]. However, this approach has several drawbacks. Perhaps the biggest of these is that the resulting systems of PDEs for the polynomial chaos expansion(PCE) is not necessary hyperbolic and may not even be well-posed. A novel solution to this is provided by [233]. The authors propose a PCE expansion of the solution, random field in terms of the entropy; thus, it can be demonstrated that the resulting nonlinear conservation law processes a strictly convex entropy and, in turn, that the resulting nonlinear system of the PCE coefficient is hyperbolic. Even so, a large number of terms of this expansion might still be necessary for hyperbolic PDEs with low spatial and stochastic regularity. However, a large number of terms of this expansion might still be necessary for hyperbolic PDEs with low spatial and stochas-

tic regularity lead to very computationally costly solution. Furthermore, this method is computationally intrusive. Hence it appears that the stochastic Galerkin method is only suitable for hyperbolic problem with a very low number of uncertain parameters.

- **Stochastic collaction type:** in this method, the solution is sampled at a determined set of sample points in the entire stochastic space. This process is non-intrusive. However, these methods are of limited utility, requiring sufficient regularity of stochastic variables to employ tools such as sparse grids, which maintain the feasibility of the computational costs. Unfortunately, solutions of the uncertain nonlinear hyperbolic PDEs are not sufficiently regular. A possible alternative is the recently proposed stochastic FVM [42]. However, it is also limited to a moderate number of stochastic parameters.

- **Monte-carlo (MC) method:** This samples the probability space, solving the underlying deterministic PDE for each sample; the samples are combined to determine statistical information about the random field. Having said that, MC methods require a large number of samples to ensure a low statistical error rate. This slow convergence entails high computational costs and makes MC methods impractical for calculating uncertainty in complex shallow water flows. This flaw has inspired the development of Multi-level Monte-Carlo(MLMC) methods [174, 157], in which a nested sequence of space-time grids are drawn from the finest grids (those with the highest computational cost) and a very large number of samples are drawn from the coarsest grids (those with little computational cost). This subtly balances stochastic errors.

1.2.3 Optimal control for bed reconstruction

The study of open channel flows often requires an accurate modelling and representation of the channel bed topography to accurately predict hydrodynamic flows. Many numerical techniques have been developed to simulate open channel flows. The characteristics of these numerical methods differ, depending on the particular problem they address. They can be used to study dam-breaks, flood plain flows, hydraulic jumps and steady flows. Comparatively, very little has been done on the numerical reconstruction of the bedrock elevation data of open channel flows. In other words, whilst there has been tremendous progress in the hydraulic modelling of open channel flows, the accurate representation of channel bed topography is still a struggle [122]. Parameters such as bed elevation and roughness coefficients are required prior to the simulation of open channel flows. The level of discrepancy in these data has a direct impact on simulation results. The existing literature presents three main solutions to this inverse problem:

- **Experimental methods:** There have been significant developments in experimental techniques for assessing bed characteristics. Researchers in [148, 120] use Synthetic Aperture Radar (SAR) digital photogrammetry to profile the North Ashburton River in New Zealand; similarly, LiDAR, for the Yakima and Trinity river basins in the USA, is deployed by researchers in [59]. Data has been retrieved from the Jordan basin using underground sensors(23 in total) at different depths and locations, which reported every half an hour [16]. These experimental techniques are considered to be direct implementations; their observations can be used to validate the numerical results. However, these

techniques are always subject to a specific set of limitations. Sensors fail and maintenance operations are difficult and costly [271]. Additionally, the hostile conditions of rivers, oceans and seas, comprising of variable currents, animals attacks, and corrosion might easily cause temporal or permanent malfunctions, resulting in unstable or incomplete readings, if any at all [271].

- **Direct approach numerical method:** In the direct approach method, SWEs are rearranged and used for the inverse problem analysis. However, there is a difference between known and unknown parameters. The discretization of the equations governing inverse problems differs from those addressing the forward problem [259]. Despite the stability restriction, this approach is easy and quick [98]. The direct solution is not a common approach to an inverse problem, which is embedded in the framework of the very few inverse problems. This strategy uses the governing equations of the forward problem to solve the model parameters, with the help of equation rearrangement if necessary [116]. The process is analogous to the determination of the observable parameters in the forward problem analysis. And yet, this approach is not always possible. The governing equations of the forward problem must allow convenient rearrangement for the determination of the unknown model parameters [98]. Thus, this approach is restricted to some inverse problems. The steps involved in this solution approach are given as:

  - Solution of the forward problem to distinguish measurable parameters from known model parameters. In this step, different hydraulic flow solution approaches can be used to produce numerical test cases.

  - Rearranging the governing equations in such a way that model parameters can be evaluated from measured ones.

  - Validating the approach; solving the unknowns and comparing the results to numerical test cases.

  This technique has been implemented by some researchers, for example, researchers in [116] well implement this technique for substrate shape identification from the know free-surface data in thin film flows. On the other hand, researchers in [98] reconstruct the river bed topography from free-surface data in one-dimensional domain.

- **Optimization-based solution approach:** is well-known for solving inverse problems. In this approach, a minimization function is defined to determine the model parameters iteratively. The following steps are involved in the parameter identification:

  - Solving the forward problem to determine measurable parameters from known model parameters. This is an important step because the minimization function (objective function) requires a reliable solution approach for the forward problem.

  - Defining a minimization function, which relates the observed and calculated data and determines their differences.

– Guessing the value of a model parameter, based on the system's previous numerical solutions, and computing the objective function.

– Estimating sensitivity to identify direction in the parameter space, which leads to a decrease of the objective function.

– Taking the largest possible step in that direction and updating the value of the unknown parameter, continuing the iteration until the error limit is reached. The resulting value of the model parameter, which minimizes the minimization function, is then regarded as the solution of the inverse problem.

1.3 Project objectives

The primary objective of this project is the development of techniques to simulate the effect of underground movement on the shallow water waves, using different coupling methods at the interface. In addition to full study for the stresses affecting the underground movement. As many models consist of differential equations, these problems may require the estimation of the time-dependent state variable and the use of noisy measurements. However, it should be acknowledged that mathematical modelling is always approximate and that error is a permanent feature. For an operational prediction system, real-world information must be added to address such uncertainty. The second goal of this study is to develop an accurate and robust optimal control techniques for bed reconstruction. The basic components for this operational forecasting system are: a network of observed data, and a numerical model for the data assimilation. To achieve these goals a full study of the forward problem as the following steps should be investigated:

- Developing a class of numerical methods that are simple, easy to implement, and accurately solve the moving wet/dry fronts in shallow water flows, without relying on complicated techniques, to solve for the water waves when reaches dry areas.

- Developing an accurate and efficient simulation of shallow water flows, under conditions of abrupt change to the bathymetry, including the effect of coupling at the interface, the bed friction force, and the influence of hydrostatic distribution forces.

- Exploring the ramifications of bed uncertainty for shallow water flow. Uncertainty parameters are quantified in a class of numerical methods for free-surface flows in order to examine its effects on the water flow.

- Developing an adaptive optimal control technique for bed reconstruction in shallow water flows, based on the given observations from the forward problems, fully studied in the previous steps and with the effect of uncertainty in the measured data.

Each of the specific goals is devised to ensure that their effects on the models are fully understood. The goal is to create a modular system, where features can be included and reviewed as

required. The presented models are adjusted for different simulation examples and test cases to ensure best computational return.

1.4 Thesis structure

This thesis is comprised of three major parts. In the first, the solution to shallow water flows over deformed beds is presented. The coupling techniques between the water free-surface and bed deformation, effects of bed friction, deformed soil stresses, and hydrostatic pressure distribution are all accounted for. In addition to presenting a new model for solving the wet/dry interface issue. In the second part, the effect of uncertainties such as bed topography and the Manning coefficient, in the single, two, and multi-layer models is explored. This study offers a clear understanding of how numerical models are affected by these uncertainties. The first two parts represent the forward model to solve for the water height, speed, and energy under different conditions. The results of these forward models considered to be the third part begins. In this third section, an adaptive optimal control technique, based on the previously supplied observed data, is given. Bed topography is inferred from known free-surface elevation data in single-layer, shallow water flows. This thesis is structured as follows:

- **Chapter 1** introduces the subject problem and describes the objectives of the thesis. It details the research motivations and the significance of the currently-encountered problems. A brief overview of the classes of techniques available is given. The study objectives are also outlined, with a brief explanation of the developed techniques. Equally, this chapter reviews the existing literature, evaluating different models and offering an overview of the widely-applied mathematical and numerical methods. In the first section, SWEs are described in terms of their main features and derivations. Proposed solutions to the wet/dry interface, from the original basic principle to the present day, are then reviewed. This contains a critical assessment of the respective advantages and disadvantages. In the third section, previous finite volume methods for water flow over deformed beds are examined, then the various techniques for addressing uncertainty in the hydraulic models parameters are covered. Finally, different adaptive techniques for bed reconstruction are discussed and evaluated. This chapter provides a comprehensive context, which is the bedrock of this study. In the last section, the structure of this thesis is detailed, including its contributions to theory and practice.

- **Chapter 2** develops new techniques for solving the wet/dry interface problem, based on the parametrization and partially wet cell concepts. The aim of this chapter is to develop a class of numerical methods that are simple, easy to implement, and accurately solve the moving wet/dry interface. The main features of the developed techniques are on one hand, the capability to satisfy the significant moving wet/dry fronts and, on the other hand, the achievement of strong stability for simulations of slowly, as well as fast varying wet/dry interfaces, embracing all shocks, discontinuities, and fluxes, with well-balanced source terms. The presented techniques are found to be conservative and accurate as no oscillations appear in the final results. The techniques are tested using different benchmarks examples and compared to experimental data, presenting accurate results.

- **Chapter 3** investigates the problem of shallow water flows under the condition of an abruptly changing bathymetry. In this section, an accurate and efficient computational

approach to simulate such flows, which pose a great challenge, due to the difference in temporal and spatial scales, are designed. The free-surface flow, modelled by SWEs, coupled with the sudden changes in bathymetry, is numerically investigated. However, deformations in the topography can be caused by a localized force, which propagates waves with different amplitudes and frequencies. The coupling conditions at the interface are also investigated, implementing a well-balanced FVM, which uses non-uniform grids, to avoid interpolation at the interface. The method proves to be fast and accurate and there is no need to refine the mesh in the finite volume shallow water system, as the control volumes are non-uniform and formed from the finite element surface nodes. This method reduces inaccurate results from interface interpolation and can be employed in different test cases and benchmarks with no major modifications to the presented techniques.

- **Chapter 4** presents a hybrid finite element/finite volume method for solving free-surface run-up problems over deformable beds. The system is fully coupled at the interface utilizing transfer conditions at the interface between the water flow and the seabed. This allows for hydrostatic pressure and friction forces to be implemented for the elastostatic equations, whereas deformed beds are accounted for in the SWEs by the bathymetric forces. A treatment of partially wet cells near the wet/dry boundaries is contained in this finite volume element method, as well as consideration of bed friction near wet/dry boundaries. Coupling conditions at the interface are also investigated in the current study, with a two-mesh procedure proposed for the transfer of information through the interface. The proposed model is tested on different examples, such as one-dimensional, single-layer wave run-up and the problem of lock-exchange in one-dimensional, two-layer case. Overall, this method is found to be accurate, well-balanced, and stable; it accurately resolves all flow features where the wet/dry interface exists.

- **Chapter 5** introduces a model to examine the performance of the shallow water numerical methods in presence of uncertainty. The aim is to evaluate the uncertainty of hydraulic states (water height and water velocity), resulting from the presumed uncertainty of bathymetric forces. This class of methods is becoming increasingly used in the hydraulics community, in both its intrusive and non-intrusive forms. The impact on uncertainties in the bathymetry and Manning coefficient is numerically assessed. Numerical results for both one-dimensional single-layer and two-layer shallow water models demonstrate the high resolution of the proposed techniques and confirm their capability of providing efficient uncertainty quantification for the simulation of free-surface water flows over stochastic beds.

- **Chapter 6** extends the uncertainty quantification technique implemented in the previous chapter to one-dimensional multi-layer shallow water flows. The results demonstrate that, in some hydraulic applications, a highly accurate numerical method yields an increase in its uncertainty. On the other hand, when the complexity of the physics increases, these highly accurate numerical methods display less uncertainty compared to low accuracy ones. The presented model offers a deeper insight into the effect of the uncertainty of bottom topography, bed friction, inter-layer viscosity, and wind stress on the numerical

model, is swift and accurate to implement.

- **Chapter 7** is the final step of this thesis, proffering an adaptive optimal control technique to numerically identify the underlying bed topography from a given dataset of free-surface observations (the results of the forward models presented in the previous chapters). In this approach, a minimization function is defined to iteratively determine the model parameters. The proposed technique can be interpreted as a fractional-stage scheme. In the first stage, the forward problem is solved to determine the measurable parameters from known data. In the second stage, adaptive control techniques are implemented, combining the optimality of observation data, in order to obtain an accurate estimation of the topography. The main features of this method are its ability to solve different, complex geometries, without requiring the rearrangement of the governing equations, as is required in other cases. Numerical results are presented for different test cases under different number and location of observations and using different numerical solvers with the existence of uncertainty in the observed data. The obtained results demonstrate the reliability and accuracy of the proposed techniques. In general, this model successfully combines all of the previous work , creating an advanced and optimal shallow water modelling tool.

- **Chapter 8** concludes the thesis, evaluating the limitations and advantages of the developed models. A brief summary of each of the developed techniques is provided, outlining the main ideas and contributions of the work completed and its relevance. It goes on to highlight possible avenues for future research, offering recommendations based on the investigative experience.

Chapter 2

Numerical treatment of moving wet/dry fronts in shallow water flows

Severe extreme natural phenomena like tsunami flooding and dam-break problems cause a huge financial loss to all over the world, and it causes major damages. Floods are a temporary condition of complete or partial inundation of dry land area. Water floods claim thousands of lives every year and render millions homeless in the world. Flood disasters account about a third of all natural disasters through the world by number of economic losses [34]. Dam-break can cause significant loss of human lifes, especially when located in highly populated regions. An example of the dam-break disaster is the Malpasset dam failure in France which occurred in 1959 caused 110 missing people and 384 deaths [267]. The same problem with tsunami where the destructive power of tsunami is a mixture of its wave height and speed, creating a huge force against any thing it hits. Tsunami can be generated by any displacement under water, and commonly it happened from the plate movement under water or by the volcanic eruption. In recent years, there have been continuous efforts to enhance the understanding of these phenomena. Real time measurements in the field is difficult and experiments in the laboratory held only for certain scales and under different limitations. The mentioned problems are few but not all which show an important development of complete shallow water systems that studies all the effects together to help developing an emergency plan in the smart cities for unlikely disasters like flooding, dam-breaks and tsunami.

Shallow water flows widely exist in nature such as rivers, open channels and estuaries. These flows have the same characteristics that the horizontal scale is much greater than the vertical one. Ignoring the vertical length and assume the pressure to be hydrostatically distributed, then the shallow water equations can be derived from the depth averaged Navier-stokes equations. In general, the shallow water flows include a complex phenomena, like wave over-topping or wave run-up which often lead to drying and wetting boundary problem. It is easy to recognize that with this movement, the computational domain changes constantly which affects the accuracy of the calculations. The solution of the wet/dry interface becoming increasingly important where the velocities normal components set to zero which leads to negative water depth and numerical instability during the simulations.

A large number of researches presented to solve the problem of shallow water flows with the wet/dry interface. Many numerical methods were developed to solve these equations such finite difference method [221], finite element method [24] and finite volume method [173]. Finite volume method has a superiority when modelling high speed flows than the other methods and

it has several advantages. Firstly the mass, momentum and energy were conserved during the simulation and the flexibility for applying over different irregular domains [161]. Different finite volume methods were developed to solve the shallow water flow with wet/dry interface. The techniques that commonly used are the characteristics method and the Lagrangian method, these techniques develop a grid which is capable of following the discontinuity fronts [3, 5]. The drawback of this method is the difficulty in correctly updating the fronts location when a source term applied to the problem, in addition to the complexity in extending this method to more than one space dimension. Recently, researchers develop new techniques to solve the same problem using approximate solvers for the Riemann-problem [4, 23]. These techniques are of general types: moving grid and fixed grid methods. The use of the cell classification concept into wet/dry and partially wet/dry cells based on the water level at each cell leads to a spurious level gradient at the wet/dry interface which leads to a solution that can not guarantee the conservation property (C-property) in the final solution. Moving grid methods based on continuous updated mesh, which means that a group of points permanently located on the domain grid at each time step, then the mesh continuously updated to match the moving fronts. The application of this method is limited to simple channel flows, because of its large elements distortion and it is used only for limited applications with flat bed. Using all of the previous methods in solving wet/dry interface simulations but specific issues relevant to the wet/dry interface simulations are still under investigations and could be summarized as follows:

- Well-balancing the discretization of fluxes and well-balancing the source term.
- Conserving the mass, momentum and energy in the presence of the wet/dry interface.

The previously mentioned properties should be guaranteed in any developed technique used for solving the problem of shallow water flow with wet/dry interfaces including all the situations with flat or non-flat beds. This is a general overview of the shallow water wet/dry interface solution techniques. Many other works can be find in the literature, but the described techniques seem to be the most used. In this chapter a new developed technique will be provided for solving the problem of the wet/dry interface based on the parametrization concept. The aim is to develop a class of numerical methods that are simple, easy to implement and accurately solve the moving wet/dry interface without relying on complicated techniques. The main features of such finite volume scheme are on one hand, the capability to satisfy the conservation property resulting in numerical solutions free from spurious oscillations in significant moving wet/dry fronts and on the other hand the achievement of strong stability for simulations of slowly varying wet/dry interfaces as well as rapidly varying wet/dry interfaces containing all shocks or discontinuities. Moreover, the numerical formulation is devised so that the discretizations of gradient fluxes and source terms are well balanced.

Nonlinear shallow water equations are typically used to model free-surface flows, river and lake hydrodynamics, and long wave run-up, as well as flows in open channels, lakes, reservoirs, coastal areas, estuaries and harbors among others [225, 49]. Many of these applications involve moving fronts in which wetting and drying over variable topography occurs, and numerically solving these processes is becoming increasingly important. For instance, predictions of flooding due to a storm surge, breached dam, or overtopped levee are crucial for disaster planning. Wave run-up estimates are needed for beach and coastal structure design [154]. Descriptions of inundation in both estuarine tidal flats and riverine flood plains are also key for predicting the transport of suspended and dissolved substances. The hydrodynamics of shallow water

flows on wetting and drying areas is of great interest in a wide range of physical flows. Such shallow water flows give rise to challenging problems in both theoretical analysis and numerical simulation. Numerical simulations of shallow water models have been devoted huge efforts so far and as a consequence, many numerical models have been developed for engineering applications in hydraulics. In real case simulations, treatment of moving wet/dry fronts is getting more and more popular in the hydraulics community to represent the complex flow features at river banks and coastal lines. The numerical approximation of water flows over wetting and drying areas requires important choices and compromises to be made when simulations of the water flow are carried out. These compromises are necessary to minimize both artificial numerical dissipation and dispersion. The resulting numerical dissipation may severely damp the free-surface flow producing exaggerated inaccurate results whereas, the artificial numerical dispersion may introduce nonphysical oscillations known by wiggles. In general, conservative Eulerian algorithms such as those based on finite volume shock-capturing techniques perform very well when applied to shallow water flows over fully wetted areas, see for example [238]. However, when such an algorithm is employed to solve shallow water flows over wetting and drying areas, numerical inaccuracies usually occur at the wet/dry interfaces due to the loss of entropy property in the discretization. To overcome this difficulty, many techniques and methods have been developed in the past two decades with an even increasing interest, see for instance [238, 82, 13, 44, 70, 92, 150, 184, 205, 270] and further references are therein. Among them, some of the resultant algorithms may not maintain the conservation property in the process of enforcing states at the moving wet/dry interface so as to suppress any undesired numerical oscillations. The objective of this study is to devise a stable, monotone and accurate numerical method able to approximate solutions to shallow water flows over wetting and drying areas.

A new numerical model for moving wet/dry fronts in shallow water equations using the parametrization concept and the point-wise Riemann solver is presented. In the current model the nonlinear shallow water equations are reformulated using the speed of the wet/dry interface. The new system is solved on the wet domain only using the well-balanced finite volume method. The object of the current work is to develop a numerical approach able to accurately approximate solutions to moving wet/dry fronts in shallow water flows. The aim is to develop a class of numerical methods that are simple, easy to implement, and accurately solve the moving wet/dry fronts in shallow water flows without relying on complicated techniques. The proposed finite volume method can be interpreted as a fractional stage scheme. In the first stage, the transport terms are solved by integrating the system along the characteristics defined by the interface velocity, while the numerical solutions are computed through a finite volume formulation of flux form in the second stage. The numerical formulation is devised so that the source terms and fluxes are discretized using well-balanced techniques. These features are verified using several test examples of shallow water flows over wetting and drying areas. Results presented in this chapter show high resolution of the proposed techniques and permit the straightforward application of the method to more complex, physically based shallow water flows.

This chapter is structured as follows. In section 2.1, the problem statement for moving wet/dry fronts in shallow water flows is presented. Numerical solution of the parametrized shallow water equations is formulated in section 2.2. This section includes the finite volume discretization of the system and the solution of the moving fronts. Section 2.4 is devoted to numerical results for several test examples in shallow water flows. The partially wet/dry treatment method is

presented in the next section. Concluding remarks end the chapter in section 2.6.

2.1 Equations for wet/dry fronts in shallow water flows

The shallow water equations can be derived by depth-averaging the Navier-Stokes equations, neglecting the vertical acceleration of water particles, and taking the pressure distribution to be hydrostatic, see [70, 238] among others. In one space dimension, ignoring viscous terms and surface stresses, the shallow water equations read

$$\begin{aligned} \frac{\partial h}{\partial t} + \frac{\partial (hu)}{\partial x} &= 0, & x \in [a,b], \\ \frac{\partial (hu)}{\partial t} + \frac{\partial}{\partial x}\left(hu^2 + \frac{1}{2}gh^2\right) &= -gh\frac{\partial z}{\partial x}, & x \in [a,b], \end{aligned} \tag{2.1a}$$

where $[a,b]$ is the fixed computational domain, $z(x)$ the function characterizing the bottom topography, $h(t,x)$ the height of the water above the bottom, g the acceleration due to gravity, $u(t,x)$ the flow velocity. The equations (2.1a) have been widely used to model water flows, flood waves, dam-break problems, and have been studied in a number of books and papers, see for instance [225, 238, 49, 149]. Computing their numerical solutions is not trivial due to the nonlinearity in the flux function, the presence of the convective terms, and the coupling of the equations through the source term. In many applications, the solutions of equations (2.1a) present steep fronts and even discontinuities, which need to be resolved accurately in applications and often cause severe numerical difficulties, compare [149, 238]. In the current study we are interested in moving wet/dry fronts in shallow water flows for which the equations (2.1a) are solved subject to the following initial conditions

$$h(0,x) = \begin{cases} h_0, & \text{if} \quad x \le x_0, \\ 0, & \text{if} \quad x > x_0, \end{cases} \qquad u(0,x) = u_0, \tag{2.1b}$$

where $x_0 \in [a,b]$ is the initial location of the wet/dry interface, h_0 and u_0 are given water height and water velocity, respectively, as shown in Figure 2.1 for more illustrations. Note that most of numerical methods for solving the equations (2.1a) perturb the dry state (zero water height) using a wetted threshold above which the solution state is considered to be dry. This is mainly used to avoid division by zero for updating the water velocity during the simulation process. However, perturbing the water height may result in inaccuracy in the computed solutions and may lead to false location of the wet/dry fronts on the coastal zones. Furthermore, if due to numerical oscillations the water height h becomes negative, the calculation will simply break down.

In the present work an alternative formulation of the equations (2.1a) to deal with wet/dry fronts is presented. The idea consists of rewriting the shallow water equations in a moving domain and solve the obtained model only for the wetted area. The advection of the wet/dry interface is achieved by using the speed of the water and the problem statement becomes: solve the system

$$\begin{aligned} \frac{\partial h}{\partial t} + \frac{\partial (hu)}{\partial x} &= 0, & x \in \Big[a, \xi(t)\Big], \\ \frac{\partial (hu)}{\partial t} + \frac{\partial}{\partial x}\left(hu^2 + \frac{1}{2}gh^2\right) &= -gh\frac{\partial z}{\partial x}, & x \in \Big[a, \xi(t)\Big], \end{aligned} \tag{2.2a}$$

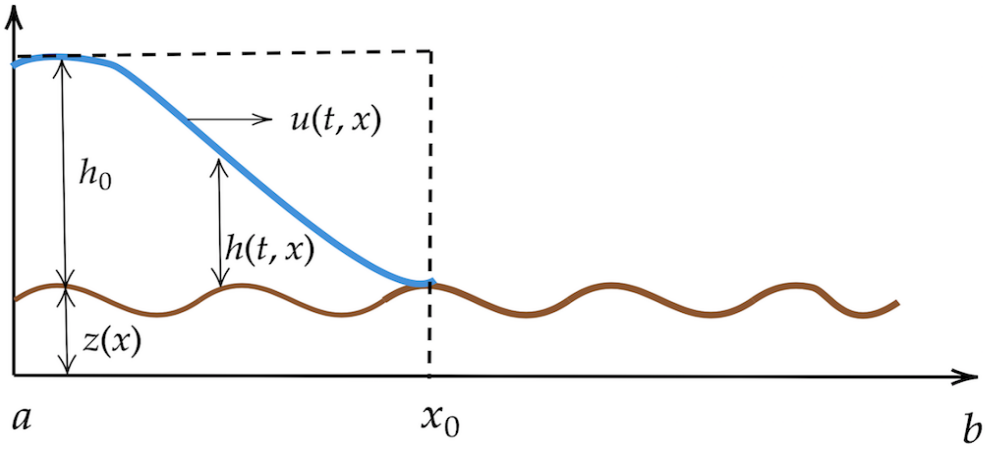

Figure 2.1: Illustration of the shallow water system including wet/dry interface.

where the interface $\xi(t)$ is defined by the ordinary differential equation

$$\begin{aligned} \dot{\xi}(t) := \frac{d\xi(t)}{dt} &= s, \\ \xi(0) &= x_0, \end{aligned} \tag{2.2b}$$

for a given speed s. Based on the analysis reported in [237], for the application to a moving wet/dry interface the maximum speed of the flow propagation in the shallow water system is bounded by $|u| + 2\sqrt{g\,h}$. Therefore a possible choice for capturing all information in the domain $[a, \xi(t)]$ is simply

$$s = |u| + 2\sqrt{g\,h}. \tag{2.3}$$

In general, other velocities s might be used to move the front in the computational domain which allows also to decouple the solution of equations (2.2a) and (2.2b). Considering the shallow water equations (2.1a) equipped with the initial data (2.1b), the solution to this Riemann problem consists of a one-rarefaction wave. The speed at the interface x_0 is therefore $u_0 + 2\sqrt{gh_0}$.

It is clear that the shallow water equations (2.2) have to be solved in a time-dependent computational domain requiring a mesh at each time step. In order to avoid this difficulty we perform a change of coordinates. Thus, the new coordinates (t, y) are defined as

$$t = t, \qquad y = \frac{x - a}{\xi(t) - a},$$

and the new solution variables in the transformed coordinate system as

$$\begin{aligned} H(t, y) &= h\Big(t, y\big(\xi(t) - a\big) + a\Big), \\ U(t, y) &= u\Big(t, y\big(\xi(t) - a\big) + a\Big), \\ Z(t, y) &= z\Big(t, y\big(\xi(t) - a\big) + a\Big). \end{aligned} \tag{2.4}$$

Hence, after some algebra, the shallow water equations (2.2a) transform to

$$\begin{aligned} \frac{\partial H}{\partial t} - \frac{\dot{\xi} y}{\xi - a}\frac{\partial H}{\partial y} + \frac{1}{\xi - a}\frac{\partial (HU)}{\partial y} &= 0, \qquad && y \in [0,1], \\ \frac{\partial (HU)}{\partial t} - \frac{\dot{\xi} y}{\xi - a}\frac{\partial (HU)}{\partial y} + \frac{1}{\xi - a}\,\frac{\partial}{\partial y}\left(HU^2 + \frac{1}{2}gH^2\right) &= -g\frac{H}{\xi - a}\frac{\partial Z}{\partial y}, && y \in [0,1]. \end{aligned} \tag{2.5}$$

Note that the above equations for (H, HU) are now defined in the fixed domain $(t, y) \in \mathbb{R}^+ \times [0, 1]$. The transformation is well-defined provided that $\xi(0) > a$ and $s \geq 0$. These conditions are satisfied for the case of a moving front in a dry area. Furthermore, boundary conditions at $x = a$ are not affected by this transformation. Introducing the advective derivative of any physical variable w as

$$\frac{Dw}{Dt} = \frac{\partial w}{\partial t} - \frac{\dot{\xi}\, y}{\xi - a}\frac{\partial w}{\partial y}, \tag{2.6}$$

the shallow water equations (2.5) reduce for $y \in [0, 1]$ to

$$(\xi - a)\frac{DH}{Dt} + \frac{\partial (HU)}{\partial y} = 0, \tag{2.7a}$$

$$(\xi - a)\frac{D(HU)}{Dt} + \frac{\partial}{\partial y}\left(HU^2 + \frac{1}{2}gH^2\right) = -gH\frac{\partial Z}{\partial y}. \tag{2.7b}$$

For simplicity in the presentation the equations (2.7) in a conservative form are rewritten as

$$(\xi - a)\frac{D\mathbf{W}}{Dt} + \frac{\partial \mathbf{F}(\mathbf{W})}{\partial y} = \mathbf{S}(\mathbf{W}), \tag{2.8}$$

where

$$\mathbf{W} = \begin{pmatrix} H \\ HU \end{pmatrix}, \qquad \mathbf{F}(\mathbf{W}) = \begin{pmatrix} HU \\ HU^2 + \frac{1}{2}gH^2 \end{pmatrix}, \qquad \mathbf{S}(\mathbf{W}) = \begin{pmatrix} 0 \\ -gH\frac{\partial Z}{\partial y} \end{pmatrix}.$$

It should be stressed that, the solution of the parametrized equations (2.7) is to be computed in a fixed domain $[0, 1]$. In addition, the system (2.7) retains the same structure for the physical fluxes as the original shallow water equations (2.1a). Remark that once the solution (H, U) of the system (2.7) and (2.2b) is computed, the solution (h, u) of the system (2.1a) can easily be recovered using the transformation (2.4). It is also well-known that modification of conservation laws lead to changes in the shock speed, see for example [151]. Here, the eigenvalues of the transformed system in the convective variables are

$$\lambda_1 = \frac{u - \sqrt{gh}}{\xi - a}, \qquad \lambda_2 = \frac{u + \sqrt{gh}}{\xi - a}. \tag{2.9}$$

Clearly, if the front speed $s = 0$ then the transformation simply scales the computational domain in the space coordinates but not in the time variable. In the simplest case of a linear advection equation for fixed (positive) velocity u

$$\frac{\partial h}{\partial t} + u\frac{\partial h}{\partial x} = 0, \qquad h(t, 0) = h_0(t),$$

It is easy to verify that the solution to the advection equation with compactly supported initial data $h_0(x)$ in $[0, \xi(t)]$ with $\xi'(t) > 0$ and $\xi(0) > 0$ coincides with the solution $H(t, y)$ to the parametrized equation

$$\frac{\partial H}{\partial t} - \frac{\xi'(t) y}{\xi} \frac{\partial H}{\partial y} + \frac{u}{\xi} \frac{\partial H}{\partial y} = 0, \qquad H(t, 0) = h_0(t),$$

where $H(0, y) = h_0\left(y\xi(0)\right)$. It should also be noted that the new parametrized system (2.7) satisfies the still-water equilibrium. Recall that for the steady state with still water $u(t, x) = 0$, the momentum equation in the original system (2.1a) yields

$$h(t, x) + z(x) = c, \tag{2.10}$$

where c is a positive constant. This property (known by C-property) is needed to be preserved at the discrete level to reconstruct a well-balanced method [30]. To derive the well-balanced scheme, the equations (2.2) have been rewritten in terms of the total height $\eta(t, x) = h(t, x) + z(x)$. A similar procedure may be applied in the parametrized system (2.7). We also consider that the rescaled water height $H(t, y)$ and the rescaled water discharge $Q(t, y) = H(t, y)U(t, y)$, and define the total water depth $\nu(t, y)$ as

$$\nu(t, y) = \eta\big(t, y\left(\xi(t) - a\right) + a\big) = h\big(y\left(\xi(t) - a\right) + a\big) + z\big(y\left(\xi(t) - a\right) + a\big) = H(t, y) + Z(t, y).$$

Hence, at still water equilibrium $U(t, y) = 0$, the parametrized system (2.7) reduces to

$$\begin{aligned} -y\dot{\xi}\frac{\partial}{\partial y} H(t, y) &= 0, \\ \frac{1}{2}\frac{\partial}{\partial y}\left(gH^2(t, y)\right) &= -gH(t, y)\frac{\partial}{\partial y} Z(t, y). \end{aligned}$$

Since at the steady state $\dfrac{d\xi}{dt} = 0$, we obtain

$$H(t, y) + Z(t, y) = C, \tag{2.11}$$

where C is a positive constant. Thus, the proposed transformation preserves the hydrostatic reconstruction and in the case of $u(t, x) = 0$ the same techniques might be used to develop a well-balanced discretization. Note however, that in a finite volume method for the rescaled equations (2.7) one needs to account for the additional temporal dependence of the bottom profile due to the rescaled bed $Z(t, y) = z(y(\xi(t) - a) + a)$.

2.2 Well-balanced finite volume methods

To approximate numerical solutions of the shallow water equations (2.7) a class of well-balanced finite volume discretizations using different methods to reconstruct the numerical fluxes are considered. This method is adapted according to the parametrized equations (2.7) including advective terms and modified bottom beds. The presented methods use an operator splitting where the transport part and the conservation part are treated separately. The major part of this section is devoted to the treatment of source terms in (2.7) using additional corrections to obtain a well-balanced finite volume method. The numerical method proposed for approximating solutions to equations (2.8) can be interpreted as a fractional step technique where the

advective part is decoupled from the conservative part in the temporal discretization. Thus, at each time step the new water height and discharge are updated by first solving the advective equation

$$(\xi - a)\,\frac{D\mathbf{W}}{Dt} = 0, \tag{2.12}$$

then the conservation system

$$\frac{\partial \mathbf{W}}{\partial t} + \frac{\partial \mathbf{F}(\mathbf{W})}{\partial y} = \mathbf{S}(\mathbf{W}). \tag{2.13}$$

Discretizing the space domain in cells $[y_{i-\frac{1}{2}}, y_{i+\frac{1}{2}}]$ with same length Δy for sake of simplicity, and dividing the time interval into subintervals $[t_n, t_{n+1}]$ with uniform size Δt. Here, $t_n = n\Delta t$, $y_{i-\frac{1}{2}} = i\Delta y$ and $y_i = (i+\frac{1}{2})\Delta y$ is the center of the control volume. Using the notation $w_i(t)$ to denote the space average of a function $w(t,x)$ in the cell $[y_{i-\frac{1}{2}}, y_{i+\frac{1}{2}}]$ at time t, by $w_i^n = w_i(t^n)$, and by $w_{i+\frac{1}{2}}$ to denote the numerical flux at $y = y_{i+\frac{1}{2}}$ and time t,

$$w_i(t) = \frac{1}{\Delta y}\int_{y_{i-\frac{1}{2}}}^{y_{i+\frac{1}{2}}} w(y,t)dy, \qquad w_{i+\frac{1}{2}}(t,y) = w(y_{i+\frac{1}{2}}, t).$$

To solve the advection equation (2.12) two steps are required namely, the computation of characteristic trajectories and the interpolation procedure. Both steps are crucial to the overall accuracy of the method of characteristics. For each mesh point $y_{i+\frac{1}{2}}$ the characteristic curves $Y_{i+\frac{1}{2}}$ associated with (2.6) are the solutions of the initial-value problem

$$\begin{aligned} \frac{dY_{i+\frac{1}{2}}(\tau)}{d\tau} &= v_{i+\frac{1}{2}}\Big(\tau, Y_{i+\frac{1}{2}}(\tau)\Big), \qquad \tau \in [t_n, t_{n+1}], \\ Y_{i+\frac{1}{2}}(t_{n+1}) &= y_{i+\frac{1}{2}}, \end{aligned} \tag{2.14}$$

where $v(\tau, y) = -\dfrac{\dot{\xi}(\tau)y}{\xi(\tau) - a}$. Where $Y_{i+\frac{1}{2}}(\tau)$ is the departure point at time τ of a particle that will arrive at gridpoint $y_{i+\frac{1}{2}}$ in time t_{n+1}. The method of characteristics does not follow the flow particles forward in time, as the Lagrangian methods do, instead it traces backwards the position at time t_n of particles that will reach the points of a fixed mesh at time t_{n+1}. The solutions of (2.14) can be expressed as

$$Y_{i+\frac{1}{2}}(t_n) = y_{i+\frac{1}{2}} - \int_{t_n}^{t_{n+1}} v_{i+\frac{1}{2}}\left(\tau, Y_{i+\frac{1}{2}}(\tau)\right) d\tau. \tag{2.15}$$

For a velocity field explicitly given independent of the solution, the integral in (2.15) can be determined analytically. In other general cases, this integral can be calculated using a second-order extrapolation based on the mid-point rule which is accurate enough to maintain a particle on its curved trajectory.

Once the characteristics curves $Y(t_n)$ are known, the method of characteristics advects the solution of (2.7) at instant t_{n+1} as

$$\widehat{\mathbf{W}}(t_{n+1}, y) := \mathbf{W}\left(t_n, Y(t_n)\right). \tag{2.16}$$

Note that the advection equation (2.12) can also be solved by assuming that its exact solution in an unbounded domain is given by

$$\mathbf{W}(t,y) = \mathbf{W}_0\left(y\frac{\xi(t)}{\xi(0)}\right),$$

where $\mathbf{W}_0$ is the initial condition associated with the system (2.8). Hence, the exact solution to the advection equation in the time interval $[t_n, t_{n+1}]$ is

$$\widehat{\mathbf{W}}_i^n := \mathbf{W}^n \left(y_i \frac{\xi^{n+1}}{\xi^n} \right). \tag{2.17}$$

Notice that in general, the departure points $Y(t_n)$ do not coincide with the spatial position of a gridpoint. Assuming a suitable approximation is made for $Y(t_n)$, the solution $\widehat{\mathbf{W}}(t_{n+1}, y)$ in (2.16) should be obtained by interpolation from known values at the gridpoints in the host cell of the departure points. The interpolation procedure used is the cubic spline interpolation most commonly used in practice. Other interpolation procedures can also be applied.
Integrating equations (2.8) along the characteristics with respect to time and space over the time-space control domain $[t_n, t_{n+1}] \times [y_{i-\frac{1}{2}}, y_{i+\frac{1}{2}}]$ the following discrete equation is obtained

$$\mathbf{W}_i^{n+1} = \widehat{\mathbf{W}}_i^n - \frac{\Delta t}{\Delta y} \left(\widehat{\mathbf{F}}_{i+\frac{1}{2}}^n - \widehat{\mathbf{F}}_{i-\frac{1}{2}}^n \right) + \frac{\Delta t}{\Delta y} \int_{y_i - \frac{1}{2}}^{y_i + \frac{1}{2}} \mathbf{S}(\widehat{\mathbf{W}}^n)\, dy, \tag{2.18}$$

where $\widehat{\mathbf{F}}_{i\pm\frac{1}{2}}^n = \mathbf{F}\left(\widehat{\mathbf{W}}_{i\pm\frac{1}{2}}^n \right)$ are the numerical fluxes at $y = y_{i\pm\frac{1}{2}}$ and time $t = t_n$. The spatial discretization (2.18) is complete when a numerical construction of the fluxes and source terms are chosen. In general this step can be carried out using any finite volume method developed in the literature for solving hyperbolic systems of conservation laws, see for example [151, 238]. In the current study the following methods are considered:

Lax-Friedrichs method [243]:

$$\widehat{\mathbf{F}}_{i+\frac{1}{2}}^n = \frac{1}{2} \left(\mathbf{F}\left(\widehat{\mathbf{W}}_{i+1}^n \right) + \mathbf{F}\left(\widehat{\mathbf{W}}_i^n \right) \right) + \frac{\Delta y}{2\Delta t} \left(\widehat{\mathbf{W}}_i^n - \widehat{\mathbf{W}}_{i+1}^n \right). \tag{2.19}$$

Rusanov method [45]:

$$\widehat{\mathbf{F}}_{i+\frac{1}{2}}^n = \frac{1}{2} \left(\mathbf{F}\left(\widehat{\mathbf{W}}_{i+1}^n \right) + \mathbf{F}\left(\widehat{\mathbf{W}}_i^n \right) \right) + \frac{1}{2} \lambda \left(\widehat{\mathbf{W}}_i^n - \widehat{\mathbf{W}}_{i+1}^n \right), \tag{2.20}$$

where the Rusanov speed is defined as $\lambda = \max\left(\lambda_1^n, \lambda_2^n\right)$.

Roe method [205]:

$$\widehat{\mathbf{F}}_{i+\frac{1}{2}}^n = \frac{1}{2} \left(\mathbf{F}\left(\widehat{\mathbf{W}}_{i+1}^n \right) + \mathbf{F}\left(\widehat{\mathbf{W}}_i^n \right) \right) + \frac{1}{2} \mathbf{A}\left(\widetilde{\mathbf{W}}_{i+\frac{1}{2}}^n \right) \left(\widehat{\mathbf{W}}_i^n - \widehat{\mathbf{W}}_{i+1}^n \right), \tag{2.21}$$

where the averaged state $\widetilde{\mathbf{W}}_{i+\frac{1}{2}}^n$ is calculated as

$$\widetilde{\mathbf{W}}_{i+\frac{1}{2}}^n = \begin{pmatrix} \dfrac{\widehat{h}_i^n + \widehat{h}_{i+1}^n}{2} \\ \dfrac{\sqrt{\widehat{h}_i^n}\, \widehat{u}_i^n + \sqrt{\widehat{h}_{i+1}^n}\, \widehat{u}_{i+1}^n}{\sqrt{\widehat{h}_i^n} + \sqrt{\widehat{h}_{i+1}^n}} \end{pmatrix}, \tag{2.22}$$

and the Roe matrix $\mathbf{A} = \mathbf{R}\mathbf{\Lambda}\mathbf{R}^{-1}$ with

$$\mathbf{R} = \begin{pmatrix} 1 & 1 \\ \widehat{\lambda}_1 & \widehat{\lambda}_2 \end{pmatrix}, \qquad \mathbf{\Lambda} = \begin{pmatrix} \widehat{\lambda}_1 & 0 \\ 0 & \widehat{\lambda}_2 \end{pmatrix},$$

where $\widehat{\lambda}_1$ and $\widehat{\lambda}_2$ are the eigenvalues in (2.9) calculated at the averaged state (2.22).

FVC method [28]: To reconstruct the numerical fluxes using the finite volume characteristics method, the equations (2.13) are first reformulated in an advective form as

$$\begin{aligned} \frac{\partial H}{\partial t} + U\frac{\partial H}{\partial y} &= -H\frac{\partial U}{\partial y}, \\ \frac{\partial U}{\partial t} + U\frac{\partial U}{\partial y} &= -gH\frac{\partial (H+Z)}{\partial y}. \end{aligned} \tag{2.23}$$

Then, the associated characteristic curves $X_{i+\frac{1}{2}}(\tau)$ are computed as

$$\begin{aligned} \frac{dX_{i+\frac{1}{2}}(\tau)}{d\tau} &= U\Big(\tau, X_{i+\frac{1}{2}}(\tau)\Big), \quad \tau \in [t_n, t_n + \Delta t], \\ X_{i+\frac{1}{2}}(t_n + \Delta t) &= x_{i+\frac{1}{2}}. \end{aligned} \tag{2.24}$$

The initial-value problem (2.24) is solved using the same algorithm as the one used for solving the equations (2.14). The numerical fluxes in the FVC scheme is obtained by integrating the advective equations (2.23) along the characteristics in the time interval $[t_n, t_n + \Delta t]$. Assume an accurate approximation of the characteristics curves $X_{i+\frac{1}{2}}(t_n)$ is made, the intermediate solutions are obtained from (2.23) as

$$\begin{aligned} H^n_{i+\frac{1}{2}} &= \widetilde{H}^n_{i+\frac{1}{2}} - \frac{\Delta t}{\Delta y}\widetilde{H}^n_{i+\frac{1}{2}}\left(U^n_{i+1} - U^n_i\right), \\ U^n_{i+\frac{1}{2}} &= \widetilde{U}^n_{i+\frac{1}{2}} - g\frac{\Delta t}{\Delta y}\left((H^n + Z)_{i+1} - (H^n + Z)_i\right), \end{aligned} \tag{2.25}$$

where

$$\widetilde{H}^n_{i+\frac{1}{2}} = H\left(t_n, X_{i+\frac{1}{2}}(t_n)\right), \qquad \widetilde{U}^n_{i+\frac{1}{2}} = U\left(t_n, X_{i+\frac{1}{2}}(t_n)\right),$$

are the solutions at the characteristic foot computed by interpolation from the gridpoints of the control volume where the departure point $X_{i+\frac{1}{2}}(t_n)$ belongs. Hence, the numerical fluxes for the FVC method are defined by

$$\widehat{\mathbf{F}}^n_{i+\frac{1}{2}} = \mathbf{F}\left(\widetilde{\mathbf{W}}^n_{i+\frac{1}{2}}\right), \tag{2.26}$$

with the intermediate state $\widetilde{\mathbf{W}}^n_{i+\frac{1}{2}}$ is given

$$\widetilde{\mathbf{W}}^n_{i+\frac{1}{2}} = \begin{pmatrix} H^n_{i+\frac{1}{2}} \\ U^n_{i+\frac{1}{2}} \end{pmatrix}.$$

It should be stressed that the Lax-Friedrichs, Rusanov and Roe methods have been widely used for the numerical solution of shallow water equations whereas, the FVC method has been recently proposed in [28], and it is more accurate and doe not need the Riemann solver.

2.3 Treatment of source terms

Obviously the above method is first-order accurate for any first-order discretization of the source term in (2.18). In order to motivate the derivation of the additional source terms necessary for well-balancing the discretization of gradient fluxes and source terms we first consider the simple case with $\frac{d\xi}{dt} = 0$, $\xi = 1$ and $a = 0$. Then, the system (2.7) and the equation (2.5) coincide and many approaches of well-balancing are known, see for example [30, 150, 13, 184, 82, 44]. In the current study, to develop a well-balanced scheme method we resolve the steady-state dynamics up to high order. Thus, for still water equilibrium the conservation property (2.11) is preserved at time t_n *i.e.*,

$$U_i^n = 0, \qquad H_i^n + Z_i^n = C,$$

where C is a constant and $Z_i^n = Z\left(y_i\xi(t^n)\right) = Z(y_i)$. A Taylor expansion up to order $\mathcal{O}(\Delta y^3)$ yields

$$H_i^{n+1} - H_i^n = \frac{1}{2}\Delta y^2 (H_{yy})_i^n = -\frac{1}{2}\Delta y^2 (Z_{yy})_i^n + \mathcal{O}(\Delta y^3),$$

and assuming that the source term in (2.18) is integrated by mid-point rule a similar computation leads to

$$(HU)_i^{n+1} - (HU)_i^n = \mathcal{O}(\Delta y^3).$$

Hence, for a flow at rest the discretization (2.18) preserves the steady-state property up to the order $\mathcal{O}(\Delta y^3)$ provided that the additional term $\mathcal{S}_i^n = \frac{1}{2}\Delta y^2 (Z_{yy})_i^n$ is added to the equation of conservation of mass. Note that far from the steady-state, including the source term $\mathcal{S}_i^n$ would not change the properties of the scheme since this additional term is below the resolution of the considered finite volume methods.
In the general case with $\frac{d\xi}{dt} \neq 0$ here but for simplicity in the derivations we assume $a = 0$ and the equations (2.7) reduce to

$$\begin{aligned} \frac{\partial H}{\partial t} - \frac{\dot{\xi} y}{\xi}\frac{\partial H}{\partial y} + \frac{1}{\xi}\frac{\partial Q}{\partial y} &= 0, \\ \frac{\partial Q}{\partial t} - \frac{\dot{\xi} y}{\xi}\frac{\partial Q}{\partial y} + \frac{1}{\xi}\frac{\partial M}{\partial y} &= -g\frac{H}{\xi}\frac{\partial Z}{\partial y}, \end{aligned} \tag{2.27}$$

where $Q = HU$ and $M = HU^2 + \frac{1}{2}gH^2$. Note that unlike the previous case with $\frac{d\xi}{dt} = 0$, the scaled bottom bed in (2.27) depends on the time variable as $Z(t, y) = z(y\xi(t))$ with $z(x)$ describes the original bottom topography in (2.5). For still water equilibrium the conservation property (2.11) should be preserved *i.e.*,

$$U(t, y) = 0, \qquad H + Z = H(t, y) + z\left(y\xi(t)\right) = C.$$

As in the previous case a discretization of the source term in (2.18) is implemented such that

$$H_i^{n+1} = C - z\left(y_i\xi^{n+1}\right) + \mathcal{O}(\Delta y^3) \qquad \text{and} \qquad Q_i^{n+1} - Q_i^n = \mathcal{O}(\Delta y^3).$$

A Taylor expansion in y of $\widehat{H}_i$ leads to

$$\widehat{H}_i = H_i^n + \Delta t (H_y)_i^n \frac{y_i\xi'(t^n)}{\xi(t^n)} + \frac{\Delta t^2}{2}(H_{yy})_i^n \left(\frac{y_i\xi'(t^n)}{\xi(t^n)}\right)^2 + \frac{\Delta t^2}{2}(H_y)_i^n \frac{y_i\xi''(t^n)}{\xi(t^n)} + \mathcal{O}(\Delta y^3),$$

with a similar expansion for the water discharge $\widehat{Q}_i$. The Taylor expansion of Z is given by

$$Z_i^{n+1} \approx z(y_i\xi(t_n+\Delta t)) = Z_i^n + \Delta t(z_x)_i^n y_i\xi'(t^n) + \frac{\Delta t^2}{2}(z_{xx})_i^n y_i^2(\xi'(t^n))^2 + \frac{\Delta t^2}{2}y_i\xi''(t^n) + \mathcal{O}(\Delta y^3).$$

For example, using the Lax-Friedrich's method (2.19), the discretization of the balance law (2.13) is given by

$$\begin{aligned} H_i^{n+1} - \widehat{H}_i &= \frac{1}{2}\left(\widehat{H}_{i+1} - 2\widehat{H}_i + \widehat{H}_{i-1}\right) - \frac{\Delta t}{2\Delta y\xi(t^n)}\left(\widehat{Q}_{i+1} - \widehat{Q}_{i-1}\right), \\ Q_i^{n+1} - \widehat{Q}_i &= \frac{1}{2}\left(\widehat{Q}_{i+1} - 2\widehat{Q}_i + \widehat{Q}_{i-1}\right) - \frac{\Delta t}{2\Delta y\xi(t^n)}\left(\widehat{M}_{i+1} - \widehat{M}_{i-1}\right) + \\ &\quad \frac{1}{\Delta y}\int_{t^n}^{t^{n+1}}\int_{y_i-\frac{1}{2}}^{y_i+\frac{1}{2}} -gH(s,\eta)\frac{\partial}{\partial x}z\big(\eta\xi(s)\big)d\eta ds. \end{aligned}$$

Using the conditions of a lake at rest in time t^n *i.e.*, $H_i^n + Z_i^n = C$ and $Q_i^n = 0$, one obtains

$$\left(\frac{\partial H}{\partial y}\right)_i^n + \xi(t^n)\frac{\partial}{\partial x}z(y_i\xi(t_n)) = 0, \quad \left(\frac{\partial^2 H}{\partial y^2}\right)_i^n + \xi(t^n)^2\left(\frac{\partial^2 z}{\partial x^2}\right)_i^n = 0, \quad \left(\frac{\partial Q}{\partial y}\right)_i^n = \left(\frac{\partial^2 Q}{\partial y^2}\right)_i^n = 0.$$

Consider now the equation for H_i^{n+1} and adding and subtracting z_i^{n+1}, $\widehat{Q}_i = 0$ yields

$$\begin{aligned} H_i^{n+1} + Z_i^{n+1} - Z_i^n + \Delta t(H_y)_i^n\frac{y_i\xi'(t^n)}{\xi(t^n)} &+ \frac{\Delta t^2}{2}\left(\left(\frac{\partial^2 H}{\partial y^2}\right)_i^n\left(\frac{y_i\xi'(t^n)}{\xi(t^n)}\right)^2 + \left(\frac{\partial H}{\partial y}\right)_i^n y_i\xi''(t^n)\right) \\ -\widehat{H}_i + \mathcal{O}(\Delta t^3) &= \frac{1}{2}\left(\widehat{H}_{i+1} - 2\widehat{H}_i + \widehat{H}_{i-1}\right) + \mathcal{O}(\Delta y^3), \\ H_i^{n+1} + Z_i^{n+1} - (H_i^n + Z_i^n) &= -\frac{1}{2}\xi(t^n)^2\left(\frac{\partial^2 z}{\partial x^2}\right)_i^n \Delta y^2 + \mathcal{O}(\Delta y^3). \end{aligned}$$

Hence, as correction to the overall scheme adding to the integration of the equation is required (2.13)

$$\mathcal{S}_i^n = \frac{\Delta y^2}{2}\xi(t^n)^2\frac{\partial^2}{\partial x^2}z(y_i\xi(t^n)).$$

This leads to a well-balanced discretization up to order $\mathcal{O}(\Delta y^3)$. A similar computation leads to

$$Q_i^{n+1} = -\frac{g\Delta t}{4\Delta y\xi(t^n)}\left(2\left(\frac{\partial\widehat{H}}{\partial y}\right)_i^n\Delta y\right)\left(2\widehat{H}_i + \Delta y^2\left(\frac{\partial^2\widehat{H}}{\partial y^2}\right)_i^n\right) + G_i^n + \mathcal{O}(\Delta y^3),$$

where

$$G_i^n = -\frac{1}{\Delta y}\int_{t^n}^{t^{n+1}}\int_{y_{i-\frac{1}{2}}}^{y_{i+\frac{1}{2}}} gh(s,\eta)\frac{\partial}{\partial x}z(\eta\xi(s))ds d\eta.$$

This leads to

$$Q_i^{n+1} = \frac{g\Delta t}{\Delta y\xi(t^n)}\Delta y\widehat{H}_i^n\frac{\partial}{\partial x}z\left(y_i\xi(t^n)\right)\xi(t^{n+1}) + G_i^n + \mathcal{O}(\Delta y^3),$$

and after further Taylor expansion $\Delta y\frac{\partial}{\partial x}z\left(y_i\xi(t^n)\right)\left(\xi(t^n) + \Delta t\xi'(t^n)\right)\widehat{H}_i^n + \mathcal{O}(\Delta t^2\Delta y)$ and mid-point integration

$$G_i^n = -\frac{g}{\Delta y}\int_{t^n}^{t^{n+1}}\int_{y_{i-\frac{1}{2}}}^{y_{i+\frac{1}{2}}} H(s,\eta)\xi(s)\frac{\partial}{\partial x}z(\eta\xi(s))ds d\eta = -\Delta t g\widehat{H}_i\frac{\partial}{\partial x}z(y_i\xi(t^n), \tag{2.28}$$

Algorithm 2.1 Wet/dry treatment algorithm used in the present study.

Require:
$Tend$: The final time for the simulation.
η: Location of the interface at each time step
x_0: Initial location of the dam-break

while $t < Tend$ **do**
  Adjust the time Δt according to the CFL condition.
  for each control volume $[y_{i-\frac{1}{2}}, y_{i+\frac{1}{2}}]$ **do**
    Compute the dam-break speed to update the location of the interface η from x_0 (2.2b).
    Compute the transport terms by integrating the system along the characteristics (2.18).
    Compute the numerical fluxes $\mathbf{F}^n_{i+\frac{1}{2}}$ using the Lax-Friedrich's, Rusanov, Roe and FVC Schemes (2.19)-(2.23).
    Discretize the source term Q_i using the well-balanced discretization (2.29).
  end for
end while

one obtains

$$Q_i^{n+1} = \frac{g\Delta t^2 \xi'(t^n)}{\xi(t^n)} \frac{\partial}{\partial x} z(y_i \xi(t^n)) \widehat{H}_i^n + \mathcal{O}(\Delta y^3).$$

Finally, this leads to the second-order correction term to the momentum equation as

$$\mathcal{Q}_i^n = -\frac{g\Delta t^2 \xi'(t^n)}{\xi(t^n)} \frac{\partial}{\partial x} z(y_i \xi(t^n)) \widehat{H}_i^n.$$

In summary, at each time step t^n the equation (2.12) is solved using a third-order interpolation on $\mathbf{W}_i^n$ as well as formula (2.17) to obtain the intermediate values $\widehat{\mathbf{W}}_i^n$. Equation (2.13) is discretized as

$$\mathbf{W}_i^{n+1} = \widehat{\mathbf{W}}_i^n - \left(\widehat{\mathbf{F}}^n_{i+\frac{1}{2}} - \widehat{\mathbf{F}}^n_{i-\frac{1}{2}} \right) + \mathbf{G}_i^n + \mathbf{S}_i^n, \tag{2.29}$$

where $\widehat{\mathbf{F}}^n_{i+\frac{1}{2}}$ are the numerical fluxes defined in (2.19), $\mathbf{S}_i^n$ and $\mathbf{G}_i^n$ are source terms defined as

$$\mathbf{G}_i^n = \begin{pmatrix} 0 \\ \\ -\Delta t g \widehat{H}_i \dfrac{\partial}{\partial x} z(y_i \xi(t^n) \end{pmatrix}, \qquad \mathbf{S}_i^n = \begin{pmatrix} \dfrac{\Delta y^2}{2} \xi(t^n)^2 \; z_{xx}(y_i \xi(t^n)) \\ \\ -\dfrac{g\Delta t^2 \xi'(t^n)}{\xi(t^n)} \dfrac{\partial}{\partial x} z(y_i \xi(t^n)) \widehat{H}_i^n \end{pmatrix}.$$

All the previously mentioned steps are summarized in Algorithm 2.1.

2.4 Numerical results

Numerical results for several test problems of shallow water flows over dry areas were presented. The main goals of this section are to illustrate the numerical performance of the techniques described above and to verify numerically their capability to solve moving wet/dry fronts in shallow water flows. In all computations reported herein, the Courant number Cr is set to

Cr = 1 and the time stepsize Δt is adjusted at each time step according to the Courant-Friedrichs-Lewy (CFL) stability condition

$$\Delta t^n = \mathrm{Cr}\frac{\Delta y}{\max\Big(\left|\lambda_1^n\right|, \left|\lambda_2^n\right|\Big)},$$

where λ_1 and λ_2 are the two eigenvalues of the parametrized shallow water system given by (2.9). Numerical results obtained using the Lax-Friedrich's, Rusanov, Roe and FVC methods and a comparison between the obtained results for the parametrized model (2.5) to those obtained for the original model (2.1a) using the same methods are presented. Here, to overcome the zero speeds in the original system, the associated characteristic speeds are perturbed by 10^{-9} far from zero. In all simulations presented in this section the gravitational acceleration is set to $g = 9.81\ m/s^2$ and comparisons between different methods are presented. The following test examples are selected:

2.4.1 Accuracy test example

In this example the accuracy of the proposed method for the shallow water equations over dry areas was investigated. The performance of the considered finite volume methods for the parametrized model (2.5) using different numbers of gridpoints were examined. The problem studied in [250] for the shallow water equations (2.1a) in the spatial domain $[0, 1]$ with a non-flat bottom given by

$$z(x) = \sin^2(\pi x),$$

and subject to the following initial conditions

$$h(0, x) = 5 + e^{\cos(2\pi x)}, \qquad u(0, x) = 0.$$

Periodic boundary conditions are used for this test example. In order to quantify the errors in this problem a reference solution computed using a fine mesh of 6400 gridpoints is used as an exact solution. We compute the solutions at time $t = 1$ using different mesh densities. The L^1-error norm defined as

$$\sum_{i=1}^{N} \left|H_i^n - \mathcal{H}_i^n\right| \Delta x, \tag{2.30}$$

where H_i^n and $\mathcal{H}_i^n$ are respectively, the computed and reference solutions at gridpoint x_i and time t, whereas N stands for the number of gridpoints used in the spatial discretization. The obtained results for the water height H and the water discharge Q are listed in Table 2.1 using different values of N. By increasing the number of gridpoints in the computational domain, the errors decrease in all considered finite volume methods. A faster decay in the errors is also observed for the errors in the water height compared to the errors in the water discharge for the methods in Table 2.1. The Lax-Friedrich's and Rusanov schemes exhibit errors of the same order whereas an improvement is detected in the errors computed using the Roe scheme. We also remark that for these schemes, nearly optimal convergence rates of first-order are observed in the L^1-error norm for both H and Q. These results also confirm that a finite volume scheme designed for solving the original shallow water equations (2.1a) will retain the same order of convergence when it is applied to the parametrized shallow water system (2.5). For this test example, the FVC method is the most accurate and based on the results presented in Table 2.1 the FVC methods is more accurate than the Lax-Friedrich's, Rusanov and Roe schemes. The convergence rates for the FVC method for both H and Q are superior than those obtained

Table 2.1: Errors in the water height H and the water discharge Q obtained for the accuracy test problem using the parametrized model for the considered finite volume methods at time $t = 1$ using different gridpoints.

	Lax-Friedrich		Rusanov		Roe		FVC	
N	Error H	Error Q	Error H	Error Q	Error H	Error Q	Error H	Error Q
100	2.174E-01	8.936E-01	1.791E-01	7.752E-01	1.283E-01	5.108E-01	1.023E-01	3.961E-01
200	1.385E-01	6.318E-01	1.102E-01	4.906E-01	7.628E-02	3.300E-01	5.295E-02	2.274E-01
400	7.683E-02	3.889E-01	5.905E-02	2.740E-01	4.173E-02	2.031E-01	2.470E-02	1.160E-01
800	3.976E-02	2.157E-01	2.952E-02	1.448E-01	1.946E-02	1.058E-01	1.003E-02	5.411E-02

Table 2.2: Errors in the water free-surface $H + Z$ and the water velocity U obtained for the verification of well-balanced property at time $t = 10$ using different gridpoints.

	Standard treatment		Well-balanced treatment	
N	Error in $H + Z$	Error in U	Error in $H + Z$	Error in U
100	3.836E-02	5.924E-02	7.655E-14	8.716E-14
200	2.764E-03	3.783E-03	9.301E-15	1.136E-14

using the other methods. Needless to mention that increasing the number of gridpoints N results in an increase of the computational cost in all considered methods. For the considered mesh densities, the required CPU time in the FVC method is more than 5 times lower than the other methods.

Next the well-balanced property proposed in the current study has been investigated. An example of a lake at rest flow using the bed given in the previous example and a free-surface initially set to 2. It is expected that the water free-surface remains constant and the water velocity should be zero at all simulation times. Here, a standard method without accounting for the terms S_i^n and the well-balanced method including the terms S_i^n. In Table 2.2 we summarize the errors in the water free-surface and the water velocity obtained at time t = 10 for both treatments using two different meshes. It is clear that the standard approach fails to exactly conserve a constant free-surface and it introduces large errors in both water free-surface and water velocity for the considered meshes. As can be seen, the water free-surface for the well-balanced approach remains constant during the simulation times and the proposed well-balanced treatment preserves the C-property to the machine precision.

2.4.2 Dam-break flow over a flat dry bed

The dam-break problem in a rectangular channel with flat bottom, $z(x) = 0$ is considered. The channel is of length 30 m and the initial conditions are given by (2.1b) with $h_0 = 1$ m and $u_0 = 0$ m/s. At $t = 0$ the dam collapses and the flow problem consists of a shock wave traveling downstream and a rarefaction wave traveling upstream. The analytical solution of

this problem is given by [82]

$$h(t,x) = \begin{cases} h_0, & \text{if} \quad x \leq -t\sqrt{gh_0}, \\ \dfrac{1}{9g}\left(2\sqrt{gh_0} - \dfrac{x}{t}\right)^2, & \text{if} \quad -t\sqrt{gh_0} < x \leq 2t\sqrt{gh_0}, \\ 0, & \text{if} \quad x > 2t\sqrt{gh_0}, \end{cases}$$

$$u(t,x) = \begin{cases} 0, & \text{if} \quad x \leq -t\sqrt{gh_0}, \\ \dfrac{2}{3}\left(\sqrt{gh_0} + \dfrac{x}{t}\right)^2, & \text{if} \quad -t\sqrt{gh_0} < x \leq 2t\sqrt{gh_0}, \\ 0, & \text{if} \quad x > 2t\sqrt{gh_0}. \end{cases}$$

In Figure 2.2 the evolution in time-space phase domain of the water height obtained for the considered finite volume methods using a mesh with 100 gridpoints is presented. In this figure both results obtained for the original model (2.1a) and the parametrized model (2.5) using the same number on gridpoints were included. It is clear that for this dam-break problem, the results obtained using the classical Lax-Friedrich's and Rusanov methods are roughly the same in both original and parametrized models. For both models, the FVC method is more accurate as it is clearly seen in the vicinity of the shock and the contact waves. To further emphasis these features, we display in Figure 2.3 a comparison between the results from Figure 2.2 at time $t = 2.1$ using two meshes with 50 and 100 gridpoints, respectively. It is also clear that for both models, the numerical diffusion is very pronounced in the numerical solutions computed using Lax-Friedrich's and Rusanov methods. This excessive numerical dissipation has been successfully removed in the water heights using the Roe method but the results obtained using the FVC method remain the best. On the other hand, the proposed parametrized model captures the wet/dry fronts more accurately compared to the original approach. For this test example, the combined parametrized model and the FVC method accurately solve the front propagation without generating nonphysical oscillations or excessive numerical dissipation in the computed results.

Next the performance of the original and parametrized models for capturing the moving wet/dry interface in this dam-break flow problem is examined. The wet/dry interface $\zeta(t)$ for this test example can be analytically computed using

$$\zeta\left(t\right) = 2t\sqrt{gh_0}.$$

Figure 2.4 depicts the time evolution of the moving wet/dry interface obtained for the original and parametrized models using the FVC method only. For comparison reasons, results obtained on two meshes with 50 and 100 gridpoints were presented. As it can be seen from these results, the wet/dry interfaces obtained by the parametrized model are more accurate than those obtained by the original model. Refining the mesh from 50 gridpoints to 100 gridpoints results in a consistent improvement in the computed results for the parametrized model but not for the original model. Obviously, the computed results verify the stability and the shock capturing properties of the proposed parametrized model. The obtained results using the FVC scheme are also in good agreement with the exact solution for this dam-break problem over dry bed. To quantify the errors in the wet/dry interface for this dam-break problem, in Table 2.3 the L^2-errors for the considered finite volume methods for both the original and parametrized

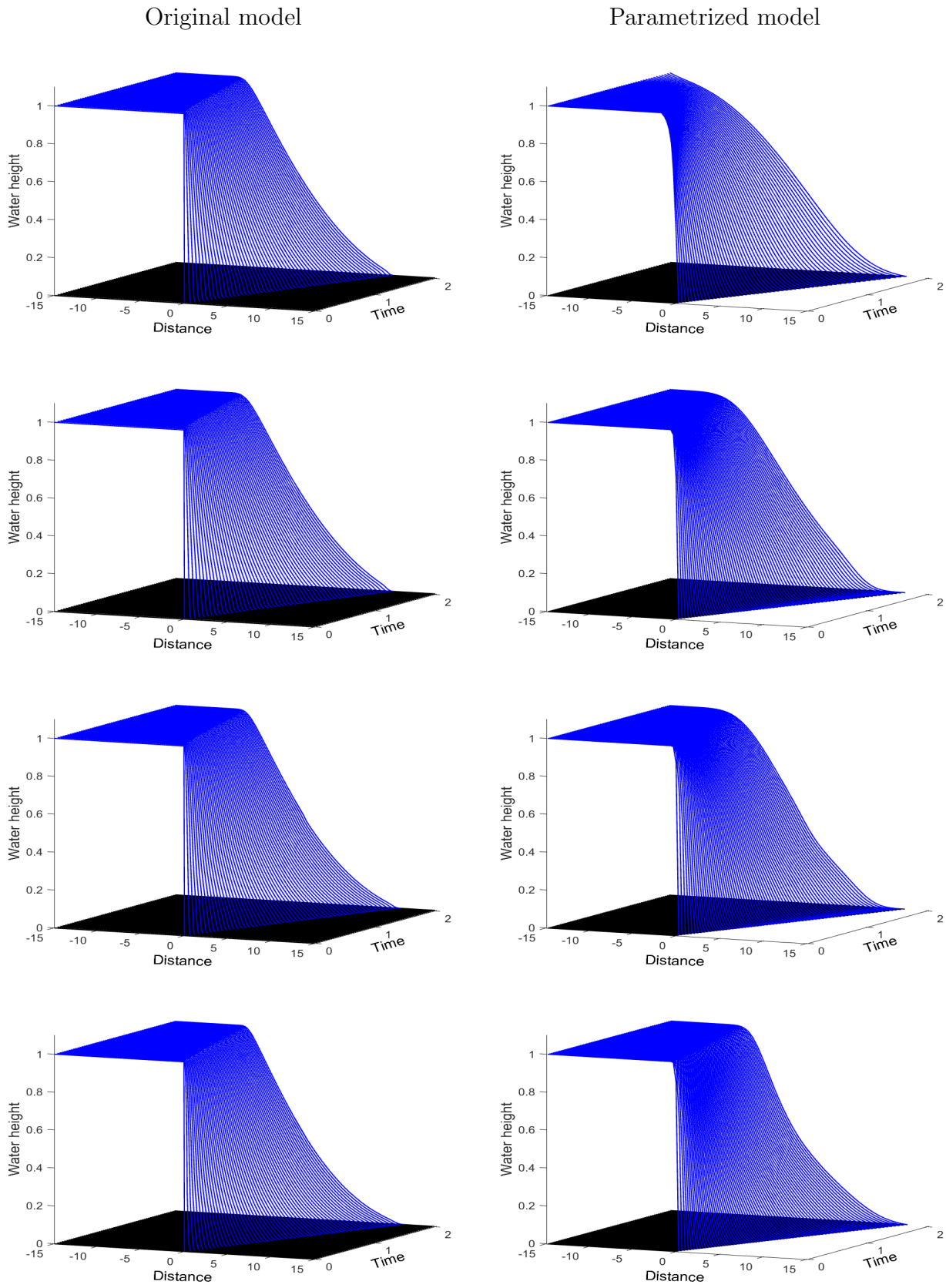

Figure 2.2: Evolution in the time-space domain of the water height for the dam-break over flat bed using the original model (left column) and the parametrized model (right column) for the Lax-Friedrichs method (first row), the Rusanov method (second row), the Roe method (third row) and the FVC method (fourth row) on a mesh with 100 gridpoints.

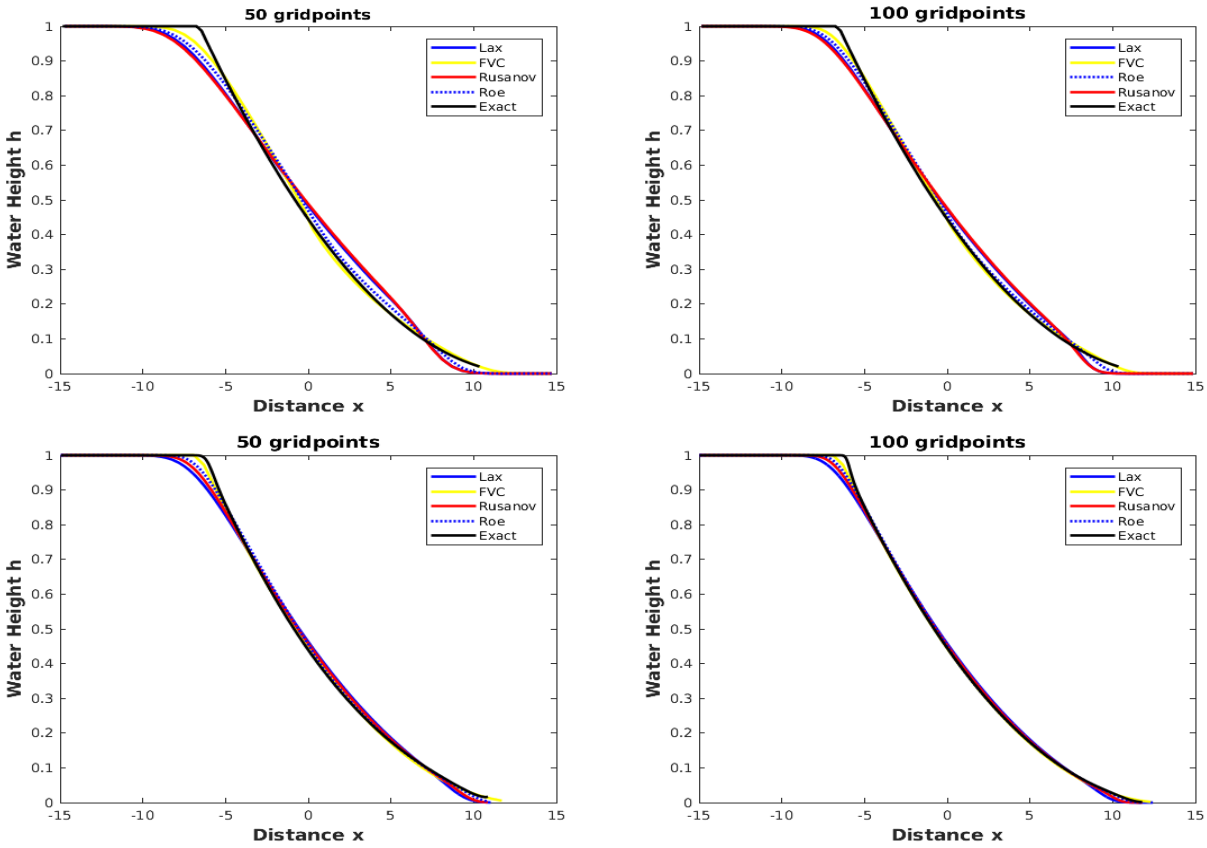

Figure 2.3: Comparison of results obtained for the dam-break over flat bed using the considered finite volume methods for the original model (first row) and the parametrized model (second row) at time $t = 2.1$ using 50 gridpoints (left column) and 100 gridpoints (right column).

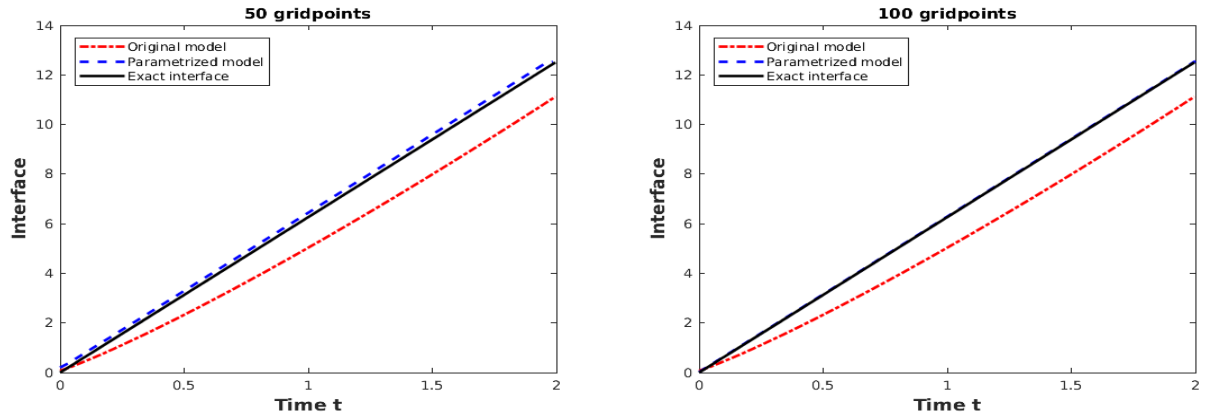

Figure 2.4: Time evolution for the wet/dry front obtained for the dam-break over flat bed using the FVC method for the original and parametrized models using 50 gridpoints (left column) and 100 gridpoints (right column).

Table 2.3: Errors in the wet/dry interface ζ obtained for the dam-break over flat bed using the original and parametrized models for the considered finite volume methods at time $t = 2.1$ using different gridpoints.

	Original model			
N	Lax-Friedrich	Rusanov	Roe	FVC
100	9.550E-01	7.895E-01	5.417E-01	1.351E-01
200	5.298E-01	4.319E-01	2.902E-01	6.754E-02
400	2.742E-01	2.204E-01	1.401E-01	2.939E-02
800	1.324E-01	1.049E-01	6.535E-02	1.113E-02

	Parametrized model			
N	Lax-Friedrich	Rusanov	Roe	FVC
100	3.142E-03	2.469E-03	1.406E-03	7.304E-04
200	1.570E-03	1.151E-03	5.710E-04	2.582E-04
400	7.324E-04	5.010E-04	2.163E-04	8.517E-05
800	3.187E-04	2.034E-04	7.647E-05	2.621E-05

models are summarized. Here the errors at time $t = 2.1$ using different numbers of gridpoints are presented. Again, the combined parametrized model with FVC method produced the most accurate results for this example. The performance of the parametrized model and the FVC method is very attractive since the computed solutions remain stable and accurate even for relatively coarse meshes without solving Riemann problems or requiring complicated treatment of wet/dry fronts in the flow problem.

2.4.3 Dam-break flow over a non-flat dry bed

The next flow problem consists of introducing a non-flat bed in the previous example of dam-break problems over dry beds. We consider an inclined bed with a slope $\alpha = \frac{\pi}{60}$ defined as

$$z(x) = (15 - x)\tan(\alpha)\,.$$

As in the previous test example, Figure 2.7 illustrates the evolution of the water free-surface in time-space phase domain for the considered finite volume schemes using a mesh with 100 gridpoints. Numerical results obtained for the original model (2.1a) and the parametrized model (2.5) using the same number of gridpoints are presented. As can be seen from these figures, the numerical diffusion is more pronounced in the results obtained using the Lax-Friedrich's and

Table 2.4: Errors in the wet/dry interface ζ obtained for the dam-break over non-flat bed using the original and parametrized models for the considered finite volume methods at time $t = 2.1$ using different gridpoints.

	Original model			
N	Lax-Friedrich	Rusanov	Roe	FVC
100	9.785E-01	8.936E-01	6.750E-01	2.715E-01
200	5.620E-01	4.957E-01	3.876E-01	1.454E-01
400	3.011E-01	2.565E-01	1.938E-01	7.270E-02
800	1.505E-01	1.238E-01	9.359E-02	3.391E-02

	Parametrized model			
N	Lax-Friedrich	Rusanov	Roe	FVC
100	4.692E-03	3.573E-03	2.358E-03	8.903E-04
200	2.346E-03	1.786E-03	1.026E-03	3.373E-04
400	1.173E-03	8.331E-04	4.166E-04	1.192E-04
800	5.472E-04	3.626E-04	1.578E-04	3.932E-05

Rusanov methods, compare the plots of the water free-surface for the mesh of 50 gridpoints. As expected, the Roe method has been successful in eliminating the numerical diffusion, but the FVC method is most accurate near regions of large gradients. On the other hand, comparing the performance of the parametrized model and the original method in Figure 2.5, results for the parametrized model are more accurate than those obtained using the original model with a negligible numerical diffusion is introduced compared to the one introduced by the original model. For this test example, no significant differences have been observed between the numerical results obtained using the parametrized model and the analytical solutions. It is also seen that for the considered dam-break conditions, the FVC method gives better results, followed by the Roe scheme. For the sake of comparison, the time evolution of the moving wet/dry interface obtained for the original and parametrized models is illustrated in Figure 2.6. For this test example, the exact equation of the interface is defined by $\zeta(t) = 2t\sqrt{gh_0\cos(\alpha)} - \frac{gt^2}{2}\tan(\alpha)$. Only results obtained using the FVC scheme are presented in Figure 2.6. The computed and analytical wet/dry interfaces are virtually indistinguishable for the simulations using the parametrized model on a mesh with 100 gridpoint. A slightly higher errors have been detected in the results obtained for the original model on the same mesh. The FVC method for the parametrized model performs very well for this test problem since it does not diffuse the moving wet/dry fronts and no spurious oscillations have been observed when the water flows over the non-flat bed. The associated L^2-errors in the wet/dry interface are given in Table 2.4 for all considered finite volume schemes at time $t = 2.1$ using different number of gridpoints. It reveals that increasing the number of gridpoints in the computational domain results in a decay of the errors for all methods. This parametrized model method exhibits good convergence behaviour for this dam-break problem over dry bed. As can be seen from the errors presented in Table 2.4, the original model is less accurate in capturing the wet/dry interface than its parametrized counterpart.

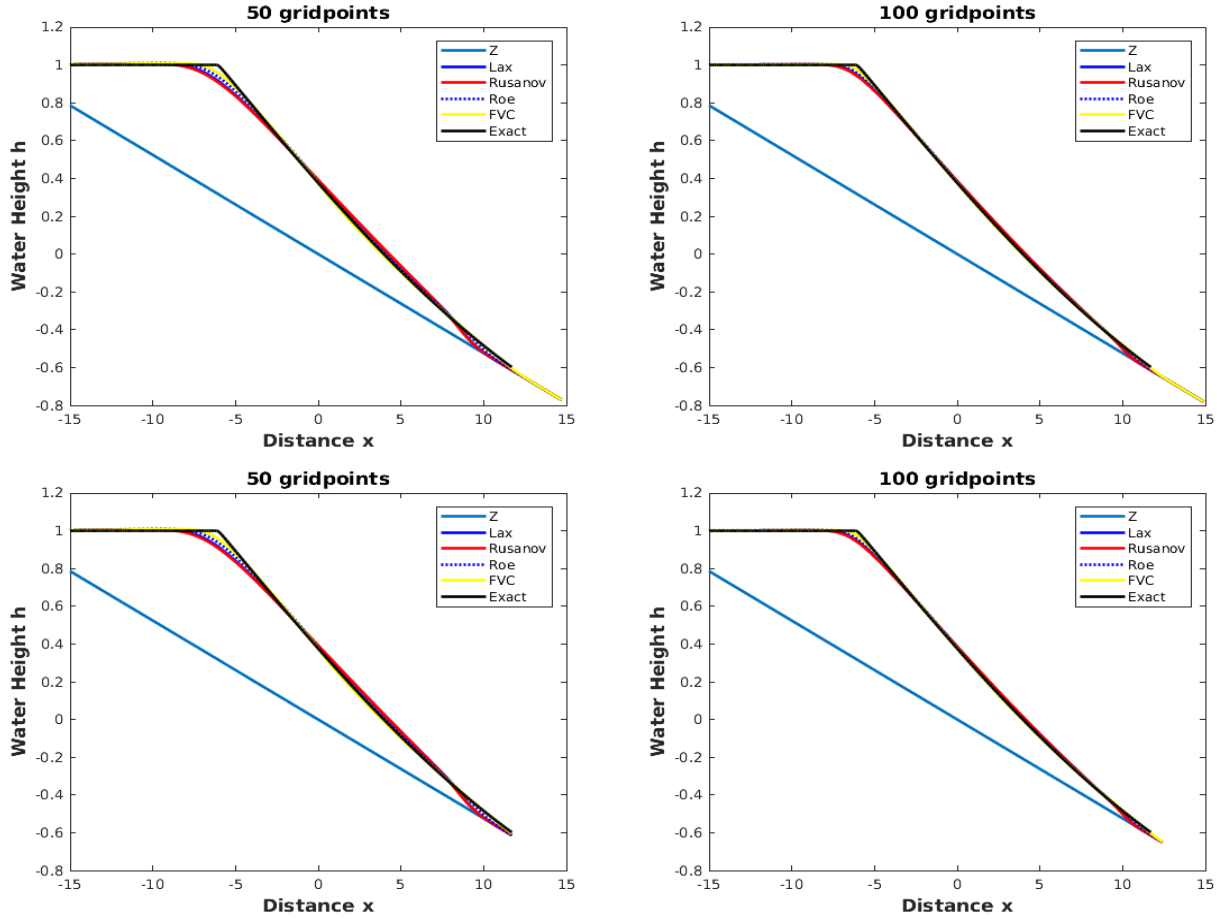

Figure 2.5: Comparison of results obtained for the dam-break over non-flat bed using the considered finite volume methods for the original model (first row) and the parametrized model (second row) at time $t = 2.1$ using 50 gridpoints (left column) and 100 gridpoints (right column).

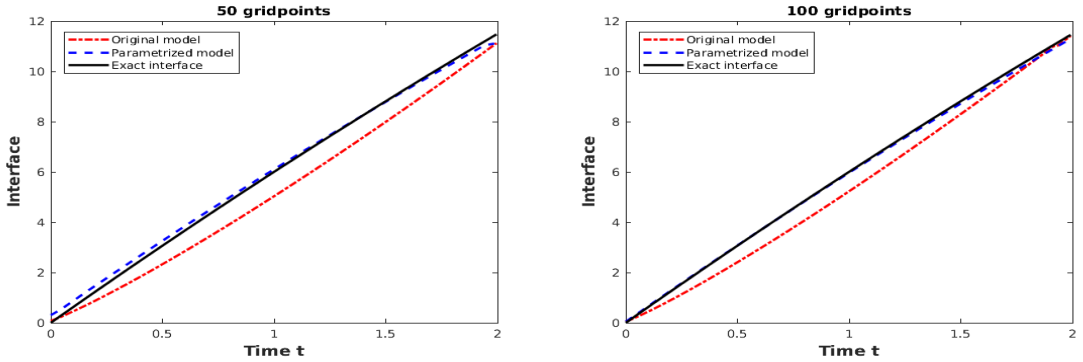

Figure 2.6: Time evolution for the wet/dry front obtained for the dam-break over non-flat bed using the FVC method for the original and parametrized models using 50 gridpoints (left column) and 100 gridpoints (right column).

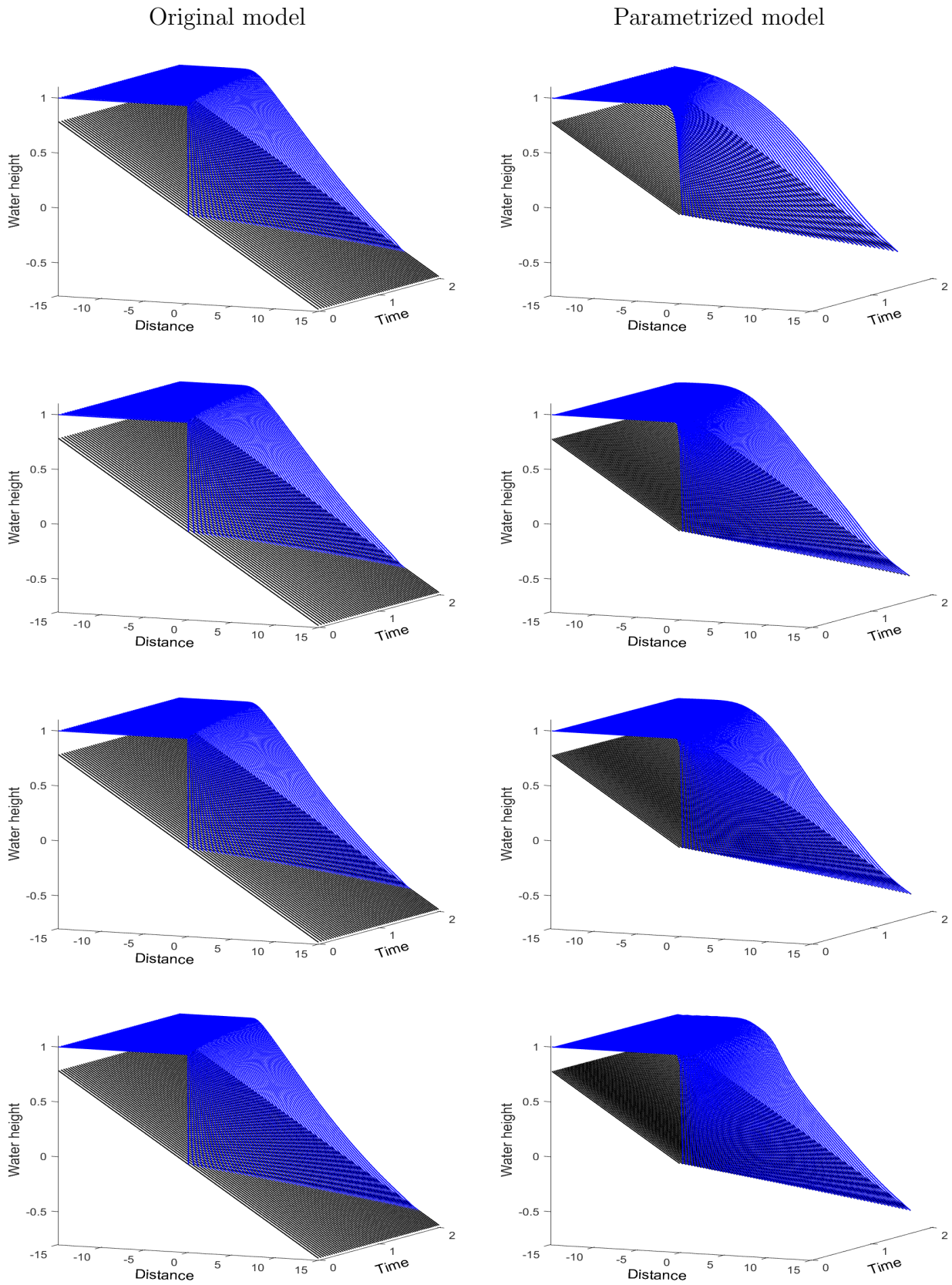

Figure 2.7: Evolution in the time-space domain of the water height for the dam-break over non-flat bed using the original and the model (left column) and the parametrized model (right column) for the Lax-Friedrichs method (first row), the Rusanov method (second row), the Roe method (third row) and the FVC method (fourth row) on a mesh with 100 gridpoints.

2.5 Treatment of partially wet/dry interface in shallow water flows

For one-dimensional problems, the shallow water equations can be reformulated in terms of surface elevation η and the water unit discharge q as

$$\begin{aligned} \frac{\partial \eta}{\partial t} + \frac{\partial q}{\partial x} &= 0, \\ \frac{\partial q}{\partial t} + \frac{\partial}{\partial x}\left(\frac{q^2}{\eta - z} + \frac{g}{2}(\eta^2 - 2\eta z)\right) &= -g\eta\frac{\partial z}{\partial x} - \tau_f, \end{aligned} \tag{2.31}$$

where $\eta = h + z$, with $h(t,x)$ is the water height and $z(x)$ the bed topography. In (2.31), $q(t,x)$ is the unit width discharge given by $q = hu$, with $u(t,x)$ is the depth-averaged velocity and τ_f the bed friction force given as

$$\tau_f = \frac{g n_b^2}{(\eta - z)^{\frac{1}{3}}} u\,|u|\,, \tag{2.32}$$

where g is the acceleration of gravity and n_b the Manning coefficient. For the numerical implementation, the shallow water system (2.31) can also be reformulated in term of h and hu as

$$\begin{aligned} \frac{\partial h}{\partial t} + \frac{\partial\,(hu)}{\partial x} &= 0, \\ \frac{\partial\,(hu)}{\partial t} + \frac{\partial}{\partial x}\left(hu^2 + \frac{1}{2}gh^2\right) &= -gh\frac{\partial z}{\partial x} - g n_b^2 \frac{u\,|u|}{h^{\frac{1}{3}}}, \end{aligned} \tag{2.33}$$

To solve the shallow water equations a finite volume method of Roe type is considered. Reformulating the equations (2.33) in a conservative form as

$$\frac{\partial \mathbf{W}}{\partial t} + \frac{\partial \mathbf{F}(\mathbf{W})}{\partial x} = \mathbf{Q}(\mathbf{W}) + \mathbf{S}(\mathbf{W}), \tag{2.34}$$

where

$$\mathbf{W} = \begin{pmatrix} h \\ hu \end{pmatrix}, \quad \mathbf{F}(\mathbf{W}) = \begin{pmatrix} hu \\ hu^2 + \frac{1}{2}gh^2 \end{pmatrix},$$

$$\mathbf{Q}(\mathbf{W}) = \begin{pmatrix} 0 \\ -gh\dfrac{\partial z}{\partial x} \end{pmatrix}, \quad \mathbf{S}(\mathbf{W}) = \begin{pmatrix} 0 \\ -g n_b^2 \dfrac{u\,|u|}{h^{\frac{1}{3}}} \end{pmatrix}.$$

The splitting operator introduced in [226] to deal with the differential source terms $\mathbf{Q}(\mathbf{W})$ and the non-differential source term $\mathbf{S}(\mathbf{W})$ in (2.34) is implemented. The splitting procedure consists of the following two steps:

Step 1: Solve for $\widetilde{\mathbf{W}}$

$$\frac{\widetilde{\mathbf{W}} - \mathbf{W}^n}{\Delta t_n} + \frac{\partial \mathbf{F}(\mathbf{W}^n)}{\partial x} = \mathbf{Q}\left(\mathbf{W}^n\right). \tag{2.35}$$

Step 2: Solve for $\mathbf{W}^{n+1}$

$$\frac{\mathbf{W}^{n+1} - \widetilde{\mathbf{W}}}{\Delta t_n} = \mathbf{S}\left(\widetilde{\mathbf{W}}\right). \tag{2.36}$$

For the space discretization of equation (2.34) the one-dimensional space domain is discretized in cells $\left[x_{i-\frac{1}{2}}, x_{i+\frac{1}{2}}\right]$ with same length Δx, also the time interval was divided into subintervals $[t_n, t_{n+1}]$ with uniform size Δt and $t_n = n\Delta t$. The notation $\mathbf{W}_i(t)$ to denote the space-averaged of $\mathbf{W} = \mathbf{W}(t,x)$ in the cell $\left[x_{i-\frac{1}{2}}, x_{i+\frac{1}{2}}\right]$ at time t, and $\mathbf{W}_{i+\frac{1}{2}}$ is the intermediate solution at $x_{i+\frac{1}{2}}$ at time t,

$$\mathbf{W}_i(t) = \frac{1}{\Delta x}\int_{x_{i-\frac{1}{2}}}^{x_{i+\frac{1}{2}}} \mathbf{W}(t,x)\, dx, \qquad \mathbf{W}_{i+\frac{1}{2}} = \mathbf{W}\left(t, x_{i+\frac{1}{2}}\right).$$

Integrating the system (2.35) over the time-space control domain $[t_n, t_{n+1}] \times \left[x_{i-\frac{1}{2}}, x_{i+\frac{1}{2}}\right]$, one obtains the following fully discrete system

$$\mathbf{W}_i^{n+1} = \mathbf{W}_i^n - \frac{\Delta t}{\Delta x}\left(\mathbf{F}^n_{i+\frac{1}{2}} - \mathbf{F}^n_{i-\frac{1}{2}}\right) + \Delta t \mathbf{Q}_i^n, \tag{2.37}$$

where $\mathbf{F}^n_{i\pm\frac{1}{2}} = \mathbf{F}\left(\mathbf{W}^n_{i\pm\frac{1}{2}}\right)$ are the numerical fluxes at $x = x_{i\pm\frac{1}{2}}$ and time $t = t_n$, and $\mathbf{Q}_i^n$ is a consistent discretization of the source term $\mathbf{Q}$ in (2.35). The spatial discretization (2.37) is complete when the numerical fluxes $\mathbf{F}_{i\pm1/2}$ and the source term $\mathbf{Q}_i$ are reconstructed. Generally, this step can be carried out using any finite volume method developed in the literature for solving hyperbolic systems of conservation laws, see for example [24, 221]. In the present study, the Roe reconstruction was considered defined as [205]

$$\mathbf{F}^n_{i+\frac{1}{2}} = \frac{1}{2}\left(\mathbf{F}(\widehat{\mathbf{W}}^n_{i+1}) + \mathbf{F}(\widehat{\mathbf{W}}^n_i)\right) + \frac{1}{2}\mathbf{A}\left(\widetilde{\mathbf{W}}^n_{i+\frac{1}{2}}\right)\left(\widehat{\mathbf{W}}^n_{i+1} - \widehat{\mathbf{W}}^n_i\right), \tag{2.38}$$

where the averaged state $\widetilde{\mathbf{W}}^n_{i+\frac{1}{2}}$ is calculated as

$$\widetilde{\mathbf{W}}^n_{i+\frac{1}{2}} = \begin{pmatrix} \dfrac{h_i^n + h_{i+1}^n}{2} \\ \dfrac{\sqrt{h_i^n}u_i^n + \sqrt{h_{i+1}^n}u_{i+1}^n}{\sqrt{h_i^n + h_{i+1}^n}} \end{pmatrix},$$

and the Roe matrix in (2.38) is defined as $\mathbf{A} = \mathbf{RLR}^{-1}$ with

$$\mathbf{R} = \begin{pmatrix} 1 & 1 \\ \widehat{\lambda}_1 & \widehat{\lambda}_2 \end{pmatrix}, \qquad \mathbf{L} = \begin{pmatrix} \widehat{\lambda}_1 & 0 \\ 0 & \widehat{\lambda}_2 \end{pmatrix}, \tag{2.39}$$

with $\lambda_1 = u - \sqrt{gh}$ and $\lambda_2 = u + \sqrt{gh}$ are the two eigenvalues associated with the system. For the approximation of the source term in (2.37), the well-balanced discretization is implemented. Hence, the discretization of the source term $\mathbf{Q}_i$ is carried out as

$$gh\frac{\partial z}{\partial x} = g\frac{h_{i+1} + 2h_i + h_{i-1}}{4}\frac{z_{i+1} - z_{i-1}}{2\triangle x}. \tag{2.40}$$

Note that, using this discretization of the source term, the scheme (2.37) satisfies the well-known C-property [28].

It should be stressed that, dealing with wetting and drying problems, most of numerical methods for solving the shallow water equations (2.33) perturb the dry state using a defined threshold above which the solution state is considered to be dry. This is mainly used to avoid division

by zero when updating the water velocity u during the simulation. Notice that, it is crucial to correctly solve this problem, as inaccurate results may lead to inaccuracy in the computed solutions or to false location of the wet/dry fronts in the run-up zones, see [100, 43, 156] for more details. In the current work, we adapt the correction procedure proposed in [43] which is well-balanced even in the presence of dry areas. Here, at each time step the control volume $\left[x_{i-\frac{1}{2}}, x_{i+\frac{1}{2}}\right]$ is either a wet cell or a dry cell or a partially wet/dry cell. Thus, the wet/dry treatment is carried out as follows

$$h(t,x_i) = \begin{cases} h_i, & \text{if} \quad \eta_i \geq z_{max}, \\ \dfrac{1}{2}(h_i + z_i - z_{min}), & \text{if} \quad \eta_i > z_{min}, \\ z_{min} - z_i, & \text{if} \quad \eta_i \leq z_{min}, \\ 0, & \text{otherwise}, \end{cases} \tag{2.41}$$

where z_{min} and z_{max} are defined as

$$z_{min} = \min\left(z_i, z_{i+1}\right), \qquad z_{max} = \max\left(z_i, z_{i+1}\right).$$

In order to maintain a stable solution, a tolerance ε is defined and new velocities are computed in a fully wet cell only if $h^{n+1} > \varepsilon$. It is also evident that for small water depths, the bed friction term dominates the other terms in the momentum equation. This is mainly due to the presence of the term $h^{\frac{1}{3}}$ in the dominator of τ_f in (2.32). To overcome this drawback we use a semi-implicit time integration of the source term $\mathbf{S}$ in (2.36) as

$$\frac{(hu)^{n+1} - \left(\widetilde{h}\widetilde{u}\right)}{\triangle t} = \frac{-gn_b^2\,(hu)^{n+1}\,|\widetilde{u}|}{\left(\widetilde{h}\right)^{\frac{4}{3}}}. \tag{2.42}$$

Solving (2.42) for $(hu)^{n+1}$ yields

$$(hu)^{n+1} = \frac{\left(\widetilde{h}\widetilde{u}\right)}{1 + \Delta t g n_b^2\,|\widetilde{u}| \,/\, \left(\widetilde{h}\right)^{\frac{4}{3}}}, \tag{2.43}$$

where $\widetilde{h}$ and $\widetilde{u}$ are the water height and velocity which computed from the first step (2.35) of the splitting procedure. Two test examples are presented in this section to illustrate the numerical performance of the techniques described above and verify numerically their capability to solve moving wet/dry fronts in shallow water flows. In the computations reported in this paper, the Courant number is set to Cr = 0.75 and the time stepsize Δt is adjusted at each time step according to the Courant-Friedrich's-Lewy (CFL) stability condition as

$$\triangle t = \mathrm{Cr}\frac{\Delta x}{\max\left(|\lambda_1|, |\lambda_2|\right)}, \tag{2.44}$$

where λ_1 and λ_2 are the two eigenvalues of the shallow water equations defined in (2.39). Numerical results for water free-surface at different times were presented. In all simulations

Algorithm 2.2 Partially wet/dry treatment algorithm used in the present study.

Require:
$Tend$: The final time for the simulation.
while $t_{n+1} \leqslant Tend$ **do**
  Adjust the time Δt according to the CFL condition (2.44).
  for each control volume $\left[x_{i-\frac{1}{2}}, x_{i+\frac{1}{2}}\right]$ **do**
    Compute the numerical fluxes $\mathbf{F}^n_{i+\frac{1}{2}}$ using the Roe scheme (2.38).
    Discretize the source term $\mathbf{Q}_i$ using the well-balanced discretization (2.40).
    Compute the solution in the first stage of the splitting $\mathbf{W}_i^{n+1}$ using (2.37).
    Update the solution in the second stage of the splitting (2.36) using (2.42)-(2.43).
    Perform the wet/dry treatment according to (2.41) as:
    Evaluate $z_{min} = \min(z_i, z_{i+1})$ and $z_{max} = \max(z_i, z_{i+1})$ and check:
    if $\eta_i^{n+1} \geq z_{max}$ **then**
      $h = h_i^{n+1}$
    else if $\eta_i^{n+1} > z_{min}$ **then**
      $h = \dfrac{1}{2}(h_i^{n+1} + z_i - z_{min})$
    else if $\eta_i^{n+1} \leq z_{min}$ **then**
      $h = z_{min} - z_i$
    else
      $h = 0$
    end if
  end for
end while

presented in this section, the water density $\rho = 1000\ kg/m^3$, the gravitational acceleration $g = 9.81\ m/s^2$, the tolerance $\varepsilon = 10^{-13}$ and the Manning coefficient $n_b = 0.05\ s/m^{1/3}$. All the previously mentioned steps are described in Algorithm 2.2.

2.5.1 Validation of wet/dry treatment

First the procedure used in this approach for the wet/dry treatment in the finite volume method were examined. The experimental benchmark of a dam-break over a dry bed described in [135] among others were considered. An illustration for the configuration of the domain and initial conditions are given in Figure 2.8. Here, a dam-break problem over a dry bed with two humps is simulated in a 7 m long channel. The dam is located on the top of the first hump with a water height of 0.342 m. The simulation is carried out for a total time of 15 s and the water height is monitored at the channel downstream in the location $x = 4.5\ m$. In Figure 2.9 the time evolution of the water height obtained at $x = 4.5\ m$ using our finite volume method compared to the experimental results were displayed. A mesh of 144 control volumes in the numerical results is used. As can be seen from these results, the finite volume method accurately captures the hydraulic jump and it resolves very well this free-surface flow. There is a good agreement between the experimental and the numerical results for this test example. Therefore, one may conclude that the wet/dry treatment performs well for dam-break problems over dry beds and it resolves all the flow features without the need for refined meshes. Note that the performance of the finite volume method is very attractive since the computed flow solutions remain stable and highly accurate even coarse meshes are used without solving nonlinear problems.

Point	x (m)	y(m)
P_1	0.00	0.000
P_2	2.00	0.000
P_3	2.20	0.108
P_4	2.25	0.108
P_5	2.30	0.108
P_6	2.50	0.000
P_7	6.10	0.000
P_8	6.50	0.213
P_9	6.60	0.213
P_{10}	7.00	0.000

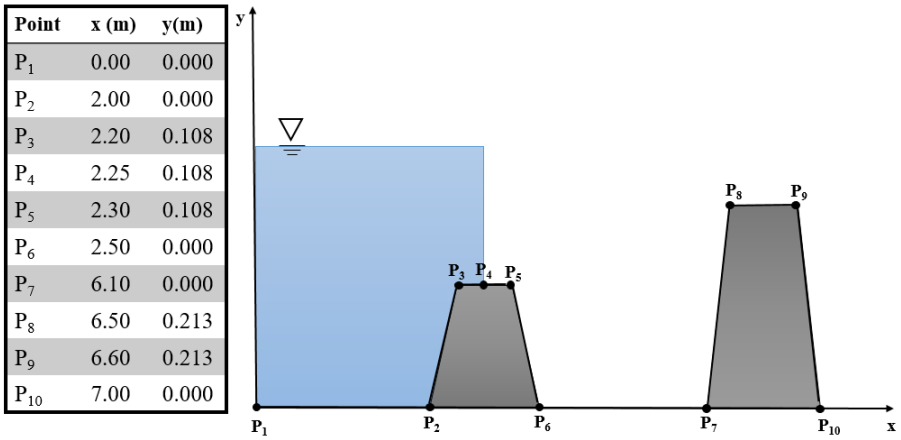

Figure 2.8: Illustration of the test example used for validation of the wet/dry treatment.

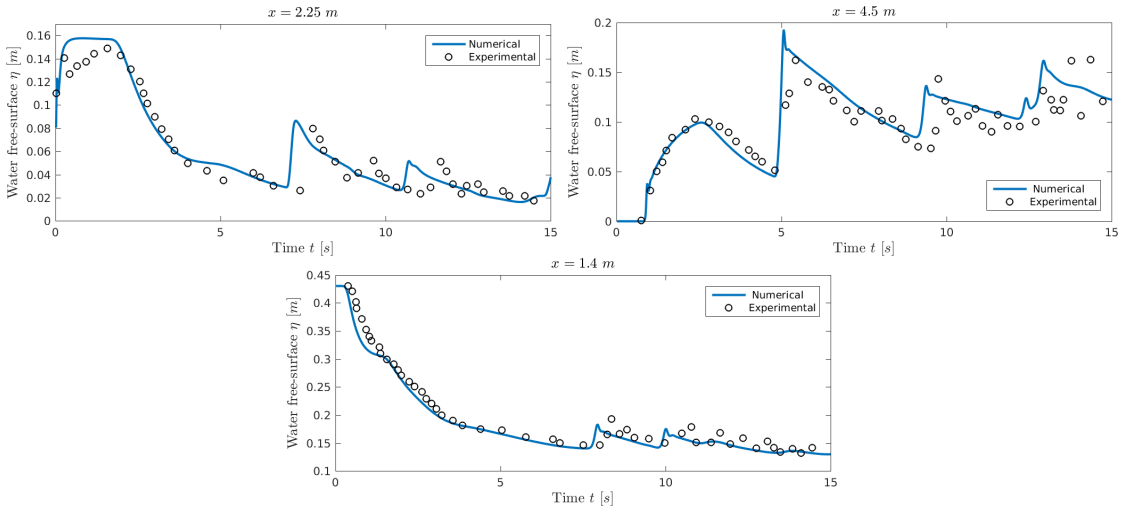

Figure 2.9: Comparison between experimental and numerical results for the dam-break problem over a non-flat dry bed.

2.5.2 Flow above a parabolic bottom topography

Analytical solutions of the nonlinear shallow water equations were derived by [210] for a perturbed flow in a frictional one dimensional container with a parabolic bed profile. This provides a perfect test for the present shallow flow model in dealing with bed slope and friction source terms as well as wetting and drying. The bed is defined by

$$z(x) = h_a\left(\frac{x}{a}\right)^2, \tag{2.45}$$

where h_a and a are constants. The analytical solutions depend on a bed friction parameter (n_b) and a hump amplitude parameter $p = \sqrt{\frac{8gh_a}{a^2}}$. The surface elevation η given as

$$\eta(t,x) = h_a + \frac{a^2B^2e^{(-n_bt)}}{8g^2h_a}\Big(-Sn_b\sin(2St) + (\frac{n_b^2}{4} - S^2)\cos(2St)\Big) - \frac{B^2e^{(-n_bt)}}{4g} - \frac{e^{(-n_bt)}}{g}\Big(BS\cos(St) + \frac{n_bB}{2}\sin(St)\Big)x, \tag{2.46}$$

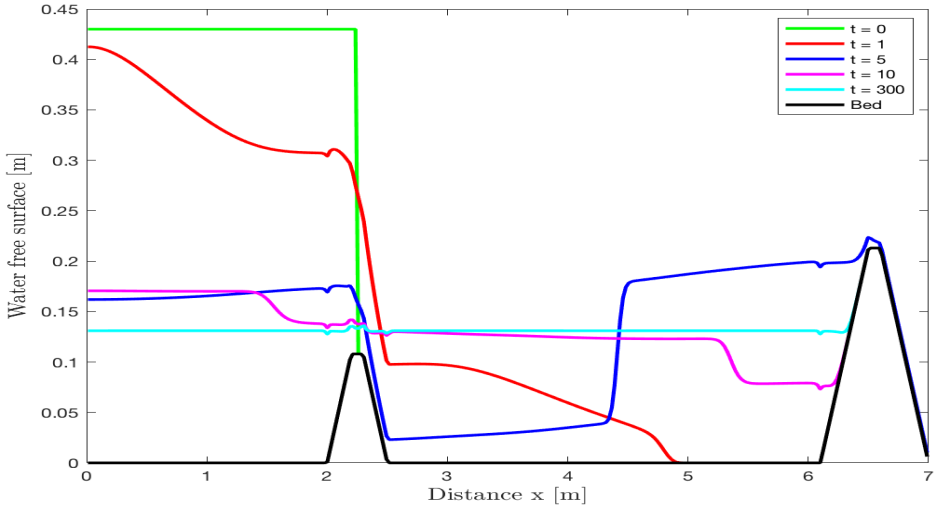

Figure 2.10: Water free-surface at different time steps for the dam-break problem over a non-flat dry bed.

Table 2.5: Errors in the water height obtained for the shallow water flow over a parabolic step for the considered partial wet/dry treatment method at different time steps using different gridpoints.

	Simulation times (s)					
N	$t = 1000$	$t = 2000$	$t = 3000$	$t = 4000$	$t = 5000$	$t = 6000$
100	0.0244	0.0284	0.0092	0.0577	0.0212	0.0839
200	0.0100	0.0169	0.0092	0.0347	0.0127	0.053
400	0.0051	0.0093	0.0043	0.0184	0.0067	0.0281
800	0.0025	0.0048	0.0023	0.0096	0.0032	0.0144
1600	0.0012	0.0025	0.0012	0.0049	0.0017	0.0074

where B is a constant and $S = \sqrt{p^2 - \frac{n_b^2}{2}}$. The location of the moving shorelines can be calculated by

$$x = \frac{a^2 e^{(-n_b t/2)}}{2gh_a}\Big(- BS\cos(St) - \frac{n_b B}{2}\sin(St)\Big) \pm a. \tag{2.47}$$

Numerical simulation is performed on a domain of 10000 m long with close boundary conditions imposed in both ends. The relevant coefficients are $a = 3000\ m$, $h = 10\ m$, $n_b = 0.001\ s/m^{-1/3}$ and $B = 5\ m/s$. Numerical simulations last for 6000 s. The moving wet/dry interfaces are correctly produced, thus validating the well-balanced wetting and drying algorithms and Figure 2.10 shows the water free-surface at different time steps. Figure 2.11 shows the predicted water surface elevation at different output times on a uniform grid with 100 gridpoints where excellent agreements are observed between the numerical predictions and analytical solutions. The errors in the water height compared to the analytical solution at different time steps are presented in Table 2.5.

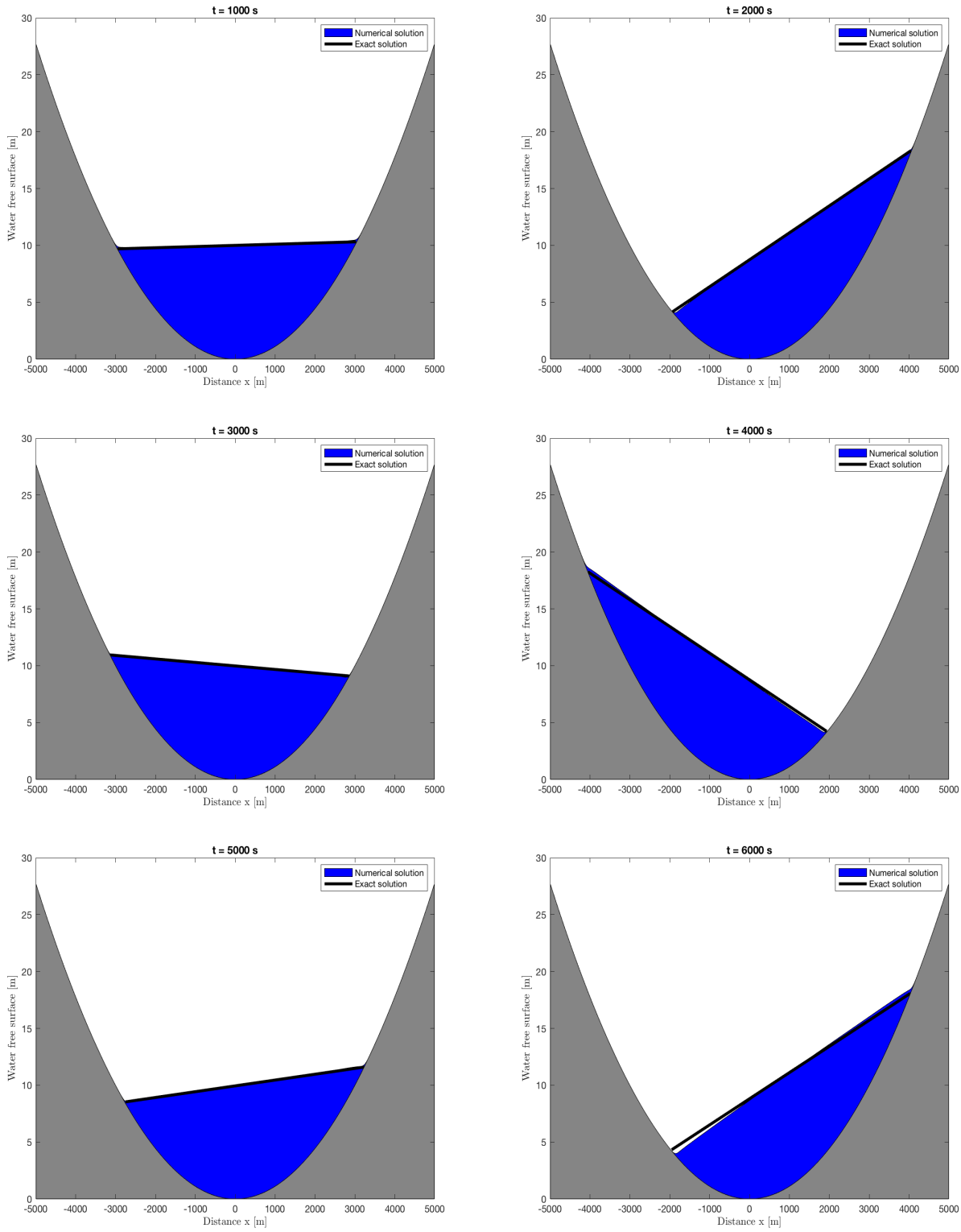

Figure 2.11: Water free-surface above the parabolic bottom topography compared to the analytical solution at six different times for partially wet/dry treatment.

2.5.3 Wet/dry front propagation over a V-shape bottom topography

In this example a water free-surface flow over a V-shape bed topography studied in [62] is implemented. In this test case, the bed topography is defined as

$$z(x) = \frac{1}{\sqrt{3}} \mid x - 1 \mid, \tag{2.48}$$

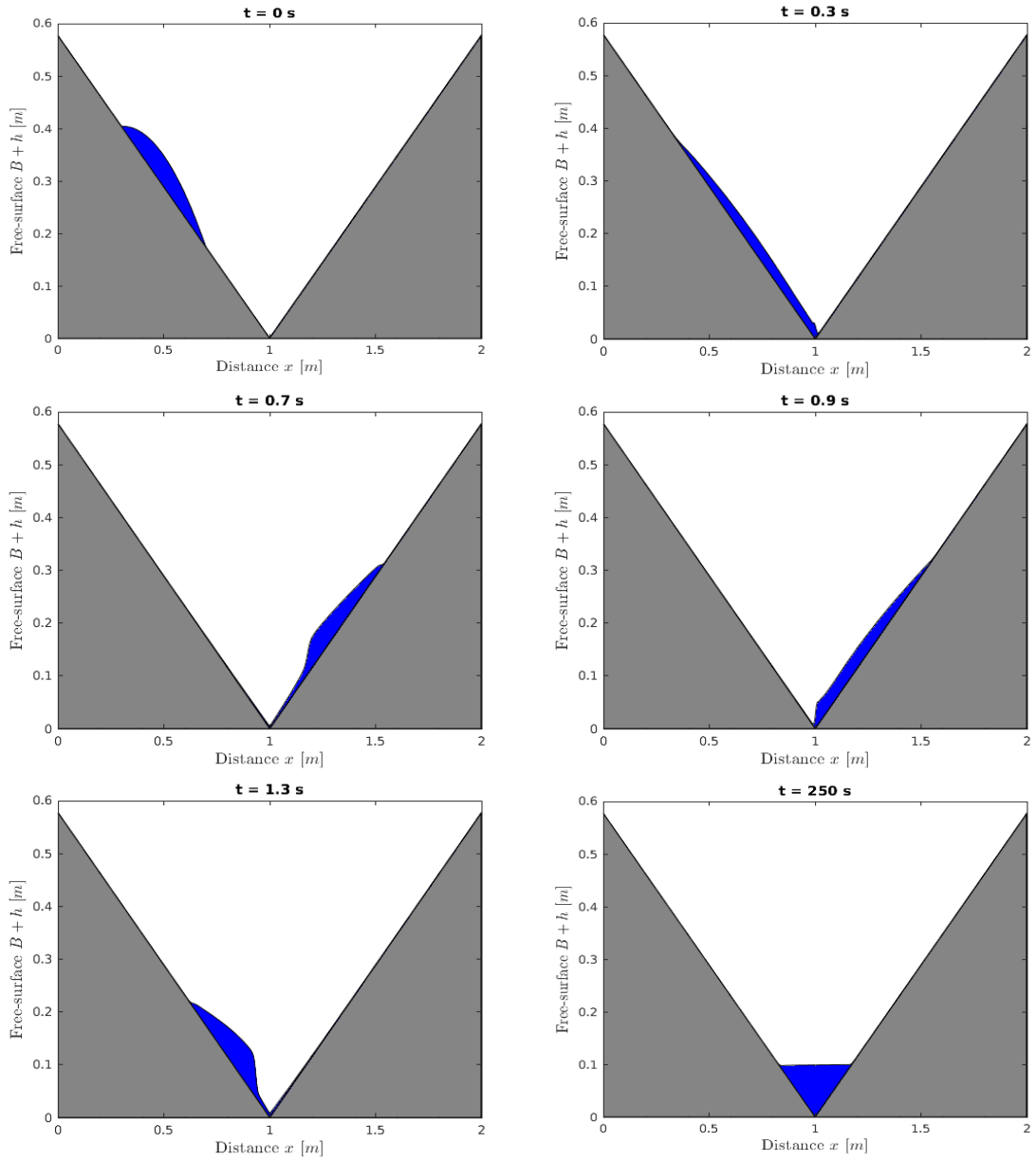

Figure 2.12: Water free-surface above the V-shape bottom topography at six different times.

subject to the following initial condition

$$h(0,x) = \max\big(0, -1.5(x-0.3)(x-0.7)\big), \qquad q(0,x) = 0. \tag{2.49}$$

In this test case the computational domain $[0,2]$ is discretized into 100 control volumes, the Manning coefficient $n_b = 0.02\ s/m^{-1/3}$, the Cr $= 0.75$. In Figure 2.12 the water free-surface is shown at six different times. Initially the water at rest, then the water flow down the left part and gradually accelerated. The water reaches the lowest point in the bed at time $t = 0.3\ s$, then gradually it starts run-up and climbing the right slope in the bed at time $t = 0.7\ s$. Because of the existence of the friction terms, the water speed starts decreasing achieving its maximum height, then starts flowing down to the left slope at time $t = 0.9\ s$, until it reaches the maximum height at the left slope at time $t = 1.3\ s$ and the water keep run-up and run-down between the right and left slopes until reaches settlement at time $t = 250\ s$. The aim of this example is to show the qualitative propagation of the water near the wet/dry fronts.

2.6 Conclusions

Shallow water flows include complex phenomena such as wave overtopping or wave run-up, which often lead to a drying and wetting boundary problem. It is easy to recognize that with this movement, the computational domain changes constantly which affects the accuracy of the calculations. The solution of the wet/dry interface becomes increasingly important, where the normal velocity components are set to zero leading to negative water depths predictions which result in numerical instabilities. Many recent investigations on wave run-up in coastal areas are based on the well known shallow water equations. Numerical simulations have also performed to understand the effects of several factors on tsunami impact and run-up in the presence of coastal areas. In all these simulations the shallow water equations are solved in entire domain including dry areas and special treatments are used for numerical solution of singularities at these dry regions. In this chapter a new method to deal with these difficulties by reformulating the shallow water equations into a new system to be solved only in the wetted domain is presented. The system is obtained by a change in the coordinates leading to a set of equations in a moving domain for which the wet/dry interface is reconstructed using the wave speed.

In this chapter, a class of accurate well-balanced finite volume methods to solve moving wet/dry fronts in shallow water flows is presented. The method combines the attractive attributes of parametrization techniques and the finite volume discretization to yield a procedure for either flat or non-flat topography. A well-established finite volume methods such as the Lax-Friedrich's and Roe solvers and we have also considered the finite volume characteristics scheme. Combining the new parametrized model with the finite volume characteristics method has several advantages. First, it can solve steady flows over irregular beds without large numerical errors, thus demonstrating that the proposed methods achieve perfect numerical balance of the gradient fluxes and the source terms. Second, it can compute the numerical flux corresponding to the real state of water flow without relying on Riemann problem solvers. Third, reasonable accuracy can be obtained easily and no special treatment is needed to treat moving wet/dry fronts. Finally, the proposed approach does not require either nonlinear solution or special front tracking techniques. Furthermore, it has strong applicability to various shallow water systems as shown in the numerical results. The proposed parametrized finite volume model has been tested on systems of shallow water equations subject to moving wet/dry fronts. The obtained results indicate good shock resolution with high accuracy in smooth regions and without any nonphysical oscillations near the shock areas. Comparisons between the proposed parametrized approach and the conventional shallow water system have also been carried out in this study. For all considered test examples the accuracy of the proposed approach is superior than the original model.

A partial wet/dry treatment in this chapter is accounted for as well. The method is well-balanced, stable and it accurately resolves the shallow water perturbations. The main purpose of this method is to efficiently solve the wet/dry interface in more complicated geometries, where the solution includes most challenging flow features which many finite volume methods fail to capture. For example wave reflections, repeatedly wetting and drying, presence of the surface curvatures, and non-differentiability topography are among these difficulties. The effectiveness and robustness of the proposed method are verified by applying it to simulate several benchmark tests and to reproduce a laboratory dam-break flow over a non-flat dry bed. The obtained results for this free-surface flow problem have shown good agreement with experimental measurements. The method performs well and it resolves all the flow features

without the need for refined meshes. The performance of the presented method is very attractive since the computed flow solutions remain stable and highly accurate even coarse meshes are used without solving nonlinear problems or requiring special wet/dry correction procedures.

Chapter 3

A hybrid finite volume/finite element method for shallow water waves by static deformation on seabeds

Unlike wind waves, water waves due to bed deformation are the result of the balance between bed stresses acting on the seabed of the ocean and the gravitational force trying to restore the equilibrium water surface. When these waves approach the coastline they begin to transform as they enter shallow water regime. As each wave begins to experience the seabed, both run-up and overtopping occur. For example, recording ocean-bottom pressures in offshore regions has increased our understanding of tsunami sources and promoted the development of rapid source estimation for early tsunami warning. Numerical solutions of the water depth and velocity at the interface have an important impact on these efforts. Full understanding of the system requires resolution of not only the water depth but also the velocity in the sea-surface and the pressure at the sea-bottom. In the present study we develop a new coupled model for numerical simulations of wave run-up by pre-defined static deformation on seabeds. The governing equations consist of the depth-averaged shallow water system including friction terms for the water free-surface coupled to the well-known second-order solid elastostatic formulation for the bed deformation. The model is fully coupled and at the interface between the water flow and the seabed, transfer conditions are implemented. Here, hydrostatic pressure and friction forces are considered for the elastostatic equations whereas bathymetric forces are accounted for in the shallow water equations. As numerical solvers, we propose a well-balanced finite volume method for the flow system and a stabilized finite element method for elastostatics. A special numerical treatment of wet/dry fronts in the proposed coupled system is also discussed in this study. We present numerical results for two test examples for wave run-up by deformation on seabeds. In the current work, the effects of bed slope and the friction force on the flow field and free-surface waves are investigated in details.

Water waves generated by the deformation on seabeds are of general interest to coastal and ocean engineering. The study of bed deformations is of great complexity since it is a class of natural phenomena that occur under certain conditions such as earthquakes, water mass movement, storms and heavy rain falls, see [115, 136, 198] among others. In such events, bed deformations are capable of generating several types of long waves due to the energy transfer to the water volume. Free-surface waves generated by bed deformations include very powerful and destructive tsunami waves which propagate and can run-up near offshore coastal areas and produce catastrophic waves causing significant coastal run-up. In recent years, a considerable

research effort has been developed regarding the mathematical modelling and numerical simulation of the interaction between bed deformation and water waves as well as the mechanisms of the surface gravity wave generations and propagations. In general, the modelling of wave run-up by static deformation is based on two components including the description of bed deformation and the governing equations of the water motion. Numerous investigations for the wave-induced by the deformations in seabeds have been carried out since the 1970s, see for example [34, 61, 138]. Numerical simulations also have been widely carried out to examine such a problem in recent years. Authors in [24] studied a buried pipeline in a region that is surrounded by two impermeable walls. Researchers in [173] have considered a similar case with a wider range of degree of saturation whereas, soil-pipeline contact effects and inertial forces in a new model have been investigated in [161]. In experimental investigations, the research contributions can be distinguished into two parts (i) field measurements and (ii) laboratory experiments. In the field measurement studies, data of pressure at the seabed surface and pore water pressure, vertical and horizontal total stresses in seabed have been collected, analyzed and compared with their theoretical counterparts in [5, 4, 23] among others. In laboratory experiment studies reported in [240], the pore pressure in seabed induced by progressive waves in wave flumes have been studied and compared with the results derived from linear wave theory. On the other hand, several numerical algorithms were proposed to accommodate complex geometry and physical conditions. For example, researchers in [95] have developed a simplified finite element model for isotropic and saturated permeable seabeds. In order to improve the computational efficiency, a radial point interpolation meshless method has been implemented in [121].

Shallow water equations have been typically used to model a wide variety of applications in free-surface flows and most of these applications involve wetting and drying over variable topography. Developing numerical techniques resolving wetting and drying fronts is becoming increasingly important in computational hydraulics. Predictions of flooding due to a breached dam, or overtopped levee are very crucial for disaster planning. Wave run-up estimates are needed for breach and coastal structure designs. Considerable numerical models have been developed for these problems and different techniques to solve the wetting and drying process have employed. Early models were initialized with a thin-layer of water everywhere in the domain [50]. To track the wet/dry boundaries, many finite element and finite difference models use a fixed computational grid to monitor the wetting and drying of grid nodes [217]. This approach may become computationally expensive and not sufficiently robust to simulate flow in arbitrary terrains as the grid must be readaptive at each time step for which computational nodes must be removed during recession or added during flooding to reduce grid distortion errors. A more robust and efficient method has been proposed in [101] in which the wet area of the computational mesh is fixed and gridpoints are added and subtracted at the wet/dry interfaces. However, all of the aforementioned methods use either finite differences or finite elements to discretize the shallow water equations. Finite element methods conserve mass over the entire domain, but not within each element or at each node. In general, most finite difference and finite element methods yield spurious oscillations at flow discontinuities unless a first-order accurate method or artificial viscosity are employed, see for instance [140] and further references are therein.

In the current study, a hybrid finite element/finite volume method for solving free-surface run-up flow problems over deformable beds is proposed. Deformations in the topography can be generated by a localized force which causes propagations of the water waves with

different amplitudes and frequencies. The governing equations consist of the nonlinear one-dimensional shallow water equations including friction terms for the water free-surface and the two-dimensional second-order solid elastostatic equations for the bed deformation. These equations are fully coupled and solved simultaneously in time using transfer conditions at the interface between the water flow and the seabed. This allow for hydrostatic pressure and friction forces to be implemented for the elastostatic equations whereas the deformed beds are accounted for in the shallow water equations through the bathymetric forces. Coupling conditions at the interface are also investigated in the current study, and the two-mesh procedure is proposed for the transfer of informations through the interface. The performance of the proposed finite volume/finite element method is examined for two test examples for wave run-up by deformation on seabeds due to a failure force applied in a circular void buried in the bed. The effects of bed slope and friction on the flow field and wave run-up are investigated in this chapter. The chapter is organized as follows: Description of the mathematical models for the coupled system is presented in section 3.1. Section 3.2 is devoted to the formulation of the numerical methods used for the solution procedure. Numerical results and examples for shallow water flows over elastic beds are presented in section 3.3. Concluding remarks are given in section 3.6.

3.1 Modelling wave run-up by elastic deformations in the topography

For a two-dimensional homogeneous isotropic material domain $\Omega \subset R^2$ as shown in Figure 3.1, the equilibrium governing equations of linear elasticity read [227]

$$\begin{aligned} \frac{\partial \sigma_x}{\partial x} + \frac{\partial \tau_{xy}}{\partial y} &= f_x, \\ \frac{\partial \sigma_y}{\partial y} + \frac{\partial \tau_{xy}}{\partial x} &= f_y, \end{aligned} \tag{3.1}$$

where σ_x and σ_y are the normal stress components in the horizontal x-direction and the vertical y-direction, respectively. Here, τ_{xy} is the shear stress, f_x and f_y are the external forces per unit volume in the x- and y-direction, respectively. The displacement vector is denoted by $\mathbf{u} = (u_x, u_y)^\top$ and the infinitesimal strain tensor is defined by

$$\boldsymbol{\epsilon} = \frac{1}{2}\Big(\nabla \mathbf{u} + (\nabla \mathbf{u})^\top\Big). \tag{3.2}$$

In the current study, we consider the constitutive relation

$$\boldsymbol{\sigma} = \mathbf{D}\, \boldsymbol{\epsilon}, \tag{3.3}$$

where the stress vector $\boldsymbol{\sigma}$ and the constitutive matrix $\mathbf{D}$ are defined by

$$\boldsymbol{\sigma} = \begin{pmatrix} \sigma_x \\ \sigma_y \\ \tau_{xy} \end{pmatrix}, \quad \mathbf{D} = \frac{E}{(1+\nu)(1-2\nu)} \begin{pmatrix} 1-\nu & \nu & 0 \\ \nu & 1-\nu & 0 \\ 0 & 0 & \dfrac{1-2\nu}{2} \end{pmatrix},$$

with ν is the Poisson ratio and E the Young modulus characterizing the bed material. Note that we solve the system (3.1) in the computational domain $\Omega \cup \Gamma \cup \Gamma_v \cup \Gamma_i$, with Ω is the interior domain, Γ the fixed boundary, Γ_v the forced boundary, and Γ_i the interface boundary between the bed topography and water body. In this case, the domain is a simple representation of a lake with two bed slopes at each end with angle β, and a pipe with given radius R is buried under the lake. The domain is subject to the following boundary conditions.

$$\begin{aligned} \mathbf{u} &= \mathbf{0}, \quad \text{on} \quad \Gamma, \\ \boldsymbol{\sigma} &= \boldsymbol{\sigma}_v, \quad \text{on} \quad \Gamma_v, \\ \sigma_y &= p, \quad \text{on} \quad \Gamma_i, \end{aligned} \tag{3.4}$$

where $\boldsymbol{\sigma}_v$ is a fixed stress on the boundary Γ_v and p is the hydrostatic pressure distribution at the interface Γ_i. Note that other boundary conditions for equations (3.1) can also be applied in the proposed finite volume/finite element method without major modifications in our formulation.
In the current work, as a consequence of bed deformations, a perturbation is expected to occur on the water surface. To solve for the water free-surface perturbations, a nonlinear shallow water system is considered. For one-dimensional problems, the shallow water equations are usually formulated in terms of surface elevation η and the water unit discharge q as [195]

$$\begin{aligned} \frac{\partial \eta}{\partial t} + \frac{\partial q}{\partial x} &= 0, \\ \frac{\partial q}{\partial t} + \frac{\partial}{\partial x}\left(\frac{q^2}{\eta - z} + \frac{g}{2}(\eta^2 - 2\eta z)\right) &= -g\eta \frac{\partial z}{\partial x} - \tau_f, \end{aligned} \tag{3.5}$$

where $\eta = h + z$, with $h(t, x)$ is the water depth and $z(x)$ the deformed bed. In (3.5), $q(t, x)$ is the unit width discharge given by $q = hv$, with $v(t, x)$ is the depth-averaged velocity and τ_f the bed friction force given as

$$\tau_f = g n_b^2 \frac{v\,|v|}{h^{\frac{1}{3}}}, \tag{3.6}$$

where g is the acceleration of gravity and n_b the Manning coefficient. For the numerical implementation, the shallow water system (3.5) can also be reformulated in term of h and hv as

$$\begin{aligned} \frac{\partial h}{\partial t} + \frac{\partial (hv)}{\partial x} &= 0, \\ \frac{\partial (hv)}{\partial t} + \frac{\partial}{\partial x}\left(hv^2 + \frac{1}{2}gh^2\right) &= -gh\frac{\partial z}{\partial x} - g n_b^2 \frac{v\,|v|}{h^{\frac{1}{3}}}, \end{aligned} \tag{3.7}$$

It should be noted that the coupled system (3.1)-(3.7) is numerically solved using a splitting operator where the bed deformation and the water free-surface are computed separately using the two-dimensional linear elastostatic equations (3.1) and the one-dimensional nonlinear shallow water equations (3.7). The coupling between the two models is achieved through the interface Γ_i by updating the bed topography $z(x)$ at each deformation step. Initially, the system is assumed at rest and a given external force $\mathbf{f} = (f_x, f_y)^\top$ is applied on the boundary Γ_v at time $t = t_v$. The response of water free-surface to the deformation generated by the bed on Γ_i is examined using the shallow water system (3.1) with variable topography z. The effect of

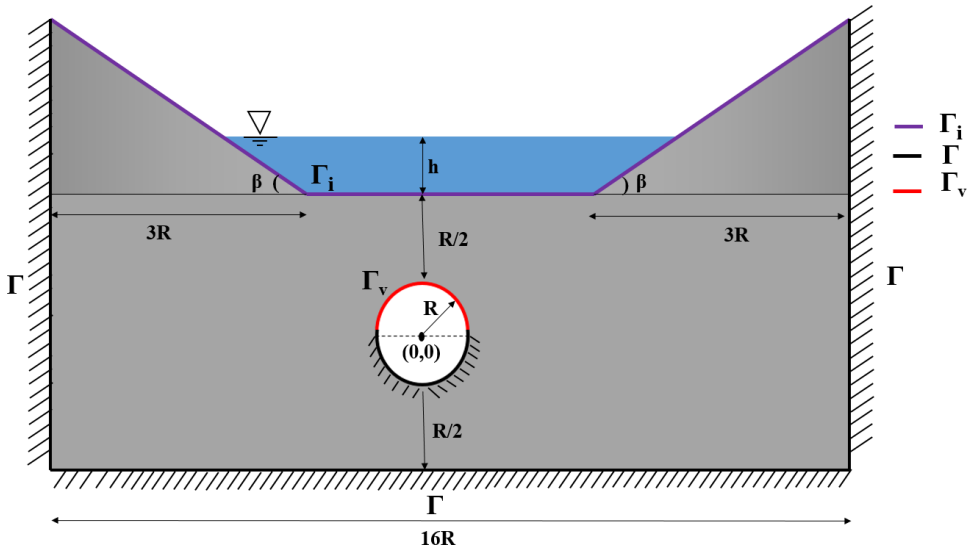

Figure 3.1: Schematic of a system for wave run-up by elastic deformations in the topography. Here, the gray domain is used for the bed deformation and the blue domain is used for the water flow.

water on the bed is accounted for using the vertical force generated by the hydrostatic pressure and the horizontal force originated by the friction term as

$$p = -\rho g(h - \eta_0), \qquad \tau_f = -g n_b^2 \frac{v\,|v|}{h^{\frac{1}{3}}}, \qquad \text{on} \quad \Gamma_i \tag{3.8}$$

where ρ is the water density and $\eta_0 = h_0 + z$ with h_0 is the initial water depth. It is worth remarking that the interaction between the bed topography and the water free-surface depends on the properties of the soil forming the bed, the magnitude of the applied force, and the initial water depth among others. It should also be stressed that, in most engineering applications, the effect of changes in the water surface at each time step on the bed is assumed negligible compared to the effects of bed deformation on the water free-surface, compare [95] among others.

3.2 Hybrid finite volume/finite element method

To solve the coupled model for wave run-up by static deformation on seabeds we consider a finite element method for the two-dimensional elasticity equations (3.1) and a finite volume method for the shallow water system (3.7). The starting point for the finite element method is the variational formulation of the strain energy in the domain Ω. Thus, multiplying the strong form of x-direction equation in (3.1) by a weight function ϕ_x and integrate over the domain yields

$$\int_\Omega \frac{\partial \sigma_x}{\partial x}\phi_x \, d\mathbf{x} + \int_\Omega \frac{\partial \tau_{xy}}{\partial y}\phi_x \, d\mathbf{x} - \int_\Omega f_x \phi_x \, d\mathbf{x} = 0.$$

Using the Green-Gauss theorem, the above equation becomes

$$\oint_{\partial\Omega} \sigma_x n_x \phi_x \, d\mathbf{x} - \int_\Omega \frac{\partial \phi_x}{\partial x}\sigma_x \, d\mathbf{x} + \oint_{\partial\Omega} \tau_{xy} n_y \phi_x \, d\mathbf{x} - \int_\Omega \frac{\partial \phi_x}{\partial y}\tau_{xy} \, d\mathbf{x} - \int_\Omega f_x \phi_x \, d\mathbf{x} = 0,$$

where $\mathbf{x} = (x, y)^\top$ and $\mathbf{n} = (n_x, n_y)^\top$ is the outward unit normal on Γ, $\partial\Omega = \Gamma \cup \Gamma_i$ Using the x-component of the traction $\mathcal{T}_x = \sigma_x n_x + \tau_{xy} n_y$, the above equation can be written as

$$\oint_{\partial\Omega} \mathcal{T}_x \phi_x \, d\mathbf{x} - \int_\Omega \left(\frac{\partial \phi_x}{\partial x} \sigma_x + \frac{\partial \phi_x}{\partial y} \tau_{xy} \right) \, d\mathbf{x} - \int_\Omega f_x \phi_x \, d\mathbf{x} = 0. \tag{3.9}$$

Similar steps applied to the y-direction equation in (3.1) give

$$\oint_{\partial\Omega} \mathcal{T}_y \phi_y \, d\mathbf{x} - \int_\Omega \left(\frac{\partial \phi_y}{\partial x} \tau_{xy} + \frac{\partial \phi_y}{\partial y} \sigma_y \right) \, d\mathbf{x} - \int_\Omega f_y \phi_y \, d\mathbf{x} = 0, \tag{3.10}$$

where $\mathcal{T}_y = \sigma_y n_y + \tau_{xy} n_x$. Adding the two equations (3.9) and (3.10) yields

$$\oint_{\partial\Omega} (\mathcal{T}_x \phi_x + \mathcal{T}_y \phi_y) \, d\mathbf{x} - \int_\Omega (f_x \phi_x + f_y \phi_y) \, d\mathbf{x} - \int_\Omega \left(\frac{\partial \phi_x}{\partial x} \sigma_x + \frac{\partial \phi_x}{\partial y} \tau_{xy} + \frac{\partial \phi_y}{\partial y} \sigma_y + \frac{\partial \phi_y}{\partial x} \tau_{xy} \right) \, d\mathbf{x} = 0,$$

which can be reformulated in a vector form as

$$\int_\Omega \widehat{\boldsymbol{\phi}} \cdot \boldsymbol{\sigma} \, d\mathbf{x} = \oint_{\partial\Omega} \boldsymbol{\phi}^\top \cdot \boldsymbol{\mathcal{T}} \, d\mathbf{x} + \int_\Omega \boldsymbol{\phi}^\top \cdot \mathbf{f} \, d\mathbf{x}, \tag{3.11}$$

where $\boldsymbol{\phi} = (\phi_x, \phi_y)^\top$, $\boldsymbol{\mathcal{T}} = (\mathcal{T}_x, \mathcal{T}_y)^\top$ and $\widehat{\boldsymbol{\phi}} = \left(\frac{\partial \phi_x}{\partial x}, \frac{\partial \phi_y}{\partial y}, \frac{\partial \phi_x}{\partial y} + \frac{\partial \phi_y}{\partial x} \right)^\top$. To solve the weak form (3.11) with the finite element method, the domain Ω is discretized into a set of elements where the solution is approximated in terms of the nodal values U_j and the polynomial basis functions $N_j(x, y)$ as

$$\mathbf{u}(x, y) = \sum_{j=1}^{N_d} \mathbf{U}_j N_j(x, y), \tag{3.12}$$

where N_d is the number of mesh nodes. In the present work, we consider quadratic triangular elements with six nodes for which the element displacement $\mathbf{u}^e = (u_x^e, u_y^e)^\top$ can be obtained by

$$\mathbf{u}^e = \begin{pmatrix} N_1^e & 0 & N_2^e & 0 & \dots & 0 \\ 0 & N_1^e & 0 & N_2^e & \dots & N_6^e \end{pmatrix} \begin{pmatrix} u_{x1} \\ u_{y1} \\ u_{x2} \\ u_{y2} \\ \vdots \\ u_{x6} \\ u_{y6} \end{pmatrix},$$

where N_j^e are the shape functions written in the local coordinates $(\xi_1, \xi_2)^\top$ as

$$N_1^e(\xi_1, \xi_2) = \xi_2 \left(2\xi_2 - 1\right), \qquad N_2^e(\xi_1, \xi_2) = \xi_1 \left(2\xi_1 - 1\right),$$
$$N_3^e(\xi_1, \xi_2) = \left(1 - \xi_1 - \xi_2\right)\left(1 - 2\xi_1 - 2\xi_2\right), \qquad N_4^e(\xi_1, \xi_2) = 4\xi_2\xi_1,$$
$$N_5^e(\xi_1, \xi_2) = 4\xi_1 \left(1 - \xi_2 - \xi_1\right), \qquad N_6^e(\xi_1, \xi_2) = 4\left(1 - \xi_2 - \xi_1\right)\xi_2.$$

To solve the fully discretized problem, the elementary matrices are assembled into a global system of equations

$$\mathbf{K}\mathbf{u} = \mathbf{b}, \tag{3.13}$$

where $\mathbf{K}$ is the global stiffness matrix, $\mathbf{u}$ the nodal displacement vector and $\mathbf{b}$ the force vector. In our simulations, the linear system (3.13) of algebraic equations is solved using the conjugate gradient solver with incomplete Cholesky decomposition.
To solve the shallow water equations we consider a finite volume method of Godunov type. We reformulate the equations (3.7) in a conservative form as

$$\frac{\partial \mathbf{W}}{\partial t} + \frac{\partial \mathbf{F}(\mathbf{W})}{\partial x} = \mathbf{Q}(\mathbf{W}) + \mathbf{S}(\mathbf{W}), \tag{3.14}$$

where

$$\mathbf{W} = \begin{pmatrix} h \\ \\ hv \end{pmatrix}, \ \mathbf{F}(\mathbf{W}) = \begin{pmatrix} hv \\ \\ hv^2 + \frac{1}{2}gh^2 \end{pmatrix}, \ \mathbf{Q}(\mathbf{W}) = \begin{pmatrix} 0 \\ \\ -gh\dfrac{\partial z}{\partial x} \end{pmatrix}, \ \mathbf{S}(\mathbf{W}) = \begin{pmatrix} 0 \\ \\ -gn_b^2 \dfrac{v\,|v|}{h^{\frac{1}{3}}} \end{pmatrix}.$$

We also use the splitting operator introduced in [226] to deal with the differential source terms $\mathbf{Q}(\mathbf{W})$ and the non-partial derivative source term $\mathbf{S}(\mathbf{W})$ in (3.8). The splitting procedure consists of the following two steps:
Step 1: Solve for $\widetilde{\mathbf{W}}$

$$\frac{\widetilde{\mathbf{W}} - \mathbf{W}^n}{\Delta t_n} + \frac{\partial \mathbf{F}(\mathbf{W}^n)}{\partial x} = \mathbf{Q}\left(\mathbf{W}^n\right). \tag{3.15}$$

Step 2: Solve for $\mathbf{W}^{n+1}$

$$\frac{\mathbf{W}^{n+1} - \widetilde{\mathbf{W}}}{\Delta t_n} = \mathbf{S}\left(\widetilde{\mathbf{W}}\right). \tag{3.16}$$

For the space discretization of equation (3.14) we discretize the one-dimensional space domain in uniform cells $\left[x_{i-\frac{1}{2}}, x_{i+\frac{1}{2}}\right]$ with same length Δx for simplicity, we also divide the time interval into subintervals $[t_n, t_{n+1}]$ with size Δt and $t_n = n\Delta t$. We also use the notation $\mathbf{W}_i(t)$ to denote the space-averaged of $\mathbf{W}(t,x)$ in the cell $\left[x_{i-\frac{1}{2}}, x_{i+\frac{1}{2}}\right]$ at time t, and $\mathbf{W}_{i+\frac{1}{2}}$ is the intermediate solution at $x_{i+\frac{1}{2}}$ at time t,

$$\mathbf{W}_i(t) = \frac{1}{\Delta x}\int_{x_{i-\frac{1}{2}}}^{x_{i+\frac{1}{2}}} \mathbf{W}(t,x)\,dx, \qquad \mathbf{W}_{i+\frac{1}{2}} = \mathbf{W}\left(t, x_{i+\frac{1}{2}}\right).$$

Integrating the system (3.15) over the time-space control domain $[t_n, t_{n+1}] \times \left[x_{i-\frac{1}{2}}, x_{i+\frac{1}{2}}\right]$, one obtains the following fully discrete system

$$\widetilde{\mathbf{W}}_i = \mathbf{W}_i^n - \frac{\Delta t}{\Delta x}\left(\mathbf{F}_{i+\frac{1}{2}}^n - \mathbf{F}_{i-\frac{1}{2}}^n\right) + \Delta t \mathbf{Q}_i^n, \tag{3.17}$$

where $\mathbf{F}_{i\pm\frac{1}{2}}^n = \mathbf{F}\left(\mathbf{W}_{i\pm\frac{1}{2}}^n\right)$ are the numerical fluxes at $x = x_{i\pm\frac{1}{2}}$ and time $t = t_n$, and $\mathbf{Q}_i^n$ is a consistent discretization of the source term $\mathbf{Q}$ in (3.15). The spatial discretization (3.17) is complete when the numerical fluxes $\mathbf{F}_{i\pm1/2}^n$ and the source term $\mathbf{Q}_i^n$ are reconstructed. Generally, this step can be carried out using any finite volume method developed in the literature

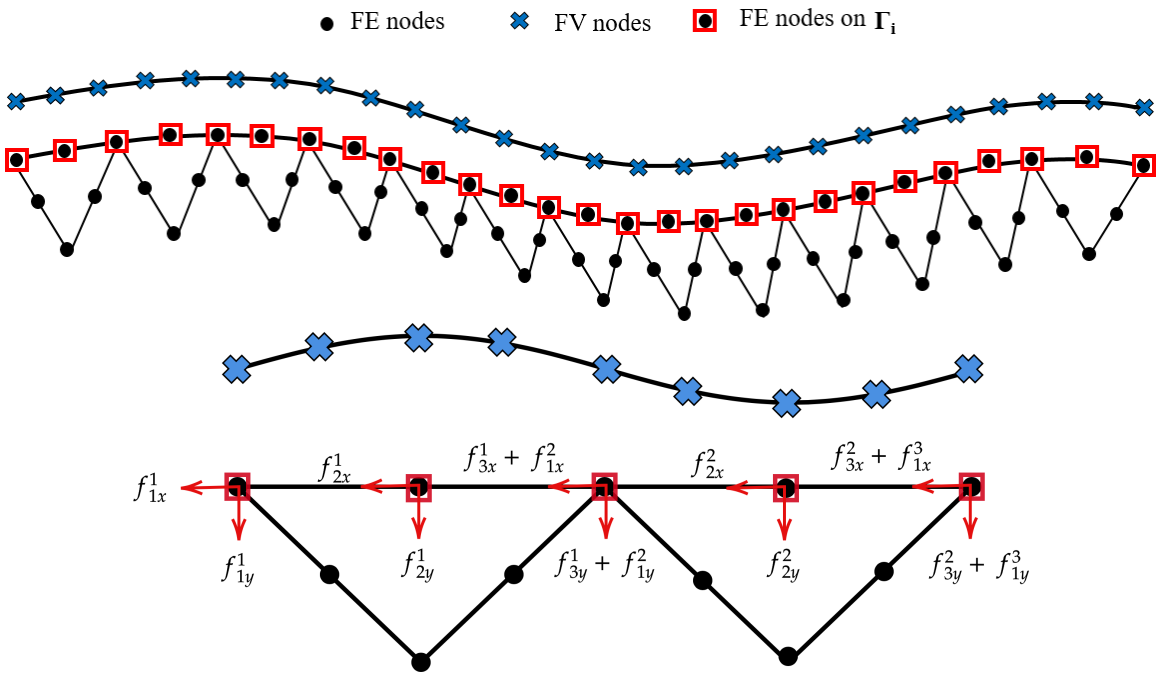

Figure 3.2: Illustration of finite element and finite volume nodes at the interface and distribution of the horizontal and vertical forces on the finite element nodes.

for solving hyperbolic systems of conservation laws, see for example [24, 221]. In the present study, we consider the Roe reconstruction defined as [205]

$$\mathbf{F}^n_{i+\frac{1}{2}} = \frac{1}{2}\left(\mathbf{F}(\mathbf{W}^n_{i+1}) + \mathbf{F}(\mathbf{W}^n_i)\right) + \frac{1}{2}\mathbf{A}\left(\widehat{\mathbf{W}}^n_{i+\frac{1}{2}}\right)\left(\mathbf{W}^n_i - \mathbf{W}^n_{i+1}\right), \tag{3.18}$$

where the averaged state $\widehat{\mathbf{W}}^n_{i+\frac{1}{2}}$ is calculated as

$$\widehat{\mathbf{W}}^n_{i+\frac{1}{2}} = \begin{pmatrix} \dfrac{h^n_i + h^n_{i+1}}{2} \\ \\ \dfrac{\sqrt{h^n_i}v^n_i + \sqrt{h^n_{i+1}}v^n_{i+1}}{\sqrt{h^n_i + h^n_{i+1}}} \end{pmatrix},$$

and the Roe matrix in (3.18) is defined as $\mathbf{A} = \mathbf{RLR}^{-1}$ with

$$\mathbf{R} = \begin{pmatrix} 1 & 1 \\ \\ \widehat{\lambda}_1 & \widehat{\lambda}_2 \end{pmatrix}, \qquad \mathbf{L} = \begin{pmatrix} \widehat{\lambda}_1 & 0 \\ \\ 0 & \widehat{\lambda}_2 \end{pmatrix}, \tag{3.19}$$

with $\lambda_1 = v - \sqrt{gh}$ and $\lambda_2 = v + \sqrt{gh}$ are the two eigenvalues associated with the system. For the approximation of the source term in (3.17), we use the well-balanced discretization discussed in [28]. Hence, the discretization of the source term $\mathbf{Q}_i$ is carried out as

$$gh\frac{\partial z}{\partial x}\Big|_{x=x_i} \approx g\frac{h_{i+1} + 2h_i + h_{i-1}}{4}\frac{z_{i+1} - z_{i-1}}{2\triangle x}. \tag{3.20}$$

Note that, using this discretization of the source term, the scheme (3.17) satisfies the well-known C-property *i.e.*, for a stationary flow at rest

$$h^n + z = C, \qquad v^n = 0,$$

where C is a positive constant. Notice that other reconstructions such as HLL and HLLC methods [260, 265] can also be used for the numerical fluxes in (3.17).
It should be stressed that, dealing with wetting and drying problems, most of numerical methods for solving the shallow water equations (3.7) perturb the dry state using a defined threshold above which the solution state is considered to be dry. This is mainly used to avoid division by zero when updating the water velocity v during the simulation. Notice that, it is crucial to correctly solve this problem, as inaccurate results may lead to inaccuracy in the computed solutions or to false location of the wet/dry fronts in the run-up zones, see [100, 43, 156] for more details. In the current work, we adapt the correction procedure proposed in [43] which is well-balanced even in the presence of dry areas. Here, at each time step the considered control volume $\left[x_{i-\frac{1}{2}}, x_{i+\frac{1}{2}}\right]$ is either a wet cell or a dry cell or a partially wet/dry cell. Thus, the wet/dry treatment is carried out as follows

$$h(t, x_i) = \begin{cases} h_i, & \text{if} \quad \eta_i \geq z_{max}, \\ \dfrac{1}{2}(h_i + z_i - z_{min}), & \text{if} \quad \eta_i > z_{min}, \\ z_{min} - z_i, & \text{if} \quad \eta_i \leq z_{min}, \\ 0, & \text{otherwise}, \end{cases} \tag{3.21}$$

where z_{min} and z_{max} are defined as

$$z_{min} = \min\left(z_i, z_{i+1}\right), \qquad z_{max} = \max\left(z_i, z_{i+1}\right).$$

In order to maintain a stable solution, a tolerance ε is defined and new velocities are computed in a fully wet cell only if $h_i^{n+1} > \varepsilon$. It should be noted that at dry cells, the source term $gh\frac{\partial z}{\partial x}$ is set to zero and at wet/dry fronts the treatment (3.21) is used for the approximation of water depth h in the discretization (3.20). It is also evident that for small water depths, the bed friction term dominates the other terms in the momentum equation. This is mainly due to the presence of the term $h^{\frac{1}{3}}$ in the dominator of τ_f in (3.6). To overcome this drawback we use a semi-implicit time integration of the source term $\mathbf{S}$ in (3.16) as

$$\begin{aligned} \frac{h^{n+1} - \widetilde{h}}{\Delta t} &= 0, \\ \frac{(hv)^{n+1} - \left(\widetilde{h}\widetilde{v}\right)}{\Delta t} &= -gn_b^2 \frac{(hv)^{n+1}\,|\widetilde{v}|}{\left(\widetilde{h}\right)^{\frac{4}{3}}}, \end{aligned} \tag{3.22}$$

where $\widetilde{h}$ and $\widetilde{v}$ are the water depth and velocity obtained from the first step (3.15) of the splitting procedure. Solving the second equation in (3.22) for $(hv)^{n+1}$ yields

$$(hv)^{n+1} = \frac{\left(\widetilde{h}\widetilde{v}\right)}{1 + \Delta t g n_b^2 \dfrac{|\widetilde{v}|}{\left(\widetilde{h}\right)^{\frac{4}{3}}}}. \tag{3.23}$$

Algorithm 3.1 Finite volume/finite element method used in the present study.

Require: T the final time for the simulation.

Assemble the stiffness matrix $\mathbf{K}$ for elastostatic system using the finite element method (3.9)-(3.13).
while $t_{n+1} \leqslant T$ **do**
  Assemble the force vector $\mathbf{b}$ for elastostatic system using the finite element method (3.9)-(3.13).
  Solve the linear system (3.13) for the displacement in the computational mesh.
  Update the displacement of the finite element nodes on the interface.
  Reconstruct the bed z using a cubic interpolation from finite element nodes to finite volume cells.
  Adjust the time step Δt according to the CFL condition (3.26).
  Solve the shallow water equations using:
  for each control volume $\left[x_i, x_{i+\frac{1}{2}}\right]$ **do**
    Compute the numerical fluxes $\mathbf{F}^n_{i+\frac{1}{2}}$ using the Roe scheme (3.18).
    Discretize the source term $\mathbf{Q}_i$ using the well-balanced discretization (3.20).
    Compute the solution in the first stage of the splitting $\mathbf{W}_i^{n+1}$ using (3.17).
    Update the solution in the second stage of the splitting (3.16) using (3.22)-(3.23).
    Perform the wet/dry treatment according to (3.21) as:
    Evaluate $z_{min} = \min(z_i, z_{i+1})$ and $z_{max} = \max(z_i, z_{i+1})$ and check:
    if $\eta_i^{n+1} \geq z_{max}$ **then**
      $h = h_i^{n+1}$
    else if $\eta_i^{n+1} > z_{min}$ **then**
      $h = \dfrac{1}{2}(h_i^{n+1} + z_i - z_{min})$
    else if $\eta_i^{n+1} \leq z_{min}$ **then**
      $h = z_{min} - z_i$
    else
      $h = 0$
    end if
  end for
  Compute the horizontal force f_x using the bed friction according to (3.24).
  Compute the vertical force f_y using the hydrostatic pressure according to (3.25).
  Interpolate the forces f_x and f_y from finite volume cells to finite element nodes on the interface.
end while

In general, the finite element and finite volume nodes on the interface do not coincide and therefore we use a cubic interpolation procedure to interchange the information between the two sets of nodes. As illustrated in Figure 3.2, at each time step coupling conditions occur at the interface for both models. In the present work, the deformed finite element nodes on the interface are used to reconstruct the bed z for the shallow water equations (3.7). This bed profile is used in the finite volume solution of the flow system to obtain the water depth h^{n+1} and the water velocity v^{n+1}. On the interface, the horizontal x-direction force f_x in the

elasticity equations (3.1) is updated as

$$f_x = -gn_b^2 \frac{v^{n+1}\left|v^{n+1}\right|}{\left(h^{n+1}\right)^{\frac{1}{3}}}. \tag{3.24}$$

The vertical y-direction force f_y is reconstructed at each time step using the change in the hydrostatic pressure in (3.8) as

$$p^{n+1} = -\rho g(h^{n+1} - \eta_0),$$

and at each node of the three finite element nodes located on the interface, the force f_y is distributed using the integral form as

$$f_y^{(1)} = \int_{-1}^{1} \frac{-1}{2}\xi\left(\xi - 1\right) p^{n+1}\frac{\hbar}{2}\, d\xi = \frac{1}{6}p^{n+1}\hbar, \qquad f_y^{(2)} = \frac{2}{3}p^{n+1}\hbar, \qquad f_y^{(3)} = \frac{1}{6}p^{n+1}\hbar, \tag{3.25}$$

where $\hbar$ is the edge length of the considered element on interface. The total y-direction force f_y is obtained by accumulating the elemental forces on the overlapping nodes, see Figure 3.2 for an illustration. Note that both horizontal force f_x and vertical force f_y have negative signs and therefore are applied in the negative x- and y-direction, respectively. In summary, the finite volume/finite element method proposed in this study to solve wave run-up by static deformation on seabeds is carried out in the steps described in Algorithm 3.1.

3.3 Numerical results

Test examples are presented in this section to illustrate the numerical performance of the techniques described above and verify numerically their capability to solve moving wet/dry fronts in shallow water flows. In the computations reported in this chapter, the Courant number is set to $C_r = 0.75$ and the time stepsize Δt is adjusted at each time step according to the Courant-Friedrichs-Lewy (CFL) stability condition as

$$\Delta t = Cr\frac{\Delta x}{\max\left(\left|\lambda_1\right|, \left|\lambda_2\right|\right)}, \tag{3.26}$$

where λ_1 and λ_2 are the two eigenvalues of the shallow water equations defined in (3.19). Notice that at each time step, the bed deformation leads to a change in the water depth and flow velocity which consequently affects the calculation of the eigenvalues (3.19). Hence, the effect of bed deformation is implicitly accounted for in updating the time step which involves in its variation the water depth and the flow velocity resulting from this deformation. We present numerical results for both, bed deformation and water free-surface at different times. In all simulations presented in this section and unless stated otherwise, the water density $\rho = 1000\ kg/m^3$, the gravitational acceleration $g = 9.81\ m/s^2$, the Young's modulus $E = 10000\ MPa$, the Poison's ratio $\nu = 0.3$, the tolerance $\varepsilon = 10^{-13}$ and the Manning coefficient $n_b = 0.05\ s/m^{1/3}$.

3.3.1 Accuracy of the proposed wet/dry treatment for dam-break problems

In this section a comparison between the performance of the proposed wet/dry treatment to the conventional procedure which consists of perturbing the dry state using a wetted threshold,

above which the solution is considered to be dry is presented. To this end we consider a dam-break problem in a frictionless flat rectangular channel ($z(x) = 0$) with known analytical solution. The channel is of 300 m length and the initial conditions are defined by

$$h(0,x) = \begin{cases} h_0, & \text{if} \quad x \leq x_0, \\ \\ 0, & \text{if} \quad x > x_0, \end{cases} \qquad v(0,x) = 0, \tag{3.27}$$

where $x_0 = 150\ m$ is the initial location of the wet/dry interface and $h_0 = 10\ m$ is the initial water depth. Here, the conventional approach uses a threshold of $\varepsilon = 10^{-13}$ and it is mainly used to avoid division by zero in updating the flow velocity during the simulation process. The analytical solution of this problem is defined by [82]

$$h(t,x) = \begin{cases} h_0, & \text{if} \quad x \leq -t\sqrt{gh_0}, \\ \\ \dfrac{1}{9g}\left(2\sqrt{gh_0} - \dfrac{x}{t}\right)^2, & \text{if} \quad -t\sqrt{gh_0} < x \leq 2t\sqrt{gh_0}, \\ \\ 0, & \text{if} \quad x > 2t\sqrt{gh_0}, \end{cases}$$

$$v(t,x) = \begin{cases} 0, & \text{if} \quad x \leq -t\sqrt{gh_0}, \\ \\ \dfrac{2}{3}\left(\sqrt{gh_0} + \dfrac{x}{t}\right)^2, & \text{if} \quad -t\sqrt{gh_0} < x \leq 2t\sqrt{gh_0}, \\ \\ 0, & \text{if} \quad x > 2t\sqrt{gh_0}. \end{cases}$$

In our simulations, we use 100 control volumes and results for water depth and velocity are presented at time $t = 5\ s$. Figure 3.3 depicts a comparison between the results obtained for the water depth and velocity using the conventional approach and the proposed wet/dry treatment. Both approaches correctly capture solutions of the water depth with the proposed approach slightly more accurate than the conventional approach. It is clear that the proposed partial wet/dry treatment is more accurate in updating the flow velocity than the conventional approach. In addition, perturbing the water depth may result in inaccuracy in the computed solutions and may lead to false or inaccurate location of the wet/dry fronts on the coastal zones.

To further compare the performance of the proposed wet/dry treatment to the conventional procedure, we consider the dam-break problem over a frictionless dry inclined plane investigated in [239] among others. The computational domain is the interval $[-15, 15]$ discretized into 100 control volumes. Here, the bed function is defined by $z(x) = x\tan(\alpha)$, with α is the bed inclination angle set in our simulation to $\alpha = \frac{\pi}{60}$. Initially,

$$h(0,x) = \begin{cases} 1 - z(x), & \text{if} \quad x \leq 0, \\ \\ 0, & \text{if} \quad x > 0, \end{cases} \qquad v(0,x) = 0. \tag{3.28}$$

In Figure 3.4 we display the time evolution of the wet/dry interface obtained using the conventional approach and the proposed wet/dry treatment along with the exact profile of the interface. Note that the analytical wet/dry front position is given as

$$\chi(t) = 2t\sqrt{g\cos(\alpha)} - 0.5gt^2\tan(\alpha).$$

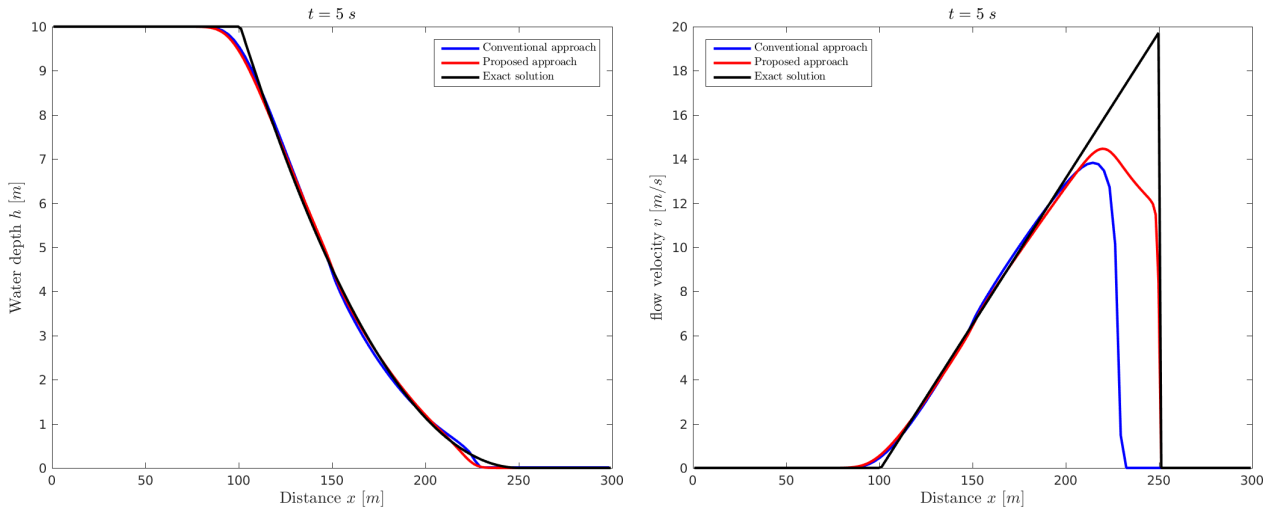

Figure 3.3: Comparison between the conventional approach and the proposed method for the wet/dry treatment in the dam-break problem over a dry bed with known analytical solution.

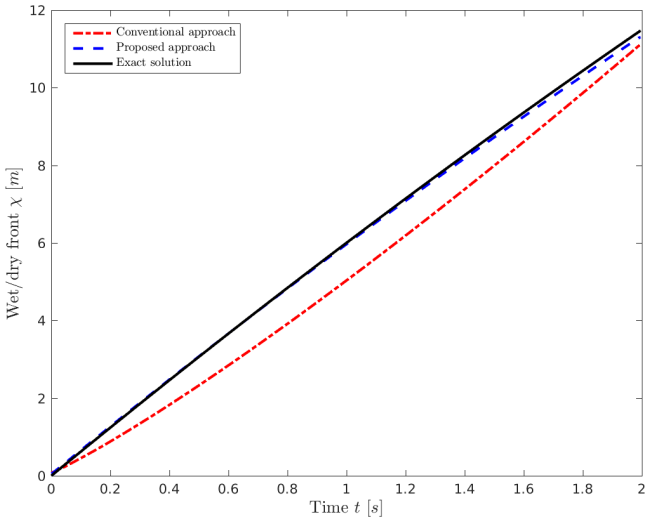

Figure 3.4: Comparison between the conventional approach and the proposed method for the wet/dry treatment in the dam-break problem over a dry inclined plane bed with known analytical wet/dry interface.

It is clear that there is a good agreement between the analytical results and those obtained using the proposed wet/dry treatment. The conventional approach fails to accurately capture the correct wet/dry interface for this dam-break problem over non-flat dry beds. Again, the results in Figure 3.4 demonstrate the accuracy of the proposed technique in better resolving the moving wet/dry fronts than the conventional method. We also validate the proposed approach for a dam-break problem over a wet bed against experimental measurements reported in [11]. As described in this reference, a glass channel with 9 m in length, 0.3 m in width and 0.34 m in height is used for the physical experiment. The dam is located at 4.65 m and the upstream water depth is fixed at $h_0 = 0.25\ m$, whereas two values are used for the downstream water depth h_1. In this experiment, the dam-break is produced by lifting the gate upward very quickly through a pulley system. At time $t = 0$ the dam collapses and the flow problem consists of a shock wave travelling downstream and a rarefaction wave travelling upstream. We examine

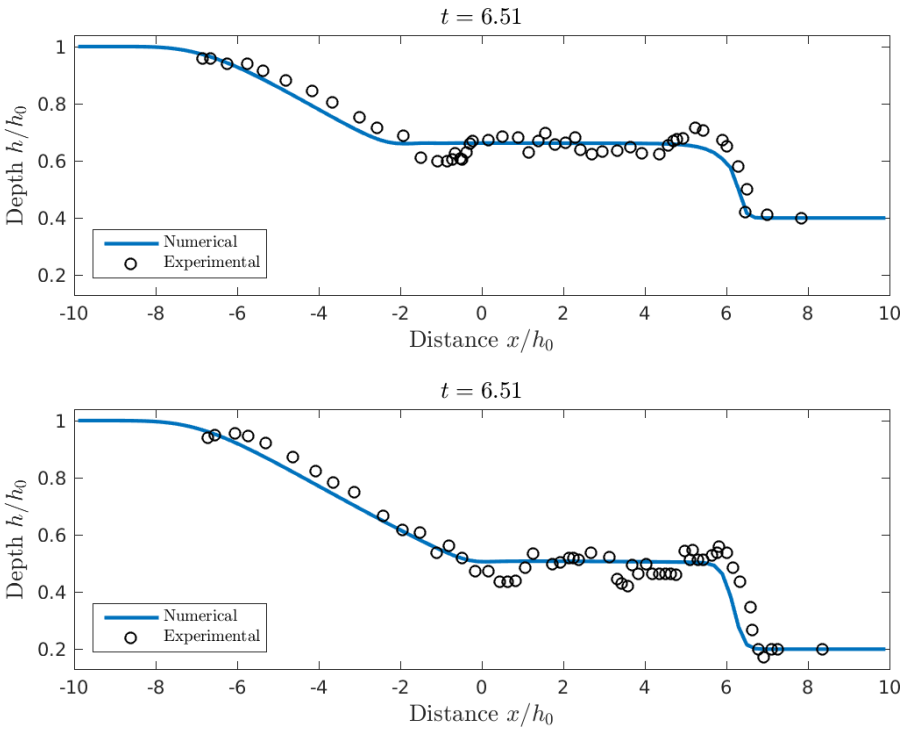

Figure 3.5: Comparison between experimental and numerical results for the dam-break problem over a wet bed at two different downstream water depths $h_1 = 0.1\ m$ and $h_1 = 0.05\ m$.

the performance of the proposed approach using 100 control volumes for $h_1 = 0.05\ m$ and $h_1 = 0.1\ m$. In Figure 3.5 we present results obtained at dimensionless time $t = 6.51$. Note that dimensionless variables are used to display the results for which the distance x, time t and water depth h are divided by h_0, $\sqrt{\frac{h_0}{g}}$ and h_0, respectively. The agreement between the numerical simulations and experimental measurements shown in Figure 3.5 is fairly good. The free-surface amplitude and the hydraulic shock are well predicted by the proposed numerical approach. Obviously, the computed results for both considered values of h_1 verify the stability and the shock capturing properties of the numerical method for this dam-break problem over a wet bed.

3.3.2 Validation of finite element method for bed deformation

To verify the finite element method for solving two-dimensional elasticity equations, we consider the benchmark problem proposed in [194]. This problem has an analytical solution and it has been widely used in the literature to validate computational methods for elastostatic models. The problem statement consists on solving the equations (3.1) in a homogeneous and isotropic rectangular domain with 100 m for the length and 10 m for the width. The domain is subject to a nodal displacement of 3 m applied upwards in the center point of the domain. Here, the computational domain is discretized using quadratic finite elements in an unstructured triangular mesh with 772 elements and 1649 nodes. In Figure 3.6 we illustrate the mesh used in our simulations before and after deformation by the nodal displacement. Note a denser mesh is used in our simulations for the area where the deformation is taken place. The comparison between the numerical results and analytical solution obtained for cross-sections of the vertical stress σ_y at the center point is presented in Figure 3.7. Notice that as discussed in [194],

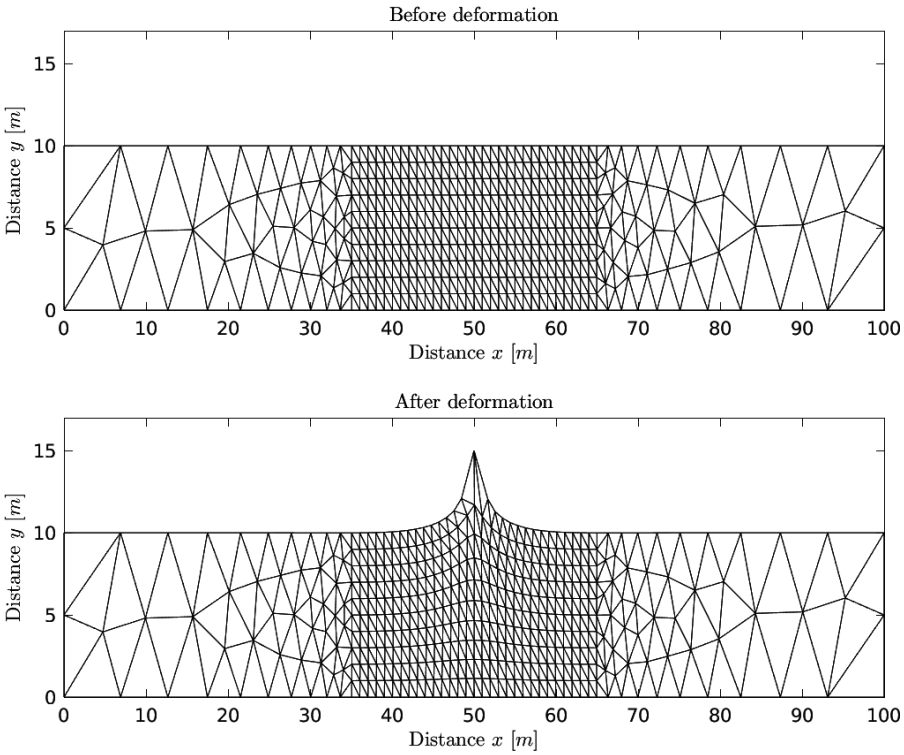

Figure 3.6: Computational mesh before deformation (top) and after deformation (bottom) used for the accuracy test example at time $t = 12s$.

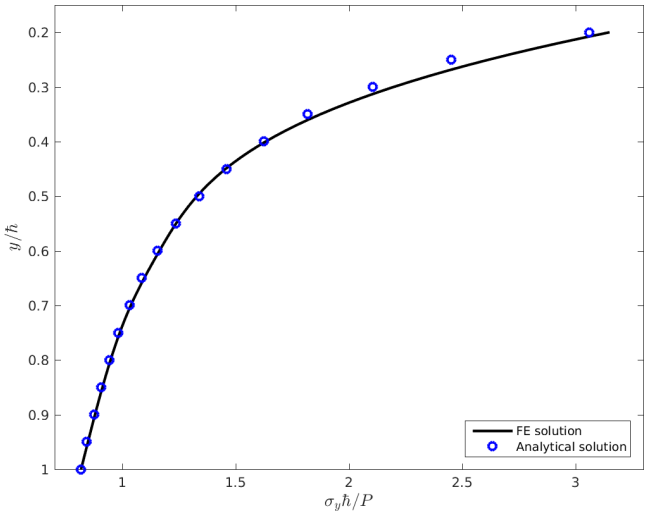

Figure 3.7: Comparison between the finite element results and the analytical solution of the vertical stress component σ_y for the accuracy test example.

dimensionless variables are presented in Figure 3.7 using the domain width $\hbar = 10\ m$ and the point load $P = 3\ N/m$. As it can be seen from the results shown in Figure 3.6, the finite element method performs very well for this benchmark problem and it produces highly accurate and stable numerical results using reasonably coarse meshes. There is a good agreement between the results obtained using the finite element method and the analytical solution reported in reference [194].

3.3.3 Free-surface flow problem over a deformable bed

Pipe failures are among common examples in nature for which several studies have taken place in civil engineering. For these applications, the source of deformation may be caused by a fatigue in the pipe or simply by a load applied below the seabed. In this example, we consider a free-surface flow over a lake with run-up slopes at both sides with open out-flow conditions at the downstream boundary and including a circular pipe as shown in Figure 3.1. Here, the pipe radius $R = 3\ m$ with a force of 100 N applied on the top surface of the pipe Γ_v, two values of the bed slope angle are considered in this section with $\beta = \frac{\pi}{5}$ and $\beta = \frac{\pi}{10}$. Initially, the system is at rest and to maintain the same water volume in the two cases, the water depth at time $t = 0$ is $h = 2.5\ m$ and $h = 2.1\ m$ for $\beta = \frac{\pi}{5}$ and $\beta = \frac{\pi}{10}$, respectively. Keeping the water volume the same in both cases and changing the bed slope angles would allow for a comparison in terms of the maximum water depth and the settling time for the waves in the considered situations. At time $t = 10\ s$ the constant force is applied on the upper part Γ_v of the pipe and consequently a deformation is expected on the pipe and therefore on the lake bed which generate water waves on the surface to run-up over both slopes.

Figure 3.8 depicts the mesh used in our simulations before and after deformation for $\beta = \frac{\pi}{5}$. An unstructured triangular mesh with 1749 quadratic elements and 3763 nodes is used in our simulations as it offers a compromise between accuracy and efficiency in the numerical method. In Figure 3.9 we present the distribution of the main stress component σ_x at time $t = 12\ s$ for the considered bed slope angles $\beta = \frac{\pi}{5}$ and $\beta = \frac{\pi}{10}$. It is clear that maximum values of stresses are located on the pipe surface where the deformation has taken place. The deformed bed has also been accurately resolved using our finite element method. Under the considered conditions, stress distributions for both bed slopes exhibit similar features in the computational domain. Note the symmetrical features in both stress distributions and the bed profile in the obtained results in Figure 3.9. Furthermore, no mesh distortion has been detected in all results obtained for this test example. It should be stressed that results from the proposed coupled model should be compared with observations of laboratory free-surface flows and bed deformations for this problem. However, there is no data available until now to carry out this comparison study. Thus, at the moment we can only perform numerical simulations and verify that results are plausible and consistent.

In Figure 3.10 we display the responses of the water free-surface at five different instants for $\beta = \frac{\pi}{5}$. Those results obtained for $\beta = \frac{\pi}{10}$ are shown in Figure 3.11. We used a mesh with 100 control volumes for the solution of shallow water equations. As can be seen from these results, the system starts from the rest and once the deformation on the pipe occurs, a water wave is generated on the surface and it flows over the deformed bed. Later the water wave reaches the two bed slopes and a run-up can be clearly seen in both bed slopes in Figure 3.10 and Figure 3.11. For longer times, the system is stabilized to a steady-state configuration with no disturbances on the water surface for both cases. A longer run-up waves have been

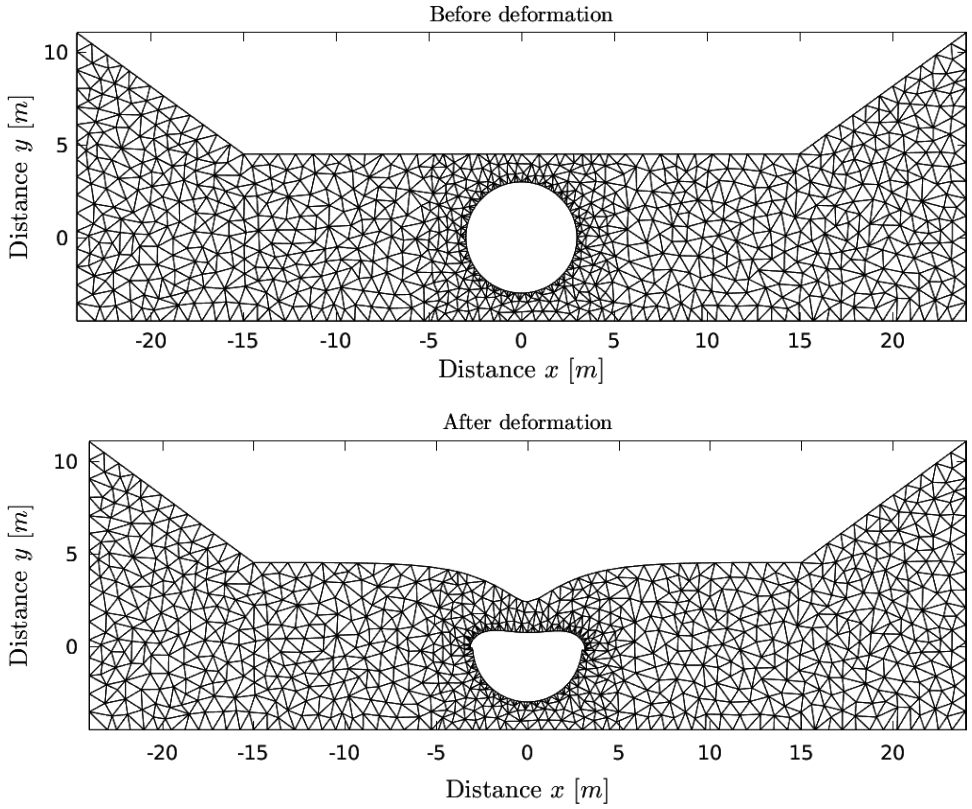

Figure 3.8: Computational mesh before deformation (top) and after deformation (bottom) used for free-surface flow problem over a deformable bed.

observed for the case with $\beta = \frac{\pi}{10}$ than for the case $\beta = \frac{\pi}{5}$. It is clear that the considered hybrid finite volume/finite element method performs well for this free-surface flow problem over a deformable bed as both the bed topography and the water free-surface are accurately captured without non-physical oscillations or excessive numerical diffusion appearing in the the numerical solutions. To assess the accuracy of the coupled model in dealing with moving boundaries of the run-up problem, Figure 3.12 illustrates the time evolution of water free-surface and the flow velocity at three different gauges in $x = -10$, 0 and 10. As expected, because of the symmetry in this problem, the water depths at the locations $x = -10$ and $x = 10$ are identical and high water depths are expected at the gauge situated at the center $x = 0$ where the deformation takes place. It is also clear that the flow velocities at the two gauges in $x = -10$ and $x = 10$ have the same amplitudes and opposite signs. As time progresses, amplitudes of both the flow velocity and the water free-surface decrease at all considered gauges. The proposed coupled model performs very well for this example and captures the correct run-up features without requiring complicated techniques or three-dimensional representations for the free-surface flows over deformable beds.

To examine the effects of friction on the water free-surface, we illustrate in Figure 3.13 the time evolution of the hydraulic energy at the center of the domain ($x = 0$) using different values of the Manning coefficient n_b for $\beta = \frac{\pi}{5}$ and $\beta = \frac{\pi}{10}$. It is evident that increasing the Manning coefficient results in a decrease in the hydraulic energy. This energy dissipation is expected in the system for high frictions on the bed. In order to quantify these results, we summarize in Table 3.1 statistics on the results shown for the hydraulic energy in Figure 3.13. Here, we present the minimum value, peak value, mean value, standard deviation, rise and settling times obtained for the considered Manning coefficients. The effect of bed frictions related to

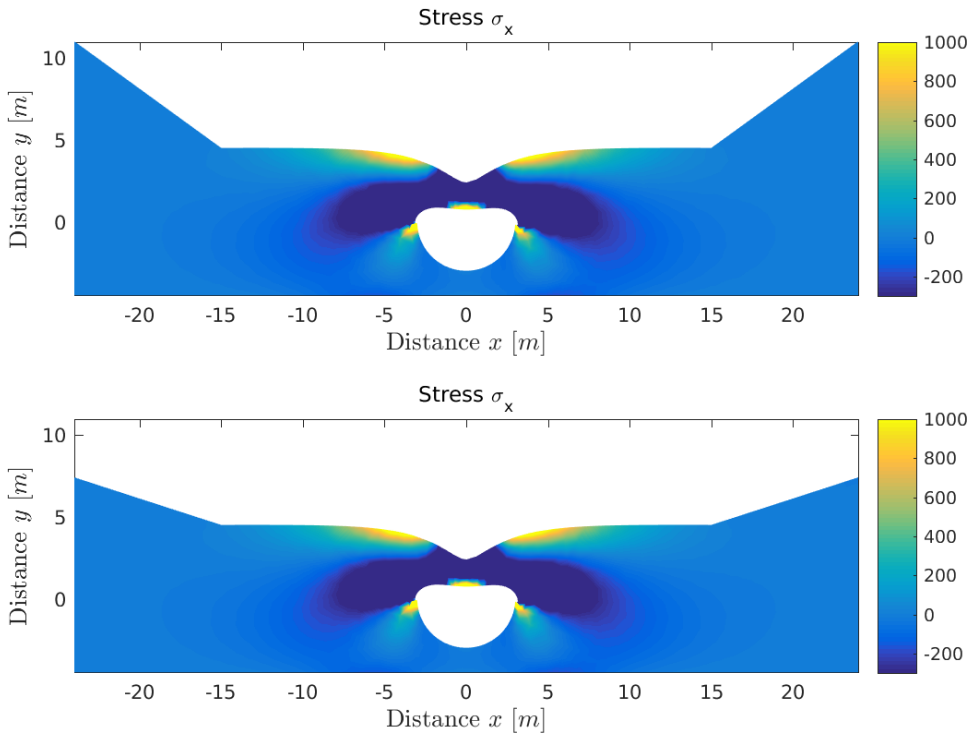

Figure 3.9: Distribution of the stress σ_x using $\beta = \frac{\pi}{5}$ (top) and $\beta = \frac{\pi}{10}$ (bottom) obtained for free-surface flow problem over a deformable bed at time $t = 12\ s$.

Table 3.1: Statistics for the hydraulic energy for free-surface flow problem over a deformable bed using different Manning coefficients.

	$\beta = \frac{\pi}{5}$					
n_b	min	Peak	Mean	Std	Rise time	Settling time
0.01	4.501	6.81	6.385	0.255	0.208	1.472×10^4
0.05	4.501	6.67	6.381	0.228	0.166	1.467×10^4
0.1	4.501	6.61	6.375	0.198	0.140	1.456×10^4

	$\beta = \frac{\pi}{10}$					
n_b	min	Peak	Mean	Std	Rise time	Settling time
0.01	4.901	7.206	6.742	0.269	0.154	1.559×10^4
0.05	4.901	7.103	6.746	0.257	0.144	1.558×10^4
0.1	7.901	7.016	6.741	0.234	0.126	1.555×10^4

the Manning roughness can be clearly seen on the rise and settling times. Same conclusions have been exhibited for similar quantitative results for the situation with $\beta = \frac{\pi}{10}$. Again, the proposed hybrid finite volume/finite element method performs very satisfactorily for this flow problem since it does not diffuse the moving bed fronts and no spurious oscillations have been detected near steep gradients of the run-up waves in the computational domain. In addition, the wet/dry treatment considered in this study resolves well the run-up waves.

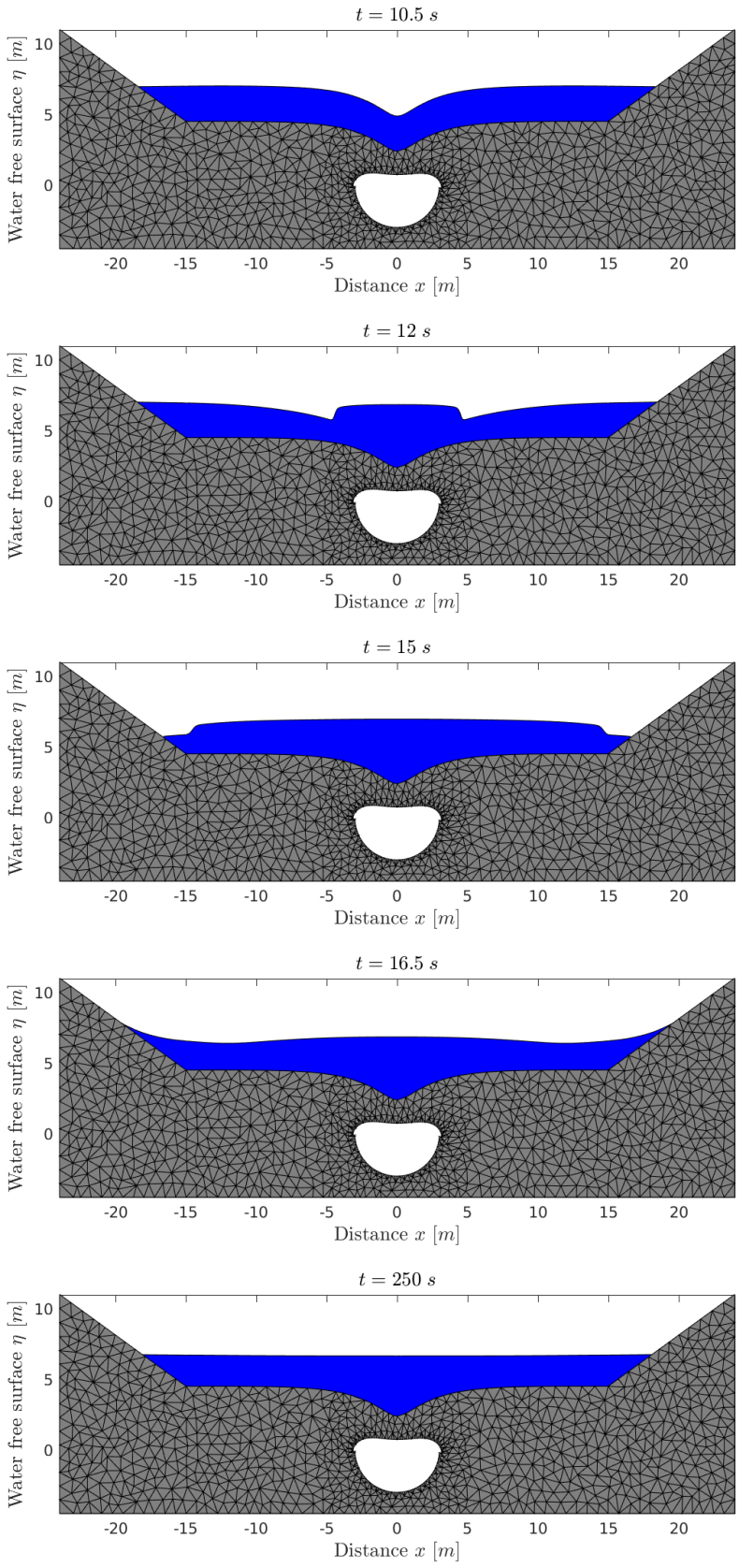

Figure 3.10: Free-surface responses at five different instants obtained for the flow problem over a deformable bed with $\beta = \frac{\pi}{5}$.

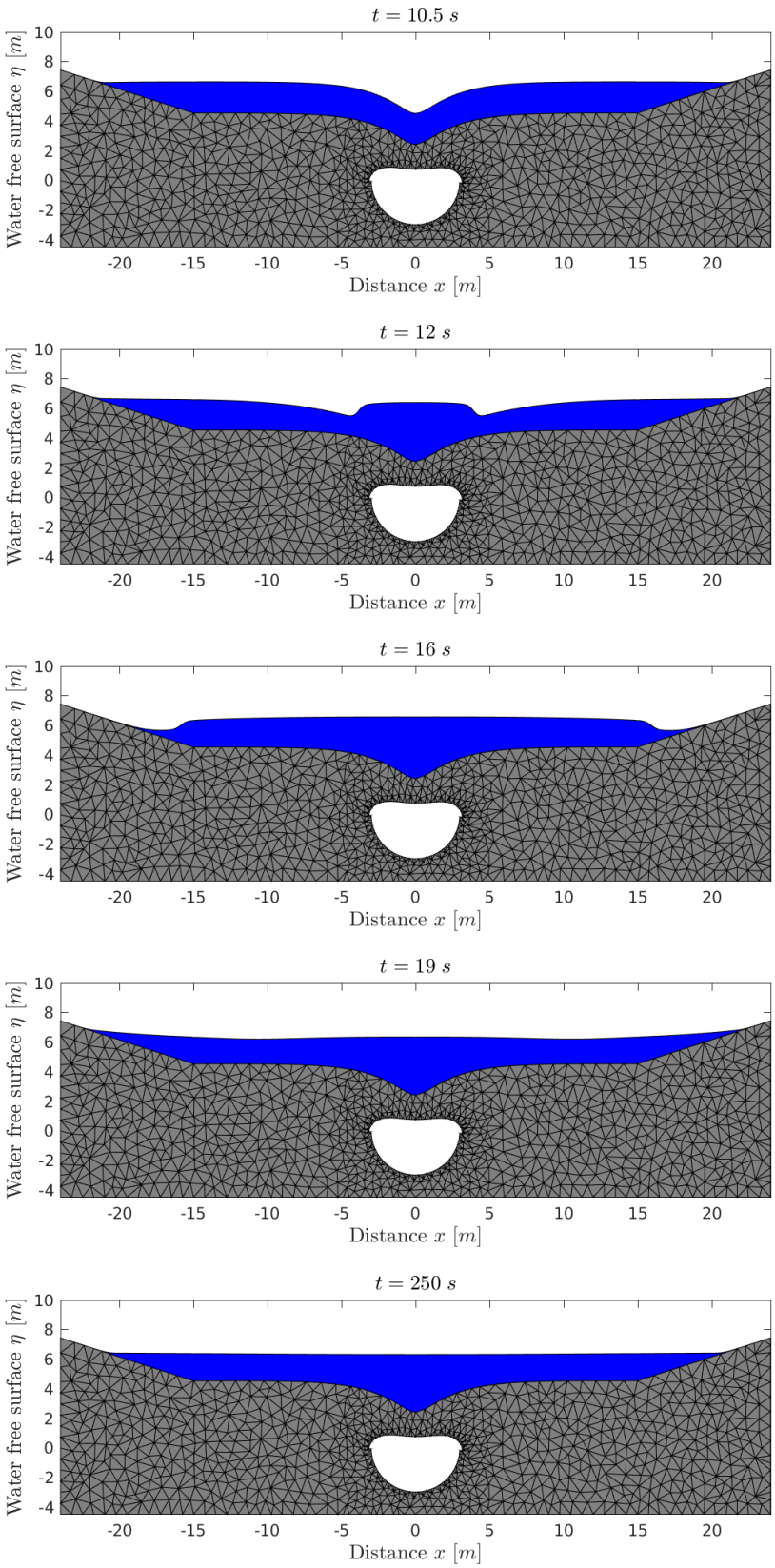

Figure 3.11: Free-surface responses at five different instants obtained for the flow problem over a deformable bed with $\beta = \frac{\pi}{10}$.

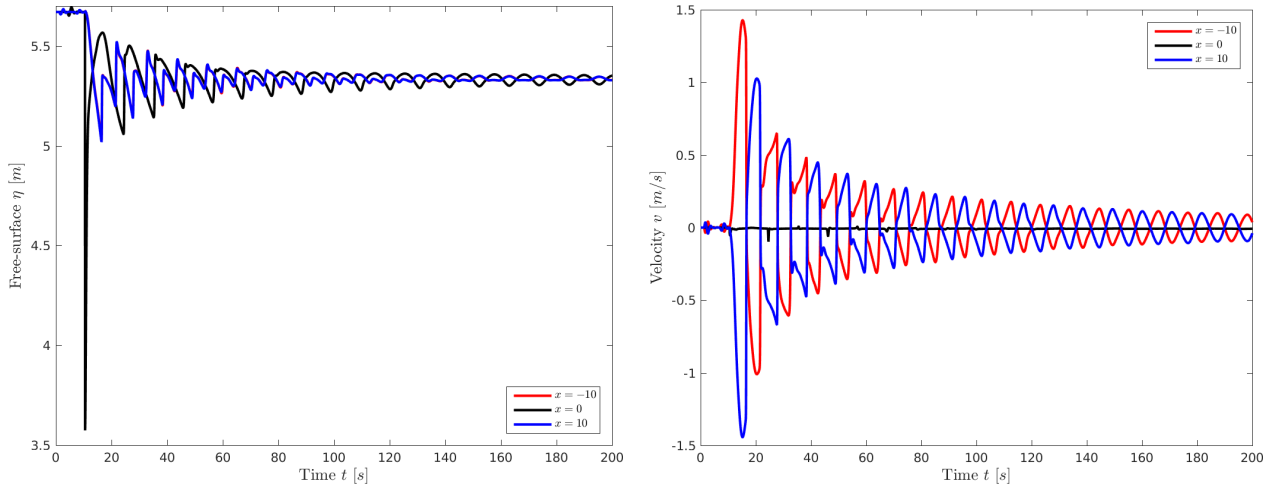

Figure 3.12: Time evolution of the water free-surface (left) and flow velocity (right) at three different gauges for the flow problem over a deformable bed with $\beta = \frac{\pi}{5}$.

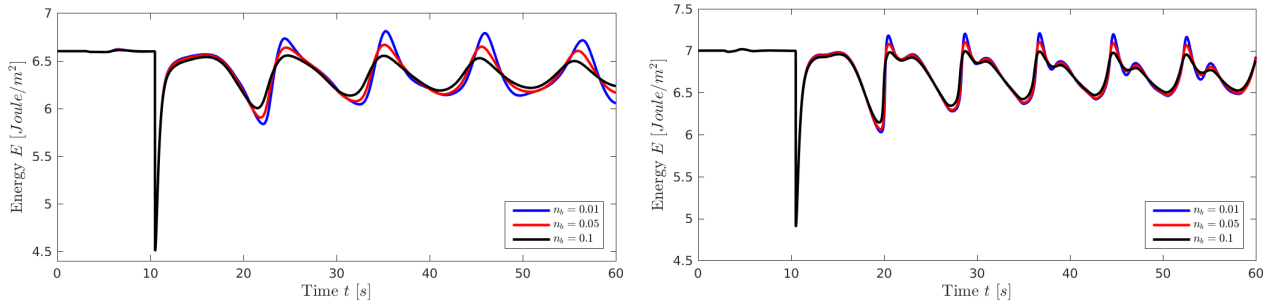

Figure 3.13: Time evolution of the hydraulic energy for free-surface flow problem over a deformable bed using different Manning coefficients with $\beta = \frac{\pi}{5}$ (left) and $\beta = \frac{\pi}{10}$ (right).

3.4 Two-layer dam-break problem over deformable beds

In this section a coupled two-dimensional equations of linear elasticity for the soil bed and the one-dimensional two-layer shallow water equations for the water flow are presented. The two-layer shallow water equations can be derived by integrating the Euler equations in the vertical coordinate direction as in the case of single-layer equations. The difference between the two-layer and single-layer shallow water equations is the addition of vertical variation in the density and velocity. The one-dimensional two-layer shallow water equations with different densities, ρ_1, ρ_2, as $\rho_1 < \rho_2$ read

$$\begin{aligned}
\frac{\partial h_1}{\partial t} + \frac{\partial (h_1 v_1)}{\partial x} &= 0, \\
\frac{\partial (h_1 v_1)}{\partial t} + \frac{\partial}{\partial x}\left(h_1 v_1^2 + \frac{1}{2} g h_1^2\right) &= -g h_1 \frac{\partial z}{\partial x} - g h_1 \frac{\partial h_2}{\partial x}, \\
\frac{\partial h_2}{\partial t} + \frac{\partial (h_2 v_2)}{\partial x} &= 0, \\
\frac{\partial (h_2 v_2)}{\partial t} + \frac{\partial}{\partial x}\left(h_2 v_2^2 + \frac{1}{2} g h_2^2\right) &= -g h_2 \frac{\partial z}{\partial x} - g h_2 \frac{\rho_1}{\rho_2} \frac{\partial h_1}{\partial x} - g h_2 M_b^2 \frac{v_2 \mid v_2 \mid}{h_2^{4/3}},
\end{aligned} \tag{3.29}$$

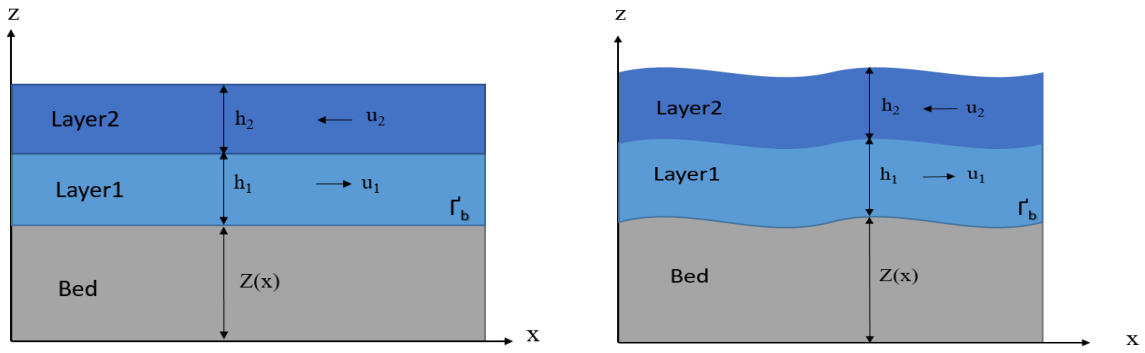

Figure 3.14: Schematic of a system of two-layer shallow water coupled to deformable bed, before deformation (left plot), after defromation (right plot). Here, the gray portion is used for the bed deformation and the blue portions are used for the water flow.

where v_1, v_2 are the water speeds in the first and second layer respectively, h_1, h_2 are the water heights in the first and second layer respectively, and g is the gravity constant. The first and third equations state the conservation of mass, and the second and fourth equations represent the conservation of the momentum at each layer. Figure 3.14 shows the system characterestics for more illustrations. The result of the vertical integration and hydrostatic assumption is a system of partial differential equations presenting two sets of single-layer shallow water equations with the addition of a coupling term between the layers. It is important to mention that this coupling between the two-layer is due to the difference of the layers densitiy and depth and does not represent momentum transfer or mass exchange due to drag between the layers.

To solve the shallow water equations, a finite volume of Rusanov type is considered. In the first step we reformulate the shallow water system of equations in a conservative form as

$$\frac{\partial \mathbf{W}}{\partial t} + \frac{\partial \mathbf{F}(\mathbf{W})}{\partial x} = \mathbf{Q}(\mathbf{W}), \tag{3.30}$$

where $\mathbf{W}$ is the vector of conserved variables, $\mathbf{F}(\mathbf{W})$ is the vector of flux functions and $\mathbf{Q}(\mathbf{W})$ is the vectors of source terms as

$$\mathbf{W} = \begin{pmatrix} h_1 \\ h_1 v_1 \\ h_2 \\ h_2 v_2 \end{pmatrix}, \quad \mathbf{F}(\mathbf{W}) = \begin{pmatrix} h_1 v_1 \\ h_1 v_1^2 + \frac{1}{2} g h_1^2 \\ h_2 v_2 \\ h_2 v_2^2 + \frac{1}{2} g h_2^2 \end{pmatrix}, \quad \mathbf{Q}(\mathbf{W}) = \begin{pmatrix} 0 \\ -g h_1 \frac{\partial h_2}{\partial x} - g h_1 \frac{\partial z}{\partial x} \\ 0 \\ -\frac{\rho_1}{\rho_2} g h_2 \frac{\partial h_1}{\partial x} - g h_2 \frac{\partial z}{\partial x} \end{pmatrix},$$

The shallow water domain is discretized into number of control volumes $[x_{i-\frac{1}{2}}, x_{i+\frac{1}{2}}]$, with uniform sizes $\triangle x$ and then divide the domain into subintervals $[t_n, t_{n+1}]$ with step size $\triangle t$ and $t_n = n\Delta t$. Integrating the previous system over the time-space control domain and obtain the relation:

$$\frac{d\mathbf{W}_i}{dt} + \frac{\mathbf{F}_{i+\frac{1}{2}} - \mathbf{F}_{i-\frac{1}{2}}}{\triangle x} = \mathbf{Q}_i, \tag{3.31}$$

where $\mathbf{W}_i(t)$ is the averaged solution $\mathbf{W}$ in the control volume at time t.

$$\mathbf{W}_i(t) = \frac{1}{\triangle x}\int_{x_{i-\frac{1}{2}}}^{x_{i+\frac{1}{2}}} \mathbf{W}(t,x)dx, \tag{3.32}$$

$$\mathbf{W}_i^{n+1} = \mathbf{W}_i^n - \frac{\Delta t}{\Delta x}\left(\mathbf{F}^n_{i+\frac{1}{2}} - \mathbf{F}^n_{i-\frac{1}{2}}\right) + \Delta t \mathbf{Q}_i^n, \tag{3.33}$$

where $\mathbf{F}_{i\pm\frac{1}{2}}$ are the numerical fluxes at $x = x_{i\pm\frac{1}{2}}$ and time $t = t_n$, and $\mathbf{Q}_i^n$ is a consistent discretization of the source term. Rusanov fluxes are considered in the present study and it is defined as [45]

$$\mathbf{F}_{i+\frac{1}{2}} = \frac{1}{2}\Big(\mathbf{F}\big(\mathbf{W}_{i+\frac{1}{2}}\big) + \mathbf{F}\big(\mathbf{W}_i\big)\Big) + \frac{1}{2}\lambda\Big(\mathbf{W}_{i+\frac{1}{2}} - \mathbf{W}_i\Big), \tag{3.34}$$

where $\lambda = \lambda_1, \lambda_2, \lambda_3$, and λ_4 are the system eigenvalues given as

$$\begin{aligned}
\lambda_1 &\approx U_m - \sqrt{g\,(h_1+h_2)},\\
\lambda_2 &\approx U_m + \sqrt{g\,(h_1+h_2)},\\
\lambda_3 &\approx U_c - \sqrt{(1-r)g\frac{h_1h_2}{h_1+h_2}\left(1 - \frac{(v_2-v_1)^2}{(1-r)g\,(h_1+h_2)}\right)},\\
\lambda_4 &\approx U_c + \sqrt{(1-r)g\frac{h_1h_2}{h_1+h_2}\left(1 - \frac{(v_2-v_1)^2}{(1-r)g\,(h_1+h_2)}\right)},
\end{aligned} \tag{3.35}$$

where:

$$U_m = \frac{h_1v_1 + h_2v_2}{h_1+h_2}, \qquad U_c = \frac{h_1v_1 + h_2v_2}{h_1+h_2}, \qquad r = \frac{\rho_1}{\rho_2}.$$

The main advantages of the above system are the fact that the two-layer shallow water models avoid the expensive computational three-dimensional Navier-Stokes equations, and to obtain satisfied horizontal flow velocities as vertical velocities are relatively small. Algorithm 3.2 summarizes all the previously mentioned steps for the two-layer finite volume/finite element coupling procedure.

Algorithm 3.2 Coupled finite element/two-layer finite volume method used in this study.

Require: T the final simulation time.

1: Assemble the stiffness matrix $\mathbf{K}$ for elastostatic system using the finite element method (3.9)-(3.13).
2: **while** $t_n \leqslant T$ **do**
3: Assemble the force vector $\mathbf{b}$ for elastostatic system using the finite element method (3.9)-(3.13).
4: Solve the linear system (3.13) for the displacement in the computational mesh.
5: Update the displacement of the finite element nodes on the interface.
6: Reconstruct the bed z on the control volumes formed by the finite element nodes on the interface.
7: Update the time step Δt according to the CFL condition (3.26).
8: Solve the shallow water equations using:
9: **for** each control volume $\left[x_i, x_{i+\frac{1}{2}}\right]$ **do**
10: Compute the numerical fluxes $\mathbf{F}^n_{i+\frac{1}{2}}$ using the Rusanov scheme (3.34).
11: Discrete the source term $\mathbf{Q}_i$ using the well-balanced discretization (3.33).
12: Update the solution in the second stage of the splitting (3.16) using (3.22)-(3.23).
13: **end for**
14: Compute the horizontal force f_x using the bed friction according to (3.24).
15: Compute the vertical force f_z using the hydrostatic pressure according to (3.25).
16: Overwrite $t_n \longleftarrow t_n + \Delta t$ and go to step 2.
17: **end while**

3.5 Numerical results

To examine the performance of this system we present numerical results for several test examples. We illustrate the accuracy for two-layer shallow water system. As with all explicit time stepping methods the time step is specified according to the Courant-Friedrichs-Lewy (CFL) condition as:

$$\triangle t = C_r \frac{\triangle x}{max \ \mid \lambda_k \mid} \tag{3.36}$$

where λ_k, k=1,2,3,4 are the approximated eigenvalues, and C_r is a constant to be chosen less than unity. In all the examples presented in this section the courant number is set to 0.5 and the time step Δt is adjusted at each step according to the stability condition.

3.5.1 Lock-exchange problem

The accuracy of the proposed two-layer shallow water were checked for validation. For this, we solve the Lock-exchange problem, where in this example the two-layer are initially separated, the lighter water is on the left, while the heavier one is on the right:

$$\big(h_1(0,x), q_1(0,x), h_2(0,x), q_2(0,x)\big) = \begin{cases} -z(x), 0, 0, 0 & x < 0 \\ 0, 0, -z(x), 0 & x > 0 \end{cases}$$

Table 3.2: L^1 errors for the Lock-exchange accuracy test problem using different gridpoints.

N	Error in H	Rate of convergence	CPU time (s)
100	6.55E-2	-	0.15
200	2.2E-2	1.07	0.35
400	7.7E-3	1.07	1.08
800	4.0E-3	1.13	3.22
1600	2.4E-3	1.2	6.22

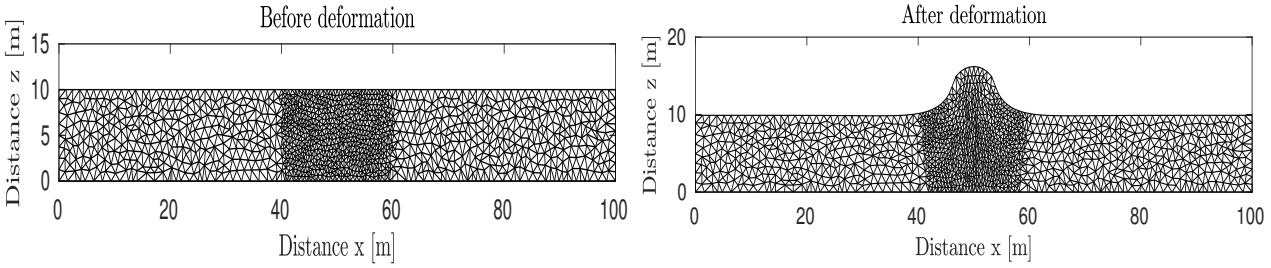

Figure 3.15: Computational mesh before deformation (left plot) and after deformation (right plot) used for free-surface flow problem over a deformable bed.

where the bottom topography is Gaussian-Shape function $z(x) = e^{-x^2} - 2$. The gravitational constant is $g = 9.81$, and the density ratio $r = 0.98$. The computational domain in this case is [-3, 3], and the boundary conditions are $q_1 = -q_2$ at each end of the interval. The problem solved using different numbers of gridpoints and the L^1-errors were calculated by comparing the results to the one obtained from using a very refined mesh with 12,800 gridpoints. The errors, rate of convergence and the computational time are shown in Table 3.2, as it can be clearly seen that the the mesh shows a good rate of convergence, and the method is first order.

3.5.2 Free-surface flows with raised bed

In this example free-surface flows over a rectangular domain with 100 m length and 10 m hight subjected to 1500 N tension force using quadratic six nodes finite element are presented. It can be seen that the mesh is finer near the load points and where largest deformations are likely to occur. Figure 3.15 represents the mesh before and after deformation. Figure 3.16 illustrates the distribution of the stresses σ_x and σ_y at the deformation time. Obviously, high stresses appear at the hump where the bed deformation is taken place. The good symmetry in these results with respect to the vertical centreline is noticed. The presented finite element method preserves the symmetry in the stresses and resolves the correct solution well for this test example. For the water simulation, a sudden deformation was introduced at $t = 0.1$ second, the water waves experiencing a smooth transition of dam-break as a response to this deformations, the water height keep decreasing till reach the steady state. Figure 3.17 presents the wave propagation at different time steps, hence the gray portion represents the soil deformations and the blue portion represents the two-layers shallow water waves.

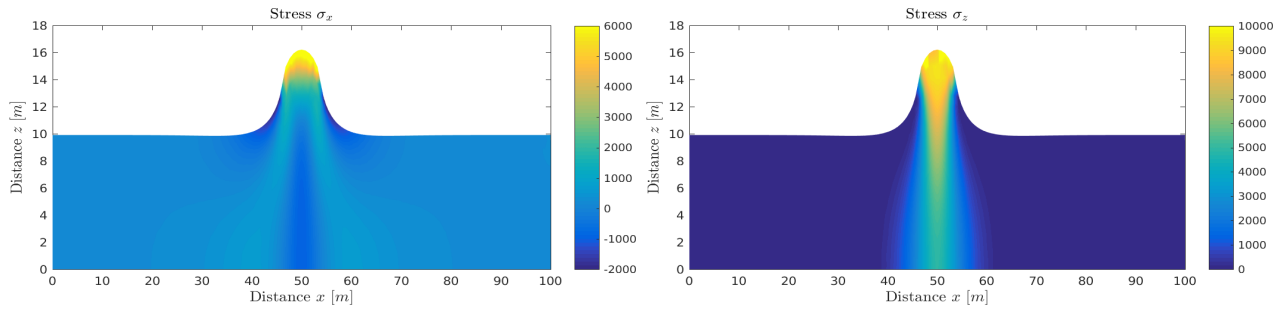

Figure 3.16: distribution of the stresses σ_x, σ_z obtained for the ftree surface two-layer flow over deformable bed at time $t = 0.1$ s.

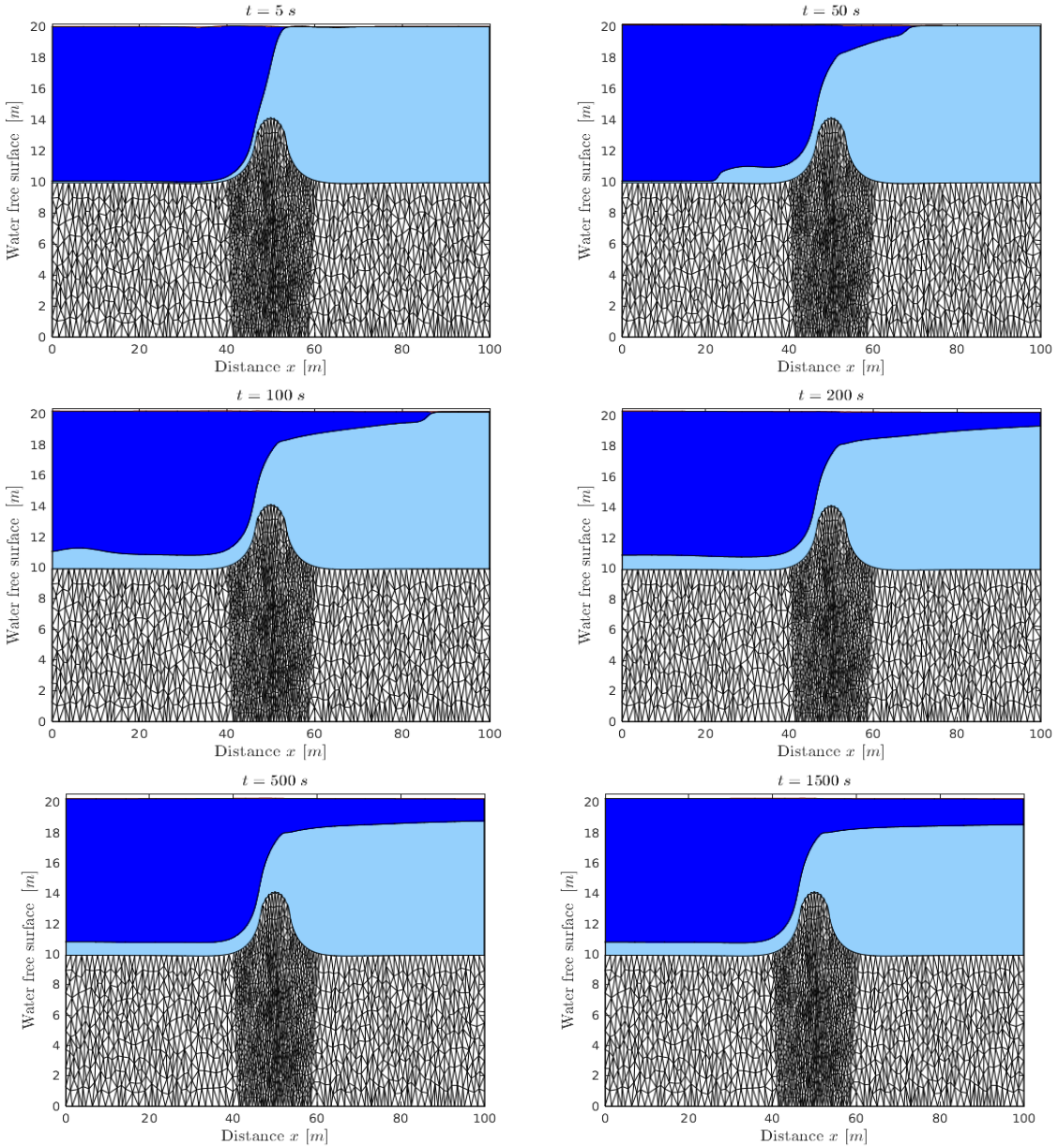

Figure 3.17: Water free-surface responses at six different instances for the two-layer flow problem over deformable bed.

3.6 Conclusions

In the present work, we have used a coupled system of nonlinear shallow water equations and linear elasticity to model and simulate wave run-up by a deformation on seabeds. In order to reduce the complexity of the problem we have considered a static approximation of the bed deformation. The system is fully coupled through transfer conditions at the interface between the water flow and the seabed. In the current study, hydrostatic pressure and friction forces are considered for the elastostatic equations whereas bathymetric forces are accounted for in the shallow water equations. A hybrid finite volume/finite element is considered for the numerical simulation and a special wet/dry treatment is accounted for in our approach. The method is well-balanced, stable and it accurately resolves both water free-surface and bed deformations. The proposed method has been applied to a dam-break problem over a non-flat dry bed. The obtained results for this free-surface flow problem using the finite volume method have shown good agreement with experimental measurements. We have also presented an application of the developed model for a free-surface flow problem over a deformable bed. The obtained results, even with a coarse mesh in complex geometry, indicate that the proposed model can be used as a robust tool to design wave run-ups by static deformation on seabeds. The new method has several advantages. First, it can solve steady flows over irregular beds without large numerical errors thus, demonstrating that the proposed scheme achieves perfect numerical balance of the gradient fluxes and the source terms. Second, it can compute the numerical flux corresponding to the real state of water flow without relying on Riemann problem solvers. Furthermore, it has strong applicability to various problems in shallow water flows over deformed beds as shown in the numerical results. The proposed approach has been numerically examined for the test example of free-surface flow problems on different topographies. As future work, we aim to include erosion and deposition effects in the coupled model to allow for sediment transport and morphodynamics in the shallow water flows. Although, we have studied only the case of two-dimensional problems of the presented method, the extension to three-dimensional problems would be an encouraging next step. The future research should also be focused on the extension of these techniques to nonlinear plasticity in the bed deformation to allow strong interactions of water flows on soft beds.

Chapter 4

A computational model for simulation of shallow water waves by elastic deformations in the topography

In this chapter the problem of shallow water flows under conditions of abrupt changes to the bathymetry is considered. The idea is to develop an accurate and efficient computational approach to simulate such flows which pose a great challenge due to the differences in temporal and spacial scales. The free-surface flow which is commonly modeled by the shallow water equations coupled with the sudden changes of bathymetry is investigated numerically. It has been observed in nature that free-surface flows can sometimes be triggered by an abrupt or a sudden change in the bathymetry see for example [1]. A clear example is the tsunamis or landslides that pour into a water body in oceans or lakes. The common practice in modeling such free-surface flows is to assume that the displacement of the free-surface is the same as the displacement of the bed, and it happens concurrently due to incompressibility of the water. Thus, as an initial condition one applies a static source together with a translation of the seabed deformation onto the free-surface flow. Such an approach was first presented for the field of modelling tsunamis in [267] and referred to as *the passive approach* in [221]. The validity of such an approach was reported in [24] among others. The passive approach neglects the so-called rupture velocity and the rise time of the fault/bathymetry change dynamics. Investigations have been undertaken to understand the rupture velocity and rise time in many engineering applications. For example, the study in [173] took into account the rise time, and the rupture velocity has also been accounted for in [161]. In [5], work has been undertaken in which a numerical integration of the time-dependent elasticity equations as well as time-dependent fluid equations was considered. Over the past years, the development of efficient and increasingly accurate numerical models of nonlinear shallow water equations over variable beds has been a continuous challenge in coastal engineering communities see [83, 236, 3] among others. Since these models are considered to be theoretically challenging and practically important, researchers are currently working on developing efficient and accurate computational tools to model shallow water waves by elastic deformations in the topography. This represents a great challenge due to the time and space scales for which the abrupt changes took places versus the evolution of the water free-surface.

The commonly used finite difference schemes in the numerical solution of the nonlinear shallow water equations are non-conservative leading to volume loss and energy dissipation as the wave steepness increases and the flow approaches discontinuities [4]. Recent advances in seismic in-

verse algorithms enable accurate descriptions of the rise time and rupture propagation over the source area. Furthermore, this model provides a time series of the vertical displacement and velocity that constitute the bottom boundary condition of a non-hydrostatic model for transfer of kinetic and potential energies to the water. One limitation of this method is the appearance of oscillations in the computational results when applied to more complex geometries [262]. The depth-integrated method was reformulated, and hence a non-hydrostatic model was derived in the spherical coordinate system for basin-wide waves propagation [263]. However, this method suffers from a drawback in that it cannot guarantee the conservation of momentum in the numerical scheme. Each of the aforementioned numerical modeling techniques has its own features and drawbacks when it is applied to the shallow water system. The finite difference scheme is considered to be easy to implement. However, the scheme is not accurate when dealing with complex geometries such as the characterization of the coastlines during the simulation [121]. To deal with these limitations, refined mesh approaches are applied to increase the resolution of certain areas of interest [50]. Nevertheless, there are still some problems facing this approach when the waves are reflected from the coastline outside the finer mesh as such waves are not well resolved.

Finite element methods are more flexible in modeling shallow water flows in a complex geometry as they can be formulated for a wide range of mesh topologies [264, 245, 235]. A limitation of the finite element method lies when the solution exhibits large gradients [71]. In addition, the finite element method also suffers from its inability to conserve mass and momentum during the simulations. The finite volume techniques are widely known by researchers for dealing with mobile beds, even though such techniques are also well suited for solving the partial differential equations that are included in shallow water flows. These methods have become standard in solving the free-surface flows and shock waves problems as they guarantee the conservation property during the simulation. The most significant problem facing the finite volume techniques when dealing with a mobile bed is the treatment of the geometric source terms, where the challenge is in the balancing between gradient and source terms when time variations are small. This problem is numerically non-trivial, and methods that are not well balanced would generate spurious oscillations in their results [209]. The transient generation of waves due to the coupling between the free-surface and sea floor has been considered by few authors only. Generally, there are some specific cases where the bottom deformation becomes a very important factor. Other studies relied on experimental techniques by lowering or raising a box at one end of the channel [165]. The purpose of this study is to develop a novel model for numerical simulation of shallow water waves by elastic deformations in the topography. Accounting for elastic deformations in the shallow water flows is new and a coupled set of partial differential equations is proposed in this work for their modelling.

In the current study, a coupled finite element/finite volume method for solving free-surface flow problems over deformable beds is proposed. The governing equations consist of the one-dimensional nonlinear shallow water equations for the water flow and a two-dimensional linear elasticity model for the bed deformation. Deformations in the topography can be caused by a localized force which causes propagations of water waves with different amplitudes and frequencies. Coupling conditions at the interface are also investigated in this study and a well-balanced finite volume method using non-uniform grids is implemented to avoid interpolation procedures at the interface between the finite element nodes and the finite volume cells. Frictional forces along with hydrodynamical forces are also accounted for in the water flow model. On the other hand a force is sampled from the hydrostatic pressure and applied on the bed surface during

the time process. To the best of our knowledge, developing a coupled finite element/finite volume method for solving free-surface flow problems over deformable beds is presented for the first time. The chapter is organized as follows. Description of the coupled model for shallow water waves induced by elastic deformations is presented in section 4.1. Section 4.2 is devoted to the formulation of the numerical methods used for the solution procedure. We consider a two-dimensional finite element method for the bed deformations whereas a well-balanced finite volume method is implemented for the free-surface waves. In section 4.3, we present numerical results and examples for shallow water flows over elastic beds. Our new approach is shown to enjoy the expected accuracy as well as the efficiency. Concluding remarks are given in section 4.4.

4.1 Shallow water waves by elastic deformation in beds

The physical model used in the present study consists of the well-known shallow water equations coupled with additional equations to describe the elastic deformation in the bed. The shallow water system has been widely used to model water flows under the influence of gravity and it uses the assumption that the vertical scale is much smaller than any typical horizontal scale. This class of equations can be derived by depth-averaging the incompressible Navier-Stokes equations subject to a hydrostatic pressure, see for example [109]. For one-dimensional problems, the equations read

$$\begin{aligned} \frac{\partial h}{\partial t} + \frac{\partial (hv)}{\partial x} &= 0, \\ \frac{\partial (hv)}{\partial t} + \frac{\partial}{\partial x}\left(hv^2 + \frac{1}{2} g h^2 \right) &= -gh\frac{\partial B}{\partial x} + \tau_f, \end{aligned} \tag{4.1}$$

where t is the time variable, x the space coordinate, $h(x,t)$ the water depth, $v(x,t)$ the water velocity, g the gravitational constant and B the bed topography. In (4.1), τ_f is the friction slope term which models the bottom friction effects using the Manning empirical form,with M_b being the Manning roughness coefficient at the bed, τ_f is defined by

$$\tau_f = -g M_b^2 h \frac{v\,|v|}{h^{4/3}}, \tag{4.2}$$

It is well known that the system (4.1) is strictly hyperbolic with real and distinct eigenvalues given as

$$\lambda_1 = v - \sqrt{gh}, \qquad \lambda_2 = v + \sqrt{gh}. \tag{4.3}$$

Notice that the equations (4.1) have to be solved in a time interval and spatial domain equipped with given boundary and initial conditions. In practice, these conditions are problem dependent and their discussion is postponed for section 4.3 where numerical examples are discussed. In the shallow water equations (4.1), the function B corresponds to the topography layer characterizing the bed level. For fixed bottom topography *i.e.* $B = B(x)$, the equations (4.1) reduce to the standard shallow water equations. In the current work, we assume that a deformation takes place such that the bed level depends on the time variable as well. This requires an additional equation for its evolution and deformation. To motivate the discussion, we consider a simple example of bed deformation as depicted in Figure 4.1. Similar techniques have been used to model elastic models of the earthquake cycle for a long strike-slip fault [131, 185].

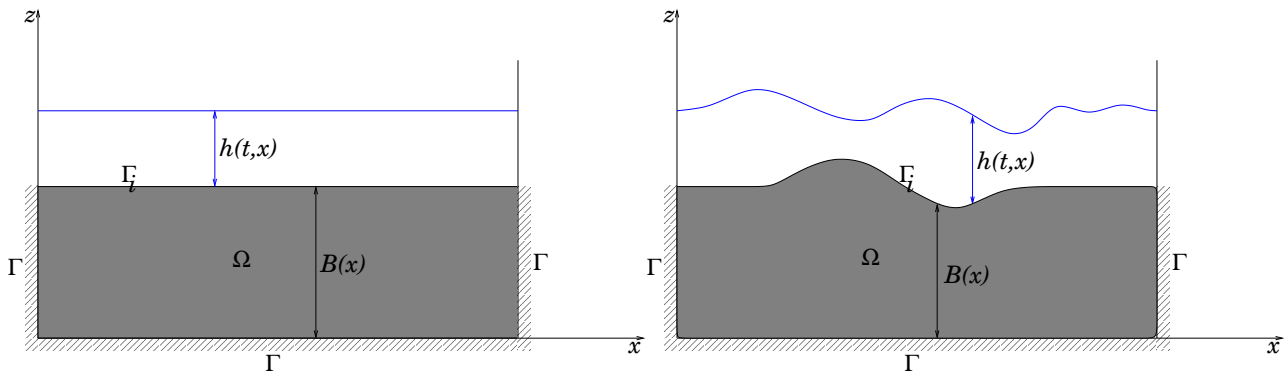

Figure 4.1: Coupled system before bed deformation (left plot) and after bed deformation (right plot).

In solid mechanics, the two-dimensional constitutive relations of an isotropic elastic bed in presence of body forces can be reformulated as [200]

$$\begin{aligned} \frac{\partial \sigma_x}{\partial x} + \frac{\partial \tau_{xz}}{\partial z} &= f_x, \\ \frac{\partial \sigma_z}{\partial z} + \frac{\partial \tau_{xz}}{\partial x} &= f_z, \end{aligned} \tag{4.4}$$

where σ_x and σ_z are the normal stress components in the x- and z-direction, respectively. Here, τ_{xz} is the shear stress, f_x and f_z are the external forces in the x- and z-direction, respectively. The displacement vector is denoted by $V = (u_x, u_z)^\top$ and the infinitesimal strain tensor is defined by

$$\boldsymbol{\epsilon} = \frac{1}{2}\Big(\nabla V + (\nabla V)^\top\Big). \tag{4.5}$$

In the current study, we consider the constitutive relation

$$\boldsymbol{\sigma} = \mathbf{D}\ \boldsymbol{\epsilon}, \tag{4.6}$$

where the stress vector $\boldsymbol{\sigma}$ and the constitutive matrix $\mathbf{D}$ are defined by

$$\boldsymbol{\sigma} = \begin{pmatrix} \sigma_x \\ \sigma_z \\ \tau_{xz} \end{pmatrix}, \qquad \mathbf{D} = \frac{E}{(1+\nu)(1-2\nu)} \begin{pmatrix} 1-\nu & \nu & 0 \\ \nu & 1-\nu & 0 \\ 0 & 0 & \dfrac{1-2\nu}{2} \end{pmatrix},$$

with ν is the Poisson ratio and E is the Young modulus characterizing the bed material. Note that we solve the system (4.4), subject to the following boundary conditions.

$$\begin{aligned} \boldsymbol{\sigma} &= \boldsymbol{\sigma}_c, \qquad \text{on} \quad \Gamma_i, \\ V &= \mathbf{0}, \qquad \text{on} \quad \Gamma, \end{aligned} \tag{4.7}$$

where Γ is the fixed boundary as shown in Figure 4.1. Note that the interface Γ_i between the water and bed depends on time and it is defined as

$$\Gamma_i(t) = \Big\{(x,z) \in \Omega : \quad z = B(x,t)\Big\}.$$

The coupled system is numerically solved using a splitting operator where the bed deformation and the water free-surface are computed separately, using the two-dimensional elastostatic equations and the one-dimensional shallow water equation, respectively. The coupling is achieved through the interface Γ_i by updating the bed topography $B(x,t)$ at each deformation step and applying frictional forces f_x and f_z generated from the water flow on Γ_i. Initially, the coupled system is at equilibrium rest and a sudden force is applied on the bed topography to generate a deformation and consequently perturbations are expected to appear on the water free-surface. During the time process, interchange conditions are transferred from the bed topography to the water flow and vice versa. It should also be stressed that in the present study, we assume that bed deformations occur suddenly which lead to a fast characteristic time-scale associated with the propagation of acoustic waves and therefore there is no need to consider the elastodynamics form the equations (4.4).

4.2 Coupled finite element/finite volume method

For the numerical solution of the coupled system we consider a finite element method for the two-dimensional elasticity equations (4.4) and a finite volume method for the one-dimensional shallow water equations (4.1). The starting point for the finite element method is the variational formulation of the strain energy in the domain Ω. Thus, multiplying the strong form of x-direction equation in (4.4) by an arbitrary weight function ϕ_x and integrate over the domain yields

$$\int_\Omega \frac{\partial \sigma_x}{\partial x}\phi_x \, dx + \int_\Omega \frac{\partial \tau_{xz}}{\partial z}\phi_x \, dx - \int_\Omega f_x \phi_x \, dx = 0.$$

Using the Green-Gauss theorem, the above equation becomes

$$\oint_{\partial\Omega} \sigma_x n_x \phi_x \, d\mathbf{x} - \int_\Omega \frac{\partial \phi_x}{\partial x}\sigma_x \, d\mathbf{x} + \oint_{\partial\Omega} \tau_{xz} n_z \phi_x \, d\mathbf{x} - \int_\Omega \frac{\partial \phi_x}{\partial z}\tau_{xz} \, d\mathbf{x} - \int_\Omega f_x \phi_x \, d\mathbf{x} = 0,$$

where $\mathbf{x} = (x,z)^\top$ and $\mathbf{n} = (n_x, n_z)^\top$ is the outward unit normal on Γ, $\partial\Omega = \Gamma \cup \Gamma_i$ Using the x-component of the traction $\mathcal{T}_x = \sigma_x n_x + \tau_{xz} n_z$, the above equation can be written as

$$\oint_{\partial\Omega} \mathcal{T}_x \phi_x \, d\mathbf{x} - \int_\Omega \left(\frac{\partial \phi_x}{\partial x}\sigma_x + \frac{\partial \phi_x}{\partial z}\tau_{xz} \right) \, d\mathbf{x} - \int_\Omega f_x \phi_x \, d\mathbf{x} = 0. \tag{4.8}$$

Similar steps applied to the z-direction equation in (4.4) give

$$\oint_{\partial\Omega} \mathcal{T}_z \phi_z \, d\mathbf{x} - \int_\Omega \left(\frac{\partial \phi_z}{\partial x}\tau_{xz} + \frac{\partial \phi_z}{\partial z}\sigma_z \right) \, d\mathbf{x} - \int_\Omega f_z \phi_z \, d\mathbf{x} = 0, \tag{4.9}$$

where $\mathcal{T}_z = \sigma_z n_z + \tau_{xz} n_x$. Adding the two equations (4.8) and (4.9) yields

$$\oint_{\partial\Omega} (\mathcal{T}_x \phi_x + \mathcal{T}_z \phi_z) \, d\mathbf{x} - \int_\Omega (f_x \phi_x + f_z \phi_z) \, d\mathbf{x} - \int_\Omega \left(\frac{\partial \phi_x}{\partial x}\sigma_x + \frac{\partial \phi_x}{\partial z}\tau_{xz} + \frac{\partial \phi_z}{\partial z}\sigma_z + \frac{\partial \phi_z}{\partial x}\tau_{xz} \right) \, d\mathbf{x} = 0,$$

which can be reformulated in a vector form as

$$\int_\Omega \widehat{\boldsymbol{\phi}} \cdot \boldsymbol{\sigma} \, d\mathbf{x} = \oint_{\partial\Omega} \boldsymbol{\phi}^\top \cdot \boldsymbol{\mathcal{T}} \, d\mathbf{x} + \int_\Omega \boldsymbol{\phi}^\top \cdot \mathbf{f} \, d\mathbf{x}, \tag{4.10}$$

where $\boldsymbol{\phi} = (\phi_x, \phi_z)^\top$, $\boldsymbol{\mathcal{T}} = (\mathcal{T}_x, \mathcal{T}_z)^\top$ and $\widehat{\boldsymbol{\phi}} = \left(\frac{\partial \phi_x}{\partial x}, \frac{\partial \phi_z}{\partial z}, \frac{\partial \phi_x}{\partial z} + \frac{\partial \phi_z}{\partial x}\right)^\top$. To solve the weak form (4.10) with the finite element method, the domain Ω is discretized into a set of elements where

the solution is approximated in terms of the nodal values U_j and the polynomial basis functions $N_j(x,z)$ as

$$V(x,z) = \sum_{j=1}^{N_d} \mathbf{U}_j N_j(x,z), \tag{4.11}$$

where N_d is the number of mesh nodes. In the present work, we consider quadratic triangular elements with six nodes for which the element displacement $V^e = (u_x^e, u_z^e)^\top$ can be obtained by

$$V^e = \begin{pmatrix} N_1^e & 0 & N_2^e & 0 & \dots & 0 \\ 0 & N_1^e & 0 & N_2^e & \dots & N_6^e \end{pmatrix} \begin{pmatrix} u_{x1} \\ u_{z1} \\ u_{x2} \\ u_{z2} \\ \vdots \\ u_{x6} \\ u_{z6} \end{pmatrix},$$

where N_j^e are the shape functions written in local coordinates $(\xi_1, \xi_2)^\top$ as

$$N_1^e(\xi_1,\xi_2) = \xi_2\,(2\xi_2 - 1), \qquad N_2^e(\xi_1,\xi_2) = \xi_1\,(2\xi_1 - 1),$$
$$N_3^e(\xi_1,\xi_2) = (1-\xi_1-\xi_2)\,(1-2\xi_1-2\xi_2), \qquad N_4^e(\xi_1,\xi_2) = 4\xi_2\xi_1, \,,$$
$$N_5^e(\xi_1,\xi_2) = 4\xi_1\,(1-\xi_2-\xi_1), \qquad N_6^e(\xi_1,\xi_2) = 4\,(1-\xi_2-\xi_1)\,\xi_2.$$

To solve the fully discretized problem, the elementary matrices are assembled into a global system of equations

$$\mathbf{K}V = \boldsymbol{b}, \tag{4.12}$$

where $\mathbf{K}$ is the global stiffness matrix, V is the nodal displacement vector and $\boldsymbol{b}$ is the force vector. In our simulations, the matrix $\mathbf{K}$ is decomposed into an $LUL^\top$ factorization, then the solution is reduced to backward/forward substitutions after updating the right-hand side vector $\boldsymbol{b}$ at every time step.

The second step in the considered coupling system is to solve for water perturbations based on the sudden changes on the bed and update the water height and velocity at each time step. For this purpose, we use a finite volume method of Roe type over non-uniform grids to avoid interpolation procedures at the interface Γ_i. A similar method has been investigated for shallow water equations in [11]. Hence, to formulate the finite volume method we rewrite the equations (4.1) in conservative form as

$$\frac{\partial \mathbf{W}}{\partial t} + \frac{\partial \mathbf{F}(\mathbf{W})}{\partial x} = \mathbf{Q}(\mathbf{W}) + \mathbf{S}(\mathbf{W}), \tag{4.13}$$

where

$$\mathbf{W} = \begin{pmatrix} h \\ \\ hv \end{pmatrix}, \mathbf{F}(\mathbf{W}) = \begin{pmatrix} hv \\ \\ hv^2 + \frac{1}{2}gh^2 \end{pmatrix}, \mathbf{Q}(\mathbf{W}) = \begin{pmatrix} 0 \\ \\ -gh\dfrac{\partial B}{\partial x} \end{pmatrix}, \mathbf{S}(\mathbf{W}) = \begin{pmatrix} 0 \\ \\ -gM_b^2 h \dfrac{v\,|v|}{h^{\frac{4}{3}}} \end{pmatrix}.$$

For the time integration of the system (4.13) we divide the time interval into subintervals $[t_n, t_{n+1}]$ with variable size Δt_n such that $t_n = t_{n-1} + \Delta t_n$, $n = 1, 2, \ldots$ and $t_0 = 0$. We use the notation $\mathbf{W}^n(x)$ to denote the discrete solution $\mathbf{W}(t_n, x)$. In the current work, we use the splitting operator introduced in [226] to deal with the differential source terms $\mathbf{Q}(\mathbf{W})$ and the non-differential source term $\mathbf{S}(\mathbf{W})$ in (4.13). The splitting procedure consists of the following two steps:

Step 1: Solve for $\widetilde{\mathbf{W}}$

$$\frac{\widetilde{\mathbf{W}} - \mathbf{W}^n}{\Delta t_n} + \frac{\partial \mathbf{F}(\mathbf{W}^n)}{\partial x} = \mathbf{Q}\left(\mathbf{W}^n\right). \tag{4.14}$$

Step 2: Solve for $\mathbf{W}^{n+1}$

$$\frac{\mathbf{W}^{n+1} - \widetilde{\mathbf{W}}}{\Delta t_n} = \mathbf{S}\left(\widetilde{\mathbf{W}}\right). \tag{4.15}$$

For the space discretization we discretize the one-dimensional space domain in non-uniform control volumes $\left[x_{i-\frac{1}{2}}, x_{i+\frac{1}{2}}\right]$ with length Δx_i and we use the notation $\mathbf{W}_i^n$ to denote the space-averaged of $\mathbf{W} = \mathbf{W}(t, x)$ in the cell $\left[x_{i-\frac{1}{2}}, x_{i+\frac{1}{2}}\right]$ at time t_n, and $\mathbf{W}_{i+\frac{1}{2}}^n$ are the intermediate solutions at $x_{i+\frac{1}{2}}$ at time t_n,

$$\mathbf{W}_i^n = \frac{1}{\Delta x_i} \int_{x_{i-\frac{1}{2}}}^{x_{i+\frac{1}{2}}} \mathbf{W}(t_n, x)\, dx, \qquad \mathbf{W}_{i+\frac{1}{2}}^n = \mathbf{W}\left(t_n, x_{i+\frac{1}{2}}\right).$$

Integrating the system (4.14) over the space-time control domain $\left[x_{i-\frac{1}{2}}, x_{i+\frac{1}{2}}\right] \times [t_n, t_{n+1}]$, one obtains the following fully discrete system

$$\mathbf{W}_i^{n+1} = \mathbf{W}_i - \frac{\Delta t_n}{\Delta x_i}\left(\mathbf{F}_{i+\frac{1}{2}}^n - \mathbf{F}_{i-\frac{1}{2}}^n\right) + \Delta t_n \mathbf{Q}_i^n, \tag{4.16}$$

where $\mathbf{F}_{i\pm\frac{1}{2}}^n = \mathbf{F}\left(\mathbf{W}_{i\pm\frac{1}{2}}^n\right)$ are the numerical fluxes at $x = x_{i\pm\frac{1}{2}}$ and time $t = t_n$, and $\mathbf{Q}_i^n$ is the space-averaged of the source term $\mathbf{Q}$ defined as

$$\mathbf{Q}_i^n = \frac{1}{\Delta x_i} \int_{x_i-\frac{1}{2}}^{x_i+\frac{1}{2}} \mathbf{Q}(\mathbf{W})\, dx. \tag{4.17}$$

The spatial discretization (4.16) is complete when the numerical fluxes $\mathbf{F}_{i\pm1/2}^n$ and the source term $\mathbf{Q}_i^n$ are reconstructed. Generally, this step can be carried out using any finite volume method developed in the literature for solving hyperbolic systems of conservation laws, see for example [24, 221]. In the present study, we consider the Roe reconstruction defined as [205]

$$\mathbf{F}_{i+\frac{1}{2}}^n = \frac{1}{2}\left(\mathbf{F}(\widehat{\mathbf{W}}_{i+1}^n) + \mathbf{F}(\widehat{\mathbf{W}}_i^n)\right) + \frac{1}{2}\mathbf{A}\left(\widehat{\mathbf{W}}_{i+\frac{1}{2}}^n\right)\left(\widehat{\mathbf{W}}_i^n - \widehat{\mathbf{W}}_{i+1}^n\right), \tag{4.18}$$

where the averaged state $\widehat{\mathbf{W}}_{i+\frac{1}{2}}^n$ is calculated as

$$\widehat{\mathbf{W}}_{i+\frac{1}{2}}^n = \begin{pmatrix} \dfrac{h_i^n + h_{i+1}^n}{2} \\ \dfrac{\sqrt{h_i^n} v_i^n + \sqrt{h_{i+1}^n} v_{i+1}^n}{\sqrt{h_i^n + h_{i+1}^n}} \end{pmatrix}, \tag{4.19}$$

and the Roe matrix in (4.18) is defined as $\mathbf{A} = \mathbf{R}\mathbf{\Lambda}\mathbf{R}^{-1}$ with

$$\mathbf{R} = \begin{pmatrix} 1 & 1 \\ \widehat{\lambda}_1 & \widehat{\lambda}_2 \end{pmatrix}, \qquad \mathbf{\Lambda} = \begin{pmatrix} \widehat{\lambda}_1 & 0 \\ 0 & \widehat{\lambda}_2 \end{pmatrix}, \tag{4.20}$$

with $\widehat{\lambda}_1 = \widehat{v} - \sqrt{g\widehat{h}}$ and $\widehat{\lambda}_2 = \widehat{v} + \sqrt{g\widehat{h}}$ are the two eigenvalues associated with the system evaluated at the averaged state (4.19).

For the discretization of the source term $\mathbf{Q}_i^n$ we implement a well-balanced reconstruction investigated in [11]. Thus, the well-balanced discretization of $\mathbf{Q}_i^n$ is achieved by in splitting the integral in (4.17) over the two sub-cells $\left[x_{i-\frac{1}{2}}, x_i\right]$ and $\left[x_i, x_{i+\frac{1}{2}}\right]$ of the control volume $\left[x_{i-\frac{1}{2}}, x_{i+\frac{1}{2}}\right]$ as

$$\mathbf{Q}_i^n = \frac{1}{\Delta x_i}\left(\frac{(x_i - x_{i-1})}{2}\mathbf{Q}^L_{i-\frac{1}{2}} + \frac{(x_{i+1} - x_i)}{2}\mathbf{Q}^R_{i+\frac{1}{2}}\right), \tag{4.21}$$

where $\mathbf{Q}^L_{i-\frac{1}{2}}$ and $\mathbf{Q}^R_{i+\frac{1}{2}}$ are the space-averaged of the source term $\mathbf{Q}$ in the sub-cells $\left[x_{i-\frac{1}{2}}, x_i\right]$ and $\left[x_i, x_{i+\frac{1}{2}}\right]$ defined as

$$\mathbf{Q}^L_{i-\frac{1}{2}} = \begin{pmatrix} 0 \\ -g\dfrac{h_i + h_{i-1}}{2}\left(B_i - B_{i-1}\right) \end{pmatrix}, \quad \mathbf{Q}^R_{i-\frac{1}{2}} = \begin{pmatrix} 0 \\ -g\dfrac{h_{i+1} + h_i}{2}\left(B_{i+1} - B_i\right) \end{pmatrix}.$$

It is evident that for small water depths, the bed friction term dominates the other terms in the momentum equation. This is mainly due to the presence of the term $h^{\frac{4}{3}}$ in the dominator of τ_f in (4.2). To overcome this drawback we use a semi-implicit time integration of the source term $\mathbf{S}$ in (4.15) as

$$\begin{aligned} \frac{h^{n+1} - \widetilde{h}}{\Delta t_n} &= 0, \\ \frac{(hv)^{n+1} - \left(\widetilde{h}\widetilde{v}\right)}{\Delta t_n} &= -gM_b^2\frac{(hv)^{n+1}\left|\widetilde{v}\right|}{\left(\widetilde{h}\right)^{\frac{4}{3}}}, \end{aligned} \tag{4.22}$$

where $\widetilde{h}$ and $\widetilde{v}$ are the water height and velocity obtained from the first step (4.14) of the splitting procedure. Solving the second equation in (4.22) for $(hv)^{n+1}$ yields

$$(hv)^{n+1} = \frac{\left(\widetilde{h}\widetilde{v}\right)}{1 + \Delta t_n g M_b^2\left|\widetilde{v}\right| / \left(\widetilde{h}\right)^{\frac{4}{3}}}. \tag{4.23}$$

As in most explicit time integration schemes, the time step in our finite volume method is selected using a Courant-Friedrichs-Lewy (CFL) condition. In our simulations, the Courant

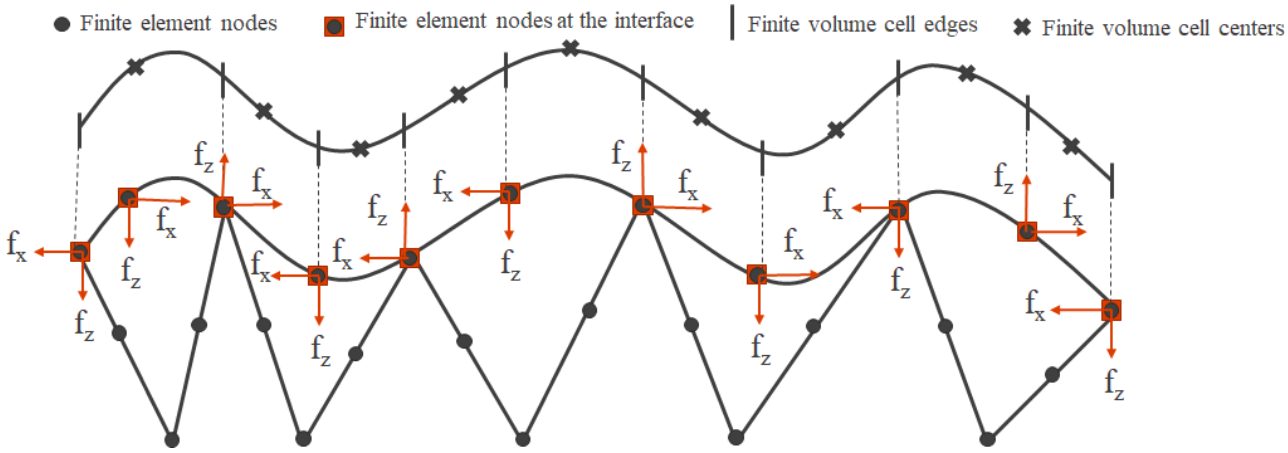

Figure 4.2: A schematic illustration of finite element and finite volume nodes at the interface.

number Cr is fixed and Δt_n is chosen at each time step according to the following CFL condition

$$\Delta t_n = Cr \frac{\min\left(\Delta x_i\right)}{\max\left(\left|\widehat{\lambda}_1^+\right|, \left|\widehat{\lambda}_1^-\right|, \left|\widehat{\lambda}_2^+\right|, \left|\widehat{\lambda}_2^-\right|\right)}, \tag{4.24}$$

where $\widehat{\lambda}_1^{\pm} = \widehat{v}_1^{\pm} - \sqrt{g\widehat{h}_1^{\pm}}$ and $\widehat{\lambda}_2^{\pm} = \widehat{v}_2^{\pm} + \sqrt{g\widehat{h}_2^{\pm}}$ with $\widehat{h}_{1,2}^{\pm}$ and $\widehat{v}_{1,2}^{\pm}$ are computed using the space-averaged solutions in the control volume $\left[x_{i-\frac{1}{2}}, x_{i+\frac{1}{2}}\right]$ and its two neighbouring cells as

$$\widehat{h}_1^+ = \frac{h_{i+1}+h_i}{2}, \quad \widehat{h}_1^- = \frac{h_i+h_{i-1}}{2}, \quad \widehat{v}_1^+ = \frac{\sqrt{h_{i+1}}v_{i+1}+\sqrt{h_i}v_i}{\sqrt{h_{i+1}}+\sqrt{h_i}}, \quad \widehat{v}_2^+ = \frac{\sqrt{h_i}v_i+\sqrt{h_{i-1}}v_{i-1}}{\sqrt{h_i}+\sqrt{h_{i-1}}}.$$

4.2.1 Implementation of coupling conditions at the interface

One of the advantages in using non-uniform grids in the finite volume solution is to avoid interpolations at the interface for interchange coupling conditions. Here, the selected control volumes in the finite volume methods coincide with the finite element nodes on the interface as shown in Figure 4.2. At each time step coupling conditions are transferred on the interface for both models to update the solutions for the displacement V, water height h and water velocity v. In the present work, the deformed finite element nodes on the interface are used to reconstruct the bed $B(x,t)$ for the shallow water equations (4.1). Here, a triangular finite element with three nodes on the interface yields two non-uniform control volumes the edges of which are the three nodes and their centres are obtained by averaging the coordinates of these nodes, compare Figure 4.2. We also assume that once the deformation occurs, the time variation in these coordinates is negligible and therefore no need for interpolation procedures to reconstruct the bed topography in the finite volume method. This bed profile is used in the finite volume solution of the flow system to obtain the water height h^{n+1} and the water velocity v^{n+1} at the next time level t_{n+1}.

For coupling conditions from the water flow to the bed on the interface, the forces f_x and f_z in the elasticity equations (4.4) are reconstructed at each time step. Here, the horizontal force f_x in the x-direction is updated using the friction term as

Algorithm 4.1 Coupled finite element/finite volume method used in the present study.

Require: T the final simulation time.

1: Assemble the stiffness matrix $\mathbf{K}$ for elastostatic system using the finite element method (4.8)-(4.12).
2: **while** $t_n \leqslant T$ **do**
3: Assemble the force vector $\mathbf{b}$ for elastostatic system using the finite element method (4.8)-(4.12).
4: Solve the linear system (4.12) for the displacement in the computational mesh.
5: Update the displacement of the finite element nodes on the interface.
6: Reconstruct the bed B on the control volumes formed by the finite element nodes on the interface.
7: Update the time step Δt_n according to the CFL condition (4.24).
8: Solve the shallow water equations using:
9: **for** each control volume $\left[x_i, x_{i+\frac{1}{2}}\right]$ **do**
10: Compute the numerical fluxes $\mathbf{F}^n_{i+\frac{1}{2}}$ using the Roe scheme (4.18).
11: Discrete the source term $\mathbf{Q}_i$ using the well-balanced discretization (4.21).
12: Compute the solution in the first stage of the splitting $\mathbf{W}_i^{n+1}$ using (4.16).
13: Update the solution in the second stage of the splitting (4.15) using (4.22)-(4.23).
14: **end for**
15: Compute the horizontal force f_x using the bed friction according to (4.25).
16: Compute the vertical force f_z using the hydrostatic pressure according to (4.26).
17: Overwrite $t_n \longleftarrow t_n + \Delta t_n$ and go to step 2.
18: **end while**

$$f_x = -gM_b^2 h^{n+1} \frac{v^{n+1}\left|v^{n+1}\right|}{\left(h^{n+1}\right)^{\frac{4}{3}}}. \tag{4.25}$$

The vertical force f_z in the z-direction is reconstructed at each time step using the change in the hydrostatic pressure as

$$p^{n+1} = -\rho g(h^{n+1} - h_0),$$

and at each node of the three finite element nodes located on the interface, the force f_z is distributed using the integral form as

$$\begin{aligned} f_z^{(1)} &= \int_{-1}^{1} -\frac{1}{2}\xi\,(1-\xi)\,p^{n+1}\frac{\hbar}{2}\,d\xi \;=\; \frac{1}{6}p^{n+1}\hbar, \\ f_z^{(2)} &= \int_{-1}^{1} \left(1-\xi^2\right)p^{n+1}\frac{\hbar}{2}\,d\xi \;=\; \frac{2}{3}p^{n+1}\hbar, \\ f_z^{(3)} &= \int_{-1}^{1} \frac{1}{2}\xi\,(1+\xi)\,p^{n+1}\frac{\hbar}{2}\,d\xi \;=\; \frac{1}{6}p^{n+1}\hbar, \end{aligned} \tag{4.26}$$

where $\hbar$ is the edge length of the considered element on the interface. It is easy to verify that $f_z^{(1)} + f_z^{(2)} + f_z^{(3)} = p^{n+1}\hbar$. The total force f_z in the z-direction is obtained by accumulating the elemental forces on the overlapping nodes, see Figure 4.2 for an illustration. In summary, the coupled finite element/finite volume method proposed in this study to solve shallow water waves by elastic deformations in the topography is carried out in the detailed steps described in Algorithm 4.1.

4.3 Numerical results and examples

In this section we examine the performance of the proposed computational model introduced in the above sections using several examples of shallow water waves by elastic deformations in the topography. For the first test example, we verify the accuracy of the techniques described in this study for two well-established test examples of shallow water flows and elastostatic deformations. In all the computations reported in this section unless stated otherwise, the Youngs modulus $E = 10000\ Mpa$, the Poison ratio $\nu = 0.3$, the gravitational acceleration $g = 9.81\ m/s^2$ and the Manning coefficient $M_b = 0.025\ s/m^{1/3}$. Here, the Courant number is fixed to $Cr = 0.85$ and the time stepsize Δt_n is adjusted at each time step according to the stability condition (4.24). All the computations were performed on an Intel® Core(TM) i7-7500U @ 2.70GHz with 16 GB of RAM.

4.3.1 Accuracy test examples

We examine the accuracy of both the finite element and finite volume methods for two well-established test examples. First we consider a dam-break problem with known analytical solution. Here, we solve the shallow water equations (4.1) over a frictionless flat bottom in the domain $[0, 1]$ with initial conditions defined as

$$h(0,x) = \begin{cases} 1.0, & \text{if} \quad x \leq 0.5, \\ \\ 0.5, & \text{elsewhere}, \end{cases} \qquad v(0,x) = 0.$$

At $t = 0$, the dam collapses and the flow problem consists of a shock wave traveling downstream and a rarefaction wave traveling upstream. The analytical solution of this problem is given by [6]

$$h(t,x) = \begin{cases} 1, & \text{if} \quad x < \dfrac{1}{2} - t\sqrt{g}, \\ \\ \dfrac{1}{9g}\left(2\sqrt{g} - \dfrac{2x-1}{2t}\right)^2, & \text{if} \quad \dfrac{1}{2} - t\sqrt{g} \leq x \leq (u_2 - c_2)\, t + \dfrac{1}{2}, \\ \\ \dfrac{1}{4}\sqrt{1 + \dfrac{16C_s^2}{g} - 1}), & \text{if} \quad (u_2 - c_2)\, t + \dfrac{1}{2} < x \leq C_s t + \dfrac{1}{2}, \\ \\ \dfrac{1}{2}, & \text{if} \quad C_s t + \dfrac{1}{2} < x, \end{cases}$$

where

$$u_2 = C_s - \frac{g}{8C_s}\left(1 + \sqrt{1 + \frac{16C_s^2}{g}}\right), \quad c_2 = \sqrt{\frac{g}{4}\left(\sqrt{1 + \frac{16C_s^2}{g}} - 1\right)}, \quad C_s = 2.957918120187525.$$

In Figure 4.3 we compare numerical results obtained for the water height at time $t = 0.1$ using the proposed finite volume method on uniform and non-uniform meshes with 50 and 100 control volumes. Notice that for the uniform meshes, the spatial step $\Delta x = 0.02$ and $\Delta x = 0.01$ for the meshes with 50 and 100 control volumes, respectively. In the non-uniform meshes, the spatial step Δx_i is selected as

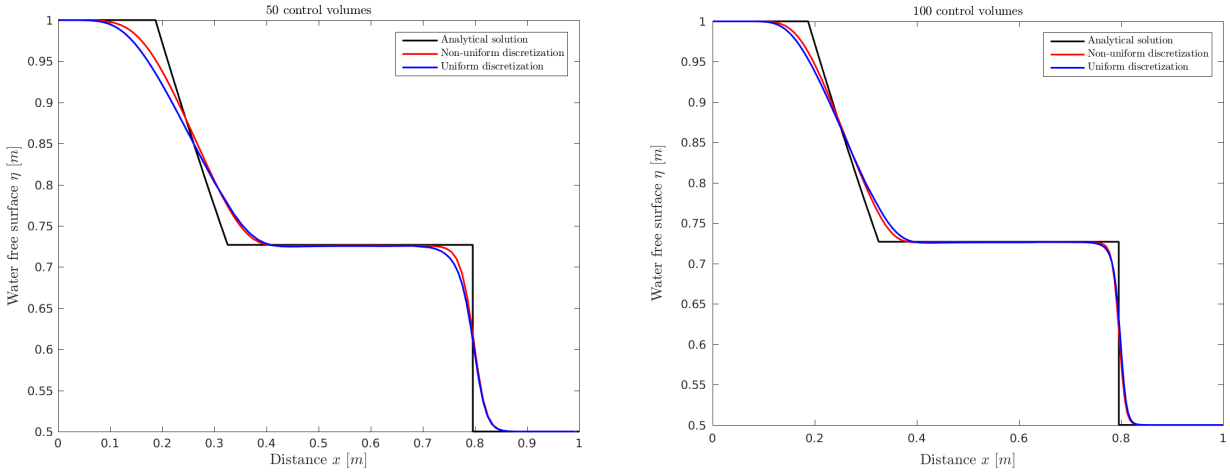

Figure 4.3: Results obtained using the finite volume method on uniform and non-uniform meshes using 50 control volumes (left) and 100 control volumes (right).

$$\Delta x_i = \begin{cases} 0.016, & \text{if} \quad 0.3 \leq x_i \leq 0.7, \\ 0.03, & \text{elsewhere}, \end{cases} \qquad \text{and} \qquad \Delta x_i = \begin{cases} 0.008, & \text{if} \quad 0.3 \leq x_i \leq 0.7, \\ 0.015, & \text{elsewhere}. \end{cases}$$

It is clear from the results in Figure 4.3 that refining the mesh improves the accuracy of the numerical results on both uniform and non-uniform meshes. Compared to the analytical solution, results obtained using non-uniform meshes are slightly more accurate than those obtained on the uniform mesh. For instance, the numerical diffusion is more pronounced at the shock and rarefaction areas in the uniform results than in their non-uniform counterparts. These features are important when the shallow water equations are solved on the non-uniform meshes reconstructed directly from the finite element nodes located on the interface in the coupled model. This would avoid interpolation procedures for matching finite element and finite volume nodes on the interface which may introduce numerical diffusion in the results obtained for the free-surface solutions.

Next we verify the finite element method for solving two-dimensional elasticity problems. We consider the well-known example proposed in [194] and for which the exact solution is provided therein. Here, we solve the elasticity equations (4.4) in a homogeneous and isotropic rectangular domain with 100 m for the length and 10 m for the width. A nodal displacement of 3 m is applied upwards in the center point of the domain and results obtained for the horizontal and vertical displacements are compared to the exact solutions. The computational domain is discretized using quadratic finite elements in an unstructured mesh with 772 elements and 1649 nodes. Figure 4.4 illustrates the obtained results for the horizontal and vertical displacements compared to the exact solutions. There is a good agreement between the results obtained using the finite element method and the analytical solutions for both horizontal and vertical displacements. The finite element method performs well for this test example and produces highly accurate and stable numerical results using reasonably coarse meshes.

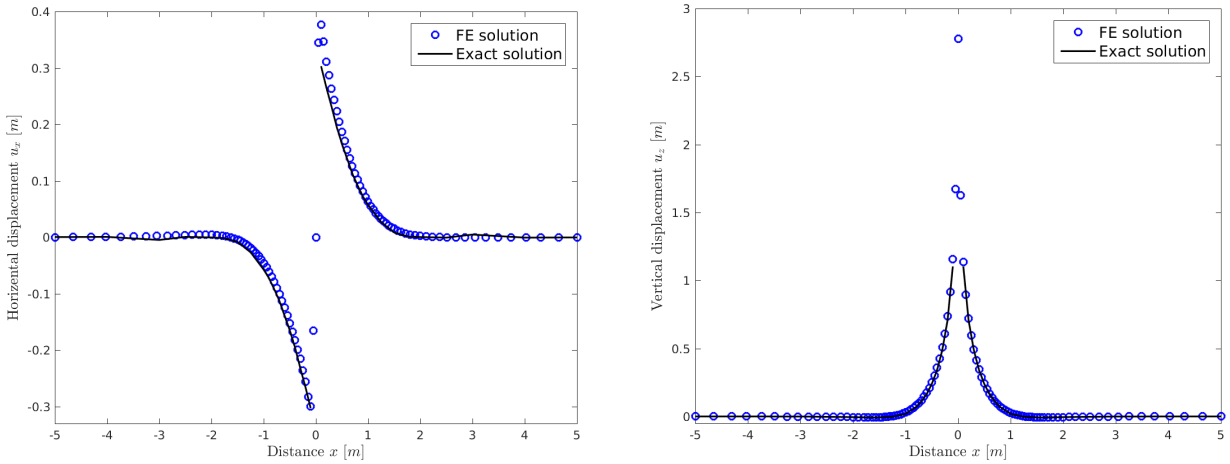

Figure 4.4: Horizontal displacement (left) and vertical displacement (right) obtained for the accuracy test example using the finite element method.

4.3.2 Shallow water waves generated by tension in the topography

In this example we consider shallow water waves generated by tension in the topography of a rectangular domain 100 m long and 10 m high subject to a localised tension force of $F = 2000\ N$ acting on the surface area between $x = 47\ m$ and $x = 53\ m$. Initially, the system is at rest with a water height set to $h = 10\ m$ and velocity $v = 0\ m/s$. Both open flow and reflective boundary conditions are imposed at both ends of the domain to model open and close flow domains, respectively. At time $t = 0.1\ s$, the considered force is applied generating a sudden deformation in the bed topography. The finite element nodes located on the interface are used for the control volumes in the finite volume solution of the shallow water equations. First we examine the grid convergence in the proposed coupled finite element/finite volume method for this example. We consider five unstructured meshes with different node and element densities as depicted Figure 4.5. Their corresponding statistics are listed in Table 4.1 along with the CPU times obtained using Mesh A, Mesh B, Mesh C, Mesh D and Mesh E. Note that, to avoid refining the mesh everywhere in the elastic domain, only the area subject to the deformation is refined in our computational mesh. This would require very small cost than considering a uniformly fine mesh in the simulations. A very fine reference mesh with 39591 elements and 80036 nodes is also used in our simulations to quantify errors in the obtained solutions obtained at time $t = 3\ s$. Note that the reference mesh is not included in Figure 4.5 because of its density which results in a heavily black plot. As can be seen for the last two mesh levels Mesh D and Mesh E, the differences in errors obtained for the stresses σ_x and free-surface η in Table 4.1 are very small. To further qualify the results for these meshes we plot in Figure 4.6 the bed profiles obtained using the considered meshes. It is easy to see that solutions obtained using the Mesh A are far from those obtained by the other meshes. Increasing the density of elements, the results for the Mesh D and Mesh E are roughly similar. This ensures grid convergence of the numerical results. Hence, the Mesh D is used in all our next computations. The reasons for choosing this mesh structure lie essentially on the computational cost required for each mesh configuration and also on the numerical resolution obtained.

The unstructured finite element with 2471 elements and 5160 nodes is used in the simulations and the results are monitored for different instants. The associated number of control volumes

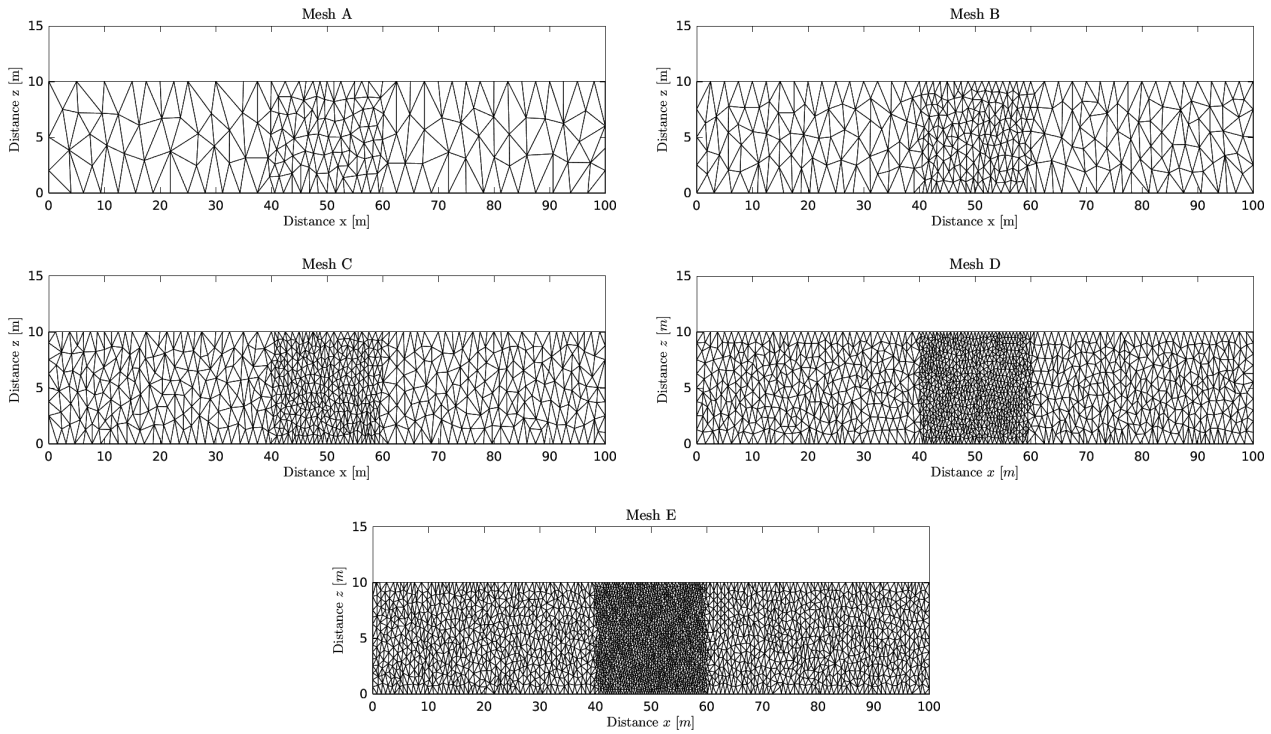

Figure 4.5: Meshes used in the simulations for shallow water waves generated by tension in the topography.

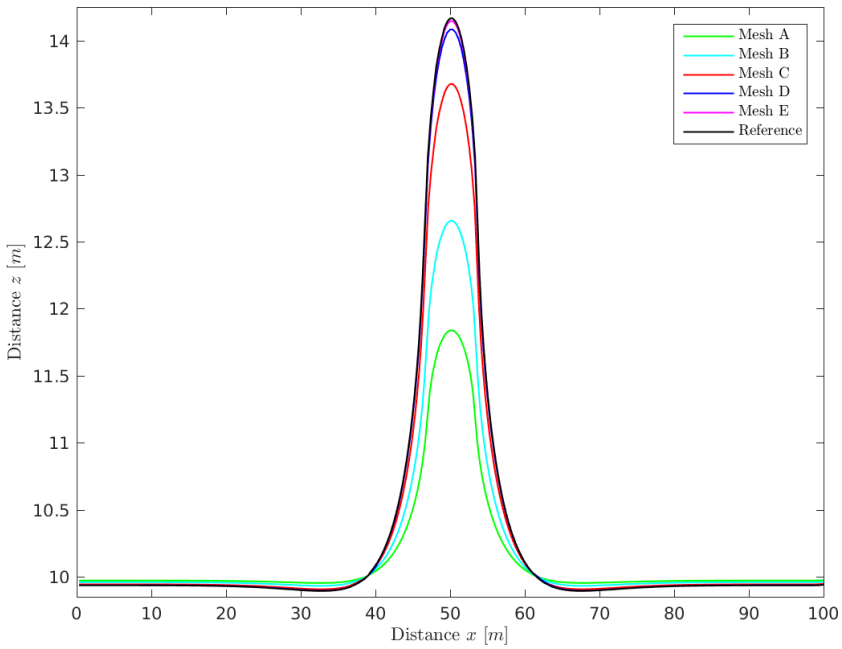

Figure 4.6: Comparison of bed profiles using different meshes for shallow water waves generated by tension in the topography at time $t = 3\ s$.

for this finite element mesh is 195 non-uniform cells. In Figure 4.9 we display the obtained results for the water height and bed deformation at six different times namely, $t = 0\ s$, $0.1\ s$, $1\ s$, $2\ s$, $3\ s$ and $10\ s$ using open flow boundary conditions at both upstream and downstream. These plots give a clear view of the overall wave patterns and the effect of the bed deformation

Table 4.1: Mesh statistics, relative errors and computational times for shallow water waves generated by tension in the topography at time $t = 3\ s$. The CPU times are given in seconds.

	# elements	# nodes	# control volumes	Error in σ_x	Error in η	CPU time
Mesh A	312	709	78	1.473E-02	3.205E-01	6.5
Mesh B	620	1349	96	4.289E-03	1.741E-01	9.2
Mesh C	1236	2639	197	1.157E-03	9.329E-02	21.7
Mesh D	2471	5160	232	2.994E-04	3.788E-02	63.4
Mesh E	4940	10213	312	7.433E-05	1.339E-02	131.5

Table 4.2: Computational results for shallow water waves generated by tension in the topography using different values of the tension force.

Force (N)	$\max \sigma_z\ (KPa)$	$\max \sigma_x\ (KPa)$	$\max B\ (m)$	$\max \eta\ (m)$	$\max p\ (KN/m^2)$
500	1.965	1.23	11.0335	21.1815	97.2559
1000	3.931	2.4599	12.0670	23.4026	106.5393
1500	5.8951	3.6899	13.1005	25.6435	115.9026
2000	7.8602	4.9198	14.1099	27.8662	125.1387
2500	9.8252	6.1498	15.3791	30.0551	134.1614

on the structure of the propagating waves in the upstream and downstream of the domain. In addition to the primary wave, a pair of waves with the same amplitude develops in both side of the hump. As expected, the sudden deformation in the bed generates a wave propagating across the computational domain. The wave splits into two waves and in later times the waves leave the domain and the water free-surface becomes flat at the initial height. This confirms the well-balanced property of the proposed finite volume method on non-uniform meshes. It is also important to mention two points concerning the non-uniform control volumes used in the flow simulations. First, there is no need for interpolation procedures to pass the information from one mesh to another in our coupled finite element/finite volume method second, there is no need to refine the mesh in the finite volume method to resolve the wave fronts as the finite element mesh would generate these refined meshes. This is a remarkable feature of the proposed coupled finite element/finite volume method to satisfactorily handle procedures using adaptive local grid refinement methods to resolve free-surface wave problems. Figure 4.7 illustrates the distribution of the stresses σ_x and σ_z at time $t = 3\ s$. Obviously, high stresses appear at the hump where the bed deformation is taken place. The perfect symmetry in these results with respect to the vertical centreline should be noted. Our finite element method preserves the symmetry in the stresses and resolves the correct solution well for this test example. For this example, we also consider the close domain with reflective boundary conditions at both upstream and downstream. In this case we compute the total water head for as

$$H = B + h + \frac{v^2}{2g}. \tag{4.27}$$

In Figure 4.10 we present the time evolution of the total water head at three surface gauges G_1, G_2 and G_3 situated at $x = 20\ m$, $x = 50\ m$ and $x = 80\ m$, respectively. The total water head obtained at these locations fluctuates with different amplitudes and frequencies but at

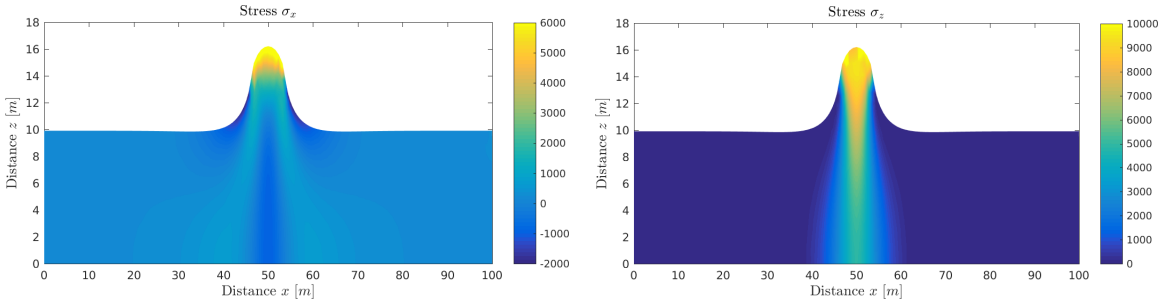

Figure 4.7: Distribution of the stresses σ_x (left) and σ_z (right) obtained for shallow water waves generated by tension in the topography at $t = 3\ s$.

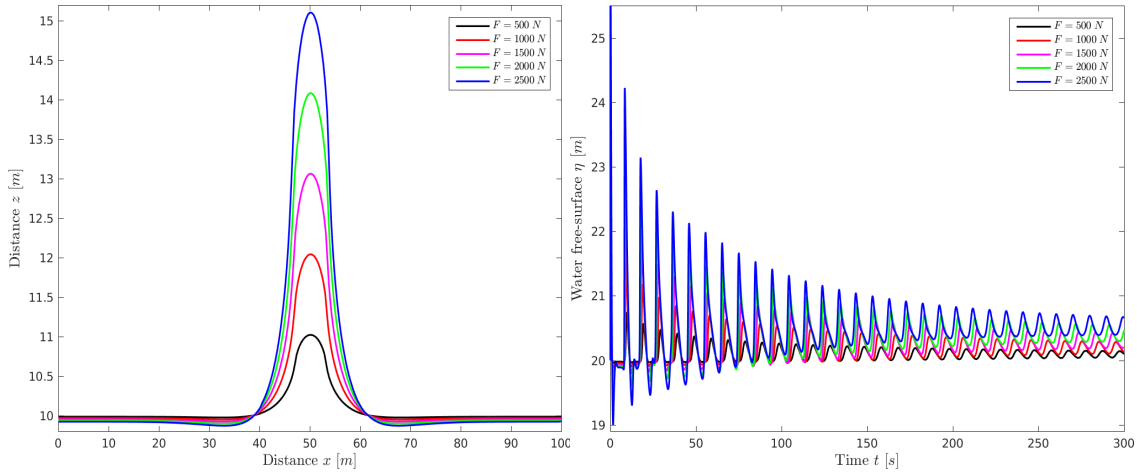

Figure 4.8: Bed deformation (top) time evolution of the free-surface at the gauge G_2 (bottom) obtained for shallow water waves generated by tension in the topography using different values of the tension force.

later time it stabilizes at the same initial value for the three considered gauges. The highest amplitudes in the total water head are observed at the gauge G_2 which is located at the center where the deformation occurs. Because of the symmetry in the location of gauges G_1 and G_3, the total water head at these locations exhibits similar features in terms of amplitudes and frequencies. In all selected gauges, the coupled finite element/finite volume method maintains correctly the wave structures without any kind of spurious oscillations over the hump. We also examine the effects of the applied force on the generated waves for this test example. Hence, in Figure 4.8 we show the bed deformations at time $t = 0.1\ s$ and the time evolution of the water free-surface at the gauge G_2 obtained using different values of the tension force namely, $F = 500\ N$, $1000\ N$, $1500\ N$, $2000\ N$ and $2500\ N$. To further quantify the results for this case we summarize in Table 4.2 the maximum values of the stress σ_z, the stress σ_x, the bed B, the free-surface η, and the hydrostatic pressure p. It is clear high responses in both bed and free-surface are obtained for high values of the tension force. It should be pointed out that the performance of the proposed method is very attractive since the obtained numerical solutions remain stable and conservative even when coarse meshes are used in the simulations without requiring nonlinear solvers or complicated techniques to reconstruct the numerical fluxes in the shallow water equations.

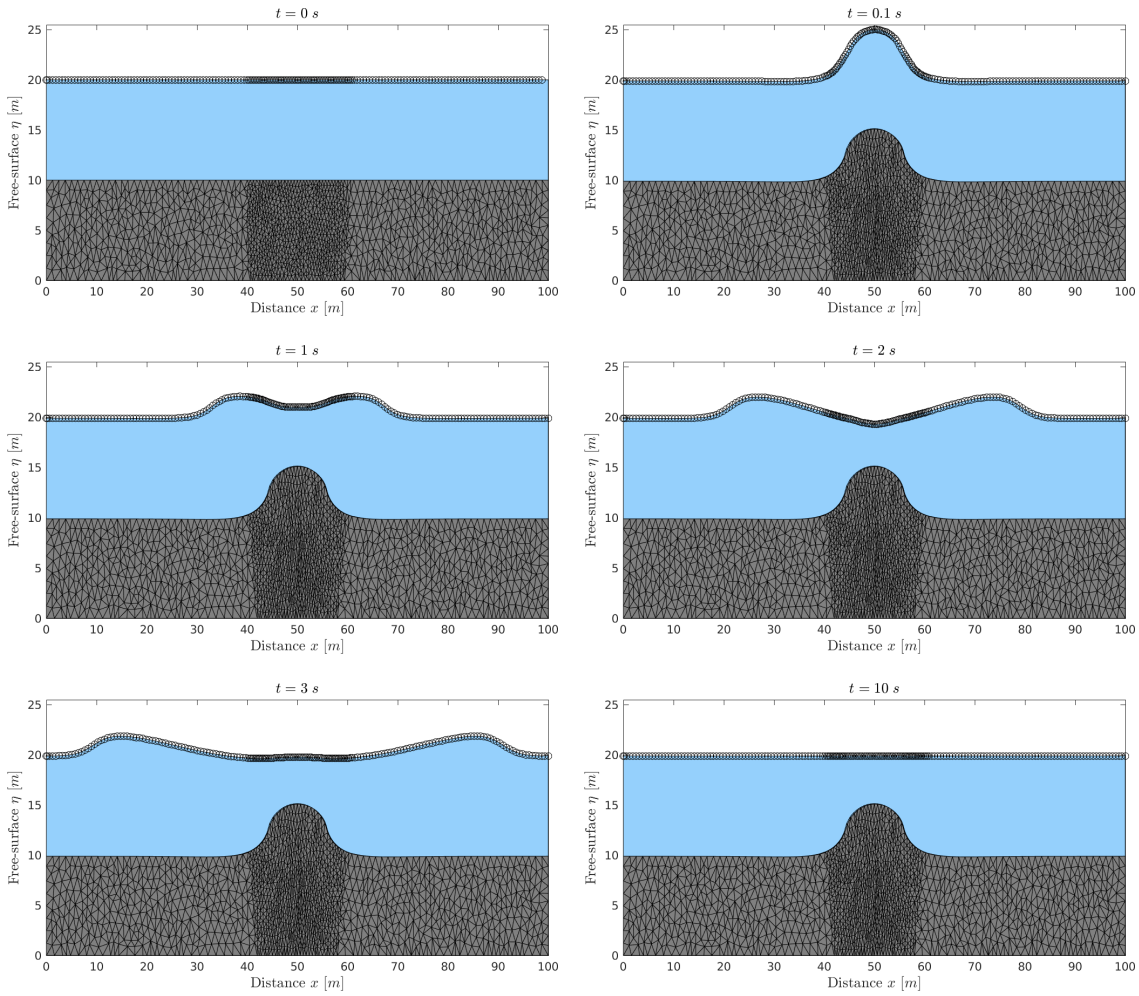

Figure 4.9: Results for the water height and bed deformation obtained for shallow water waves generated by tension in the topography at six different times.

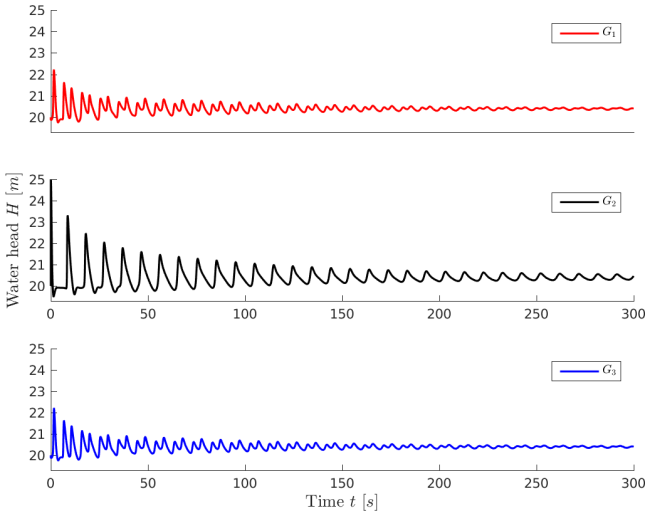

Figure 4.10: Time evolution of the total water head at the three gauges G_1, G_2 and G_3 obtained for shallow water waves generated by tension in the topography.

4.3.3 Shallow water waves generated by tension-compression in the topography

This example considers the same configuration as in the previous problem but using both tension and compression forces on the bed topography. Thus, a force of 2000 N is applied as a tension in the surface area between $x = 28\ m$ and $x = 32\ m$, and as a compression in the surface area between $x = 78\ m$ and $x = 82\ m$ in the computational domain. Initially, the system is assumed at the equilibrium with the water height set to $h = 11\ m$ and the velocity $v = 0\ m/s$. For the boundary conditions, open flow and reflective conditions are imposed at both ends of the domain. The solid domain is discretized using an unstructured mesh with local refinements in the areas where tension and compression forces are applied. The total numbers of elements and nodes in this mesh are 3417 and 7086, respectively. This results in 193 non-uniform control volumes to be used in the finite volume method. Note that, to break in the symmetry in this problem, the forces are applied in areas with different distances to the centreline $x = 50\ m$.

The considered tension and compression forces are applied at time $t = 0.1\ s$ and a sudden deformation occurs in the bed topography. After each deformation step, the finite volume solution of the shallow water equations uses the non-uniform control volumes obtained from the finite element nodes located on the interface. Figure 4.14 presents the obtained results for the bed deformation and water height at six different times namely, $t = 0\ s$, $0.1\ s$, $1\ s$, $4\ s$, $5\ s$ and $17\ s$ using open flow boundary conditions at both ends of the channel. As can be seen, the tension and compression forces generate two water waves with different crests and troughs propagating along the computational domain. The interaction between these waves generates reflecting waves with different amplitudes in the water free-surface. At later time, the waves are settled out and the system returns to its initial equilibrium state. Again, the proposed coupled finite element/finite volume method performs well for this test problem as the deformed bed topography is accurately resolved using the finite element method and the wave features are well captured using the finite volume method on non-uniform meshes.

In Figure 4.12 we show distributions of the computed stresses σ_x and σ_z at time $t = 5\ s$. It is clear that high stresses are localized at the hump generated from the tension force whereas, low stresses appear at the scour resulting from the compression force. The results also show different aspects in the stresses generated by tension force and those obtained using the compression force. The finite element method performs well for this deformation test example and it reproduces stable solutions without nonphysical oscillations at the bed topography and at stress distributions. The total water head H defined in (4.27) is also considered for this test example using reflective boundary conditions at both ends of the domain. Figure 4.13 shows the time evolution of the total water head at three selected gauges G_1, G_2 and G_3 at $x = 30\ m$, $x = 50\ m$ and $x = 80\ m$, respectively. Unlike the previous example, the time series in the present case exhibit periodic behaviour with low amplitudes and frequencies. In addition, compared to the previous case, the propagating waves generated by both tension and compression in the topography persist longer on the free-surface than in those originated by tension only. It is clear that the total water head experiences high values at the gauge G_1 located at the downstream of the domain. The coupled finite element/finite volume method captures well the periodic features in the water waves at all selected gauges for this example.

This test example is also used to assess effects of the Poisson ratio ν on the bed deformation and the generated free-surface waves. To this end, we run the simulations for the bed formed by different homogeneous and isotropic materials with $\nu = 0.1$, 0.2, 0.3 and 0.4. In Figure 4.11 we

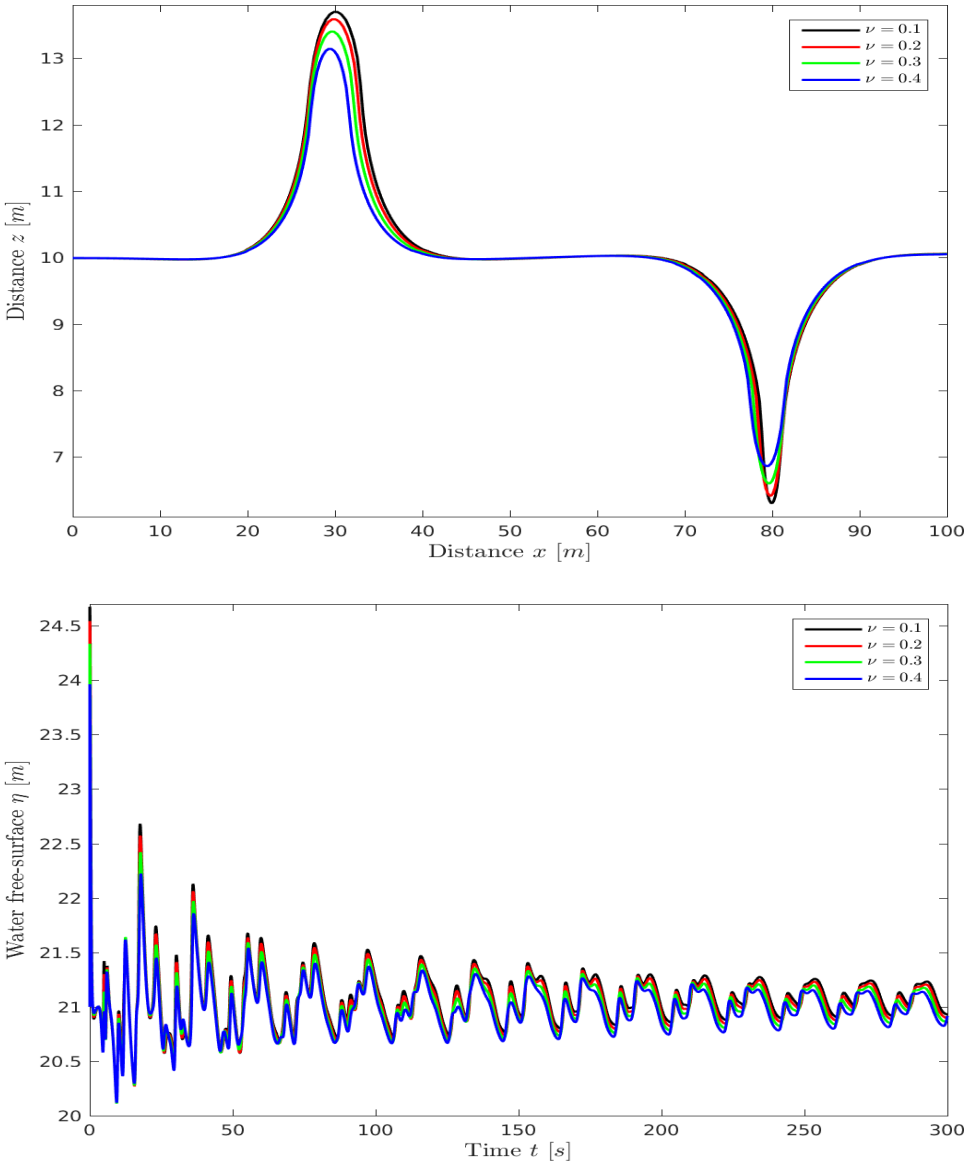

Figure 4.11: Bed deformation (top) time evolution of the free-surface at the gauge G_1 (bottom) obtained for shallow water waves generated by tension-compression in the topography using different values of the Poisson ratio.

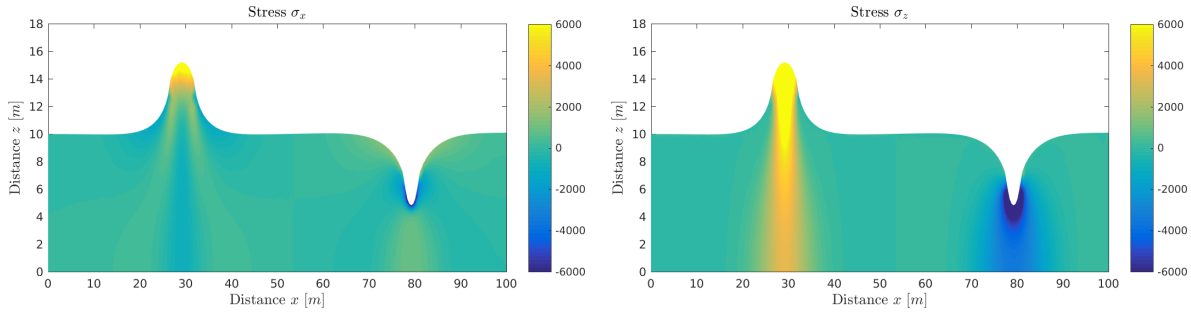

Figure 4.12: Distribution for the stresses σ_x (left) and σ_z (right) obtained for shallow water waves generated by tension-compression in the topography at $t = 5$ s.

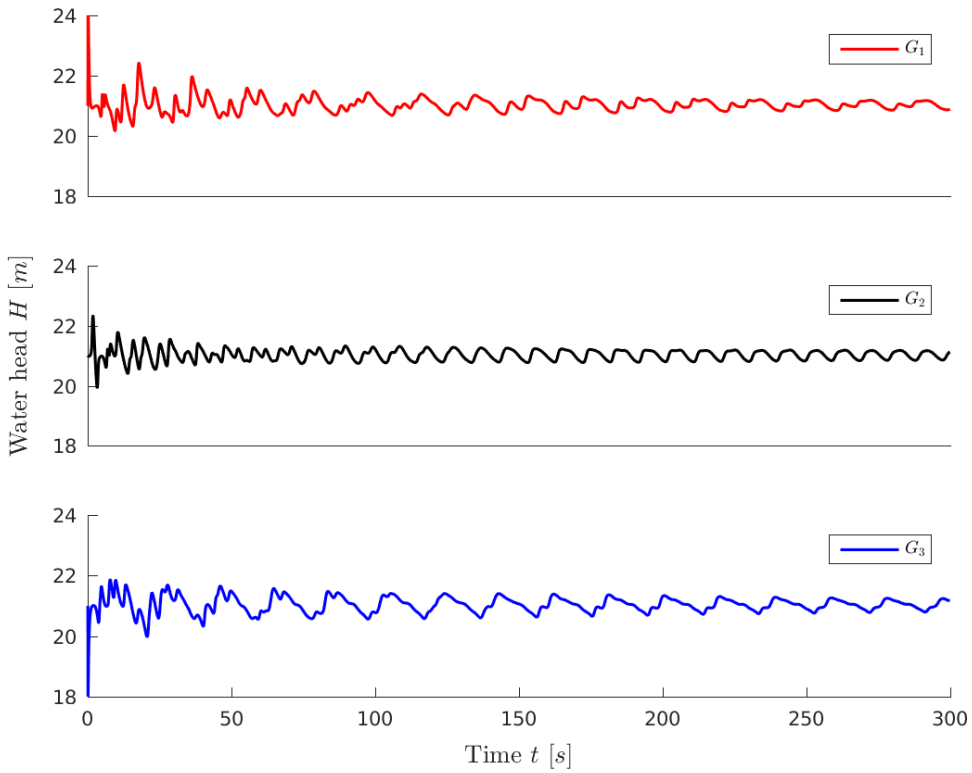

Figure 4.13: Time evolution of the total water head at the three gauges G_1, G_2 and G_3 obtained for shallow water waves generated by tension-compression in the topography.

Table 4.3: Computational results for shallow water waves generated by tension-compression in the topography using different values of the Poisson ratio.

ν	$\max \sigma_z$ (KPa)	$\max \sigma_x$ (KPa)	$\max B$ (m)	$\max \eta$ (m)	$\max p$ (KN/m^2)
0.1	7.265	5.6249	13.6954	27.3934	134.0797
0.2	7.3601	5.4965	13.5848	27.1569	132.7335
0.3	7.5260	5.2995	13.3993	26.5743	129.3346
0.4	7.8963	5.0911	13.1385	26.1080	126.7165

display the bed deformations at time $t = 0.1$ s and the time evolution of the water free-surface at the gauge G_1 obtained using the considered values of the Poisson ratio. The maximum values of the stress σ_z, the stress σ_x, the bed z, the free-surface η and the hydrostatic pressure p are summarized in Table 4.3. As can be seen from these results, slightly high responses in both bed topography and free-surface are obtained for low values of the Poisson ratio, compare the results for $\max B$ in Table 4.3.

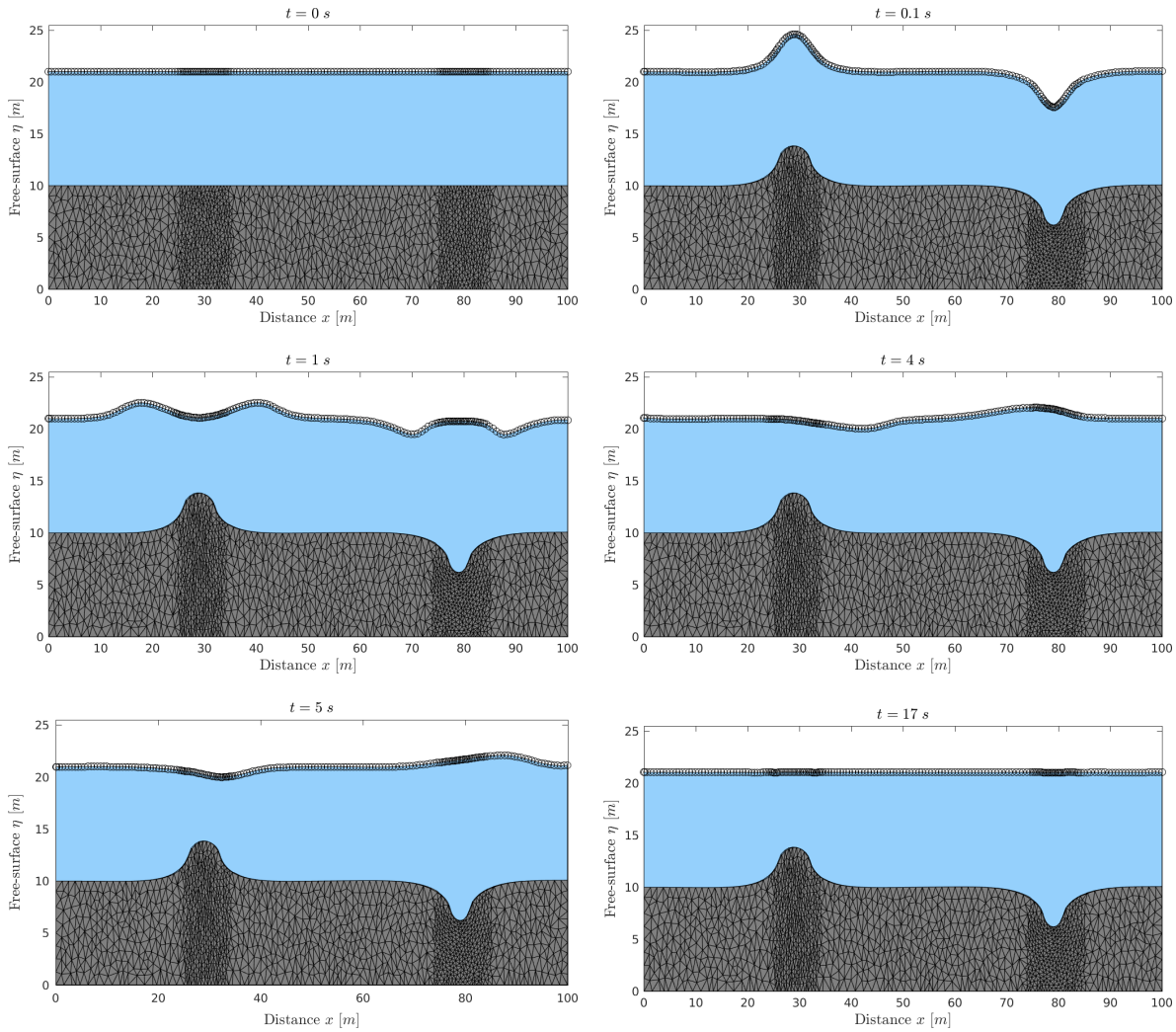

Figure 4.14: Results for the water height and bed deformation obtained for shallow water waves generated by tension-compression in the topography at six different times.

4.3.4 Shallow water waves generated by pipe failure in the topography

Pipe failures are among common examples in nature for which several studies have taken place in civil engineering and geotechnics, see for example [153, 272, 93]. For these applications, the source of deformation may be caused by a fatigue in the pipe or simply by a load applied below the seabed. In this example, we consider shallow water waves generated by pipe failure in the bed topography. Hence, we solve the coupled equations (4.1) and (4.4) in a rectangular domain 50 m long and 10 m high including a circular pipe with radius $R = 3\ m$ and the initial water height is 5 m above the bed. A compressive force of 200 N is applied only at the upper half boundary of the pipe. Initially, the system is at rest and at time $t = 0.1\ s$ the constant force is applied on the upper surface of the pipe. Consequently a deformation is expected on the pipe and therefore on the shallow water bed which generate water waves on the free-surface. An unstructured finite element mesh with 3196 elements and 6822 nodes is used in our simulations and numerical results are presented for different instants. To avoid refining the mesh everywhere in the computational domain, only the area around the pipe is refined in our simulations. This local refinement is needed to accurately resolve the deformed

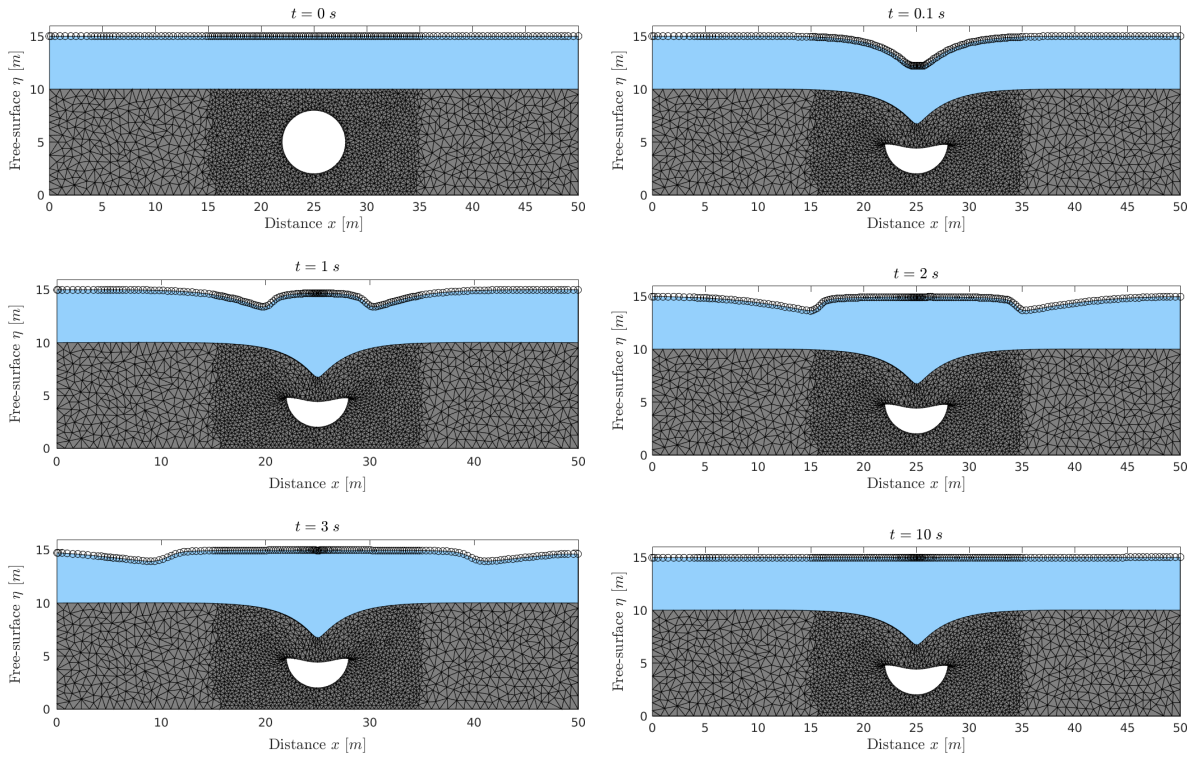

Figure 4.15: Results for the water height and bed deformation obtained for shallow water waves generated by pipe failure in the topography at six different times.

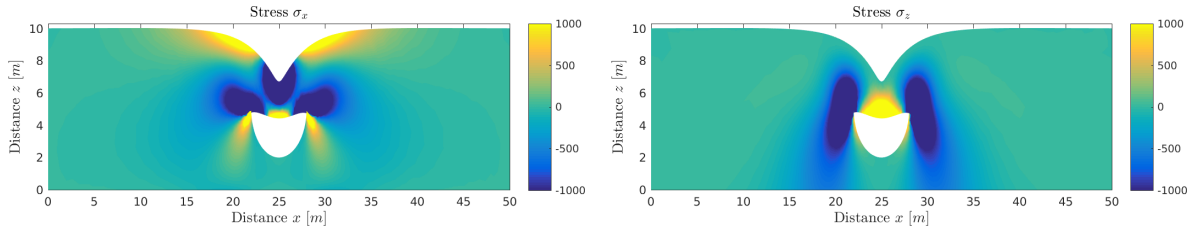

Figure 4.16: Distribution for the stresses σ_x (left) and σ_z (right) obtained for shallow water waves generated by pipe failure in the topography at $t = 3\ s$.

topography with less computational cost than using a global refinement for the entire domain. The finite volume method employs 182 non-uniform control volumes reconstructed from the finite element nodes located on the interface.

In Figure 4.15 we display the responses of the water free-surface at six different instants namely, $t = 0\ s$, $t = 0.1\ s$, $t = 1\ s$, $t = 2\ s$, $t = 3\ s$, $t = 10\ s$ using open flow boundary conditions at both downstream and upstream. As can be seen from these results, the system starts from the rest and once the deformation on the pipe occurs, a water wave is generated on the free-surface and it flows over the deformed bed. For longer times, the system is stabilized to a steady-state configuration with no disturbances on the water free-surface. For the considered force on the pipe, the bed topography experiences a maximum vertical displacement of 3.25 m downwards. It is clear that the considered coupled finite element/finite volume method performs well for this free-surface flow problem over a deformable bed as both the bed topography and the water free-surface are accurately captured without non-physical oscillations or excessive numerical

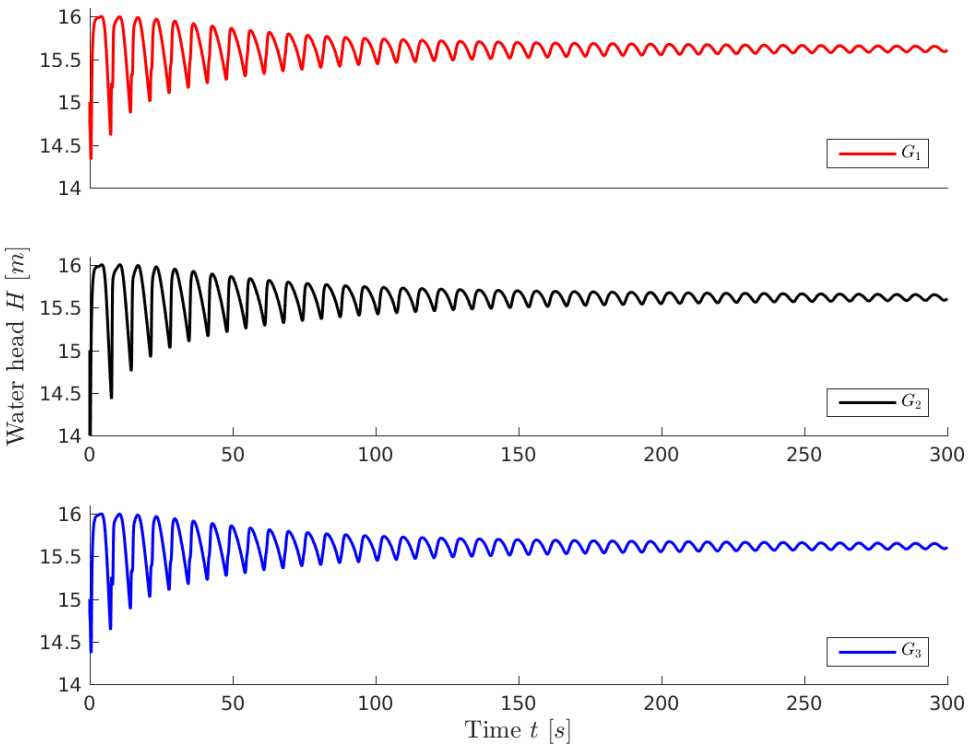

Figure 4.17: Time evolution of the total water head at the three gauges G_1, G_2 and G_3 obtained for shallow water waves generated by pipe failure in the topography.

Table 4.4: Computational results for shallow water waves generated by pipe failure in the topography using different values of the pipe radius.

Radius (m)	$\max \sigma_z$ (KPa)	$\max \sigma_x$ (KPa)	$\max B$ (m)	$\max \eta$ (m)	$\max p$ (KN/m^2)
1	8.973	16.65	0.7178	16.7295	65.9574
2	3.3655	10.816	1.8370	17.8588	76.9677
3	2.2391	11.633	3.2926	19.2992	91.0519

diffusion appearing in the numerical solutions.

Figure 4.16 depicts distributions of the computed stresses σ_x and σ_z at time $t = 3$ s. Again, high stresses appear at the upper part of the pipe where the bed deformation is taken place. The results also illustrate localized stresses σ_x on the bed topography for this example. The perfect symmetry in the distribution of both stresses σ_x and σ_z should also be noted in Figure 4.16. Next we consider reflective boundary conditions and in Figure 4.17 we display the total water head at three gauges G_1, G_2 and G_3 selected at $x = 22$ m, $x = 25$ m, $x = 28$ m, respectively. It can be clearly shown from this figure that the waves at three considered gauges exhibit similar amplitudes and frequencies. On the other hand, because of the symmetry in the location, the wave features at the gauges G_1 and G_3 are almost the same.

Our next concern with this test example is to examine the impact of pipe size on the bed deformation and the free-surface waves. Here, we run the simulations using three pipes with radius $R = 1$ m, 2 m and 3 m keeping all the other parameters fixed as in the previous run. Figure 4.18 shows the bed deformation and the time evolution of the free-surface at the gauge

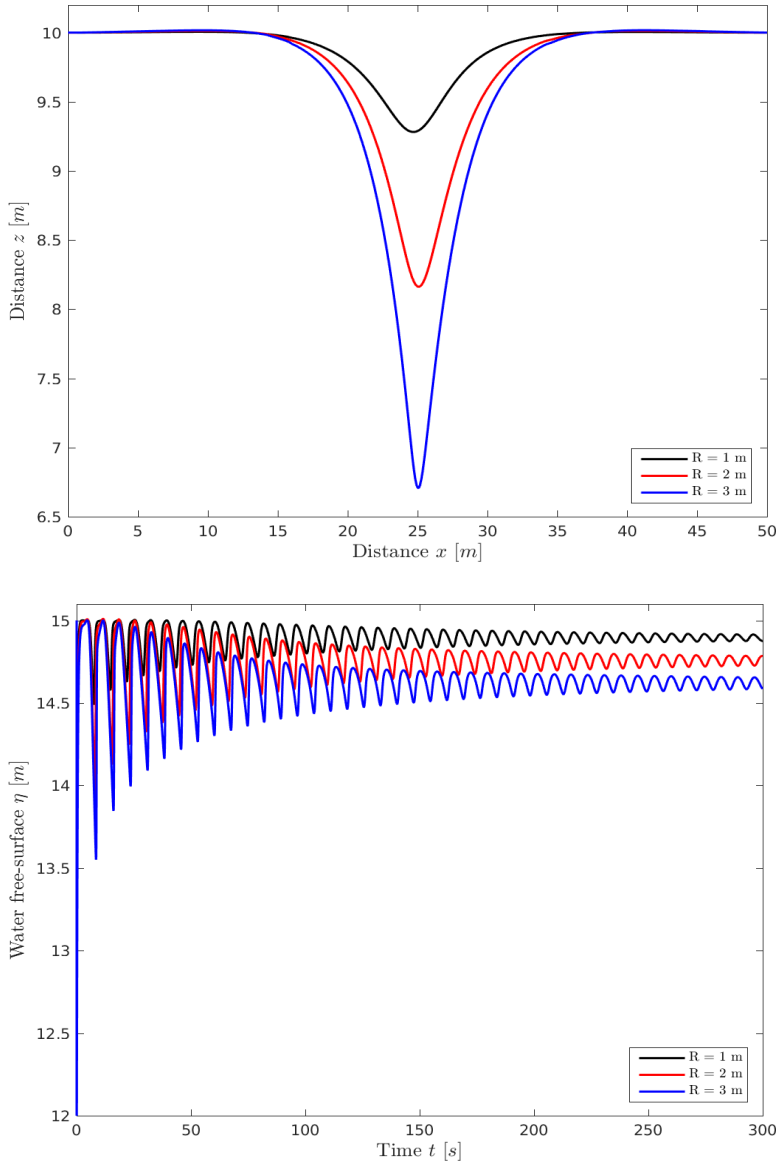

Figure 4.18: Bed deformation (top) time evolution of the free-surface at the gauge G_2 (bottom) obtained for shallow water waves generated by pipe failure in the topography using different values of the pipe radius.

G_2 obtained for the considered values of the pipe radius. Table 4.4 summarizes the maximum values of the stress σ_z, the stress σ_x, the bed z, the free-surface η and the hydrostatic pressure p obtained for this run. It is evident that larger deformations in the bed topography are obtained for pipes with larger radius and consequently waves with higher amplitudes on the free-surface, compare the values of $\max B$ and $\max \eta$ in Table 4.4. The presented results demonstrate that the proposed computational model is suited for the prediction of shallow water waves by elastic deformations in the topography. It should be stressed that results from the proposed model should be compared to experimental measurements. However, there is no data available until now to carry out this work. Thus, at the moment we can only perform simulations and verify that results are plausible and consistent.

4.4 Conclusions

Different natural phenomena such as earthquakes, volcanic eruptions, landslides lead to a series of waves generated when the water in a lake or in the sea is rapidly displaced on a massive scale. During these movements the sea floor abruptly deforms and vertically displaces the overlying water. Such large vertical movements of the earth floor create these huge waves. Tsunami flooding is one example of these deformations. Tsunami claims thousands of lives every year and cause a huge financial loss to all over the world. A diverse series of research projects have taken place or under way to understand the effect of the underground motion to the free-surface shallow water motion. Researches range from the simulation of the processes and effects of waves generated from submarine landslides, model comparisons of waves induced motions on rigid and free bodies, projects seek to improve the understanding of the stresses from the wave generations and bed movement. In this chapter a class of computational tools for coupling fluid-structure interaction including shallow water flows has been presented.

To understand the physical processes that occur during the bed movement and creating the free-surface waves including the main effective stresses, a simple and accurate computational model is proposed to simulate shallow water waves induced by elastic deformations in the bed topography. The mathematical model consists on coupling the nonlinear one-dimensional shallow water equations to the linear two-dimensional equations for elasticity. This coupling technique is a fractional-stage technique. In the first stage the linear elastic finite element method is implemented to solve for the under water bed deformation, as these deformations will create the deformed bed. For the second stage a Roe-scheme finite volume numerical model was developed for simulating the shallow water flow over mobile bed. The coupling conditions between the two sets of equations are achieved through the interface between the water flow and the bed topography. The hydrostatic pressure and friction forces calculated from the water flow are applied as external forces on the interface for the elasticity model whereas, bathymetric forces are accounted for in the shallow water equations. As numerical solvers we considered well-balanced finite volume method for the free-surface flow using non-uniform meshes and a robust finite element method for the bed deformation using unstructured meshes. The approach combines the attractive attributes of the finite volume discretization and the finite element method to yield a procedure for either flat or non-flat topography. The developed model was tested by simulating three cases: shallow water waves generated by tension in the topography, shallow water waves generated by tension-compression in the topography and the shallow water waves generated by pipe failure in the topography. The main idea behind these examples is to investigate the accuracy of the proposed coupling technique under different cases of bed deformations and different stresses distribution in the affected domain. It can be clearly noted from the results, the effectiveness and robustness of the proposed method. The method performs well and it resolves all the flow features without the need to a very refined mesh. The results make it promising to be applicable also to real situations where, beyond the many sources of complexity, there is a more severe demand for accuracy in predicting free-surface waves induced by sudden bed deformations. This method is currently implemented in one-dimensional shallow water domains but can be extended to two dimensional domains.

Chapter 5

Uncertainty quantification for numerical simulation of free-surface water flows over stochastic beds

Free-surface water flows over stochastic beds are complex due to the uncertainties in topography profiles being highly heterogeneous and imprecisely measured. In the present study, the propagation and influence of several uncertainty parameters are quantified in a class of numerical methods for free-surface flows. The governing equations consist of both single-layer and two-layer shallow water equations on either flat and non-flat topography. For this purpose, the free-surface profiles are computed for different realizations of the random variables when the bed is excited with sources whose statistics are well defined. Many research works have been dedicated to the development of numerical methods to achieve some order of accuracy in free-surface flows. However, little concern was given to examine the performance of these numerical methods in presence of uncertainty. The present study addresses this specific area in computational hydraulics with regards to the uncertainty generated from bathymetric forces. As numerical methods for shallow water equations, four finite volume schemes have been implemented. To reduce the required number of samples for uncertainty quantification, the proper orthogonal decomposition method with the polynomial chaos expansions for efficient uncertainty quantification of complex hydraulic problems with large number of random variables have been combined. Numerical results are shown for several test examples including dam-break problems for single-layer and two-layer shallow water flows. The problem of flow exchange through the Strait of Gibraltar is also solved in this study. The obtained results demonstrate that in some hydraulic applications, a highly accurate numerical method yields an increase in its uncertainty and makes it very demanding to use in an operational manner with measured data from the field. On the other hand, when the complexity of the physics increases, these highly accurate numerical methods display less uncertainty compared to the low accurate methods.

Free-surface models in hydraulics have gained an increasing interest during last decades. Ranging from flood forecasting [273] to monitoring hydraulic infrastructures such as dams, hydraulic simulations serve several purposes to support decision making. Water free-surface flows under the influence of gravity can be modelled using the well-established shallow water equations subject to the assumption that the vertical depth is much smaller than any typical horizontal length within the hydraulic system. The governing equations in these models are derived by depth-averaging the incompressible Navier-Stokes equations, see for example [225, 238].

However, the main drawback resulting from such assumption remains the lack of capturing some physical dynamics in the vertical motion of the water flow. Therefore, during the recent years, multi-layer shallow water models have attracted enormous attention and have became very useful tools to solve many hydraulic problems such as rivers, estuaries, bays and other nearshore regions where water flows interact with the bed topography and wind shear stresses, see for instance [87, 81, 124]. In the current work, the two-layer shallow water system is considered for modelling the hydraulic exchange in presence of non-flat beds. Note that analytical solutions to these equations are limited to only very special cases and numerical methods are the only techniques that can be used to approximate solutions to practical problems which include complex bathymetry, steep gradients and moving water fronts. The focus in this study is on free-surface water flows over complex bed topography using both the single-layer and two-layer shallow water equations.

From a numerical view point, the most challenging features of the single-layer shallow water equations are the fact that they admit discontinuous and smooth solutions. Even for problems in which the initial data is smooth can lead to discontinuous solutions in a finite time. The hyperbolic nature of the system and its nonlinearity are also among the difficulties that arise in numerically solving these equations. On the other hand, numerical treatment of the two-layer shallow water system often presents difficulties due to their nonlinear form, presence of the non-conservative product terms, lost of hyperbolicity, and difficulty to explicitly obtain its eigenstructure form, see for example [124]. Many numerical tools have been proposed in the literature in order to overcome such problems and, as numerical solvers for the hydraulics systems, the well-established finite volume methods including Lax-Friedrichs, Rusanov and Roe schemes have been considered , see for instance [238]. Despite the continuous efforts to improve the accuracy of hydraulic simulations, uncertainty remains ubiquitous for different reasons as discussed in [201] among others. For example, the aforementionned assumptions in the modelling stage introduce intrinsic uncertainties that propagate in the resulting simulations. Hence, the numerical methods to solve the shallow water systems discretize the continuous equations in space and time which will introduce numerical uncertainties. Furthermore, the empirical modelling of the bed bathymetry and the friction coefficients introduce additional errors. In practice, these parameters are estimated by means of calibration (or inverse problem) where data for a specific event is used, see for example [246, 214, 127]. Indeed, exact estimations are not possible for all ranges of variation in hydraulics for which modelling uncertainties is required. There is also a natural variability due to the insufficient description of boundary conditions which lead to stochastic uncertainties.

Nowadays, uncertainty quantification in hydraulics is gradually growing along with the consciousness of its importance to improve the management of water resources, see for example [189] and further references are therein. Several works in the literature have shown the appealing advantages of including uncertainty quantification in order to approve knowledge of different rivers, lake and ocean flows [78, 188]. Boundary conditions describing the flow are often pointed out as the responsible for the uncertainty in hydraulic calculations [203]. This is mainly because these conditions suffer from both epistemic and stochastic errors which are often indistinguishable [170]. Consequently, their accuracy significantly affects the hydraulic simulations [46]. However, it turns out that other works including [10, 190, 113, 46, 208, 80] have highlighted that uncertainty quantification in hydraulics should also include the friction terms, as for some specific flow configurations the uncertainty in hydraulics is more sensitive to these terms than the upstream flow conditions. In fact, the main factors driving a hydraulic

flow are: (i) balance between inertia effects and bathymetric effects, (ii) balance between water height and water velocity, and (iii) balance between friction and bathymetry. Thus, the main parameters that ought to be calibrated correctly in a hydraulic model are the bathymetry and the friction coefficient known also by the Roughness Manning coefficient. In general, this term is described with an empirical coefficient and its identification results from a calibration method using available field data. As a result, the uncertainty expressed around this value is great and its accuracy would significantly impact the overall computational results obtained for the hydraulic simulations [32, 46, 113]. Furthermore, the Manning coefficient may also compensate a local lack of information in the bathymetry description, see for example [112]. There exists also hydraulic situations for which the Manning coefficient is not constant and it may also depends on the space. In the current work, only constant Manning coefficients in the free-surface water flows has been considered and techniques developed in this study can be extended to space-dependent coefficients without major conceptual modifications. The bathymetry constitutes also an important source of uncertainty in the numerical simulation of hydraulics. For practical hydraulic applications, its description is performed through interpolation of several scarce topographic measurements. For many realistic hydraulic applications, these data are either not available or not functional which make the hydraulic simulations even more uncertain, see for instance [191, 31, 60]. Recent studies have also emphasized the importance of estimating the bathymetry in hydraulics specially with the upcoming spatial Surface Water and Ocean Topography (SWOT) mission. However, the main drawback of the Data Assimilation (DA) approaches remains the difficulties to account for uncertainties of the hydraulic simulation in the numerical model, see for example the discussions reported in [177, 97, 187]. In addition, the accuracy of the correction is considerably impacted by the accuracy of the uncertainty estimation in these approaches. In fact, when using variational-based DA methods, the uncertainty is estimated using an adjoint approach whereas, when using ensemble-based DA methods, the uncertainty is estimated with stochastic computation. In [108], both methods have been successfully implemented and assessed for hydraulic computations. However, the accuracy of uncertainty estimation is considerably increased when using a surrogate model, compare [208] and further references are therein. In [78], the Polynomial Chaos Expansion (PCE) has been implemented for uncertainty quantification in an ensemble-based DA approach and it has been compared with the classical ensemble Kalman filter approach. The results presented in [78] demonstrate that the PCE considerably decreases the computational cost and increases the uncertainty estimation for the ensemble Kalman filter which improve the quality of DA in hydraulics using SWOT data. For these reasons, the PCE is chosen to quantify the uncertainty in free-surface water flows. The focus of the present study is on quantifying uncertainties related to hydraulic computations resulting from bathymetric parameters.

In most hydraulic applications, the Manning coefficient is often presented as a constant parameter or piecewise constant over the hydraulic domain and consequently, the common approach it is considered as a random variable, see [80, 208] among others. On the other hand, the bathymetry has barely been considered for an uncertainty quantification problem. Indeed, the bathymetry field being a function depending on the space, it should be presented as a stochastic process [99, 166]. Therefore, it does not fall under the classical way to tackle uncertainty quantification where the model parameters are random variables described with a probabilistic law often defined by field experts [251]. This is mainly the reason why only few works have been dedicated to quantify its measurement [122]. In fact, when considering an uncertainty quantification problem using the PCE, one needs to sample the input parameters following a probability density function. As discussed in [145, 251], assessing stochastic processes such as

bathymetry using each value of the vector representing the process as a random variable is very demanding. This is due to the fact that (i) the random variables need to be uncorrelated for the PCE consideration and (ii) the accuracy of the numerical model depends on the discretization level of the process such that accurate models yield to an increase in the stochastic dimension which will reduce significantly the accuracy of the PCE because of the *curse of dimensionality.* In this study, the Karhunen-Loève (KL) expansion to sample the bathymetric process has been considered. The KL expansion allows to overcome both problems cited before as it reduces the stochastic dimension and the resulting eigenvalues are uncorrelated therefore they fit as random variables for the PCE. This method has been widely used in the framework of random processes especially in uncertainty quantification, see [212, 186, 223] for a detailed review. In applications of open-channel hydraulics, such methods have been introduced in [141] to quantify the uncertainty resulting from time-based processes such as wind forces. Furthermore, as mentioned above, the PCE is used in order to propagate the uncertainty in hydraulic models. The aim is to evaluate the uncertainty on hydraulic states (water height and water velocity) resulting from the supposed uncertainty in the bathymetric forces. This class of methods is becoming increasingly used in hydraulics community with its intrusive and non-intrusive forms. The intrusive formulation appears to be less appealing because of the hyperbolic nature of the shallow water equations whereas, the classical intrusive PCE struggles with the physical shock occurring in open-channel hydraulics. A recent study reported in [216] overcomes this issue by using a wavelet basis instead of the classical orthogonal polynomial basis. The main advantage of the method lies on the fact that the uncertainty of the hydraulic state is obtained in a straightforward way. However, the main drawback related to the *curse of dimensionnality* as a sparse basis is hardly achievable with such methods. On the other hand, the non-intrusice PCE has been successfully implemented for open-channel hydraulics in numerous studies, see for example [96, 80, 208, 108, 141]. The appealing advantage of this method relies mainly in the possibility to use the adaptive PCE introduced by [38]. However, the computational cost of the method could be impacted by the discretization level of the hydraulic state. This issue has also been treated in previous studies using methods like the Proper Orthogonal Decomposition (POD), see for instance [40, 79]. The idea in this approach is to decompose the hydraulic state using a POD technique. The uncertainty is then expressed on the eigenvalues of this decomposition. In the present study, the impact on uncertainties in the bathymetry and the Manning coefficient on the hydraulic state is numerically assessed. Therefore choosing to use a KL expansion to sample the bathymetry and the PCE to propagate uncertainty over the POD modes of the hydraulic state.

In general, the metric that allows the choice between different numerical schemes is based on the distance between the computational hydraulic states and the analytical solutions or the observations. However, uncertainty has never been a choice metric for operational use. In the present study, uncertainty is quantified using four different finite volume schemes for both single-layer and two-layer shallow water flows. The aim here is to assess how the accuracy of a numerical scheme for a hydraulic model affects its uncertainty. Numerical results are presented for dam-break problems and lock-exchange flows. Results for the exchange flow through the Strait of Gibraltar subject to stochastic bathymetry have been also presented. Numerical results presented in the current study demonstrate high resolution of the proposed techniques and confirm their capability to provide efficient uncertainty quantification for simulation of free-surface water flows over stochastic beds.

This chapter is organized as follows. The equations for free-surface water flows are presented

in Section 5.1. In Section 5.2 the numerical methods considered in the present work for solving the shallow water systems have been presented. The formulation of the finite volume modified method of characteristics for the numerical solution of two-layer models is also presented in this section. The general methodology used to address the problem of uncertainty quantification is described in section 5.3. This section includes the reduction methodology along with the PCE and the POD techniques. Sections 5.4 and 5.5 are devoted to numerical results for several test examples of free-surface water flows over stochastic topography for single-layer and two-layer models, respectively. The new approach is shown to enjoy the expected accuracy as well as the robustness. Section 5.6 contains concluding remarks.

5.1 Governing equations for free-surface water flows

Systems of shallow water equations have widely been used in the literature to model free-surface flows in rivers and coastal areas as well as to study a wide variety of phenomena in hydraulics and oceanography. The main feature in these equations is related to the fact that vertical effects can be neglected compared to the horizontal ones with a good approximation by replacing the vertical momentum equation by the hydrostatic pressure distribution. Indeed, the shallow water equations have been derived by integrating the three-dimensional incompressible Navier-Stokes equations along the vertical direction based on the assumptions that the vertical motion is ignored and the pressure distribution is hydrostatic, see [225, 238] among others. Thus, in terms of the dependent variables water height $h(t,x)$ and water velocity $u(t,x)$, the single-layer shallow water equations read

$$\begin{aligned} \frac{\partial h}{\partial t} + \frac{\partial (hu)}{\partial x} &= 0, \\ \frac{\partial (hu)}{\partial t} + \frac{\partial}{\partial x}\left(hu^2 + \frac{1}{2}gh^2\right) &= -gh\frac{\partial Z}{\partial x} - ghM_b^2\frac{u \mid u \mid}{h^{4/3}}, \end{aligned} \tag{5.1}$$

where $Z(x)$ is the function characterizing the bottom topography, g the acceleration due to gravity, M_b the Manning roughness coefficient at the bed, see the left plot in Figure 5.1 for an illustration. The system (5.1) is strictly hyperbolic with real and distinct eigenvalues given by

$$\lambda_1 = u - \sqrt{gh}, \qquad \lambda_2 = u + \sqrt{gh}. \tag{5.2}$$

In the current study, we also consider the two-layer shallow water equations for modelling free-surface water flows. For this situation, the governing equations are written in a conservative form as

$$\begin{aligned} \frac{\partial h_1}{\partial t} + \frac{\partial (h_1u_1)}{\partial x} &= 0, \\ \frac{\partial (h_1u_1)}{\partial t} + \frac{\partial}{\partial x}\left(h_1u_1^2 + \frac{1}{2}gh_1^2\right) &= -gh_1\frac{\partial Z}{\partial x} - gh_1\frac{\partial h_2}{\partial x}, \\ \frac{\partial h_2}{\partial t} + \frac{\partial (h_2u_2)}{\partial x} &= 0, \\ \frac{\partial (h_2u_2)}{\partial t} + \frac{\partial}{\partial x}\left(h_2u_2^2 + \frac{1}{2}gh_2^2\right) &= -gh_2\frac{\partial Z}{\partial x} - gh_2\frac{\rho_1}{\rho_2}\frac{\partial h_1}{\partial x} - gh_2M_b^2\frac{u_2 \mid u_2 \mid}{h_2^{4/3}}, \end{aligned} \tag{5.3}$$

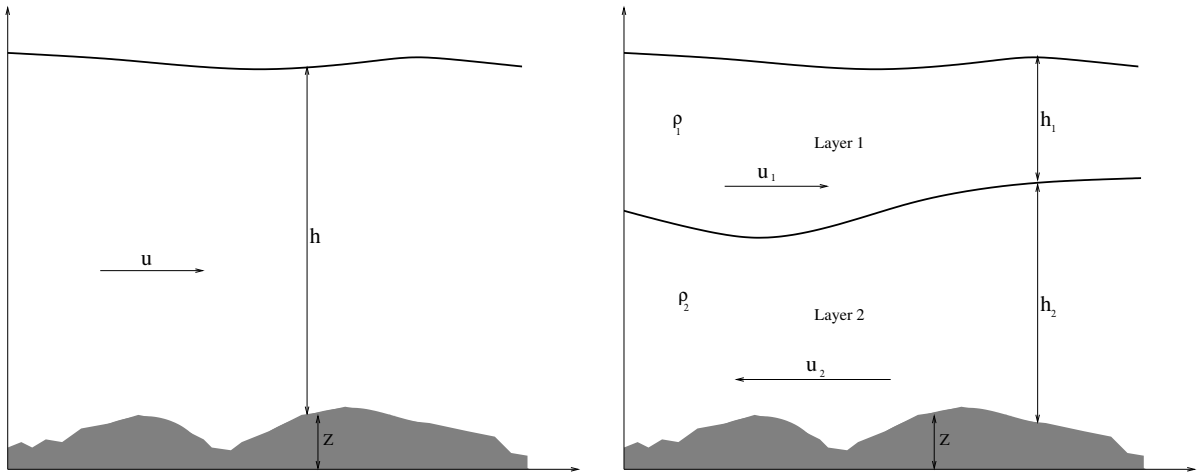

Figure 5.1: Schematic illustration of a single-layer shallow water flow (left plot) and a two-layer shallow water flow (right plot) over a given non-flat topography.

where the subscripts 1 and 2 represent respectively, the upper and lower layers in the hydraulic system, see the right plot in Figure 5.1 for an illustration. Here, ρ_j is the water density of the jth layer, $h_j(t,x)$ is the water height of the jth layer and $u_j(t,x)$ is the local water velocity for the jth layer, $j = 1, 2$. It should be stressed that the exact calculation of eigenvalues associated with the two-layer system (5.3) is not trivial, see for instance [124]. Indeed, the four eigenvalues λ_k $(k = 1, \ldots, 4)$ of the system are the zeros of the characteristic polynomial

$$P(\lambda) = \left(\lambda^2 - 2u_1\lambda + u_1^2 - gh_1\right)\left(\lambda^2 - 2u_2\lambda + u_2^2 - gh_2\right) - g^2 r h_1 h_2, \tag{5.4}$$

where the density ratio $r = \rho_1/\rho_2$. It should be stressed that, in many applications for free-surface flows, the density ratio $r \approx 1$ and the velocities $u_1 \approx u_2$. In these situations, a first-order approximation of the eigenvalues can be obtained by expanding (5.4) in terms of $1 - r$ and $u_2 - u_1$ as

$$\begin{aligned}
\lambda_1 &\approx U_m - \sqrt{g\,(h_1 + h_2)}, \\
\lambda_2 &\approx U_m + \sqrt{g\,(h_1 + h_2)}, \\
\lambda_3 &\approx U_c - \sqrt{(1-r)g\frac{h_1 h_2}{h_1 + h_2}\left(1 - \frac{(u_2 - u_1)^2}{(1-r)g\,(h_1 + h_2)}\right)}, \\
\lambda_4 &\approx U_c + \sqrt{(1-r)g\frac{h_1 h_2}{h_1 + h_2}\left(1 - \frac{(u_2 - u_1)^2}{(1-r)g\,(h_1 + h_2)}\right)},
\end{aligned} \tag{5.5}$$

with

$$U_m = \frac{h_1 u_1 + h_2 u_2}{h_1 + h_2}, \qquad U_c = \frac{h_1 u_2 + h_2 u_1}{h_1 + h_2}.$$

Note that, depending on the values of the density ratio r, the eigenvalues in (5.5) may become complex. In this case, the system is not hyperbolic and it yields the so-called Kelvin-Helmholtz instability at the interface separating the two layers. Therefore, a necessary condition for the two-layer system (5.3) to be hyperbolic is

$$(u_2 - u_1)^2 < (1 - r)g\,(h_1 + h_2)\,. \tag{5.6}$$

The system (5.3) can be rearranged in a vector form as

$$\frac{\partial \mathbf{W}}{\partial t} + \frac{\partial \mathbf{F}(\mathbf{W})}{\partial x} = \mathbf{Q}(\mathbf{W}) + \mathbf{R}(\mathbf{W}), \tag{5.7}$$

where $\mathbf{W}$ is the vector of conserved variables, $\mathbf{F}$ the vector of flux functions, $\mathbf{Q}$ and $\mathbf{R}$ the vectors of source terms defined as

$$\mathbf{W} = \begin{pmatrix} h_1 \\ h_1 u_1 \\ h_2 \\ h_2 u_2 \end{pmatrix}, \qquad \mathbf{F}(\mathbf{W}) = \begin{pmatrix} h_1 u_1 \\ h_1 u_1^2 + \frac{1}{2} g h_1^2 \\ h_2 u_2 \\ h_2 u_2^2 + \frac{1}{2} g h_2^2 \end{pmatrix},$$

$$\mathbf{Q}(\mathbf{W}) = \begin{pmatrix} 0 \\ -g h_1 \frac{\partial}{\partial x}(h_2 + Z) \\ 0 \\ -g h_2 \frac{\partial}{\partial x}(r h_1 + Z) \end{pmatrix}, \qquad \mathbf{R}(\mathbf{W}) = \begin{pmatrix} 0 \\ 0 \\ 0 \\ -g h_2 M_b^2 \frac{u_2 \mid u_2 \mid}{h_2^{4/3}} \end{pmatrix}.$$

Similarly, the equations (5.1) can be reformulated in the vector form (5.7) with

$$\mathbf{W} = \begin{pmatrix} h \\ hu \end{pmatrix}, \qquad \mathbf{F}(\mathbf{W}) = \begin{pmatrix} hu \\ hu^2 + \frac{1}{2} g h^2 \end{pmatrix},$$

$$\mathbf{Q}(\mathbf{W}) = \begin{pmatrix} 0 \\ -gh \frac{\partial Z}{\partial x} \end{pmatrix}, \qquad \mathbf{R}(\mathbf{W}) = \begin{pmatrix} 0 \\ -g h M_b^2 \frac{u \mid u \mid}{h^{4/3}} \end{pmatrix}.$$

Note that equations (5.7) for free-surface flows has been solved in a time interval and a spatial domain equipped with given initial and boundary conditions with fixed topography and constant Manning roughness. In many hydraulic applications, these parameters are not deterministic and may be hard to estimate.

5.2 Numerical simulation of free-surface water flows

For the numerical solution of the free-surface equations (5.7) a class of finite volume methods has been considered. The spatial domain has been discretized into control volumes $[x_{i-1/2}, x_{i+1/2}]$ with uniform size $\Delta x = x_{i+1/2} - x_{i-1/2}$ and divide the temporal domain into subintervals $[t_n, t_{n+1}]$ with stepsize Δt. Here, $t_n = n\Delta t$, $x_{i-1/2} = i\Delta x$ and $x_i = (i + 1/2)\Delta x$ is the center of the control volume. Integrating the equation (5.7) with respect to space over the control volume $[x_{i-1/2}, x_{i+1/2}]$, and obtain the following semi-discrete equations

$$\frac{d\mathbf{W}_i}{dt} + \frac{\mathcal{F}_{i+1/2} - \mathcal{F}_{i-1/2}}{\Delta x} = \mathcal{Q}_i + \mathcal{R}_i, \tag{5.8}$$

where $\mathbf{W}_i(t)$ is the space average of the solution $\mathbf{W}$ in the control volume $[x_{i-1/2}, x_{i+1/2}]$ at time t, *i.e.*,

$$\mathbf{W}_i = \frac{1}{\Delta x}\int_{x_{i-1/2}}^{x_{i+1/2}} \mathbf{W}(t,x)\, dx,$$

and $\mathcal{F}_{i\pm1/2} = \mathbf{F}(\mathbf{W}_{i\pm1/2})$ are the numerical fluxes at $x = x_{i\pm1/2}$ and time t. In (5.8), $\mathcal{Q}_i$ and $\mathcal{R}_i$ are the difference approximations of the discretized source terms $\mathbf{Q}(\mathbf{W}_i)$ and $\mathbf{S}(\mathbf{W}_i)$ in (5.7), respectively. To integrate the system (5.8) in time, an operator splitting method consisting first of the predictor step has been considered as

$$\mathbf{W}_i^{n+1/2} = \mathbf{W}_i^n + \Delta t \mathcal{R}_i^n, \tag{5.9}$$

followed by the corrector step

$$\mathbf{W}_i^{n+1} = \mathbf{W}_i^{n+1/2} - \Delta t \frac{\mathcal{F}_{i+1/2}^{n+1/2} - \mathcal{F}_{i-1/2}^{n+1/2}}{\Delta x} + \Delta t \mathcal{Q}_i^{n+1/2}. \tag{5.10}$$

It should be pointed out that as with all explicit time stepping methods, the theoretical maximum stable time step Δt is specified according to the Courant-Friedrichs-Lewy (CFL) condition

$$\Delta t = Cr \frac{\Delta x}{\max_k\big(|\lambda_k^n|\big)}, \tag{5.11}$$

where Cr is a constant (Courant number) to be chosen less than unity and λ_k are the eigenvalues given by (5.2) or (5.5) for single-layer or two-layer shallow water equations, respectively. The spatial discretization of the equation (5.10) is complete when a reconstruction of the numerical fluxes $\mathcal{F}_{i\pm1/2}^{n+1/2}$ and source terms $\mathcal{Q}_i^{n+1/2}$ is chosen. In general, the reconstruction of the numerical fluxes requires a solution of Riemann problems at the interfaces $x_{i\pm1/2}$, see for example [205, 238]. In the current study the following reconstructions have been considered:

Lax-Friedrichs method: The numerical fluxes $\mathcal{F}_{i+1/2}^n$ are defined by

$$\mathcal{F}_{i+1/2}^n = \frac{1}{2}\Big(\mathbf{F}\left(\mathbf{W}_{i+1}^n\right) + \mathbf{F}\left(\mathbf{W}_i^n\right)\Big) + \frac{\Delta x}{2\Delta t}\left(\mathbf{W}_i^n - \mathbf{W}_{i+1}^n\right). \tag{5.12}$$

Rusanov method: The numerical fluxes $\mathcal{F}_{i+1/2}^n$ are defined by

$$\mathcal{F}_{i+1/2}^n = \frac{1}{2}\Big(\mathbf{F}\left(\mathbf{W}_{i+1}^n\right) + \mathbf{F}\left(\mathbf{W}_i^n\right)\Big) + \frac{\lambda}{2}\left(\mathbf{W}_i^n - \mathbf{W}_{i+1}^n\right), \tag{5.13}$$

where λ is the Rusanov speed defined by $\lambda = \max_k(\lambda_k^n)$, with λ_k are the eigenvalues given by (5.2) or (5.5) for single-layer or two-layer shallow water equations, respectively.

Roe method: The numerical fluxes $\mathcal{F}_{i+1/2}^n$ are defined by

$$\mathcal{F}_{i+1/2}^n = \frac{1}{2}\left(\mathbf{F}(\widehat{\mathbf{W}}_{i+1}^n) + \mathbf{F}(\widehat{\mathbf{W}}_i^n)\right) + \frac{1}{2}\mathbf{A}\left(\widehat{\mathbf{W}}_{i+1/2}^n\right)\left(\widehat{\mathbf{W}}_i^n - \widehat{\mathbf{W}}_{i+1}^n\right), \tag{5.14}$$

where the averaged state $\widehat{\mathbf{W}}_{i+1/2}^n$ is calculated as

$$\widehat{\mathbf{W}}_{i+1/2}^n = \begin{pmatrix} \dfrac{\widehat{h}_i^n + \widehat{h}_{i+1}^n}{2} \\ \dfrac{\sqrt{\widehat{h}_i^n}\widehat{u}_i^n + \sqrt{\widehat{h}_{i+1}^n}\widehat{u}_{i+1}^n}{\sqrt{\widehat{h}_i^n} + \sqrt{\widehat{h}_{i+1}^n}} \end{pmatrix},$$

and $\mathbf{A} = \mathbf{R}\mathbf{\Lambda}\mathbf{R}^{-1}$ is the Roe matrix defined by

$$\mathbf{R} = \begin{pmatrix} 1 & 1 \\ \widehat{\lambda}_1 & \widehat{\lambda}_2 \end{pmatrix}, \qquad \mathbf{\Lambda} = \begin{pmatrix} \widehat{\lambda}_1 & 0 \\ 0 & \widehat{\lambda}_2 \end{pmatrix},$$

where $\widehat{\lambda}_1$ and $\widehat{\lambda}_2$ are the eigenvalues in (5.2) calculated at the averaged state. Note that the extension of the Roe scheme to the two-layer system is not possible since (5.5) is only an approximation and no explicit exact formulation is provided for eigenvalues associated to the system. Therefore, a finite volume modified method of characteristics (FVC) is considered in the current study. The FVC method is simple, easy to implement, and accurately solves the equations (5.7) without relying on a Riemann problem solver. This method has been proposed in [28] for solving single-layer shallow water equations (5.1) and its extension to the two-layer shallow system (5.3) is presented in the present work.

5.2.1 Finite volume modified method of characteristics

To reconstruct the numerical fluxes $\mathcal{F}^n_{i\pm1/2}$ in (5.10), the method of characteristics applied to the advective version of the system (5.3) has been considered. In general, the advective form of the two-layer system (5.3) is built such that the non-conservative variables are transported with the same velocity field associated with each layer. Here, the two-layer shallow water equations (5.3) are reformulated in an advective form as

$$\begin{aligned} \frac{\partial \mathbf{U}_1}{\partial t} + u_1 \frac{\partial \mathbf{U}_1}{\partial x} &= \mathbf{S}_1, \\ \frac{\partial \mathbf{U}_2}{\partial t} + u_2 \frac{\partial \mathbf{U}_2}{\partial x} &= \mathbf{S}_2, \end{aligned} \tag{5.15}$$

where

$$\mathbf{U}_1 = \begin{pmatrix} h_1 \\ u_1 \end{pmatrix}, \qquad \mathbf{S}_1 = \begin{pmatrix} -h_1 \partial_x u_1 \\ -g \dfrac{\partial}{\partial x}\left(Z + h_1 + h_2\right) \end{pmatrix}, \tag{5.16}$$

$$\mathbf{U}_2 = \begin{pmatrix} h_2 \\ u_2 \end{pmatrix}, \qquad \mathbf{S}_2 = \begin{pmatrix} -h_2 \partial_x u_2 \\ -g \dfrac{\partial}{\partial x}\left(Z + r h_1 + h_2\right) \end{pmatrix}. \tag{5.17}$$

The fundamental idea of the method of characteristics is to impose a regular grid at the new time level and to backtrack the flow trajectories to the previous time level. At the old time level, the quantities that are needed are evaluated by interpolation from their known values on a regular grid, for more discussions [213] among others. Thus, the characteristic curves associated with the equations (5.15) are solutions of the initial-value problems

$$\begin{aligned} \frac{dX_{j,i+1/2}(\tau)}{d\tau} &= u_{j,i+1/2}\Big(\tau, X_{j,i+1/2}(\tau)\Big), \quad \tau \in [t_n, t_{n+1}], \\ X_{j,i+1/2}(t_{n+1}) &= x_{i+1/2}, \qquad j = 1, 2. \end{aligned} \tag{5.18}$$

Note that $X_{j,i+1/2}(\tau)$ is the departure point at time τ of a particle that will arrive at point $x_{i+1/2}$ in time t_{n+1}. The method of characteristics does not follow the flow particles forward

in time, as the Lagrangian schemes do, instead it traces backward the position at time t_n of particles that will reach the points of a fixed mesh at time t_{n+1}. To compute the solutions of (5.18) an explicit second-order Runge-Kutta scheme has been used. Once the characteristics curves $X_{j,i+1/2}(t_n)$ are known, a solution at the cell interface $x_{i+1/2}$ is reconstructed as

$$\mathbf{U}^n_{j,i+1/2} = \mathbf{U}_j\left(t_{n+1}, x_{i+1/2}\right) = \widetilde{\mathbf{U}}_j\left(t_n, X_{j,i+1/2}(t_n)\right), \tag{5.19}$$

where $\widetilde{\mathbf{U}}_j\left(t_n, X_{j,i+1/2}(t_n)\right)$ is the solution at the characteristic foot computed by interpolation from the gridpoints of the control volume where the departure point resides. In the present work a quadratic Lagrange interpolation to perform this stage has been considered.
Applied to the equations (5.15), the characteristic solutions are given by

$$\begin{aligned}
h^n_{1,i+1/2} &= \widetilde{h}^n_{1,i+1/2} - \frac{\nu}{2}\widetilde{h}^n_{1,i+1/2}\left(u^n_{1,i+1} - u^n_{1,i}\right),\\
u^n_{1,i+1/2} &= \widetilde{u}^n_{1,i+1/2} - \frac{\nu}{2}g\Big((Z + h^n_1 + h^n_2)_{i+1} - (Z + h^n_1 + h^n_2)_i\Big),\\
h^n_{2,i+1/2} &= \widetilde{h}^n_{2,i+1/2} - \frac{\nu}{2}\widetilde{h}^n_{2,i+1/2}\left(u^n_{2,i+1} - u^n_{2,i}\right),\\
u^n_{2,i+1/2} &= \widetilde{u}^n_{2,i+1/2} - \frac{\nu}{2}g\Big((Z + rh^n_1 + h^n_2)_{i+1} - (Z + rh^n_1 + h^n_2)_i\Big),
\end{aligned} \tag{5.20}$$

where $\nu = \frac{\Delta t}{\Delta x}$ and

$$\widetilde{h}^n_{1,i+1/2} = h_1\left(t_n, X_{1,i+1/2}(t_n)\right), \qquad \widetilde{u}^n_{1,i+1/2} = u_1\left(t_n, X_{1,i+1/2}(t_n)\right),$$
$$\widetilde{h}^n_{2,i+1/2} = h_2\left(t_n, X_{2,i+1/2}(t_n)\right), \qquad \widetilde{u}^n_{2,i+1/2} = u_2\left(t_n, X_{2,i+1/2}(t_n)\right),$$

are the solutions at the characteristic foot computed by interpolation from the gridpoints of the control volume where the departure points $X_{1,i+1/2}(t_n)$ and $X_{2,i+1/2}(t_n)$ belong. The numerical fluxes $\mathcal{F}_{i\pm1/2}$ in (5.8) are calculated using the intermediate states $\mathbf{W}^n_{i\pm1/2}$ recovered accordingly from the characteristic solutions $\mathbf{U}^n_{j,i\pm1/2}$ in (5.19). Hence, the FVC method (5.10) reduces to

$$\begin{aligned}
h^{n+1}_{1,i} &= h^n_{1,i} - \nu\left((h_1u_1)^n_{i+1/2} - (h_1u_1)^n_{i-1/2}\right),\\
q^{n+1}_{1,i} &= q^n_{1,i} - \nu\left(\left(h_1u_1^2 + \frac{1}{2}gh_1^2\right)^n_{i+1/2} - \left(h_1u_1^2 + \frac{1}{2}gh_1^2\right)^n_{i-1/2}\right)\\
&\quad -\frac{1}{2}\nu g\hat{h}^n_{1,i}\left((Z + h_2)_{i+1} - (Z + h_2)_{i-1}\right),\\
h^{n+1}_{2,i} &= h^n_{2,i} - \nu\left((h_2u_2)^n_{i+1/2} - (h_2u_2)^n_{i-1/2}\right),\\
q^{n+1}_{2,i} &= q^n_{2,i} - \nu\left(\left(h_2u_2^2 + \frac{1}{2}gh_2^2\right)^n_{i+1/2} - \left(h_2u_2^2 + \frac{1}{2}gh_2^2\right)^n_{i-1/2}\right)\\
&\quad -\frac{1}{2}\nu g\hat{h}^n_{2,i}\left((Z + rh_1)^n_{i+1} - (Z + rh_1)^n_{i-1}\right),
\end{aligned} \tag{5.21}$$

where $q_1 = h_1u_1$ and $q_2 = h_2u_2$ are the water discharges associated with upper layer and lower layer, respectively. In this FVC method, the reconstruction of the term $\hat{h}^n_{1,i}$ and $\hat{h}^n_{2,i}$ in

Algorithm 5.1 Finite volume modified method of characteristics used in the present study.

Require:

$Tend$: Final simulation time.

h: Water height.

u: Water velocity.

1: Discretize the given domain into set of control volumes.

2: Define the physical and numerical parameters.

3: Set the initial dam-break condition.

4: **while** $t \leqslant Tend$ **do**

5: Update the time step.

6: Compute the departure points $X_{1,i+1/2}(t_n)$ and $X_{2,i+1/2}(t_n)$ using the explicit second-order Runge-Kutta scheme for solving (5.18).

7: Compute the approximations

$$\widetilde{h}^n_{1,i+1/2} = h_1\left(t_n, X_{1,i+1/2}(t_n)\right), \qquad \widetilde{u}^n_{1,i+1/2} = u_1\left(t_n, X_{1,i+1/2}(t_n)\right),$$

$$\widetilde{h}^n_{2,i+1/2} = h_2\left(t_n, X_{2,i+1/2}(t_n)\right) \quad \text{and} \quad \widetilde{u}^n_{2,i+1/2} = u_2\left(t_n, X_{2,i+1/2}(t_n)\right),$$

employing a quadratic Lagrange interpolation procedure.

8: Evaluate the intermediate states $h^n_{1,i+1/2}$, $u^n_{1,i+1/2}$, $h^n_{2,i+1/2}$ and $u^n_{2,i+1/2}$ from the predictor stage (5.20).

9: Update the solutions $h^{n+1}_{1,i}$, $q^{n+1}_{1,i}$, $h^{n+1}_{2,i}$ and $q^{n+1}_{2,i}$ using the corrector stage (5.21).

10: **end while**

(5.21) is carried out such that the discretization of the source terms is well balanced with the discretization of the flux gradients using the concept of C-property as detailed in [28]. Hence, if the source terms $\hat{h}^n_{1,i}$ and $\hat{h}^n_{2,i}$ in the stage of (5.21) are discretized as

$$\hat{h}^n_{1,i} = \frac{1}{4}\left(h^n_{1,i+1} + 2h^n_{1,i} + h^n_{1,i-1}\right), \qquad \hat{h}^n_{2,i} = \frac{1}{4}\left(h^n_{2,i+1} + 2h^n_{2,i} + h^n_{2,i-1}\right), \tag{5.22}$$

then the proposed FVC method satisfies the C-property. In summary, the implementation of FVC algorithm to solve the two-layer shallow water equations (5.3) is carried out in the following steps. Given $\left(h^n_{1,i}, q^n_{1,i}, h^n_{2,i}, q^n_{2,i}\right)$, we compute $\left(h^{n+1}_{1,i}, q^{n+1}_{1,i}, h^{n+1}_{2,i}, q^{n+1}_{2,i}\right)$ as shown in the steps in algorithm 5.2.

5.3 Uncertainty quantification methods

In general, the purpose of uncertainty quantification is to identify the main sources of uncertainty in a physical model (*e.g.* parameters, external forcing, boundary conditions, initial conditions) and to quantify their impact on the quantities of interest simulated by the numerical model (prognostic variables, probability of exceeding the threshold). This allows to associate every forecast with a level of uncertainty since the accuracy of a simulation significantly depends on both the quantity and the quality of the input data. Therefore, to better understand the results of numerical simulations it is necessary to take into account these uncertainties in the simulations. In addition, a problem of quantification of uncertainties is a problem which aims at estimating uncertainty on the outputs of a numerical simulation according to the uncertainties in knowledge of its input parameters. Because of the random nature of uncertainty,

the probabilistic approach to deal with a problem of uncertainty quantification is to consider the uncertain data of the model as random variables or random processes, and to reconsider the real deterministic numerical model as a stochastic model. This section presents the techniques used in the current study for uncertainty quantification. First, the methods of generating different independent realization of the bathymetric field are presented. Therefore, the classical PCE method is used as a surrogate tool to alleviate the computational cost. Finally, as the hydraulic state is also considered as a stochastic process, suggestion to reduce the dimension of the problem using the POD and to compute a PCE only for the associated nonphysical variables.

5.3.1 Karhunen-Loève expansion for stochastic process

A stochastic process is defined by the means of an indexation set X, E is a measurable space and $(\Omega, \mathcal{F}, \mathcal{P})$ is a σ-algebra representing the probability space [249]. The stochastic process $\mathbf{z}$ is then defined as a collection $\{\mathbf{z}_x, x \in X\}$ which the random values are in the state space E and described statistically by the probabilistic space $(\Omega, \mathcal{F}, \mathcal{P})$

$$\mathbf{z}_x : \Omega \longrightarrow E. \tag{5.23}$$

Consequently, one is able to define a realization $\omega \in \Omega$ for a stochastic process as

$$\mathbf{z}(\omega) : \begin{array}{ccc} X & \longrightarrow & E \\ x & \longmapsto & \mathbf{z}(\omega) \end{array} \tag{5.24}$$

The Karhunen-Loève expansion (KL) allows to model a random process based on a spectral decomposition of its spatial covariance matrix $\mathcal{C}(x, x')$, see for example [128, 160]. Note that, by construction the covariance function is real, symmetric and positive definite. Consequently, the set of eigenfunctions form a complete orthogonal basis for the space in which the process belongs. Hence, a stochastic process can be defined as

$$\boldsymbol{z}(x, \boldsymbol{\omega}) = \overline{\boldsymbol{z}}(x) + \sum_{i=0}^{\infty} \omega_i l_i \phi_i(x), \tag{5.25}$$

where x is the curvilinear abscissa, $\overline{\boldsymbol{z}}$ the mean of the random process, $\boldsymbol{\omega} = \{\omega_1, \dots, \omega_\infty\}$ a set of independent random variables, (l_i) $(i = 0, 1, \dots)$ the set of the eigenvalues of the covariance function, and $(\phi_i(x))$ $(i = 0, 1, \dots)$ the set of the eigenfunctions. In practice and for computational reasons, the equation (5.25) is truncated at a certain degree d. The choice of this latter is often determined by a threshold ϵ from which the eigenvalues could be neglected *i.e.*

$$\frac{\sum_{i=0}^{d} l_i}{\sum_{i=0}^{\infty} l_i} > 1 - \epsilon.$$

Thus, the expansion (5.25) is replaced by

$$\mathbf{z}(x, \boldsymbol{\omega}) = \overline{\mathbf{z}}(x) + \sum_{i=0}^{d} \omega_i l_i \phi_i(x), \tag{5.26}$$

where ω is the stochastic input parameter. It should be stressed that the major limitation of the KL decomposition is the *a priori* knowledge of the covariance matrix. This expansion is commonly used to model the uncertainty of stochastic input parameters for two reasons: firstly the mean-square error of the finite representation (5.26) is minimized such that the equation (5.25) converges following the ℓ_2-norm. The second reason is related to the generation of random samples. In fact, making a realization of $\boldsymbol{z}(x, \boldsymbol{\omega})$ amounts to randomly draw the different ω_i following a defined probability density function. Those parameters are considered independent random variables. Therefore, the KL decomposition offers a good representation of the input parameters when the covariance is known. In this study, The covariance matrix $\mathcal{C}(x, x')$ is supposed to be exponential. Indeed, [261] showed that the uncertainty in the description of bathymetric fields followed this spatial correlation function. Thus, the correlation matrix is defined as

$$\mathcal{C}(x, x') = \sigma^2 \exp\left(-\frac{|x - x'|}{\theta}\right), \tag{5.27}$$

where σ and θ are the hyper-parameters of the covariance function with σ is the standard deviation of the process and θ is the correlation length. Note that, calculating the eigenvalues and eigenvectors is well known by the Fredholm problem. There exits many algorithms that aim to solve this latter given a well defined matrix. Once, l_i and $\phi_i(x)$ are known, the KL expansion is implemented in as straightforward manner. Therefore, the bathymetry could be written as described in (5.26) and could be sampled in order to consider its uncertainty in hydraulic computations.

5.3.2 Polynomial chaos expansions

The PCE has been intensively used as a surrogate model in the context of uncertainty quantification, see [108, 80] among others. It aims to reproduce the global behavior of the considered shallow water models. Supposing that the input parameters of this model are represented by M independent random variables $\boldsymbol{\zeta} = \{\zeta_1, \zeta_2, \ldots, \zeta_M\}$ with finite variance well defined in a probabilistic space, the response $\mathbf{U}$ of this model is also random. Note that $\mathbf{U}$ is a vector-valued response as it represents the spatial variability of the hydraulic states. Considering that the expectation $\mathbb{E}[\|\mathbf{U}\|^2]$ is finite, the behavior of $\mathbf{U}$ could be reproducible following a polynomial decomposition namely PCE [219] as

$$\mathbf{U}(x, \boldsymbol{\zeta}) = \sum_{i \in \mathbb{N}} \alpha_i(x) \Psi_i(\boldsymbol{\zeta}), \tag{5.28}$$

where Ψ_i are the multivariate polynomials that form the basis are chosen in such way they are orthonormal with respect to the associated probability density function of $\boldsymbol{\zeta}$, compare for example [248, 252]. In (5.28), α_i are the unknown spectral coefficients of the decomposition to be determined. Again, the sum in (5.28) is truncated to a finite series as

$$\mathbf{U}(x, \boldsymbol{\zeta}) \approx \sum_{i \in \mathcal{I}} \alpha_i(x) \Psi_i(\boldsymbol{\zeta}), \tag{5.29}$$

where $\mathcal{I} \subset \mathbb{N}$ is the finite set of indices. The determination of a PCE is therefore conditioned by the estimation of the spectral coefficients α_i. There are many methods used in the literature to achieve this step and we refer to [251, 252, 144] for a review on these methodologies. In the current work, only the regression method is used and this choice comes from the fact that these methods coupled with compressed sensing techniques are advantageous when the

stochastic dimension M of the problem is high (which is more likely to be the case here after the use of the KL decomposition). The regression method is based on solving a least-square minimization problem in some ℓ_2-norm to estimate the coefficients α_i, see for instance [65, 33]. In practice, we begin by defining an error $\boldsymbol{\epsilon}$ as the distance between the model and the PCE for a finite set of randomly sampled input variables of size N_{ls} as

$$\boldsymbol{\epsilon} = \left\| \mathbf{U}(x, \boldsymbol{\Xi}) - \sum_{i \in \mathbb{N}} \alpha_i(x) \Psi(\boldsymbol{\Xi}) \right\|_2 \equiv \boldsymbol{\mathcal{W}} - \boldsymbol{\alpha}^\top \boldsymbol{\Psi}, \tag{5.30}$$

where $\boldsymbol{\Xi} = \left(\boldsymbol{\zeta}^{(1)}, \ldots, \boldsymbol{\zeta}^{(N_{ls})}\right)^\top$ is the set of realizations for the stochastic input variables $\boldsymbol{\zeta}$ and $\boldsymbol{\mathcal{W}} = \left(\mathbf{U}^{(1)}, \ldots, \mathbf{U}^{(N_{ls})}\right)^\top$ the vector of associated model outputs. Defining $\boldsymbol{\alpha} = \left(\alpha_0, \ldots, \alpha_{N_{PC-1}}\right)^\top$ as the vector of the $N_{PC} = Card(\mathcal{I})$ unknown coefficients and $\boldsymbol{\Psi}$ is the matrix of size $N_{PC} \times N_{ls}$ assembling the values of all orthonormal polynomials at the stochastic input realizations values $\boldsymbol{\Psi}_{ik} = \Psi_i(\boldsymbol{\zeta}^{(k)})$, with $i = 0, 1, \ldots, N_{PC-1}$ and $k = 1, 2, \ldots, N_{ls}$. Following the ordinary least-square solver (5.30), the estimation of the set of coefficients $\boldsymbol{\alpha}$ is equivalent to minimize the following function

$$\mathrm{J}(\boldsymbol{\alpha}) = \boldsymbol{\epsilon}^\top \boldsymbol{\epsilon} = \left(\boldsymbol{\mathcal{W}} - \boldsymbol{\alpha}^\top \boldsymbol{\Psi}\right)^\top \left(\boldsymbol{\mathcal{W}} - \boldsymbol{\alpha}^\top \boldsymbol{\Psi}\right), \tag{5.31}$$

which leads to a standard well-known linear algebraic solution as

$$\boldsymbol{\alpha} = \left(\boldsymbol{\Psi}^\top \boldsymbol{\Psi}\right)^{-1} \boldsymbol{\Psi}^\top \boldsymbol{\mathcal{W}}. \tag{5.32}$$

Here, the input space exploration is fulfilled using a Monte-Carlo sampling-based approach [39, 80]. It is worth mentioning that the number of coefficients N_{PC} needed is directly affected by the stochastic dimension M as well as the polynomial degree p. As a consequence, the Monte-Carlo size N_{ls} will also increase significantly with M and p. This is a classical problem of PCE also known as *the curse of dimensionality*. The adaptive Least Angle Regression (LAR) method [48] has been introduced and used to overcome this specific problem [39]. This method introduced in the context of compressed sensing has made it possible to recover accurately the solution with fewer model simulations. It will be used in the present work as it has been demonstrated to be very efficient in this framework. The idea behind this method is to select with an iterative manner an optimal sparse basis among the original one and then to compute a limited number of coefficients using a standard regression method. In the context of PCE, a hybrid LAR method is used. The method consists on using LAR to evaluate the best set of predictors among the full basis elements with the help of a cross-validation method. These coefficients are estimated using the classical least square method, see [39] for more details. The infinite expansion (5.28) describing the PCE converges with respect to the standard ℓ_2-norm known by the mean-squared convergence, see for example [251]. However, due to the errors of truncation and spectral coefficient estimation, the accuracy of this expansion must be evaluated in the same error norm. There are many different error metrics that allow to assess the accuracy of the PCE, see [80, 251] among others. In the present work, all the PCEs are assessed using the Leave-One-Out (LOO) error. This method avoids integrating the model over another set of validation samples and therefore the computational cost is optimized. It has been introduced in this context with the introduction of sparse PCE [33] and the LOO technique required the formulation of several surrogate models [75, 39]. Each surrogate model is built excluding one point out of the input sample and the accuracy of the surrogate model

is then quantified at this particular point. Following this theory, the error ϵ_{LOO} is defined by

$$\epsilon_{LOO} = \frac{\sum_{k=1}^{N_{ls}} \left(\mathbf{U}^{(k)} - \mathbf{U}^{(-k)}\right)^2}{\sum_{k=1}^{N_{ls}} \left(\mathbf{U}^{(k)} - \overline{\mathbf{U}}\right)^2}, \tag{5.33}$$

where $\overline{\mathbf{U}}$ denotes the sample-averaged model simulations and $\mathbf{U}^{(-k)}$ stands for the evaluation of the PCE at $\boldsymbol{\zeta}^{(k)}$ when the surrogate has been built using an experimental design in which $\boldsymbol{\zeta}^{(k)}$ was excluded. It should be stressed that, in the context of PCE it has been proven that the LOO error could be computed analytically using all the samples. In this case, a corrected LOO error is computed using only a full PCE rather than several decompositions, compare [38]. Furthermore, it has been proven that in the case of sparse PCE, the LOO error is robust and conservative, see [37]. The relative error and the LOO error have also been compared in [80] for the case of PCE applied to hydraulic uncertainties and the results reported in this reference have shown a good agreement between the two metrics. In the present work, the determination of the optimal polynomial degree is performed using an iterative procedure. Thus, a PCE is computed for different degrees varying from 1 to 20 and the optimal degree is determined based on the value of the corresponding ϵ_{LOO} error. For the same value of a given error, the lowest value of the degree is retained.
Note that, when dealing with numerical models with spatial or temporal dependency, the classical way used in numerical simulations is to discretize the physical domain and resolve the governing equations for each control volume. This procedure leads to multiple decompositions to ensure the numerical convergence. As a result, uncertainty quantification becomes computationally very demanding not only because of the stochastic dimensions but also because of the spatial or temporal dimensions of the output variables. For these reasons, many methods have been introduced in the literature in order to reduce the dimensionality of the output vector, see for instance [197, 41, 63, 40]. Among all these different techniques, the POD have proven to be more efficient in the context of physical fields with rapid variability as in the case of hydraulics [197].

5.3.3 Stochastic proper orthogonal decomposition

The proper orthogonal decomposition (POD) is a well-established technique that allows a high-dimensional system to be approached by a low-dimensional one, compare [68] among others. This method is based on determining a basis of orthogonal eigenvalues representative of the simulated physics. The eigenvectors are obtained by solving the integral of Fredholm problem whereas, the kernel of this integral is constructed from a set of simulations constructed using a set of experiments. The interesting property of this representation lies in the fact that the eigenfunctions associated with the problem are optimal in the sense of the energetic representation which makes it possible to use them to construct a reduced representation of the physics under study. Notice that the POD is used in the uncertainty quantification to reduce the size of a random vector at the output of the model. The uncertainty is therefore carried out over each direction defined by the eigenvectors $\phi_i(x)$. The idea is based on projecting the solution $\mathbf{U}$ of the model into a finite and orthonormal basis $\{\phi_i,\ i \in \mathcal{I}_{POD}\}$, where $\mathcal{I}_{POD}$ is a discrete finite set of indices. Thus, the process $\mathbf{U}(x, \boldsymbol{\zeta})$ is decomposed as

$$\mathbf{U}(x, \boldsymbol{\zeta}) = \sum_{i \in \mathcal{I}_{POD}} \widehat{\lambda}_i(\boldsymbol{\zeta})\phi_i(x). \tag{5.34}$$

Algorithm 5.2 Stochastic proper orthogonal decomposition used in the present study.

Require:

$Tend$: Final simulation time

1: **while** $t \leqslant Tend$ **do**
2: Define the covariance matrix (5.35)
3: Expand the matrix $\mathbf{C}$ using an SVD algorithm to determine λ_i and $\phi_i(x)$
4: Retain only the first k eigenvalues and eigenvectors in the expansion using the condition (5.34)
5: Reconstruct the stochastic solutions $\mathbf{U}(x, \boldsymbol{\zeta})$ using (5.34)
6: **end while**

where $\widehat{\lambda_i}$ is the mean value of $\lambda_i(\boldsymbol{\zeta})$. The estimation of the finite basis $\{\phi_i,\ i \in \mathcal{I}_{POD}\}$ is performed by decomposing the covariance matrix as

$$\mathbf{C} = \frac{1}{N_{ls}} \mathbf{U}\mathbf{U}^{\top}. \tag{5.35}$$

Indeed, the literature is rich of techniques that aim to decompose a covariance matrix. One of the most known methods is the Singular Value Decomposition (SVD) algorithm [74]. Hence, we define a POD-truncated error ϵ such as only the most k invaluable eigenvectors are retained as

$$\frac{\sum_{i=0}^{k} \lambda_i}{\frac{N_{ls}}{\sum_{i=0} \lambda_i}} > 1 - \epsilon, \tag{5.36}$$

In summary, the stochastic POD procedure can be implemented as in algorithm 5.2.

It is worth remarking that the selection of convergence criterion is problem dependent and therefore the selection of ϵ for test examples in the present investigation is discussed in sections 5.4 and 5.5 where numerical examples are described.

5.3.4 The POD-PCE surrogate model

Once the stochastic POD is reconstructed, the eigenvalues are considered as stochastic independent variables (since the eigenvectors form a basis). This means that defining a PCE for each eigenvalue following the same manner as described in the previous section on polynomial chaos expansions leaving the spatial dependence described by the eigenvectors $\phi_i(x)$ as

$$\lambda_i(\boldsymbol{\zeta}) = \sum_{j=0}^{N_{PC}} \gamma_j \Psi_j(\boldsymbol{\zeta}), \tag{5.37}$$

where γ_j are the corresponding spectral coefficients. Hence, using (5.37), the equation (5.29) reduces to

$$\mathbf{U}(x, \boldsymbol{\zeta}) = \sum_{i \in \mathcal{I}_{POD}} \left(\sum_{j=0}^{N_{PC}} \gamma_j \Psi_j(\boldsymbol{\zeta}) \right) \phi_i(x). \tag{5.38}$$

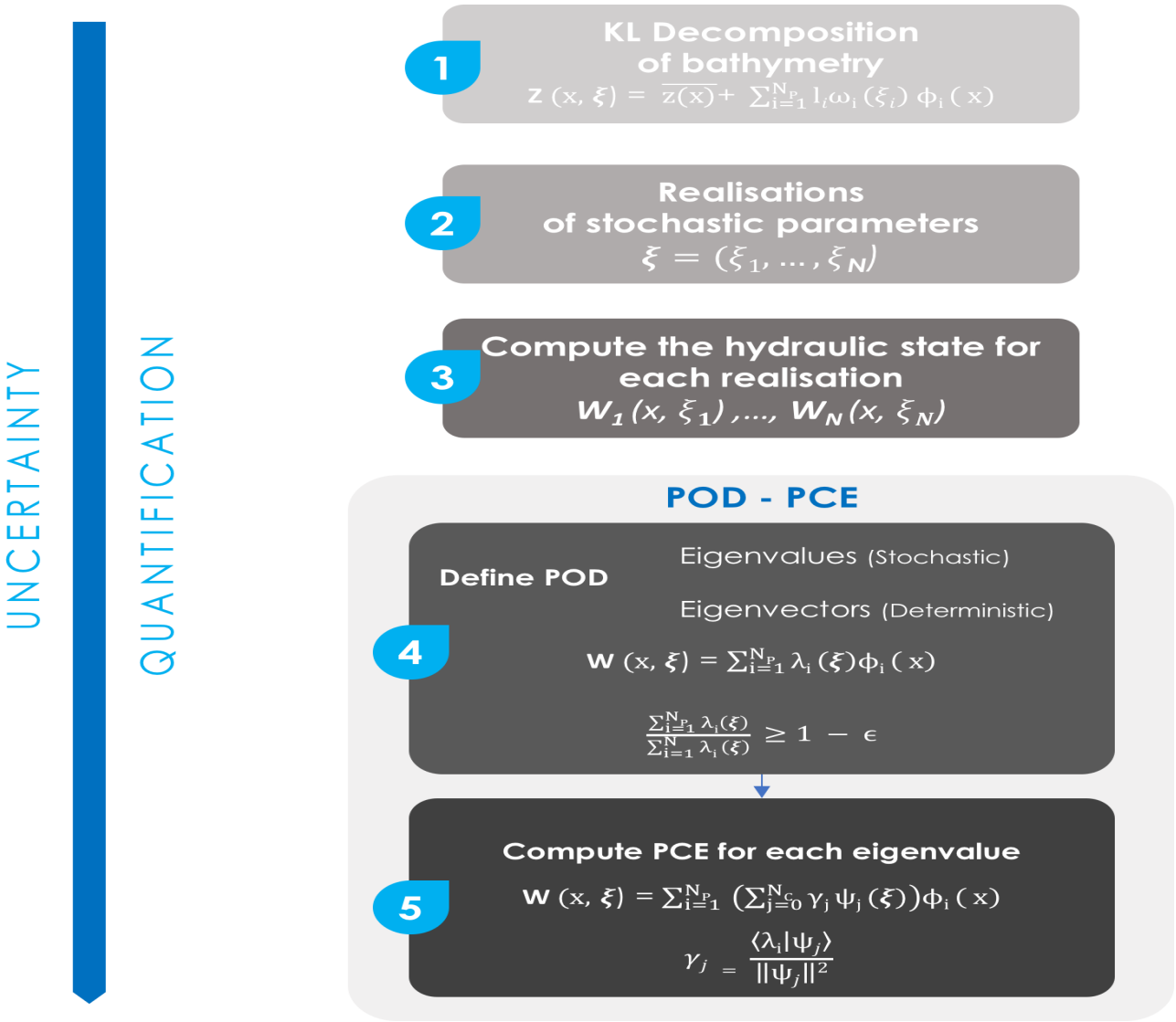

Figure 5.2: Schematic representation of the POD-PCE based surrogate model.

Figure 5.2 summarizes both algorithms considered in the present work for the quantification of uncertainty. Here, the first step consists of developing the KL decomposition to be able to sample the bathymetric fields. Obviously, this step depends mainly on the definition of a spatial correlation associated with the problem under consideration. In practice, the covariance matrix could be inferred from observational data, compare for example [222, 199]. For all simulations carried out in this study, the correlation matrix is assumed to be exponential with given correlation length for each test problem and the associated eigenvalues and eigenvectors are obtained analytically as in [145]. The second step in the algorithm for uncertainty quantification is sampling the different random variables using a Monte Carlo approach which includes the eigenvalues of the KL decomposition and the Manning coefficient following a well defined probabilistic distribution. For each realization, the hydraulic state is computed as shown by step 3 in the algorithm shown in Figure 5.2. Next, a resulting hydraulic state is obtained for each realization which allow to perform a POD over the hydraulic state. Note that the eigenvectors represent the spatial variability while, the eigenvalues are responsible for the

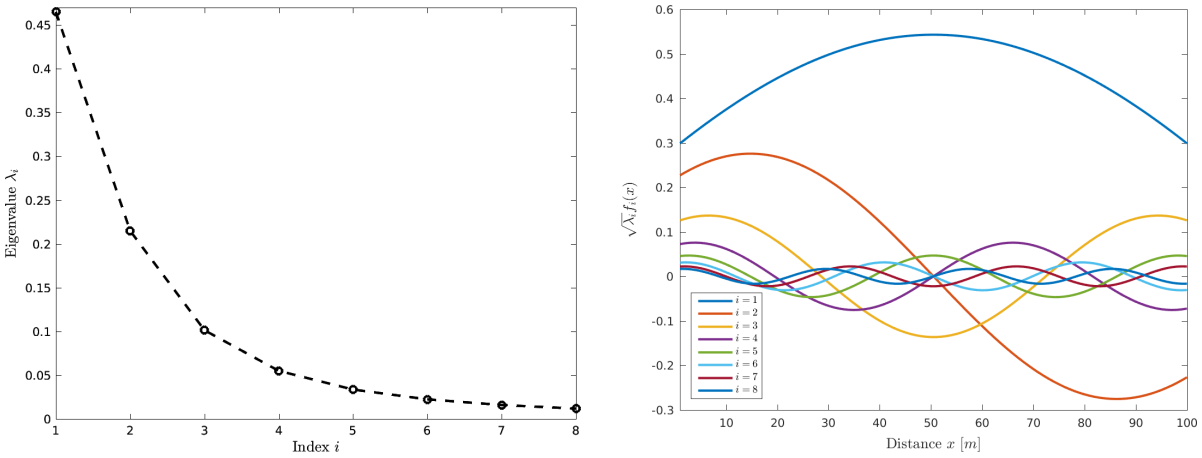

Figure 5.3: Eigenvalues (left plot) and associated eigenfunctions (right plot) of the correlation matrix in the KL decomposition for the dam-break problem over a flat bed.

uncertainty as explained in [40, 79]. The final step in this algorithm is to carry an adaptive spare PCE over the eigenvalues of the POD. It is evident that, using this surrogate model, one is able to quantify the uncertainty for each numerical solver.

5.4 Numerical results and examples

Numerical results for several test problems of shallow water flows using single-layer and two-layer shallow water equations over flat and non-flat beds have been presented in this section. The main goal of this section is to illustrate the numerical performance of the techniques described above. In all the computations reported herein, the Courant number is set to $Cr = 0.7$ and the time stepsize Δt is adjusted at each time step according to the CFL stability condition (5.11). Numerical results obtained using the Lax-Friedrich's, Rusanov, Roe and FVC methods have been presented.

5.4.1 Results for single-layer shallow flows

In this class of flow problems, the uncertainty using the proposed finite volume methods for the single-layer shallow water equations (5.1) has been investigated. More precisely quantifying the uncertainty related to the bathymetry displayed by the considered numerical methods. The aim here is to rank these finite volume methods regarding the uncertainty on the computed water height and water velocity variables when the knowledge about the bathymetry is uncertain. Here, the POD-PCE meta-model is built using 1000 forward simulations. The uncertainty in this case with the model using two different meshes with 100 and 200 control volumes have been evaluated. In all cases considered in this section, the general methodology described in section 5.4 has been followed. Thus, first the bathymetry field using the KL decomposition has been decomposed, then running the Monte-Carlo simulations to obtain a set of fields for both water height and water velocity. These fields are then reduced using the POD approach and then reduced further by using a truncation threshold in the PCE over each POD mode.

Table 5.1: Best polynomial degree along with the LOO error for the two POD modes in the water height and water velocity using different numerical schemes for the dam-break problem over a flat bed.

	First POD mode			
	FVC	Lax-Friedrichs	Roe	Rusanov
Optimal polynomial degree (h)	3	3	3	3
Optimal polynomial degree (u)	3	3	3	3
LOO error (h)	1.5×10^{-9}	1.8×10^{-9}	4.5×10^{-11}	3.8×10^{-11}
LOO error (u)	10^{-7}	1.6×10^{-6}	2.3×10^{-8}	2.2×10^{-9}
	Second POD mode			
	FVC	Lax-Friedrichs	Roe	Rusanov
Optimal polynomial degree (h)	3	3	3	3
Optimal polynomial degree (u)	3	3	3	3
LOO error (h)	4.8×10^{-9}	3.6×10^{-9}	0.75×10^{-11}	0.4×10^{-11}
LOO error (u)	8.8×10^{-7}	2×10^{-6}	1.3×10^{-8}	5.8×10^{-9}

Dam-break problem over a flat bed

For this test example, the uncertainty quantification is performed for a dam-break flow problem over a stochastic frictionless flat bed (*i.e.* $Z = 0$ and $M_b = 0$). The channel is of length 30 m and subject to the following initial conditions

$$h(0,x) = \begin{cases} 1\ m, & \text{if} \quad x \leq 15\ m, \\ \\ 0.3\ m, & \text{if} \quad x > 15\ m, \end{cases} \qquad u(0,x) = 0\ m/s.$$

At time $t = 0$ the dam collapses and the flow problem consists of a shock wave travelling downstream and a rarefaction wave travelling upstream. The computed results are presented at time $t = 2\ s$.

Figure 5.3 presents the eigenvalues and eigenvectors obtained for the bathymetry process. This latter is supposed to be a Gaussian process described with an exponential spatial autocorrelation function. Given a value of threshold $\epsilon = 10^{-2}$, 8 eigenvalues are required to correctly sample the bathymetric field. In other words, the stochastic dimension of this problem is set at 8. For each of the four numerical methods tested in this study, a 1000 Monte-Carlo simulations are run while the POD is then used to reduce the output space. In this case, only two modes are retained to correctly represent the water height and the water velocity fields. The PCE is built over each POD mode corresponding to 4 PCEs (2 for the water height and 2 for the water velocity) instead of 2×100 decompositions in the conventional approach. An iterative procedure is used to determine the best polynomial degree along with the LOO error that is used to assess the robustness of the considered PCE.

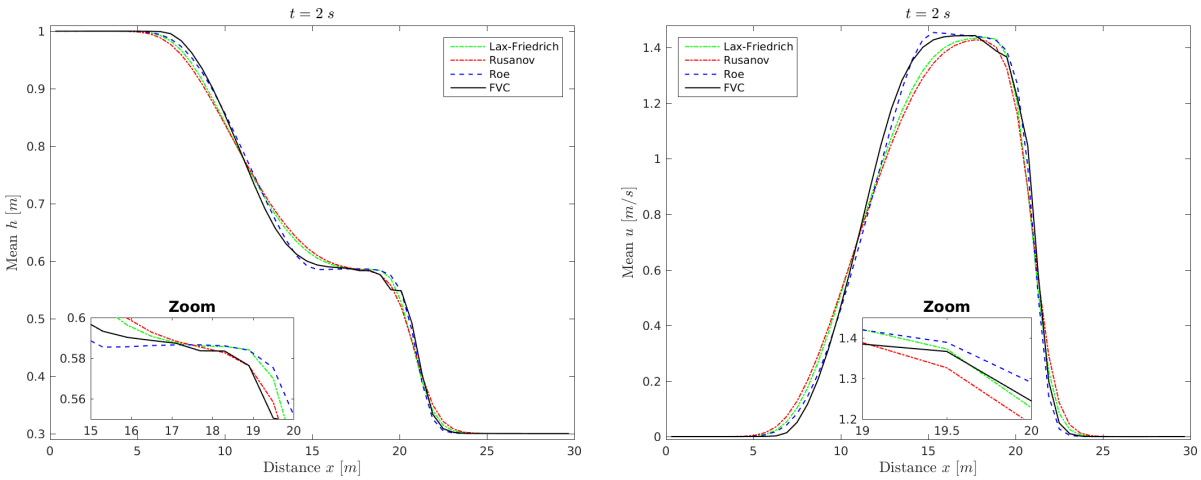

Figure 5.4: Mean solutions obtained using Lax-Friedrichs, Roe, Rusanov and FVC methods for water height (left plot) and water velocity (right plot) for the dam-break problem over a flat bed.

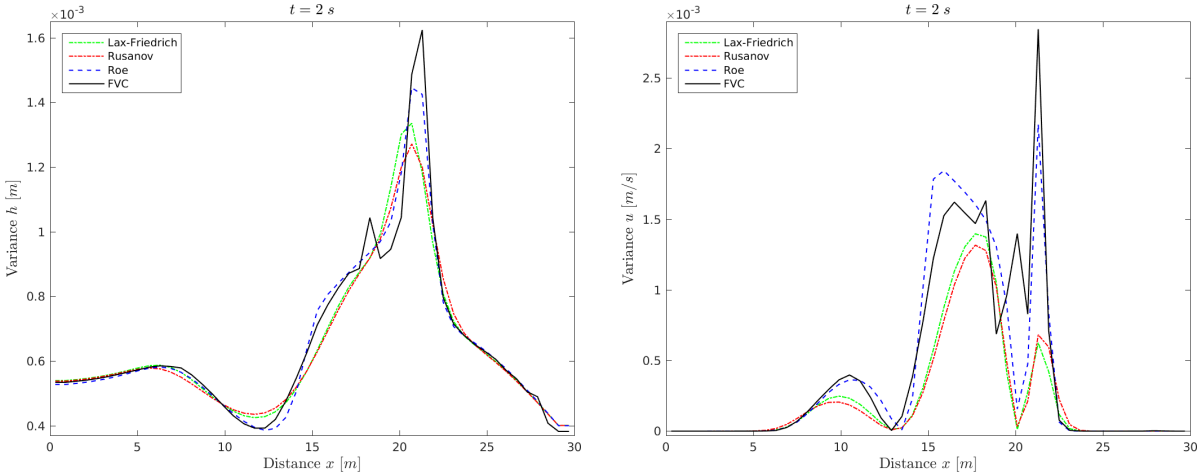

Figure 5.5: Variance solutions obtained using Lax-Friedrichs, Roe, Rusanov and FVC methods for water height (left plot) and water velocity (right plot) for the dam-break problem over a flat bed.

Table 5.1 summarizes the results obtained for the first and the second POD modes. It is evident that a polynomial of degree 3 is enough to correctly reproduce the uncertainty translated from errors in the bathymetry in the four methods considered in this study. Depending on the numerical method and the output field (water height or water velocity), the LOO error varies from 10^{-11} to 10^{-6} which makes the surrogate model very reliable for uncertainty quantification in this class of dam-break problems. The results obtained for the mean and variance fields are reported in Figure 5.4 and Figure 5.5, respectively. As can be seen from these results, the mean fields highlight some well-established results on the accuracy of the numerical methods, *i.e.* the numerical diffusion is more pronounced for the Lax-Friedrich's method than the FVC method. However, the variance fields show noticeable differences in these numerical methods particularly where the hydraulic jump occurs. It is also clear that the FVC and Roe methods are more sensitive to changes in the bathymetry than the Rusanov and Lax-Friedrich's methods. The FVC and Roe methods, being more accurate than the Rusanov and Lax-Friedrich's

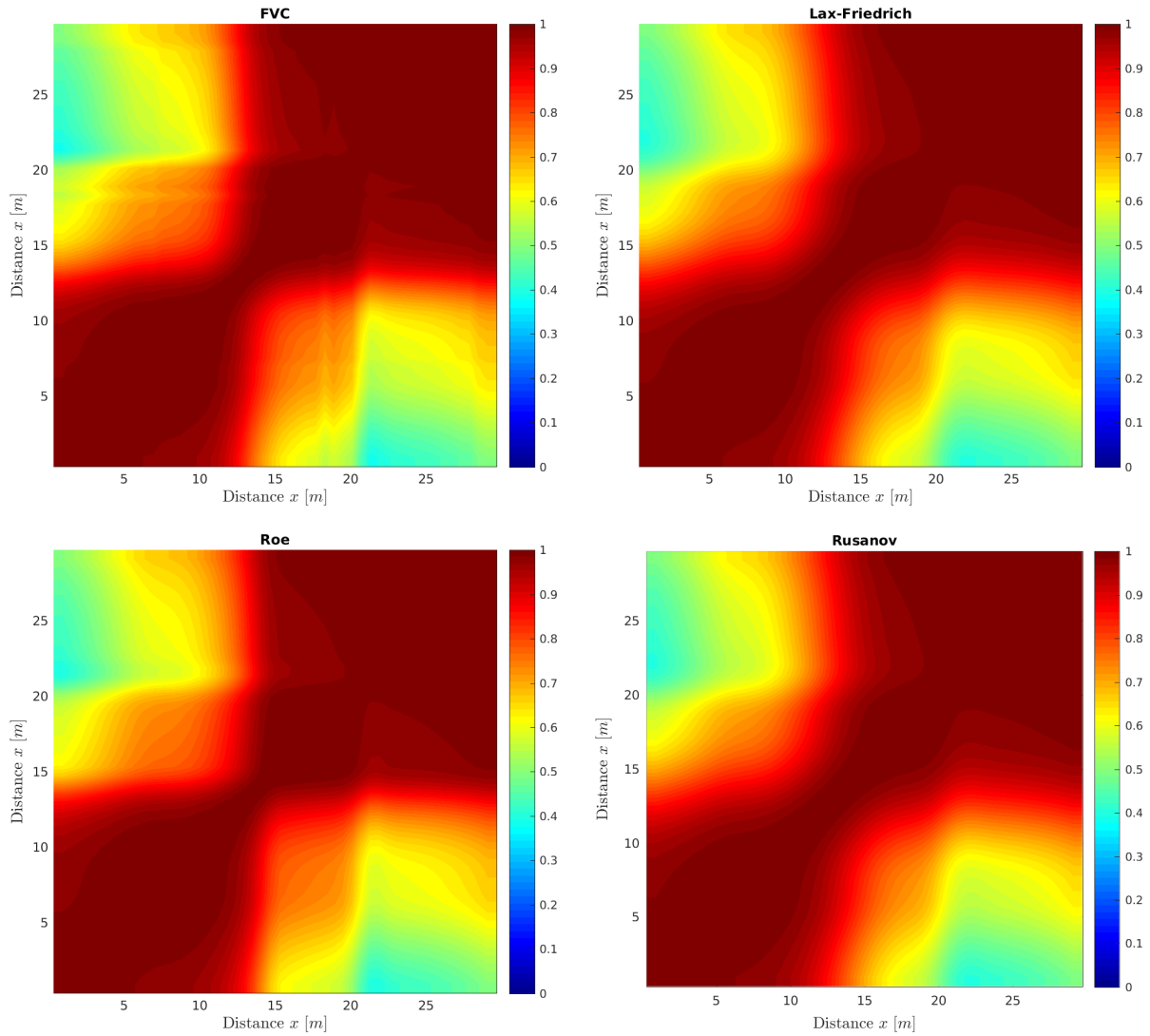

Figure 5.6: Spacial correlation field for water height using Lax-Friedrichs, Roe, Rusanov and FVC methods for the dam-break problem over a flat bed.

methods, are more sensitive to the stochastic inputs. Therefore, these numerical methods display more uncertainty in both water height and water velocity solutions. Furthermore, regarding their importance in the context of data assimilation for bathymetric corrections, the correlation matrices and functions are presented for this test example. Figure 5.6 illustrates the correlation matrices using the four numerical methods whereas, Figure 5.7 represents the correlation function in the spatial points located at $x = 1\ m$ and $15\ m$ in the computational domain. There are no obvious differences in these statistical informations for this test case. This reveals that for the considered hydraulic conditions, the numerical diffusion present in some of the numerical methods does not impact the correlation matrices.

Next, numerical results for later time ($t = 4\ s$) to quantify the propagation of uncertainty in the hydraulic model have been presented. Figure 5.8 displays the obtained results at this simulation time. Comparing these results with those shown in Figure 5.5, clearly the uncertainty is very sensitive to the simulation time and therefore to the physical hydraulic itself. This confirms that the uncertainty quantification should be addressed carefully regarding the considered physics

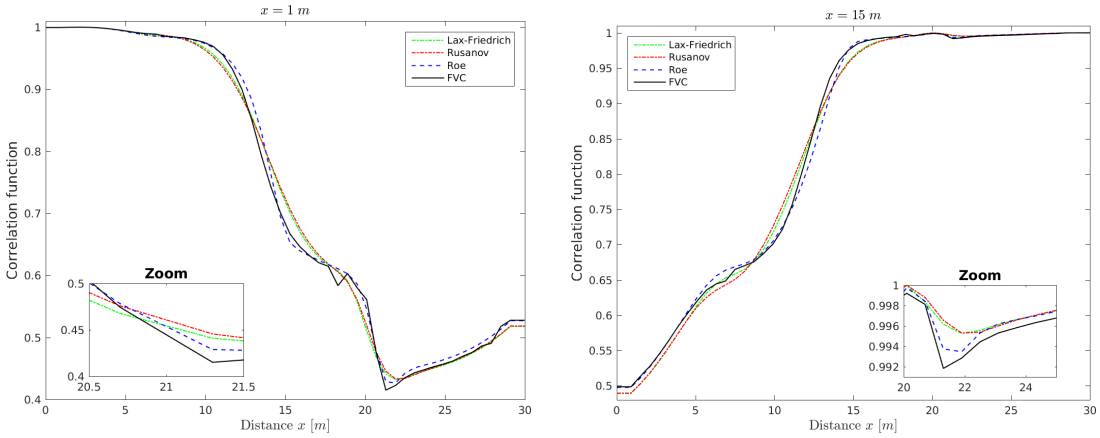

Figure 5.7: Correlation functions for water height at $x = 1\ m$ (left plot) and $x = 15\ m$ (right plot) using Lax-Friedrichs, Roe, Rusanov and FVC methods for the dam-break problem over a flat bed.

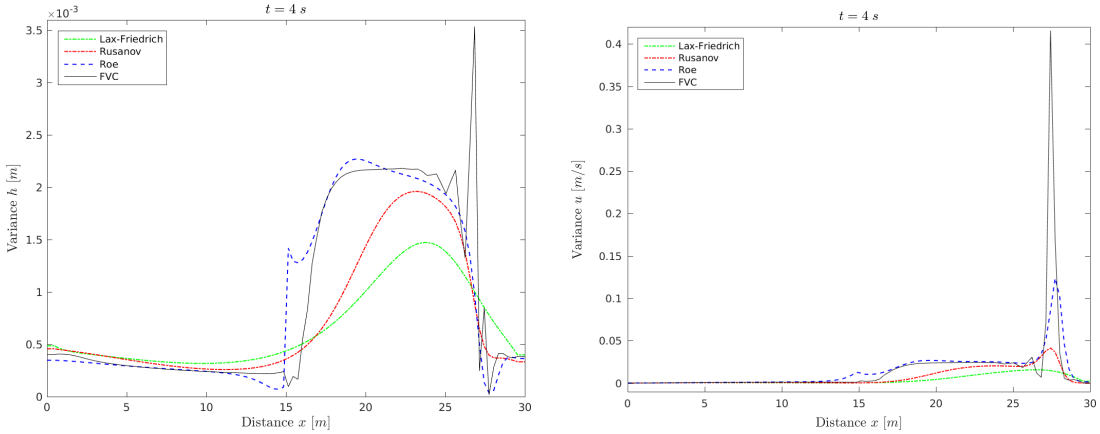

Figure 5.8: Same as Figure 5.5 but at time $t = 4\ s$.

and the results for one simulation time are far to be generalized to another simulation time. Regarding the numerical methods considered in this study, the results are quite similar to the previous case and the high-accurate methods such as FVC and Roe methods, display more uncertainties than the low accurate ones, and this uncertainty tends to propagate spatially within the simulation time. In the contrary, methods with large numerical diffusion such as Rusanov and Lax-Friedrich's methods display less uncertainty and this uncertainty is more localized depending on the physical hydraulics studied.

Next comparing the sensitivity results of uncertainty quantification for two different meshes with 100 and 200 control volumes. Figure 5.9 shows the results of the uncertainty and its sensitivity to the spatial discretization using Rusanov fluxes. Note that refining the mesh will ultimately improve the accuracy of the model and intuitively the uncertainty should decrease. This statement is only true for the upstream region and it is especially highlighted for the water height. However, around the area where the shock occurs, refining the spatial discretization will lead to more uncertainty mainly because of the complex physics occurring in this area. From the obtained results, it is clear that the uncertainty is mainly driven by the numerical diffusion generated by the numerical methods.

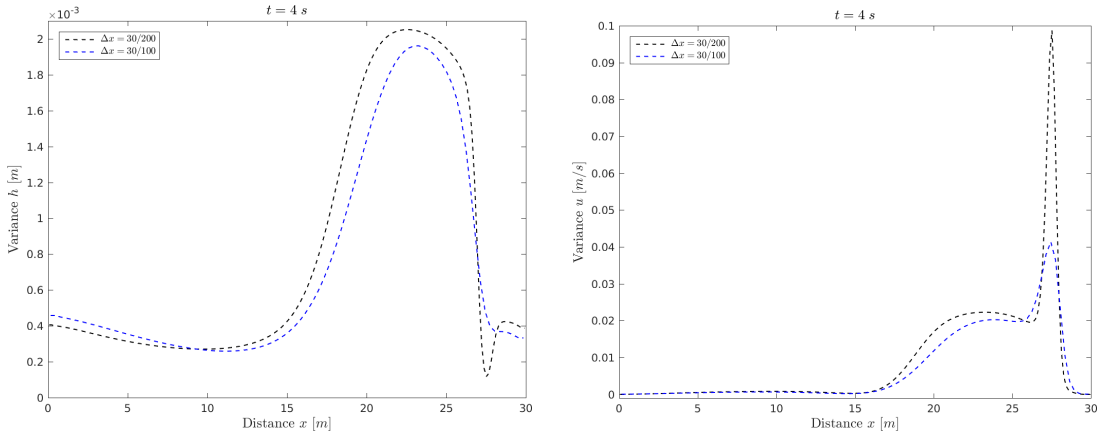

Figure 5.9: Variance solutions obtained using Rusanov method for water height (left plot) and water velocity (right plot) at time $t = 4\ s$ for the dam-break problem over a flat bed using two different meshes with 100 and 200 control volumes.

Table 5.2: Variation coefficients in the bathymetry CV_b and in the Manning CV_m used in our simulations for the dam-break problem over a non-flat bed.

	Test 1	Test 2	Test 3	Test 4
CV_m	0.05	0.01	0.01	0.05
CV_b	0.05	0.05	0.1	0.1

5.4.2 Dam-break problem over non-flat bed

In this test example a dam-break problem over a non-flat bed is considered, the bed is defined as

$$Z(x) = \frac{1}{5}\exp\left(-\frac{(x-15)^2}{20}\right).$$

The aim here is to study effects of the supposed uncertainty in both the bathymetry and the Manning coefficient on the hydraulic state over a non-flat bed. In this example, the Manning coefficient used to equal 0.025, a mesh with 100 control volumes and a simulation time of $t = 2\ s$ have been implemented. Four different tests, as described in Table 5.2, are considered in this study. The aim here is to assess the sensitivity of the uncertainty on the supposed stochasticity in the input. Following the same strategy to quantify the uncertainty as discussed in section 5.2. As described in Table 5.3, two POD modes are enough to represent all the uncertainty displayed by the hydraulic state. In general, a polynomial of degree 3 is able to correctly study the uncertainty as the LOO error ranges from 10^{-11} to 10^{-6} depending on which numerical method is used.

It should be stressed that, since the purpose of the current work is to study the sensitivity of uncertainty in hydraulic calculations to the bathymetric effects. The variance of both water heights and velocity fields using the considered numerical methods and for the cases listed in Table 5.2 are displayed in Figure 5.10. The comments in the previous section are still valid for these simulations here as well. The variance does not significantly change from a numerical

method to another however, near the hydraulic jump, the uncertainty increases and therefore the numerical settings need to be more accurate. It is clear that the variance around the

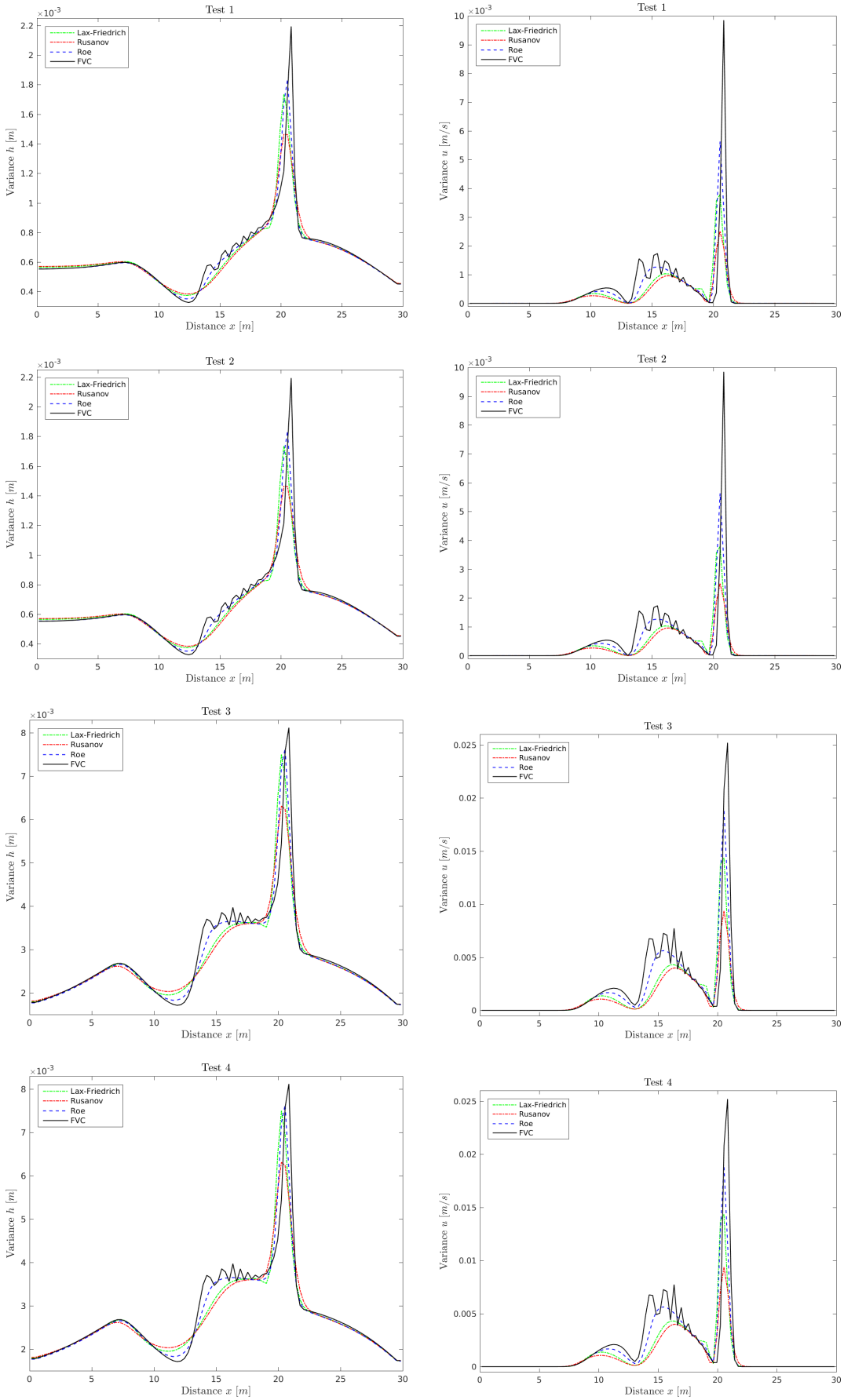

Figure 5.10: Variance solutions for the water height h (left plots) and water velocity u (right plots) obtained for the dam-break problem over a non-flat bed at time $t = 2$ s in the four considered tests listed in Table 5.2.

Table 5.3: Best polynomial degree along with the LOO error for the two POD modes in the water height and water velocity using different numerical schemes for the dam-break problem over a non-flat bed.

	First POD mode			
	FVC	Lax-Friedrichs	Roe	Rusanov
Optimal polynomial degree (h)	3	3	3	3
Optimal polynomial degree (u)	3	3	3	3
LOO error (h)	0.2×10^{-10}	0.5^{-9}	2.3^{-11}	2.2^{-11}
LOO error (u)	10^{-8}	1.6^{-6}	0.8^{-8}	1.1^{-8}
	Second POD mode			
	FVC	Lax-Friedrichs	Roe	Rusanov
Optimal polynomial degree (h)	3	3	3	3
Optimal polynomial degree (u)	3	3	3	3
LOO error (h)	$1.3\ 10^{-10}$	$2.4\ 10^{-9}$	$3.7\ 10^{-11}$	$1.5\ 10^{-11}$
LOO error (u)	$1.1\ 10^{-8}$	$0.6\ 10^{-6}$	$1.6\ 10^{-8}$	$0.7\ 10^{-8}$

hydraulic jump for the FVC method attends the highest values. Figure 5.10 points also out that the hydraulic state is more sensitive to the bathymetry than the Manning coefficient. For instance, the variance of the two last tests in Table 5.2 is four times the variance of the first two tests regardless the uncertainty taken in the Manning coefficient.

5.5 Results for two-layer shallow water flows

Numerical results for the two-layer shallow water equations (5.3) subject to different hydraulic conditions are presented in this section. Considering two test examples including a lock-exchange flow problem and the problem of flow exchange in the Strait of Gibraltar. Focusing mainly on assessing the uncertainty of the hydraulic states composed by the hydraulic layers and two velocities related to these layers with respect to the bathymetry. Notice that, in absence of exact expressions for the eigenvalues in the system (5.3), the Roe method can not be applied and only results obtained using the Lax-Friederich, Rusanov and FVC methods are presented in this section. Since the purpose here is to quantify the uncertainty regarding the numerical method used, a small variation of the bathymetry around the mean is considered to guaranty stability in the considered numerical methods.

5.5.1 Lock-exchange flow problem

In the first example, the lock-exchange problem proposed in [87] is considered. The bottom topography is considered to be a Gaussian function defined as

$$Z(x) = \exp\left(-x^2\right) - 2. \tag{5.39}$$

Table 5.4: Best polynomial degree along with the LOO error for the POD mode in the water height and water velocity using different numerical schemes for the lock-exchange flow problem.

	FVC	Lax-Friedrich's	Rusanov
Optimal polynomial degree (h_1)	2	2	3
Optimal polynomial degree (h_2)	2	2	2
Optimal polynomial degree (u_1)	2	2	2
Optimal polynomial degree (u_2)	2	2	2
LOO error (h_1)	2×10^{-5}	1.9×10^{-5}	8.8×10^{-6}
LOO error (h_2)	5.8×10^{-6}	4.7×10^{-6}	1.2×10^{-8}
LOO error (u_1)	8.8×10^{-6}	10^{-5}	1.6×10^{-8}
LOO error (u_2)	1.1×10^{-5}	1.2×10^{-5}	1.1×10^{-8}

The two layers are initially separated and the lighter water is on the left while the heavier one is on the right *i.e.*,

$$(h_1(x,0), h_2(x,0))^\top = \begin{cases} (-Z(x), 0)^\top, & \text{if} \quad x \leq 0, \\ (0, -Z(x))^\top, & \text{elsewhere,} \end{cases} \qquad u_1(x,0) = u_2(x,0) = 0. \tag{5.40}$$

The density ratio is $\rho_1/\rho_2 = 0.98$, the computational domain is $[-3, 3]$ and the boundary conditions are imposed on the water discharges $q_1 = h_1 u_1$ and $q_2 = h_2 u_2$ as $q_1 = -q_2$ at each end of the domain. In this hydraulic problem, the heavier water propagates to the left while the lighter one moves to the right. The solution is expected to converge to a smooth steady state and computing the numerical steady-state solution on a mesh with 100 control volumes. Following the same methodology described in section 5.1, the uncertainty of the hydraulic state is quantified. For this flow problem, first the assessment of the surrogate model is performed. The obtained results show that given the uncertainty of the bathymetry, only one POD mode is needed. Indeed, the perturbation in the bathymetry highly affects the numerical stability and therefore, the domain of randomness of this parameter has been narrowed which would also translate to a narrow domain of uncertainty in the hydraulic state. Table 5.4 summarizes the results of the surrogate model built for each component of the hydraulic state and for each numerical method. Here, a polynomial degree of 2 is enough to correctly estimate the uncertainty and the LOO error ranges from 10^{-8} to 10^{-5}. This makes the proposed surrogate model very reliable for the purpose of uncertainty quantification.
Figure 5.11 illustrates the mean values of the water free-surface and water interface corresponding to the two water layers whereas, Figure 5.12 reports the mean value of the water velocities for the three numerical methods considered in the present study. It is clear that there are no large differences between the results obtained for the water free-surface solutions. For the water velocities, the Rusanov method is underestimating the mean solutions compared to the Lax-Friedrich's and FVC methods, but the differences are also very small. It is also worth noting that it could be corrected using observations. Figure 5.13 and Figure 5.14 display the results obtained for the variance in water height and water velocity, respectively. In contrary to the mean value, these results are very different. It is clear that the Lax-Friedrich's method generates the largest amount of the uncertainty compared to the other methods. This large

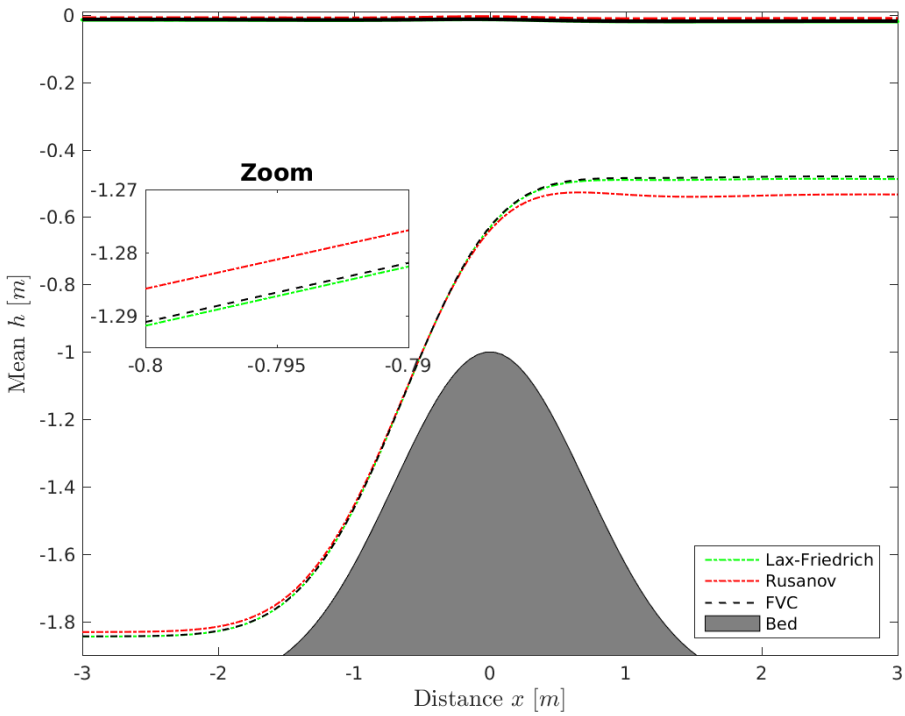

Figure 5.11: Mean value of the hydraulic state for the lock-exchange flow problem.

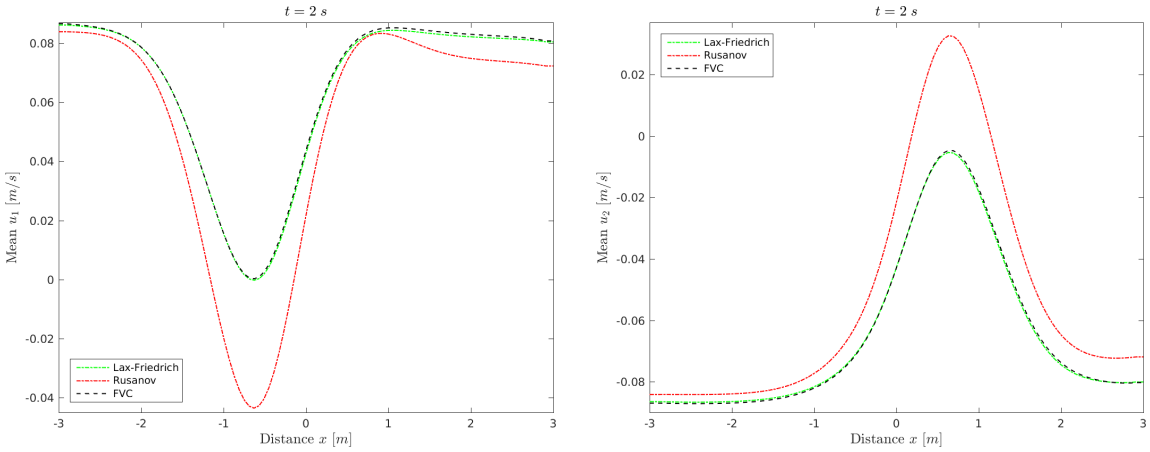

Figure 5.12: Mean values for water velocity u_1 (left plot) and u_2 (right plot) for the lock-exchange flow problem.

amount of uncertainty is mainly driven by the model itself as the numerical diffusion in this case is also very important compared to the single-layer shallow water model. The hydraulic calculations using the FVC method are also very uncertain compared to the Rusanov method. However, the uncertainty in this case is explained by the uncertainty of the bathymetry rather than the model itself. This means that the choice of the accurate numerical method to be used for the operational analysis should be accurate enough to take into account the complexity of the physical hydraulics but its uncertainty should not exceed some amounts that will make this error uncorrectable even with the use of observational data.

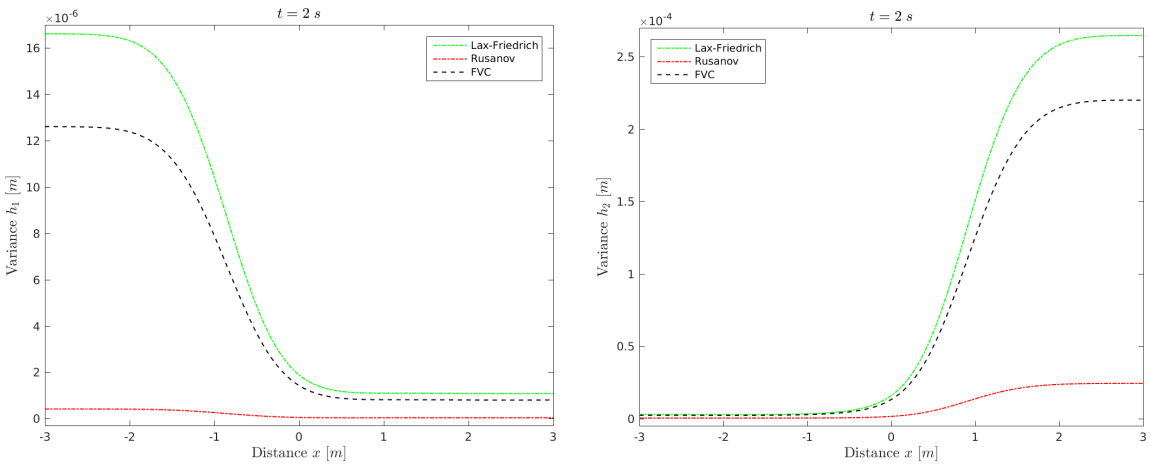

Figure 5.13: Variance in water height h_1 (left plot) and h_2 (right plot) for the lock-exchange flow problem.

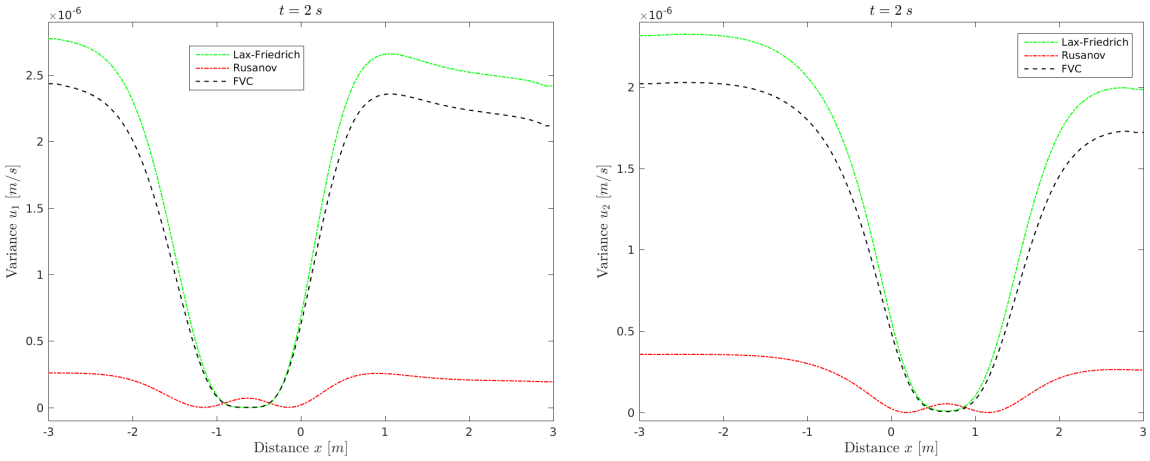

Figure 5.14: Variance in water velocity u_1 (left plot) and u_2 (right plot) for the lock-exchange flow problem.

5.5.2 Flow exchange through the Strait of Gibraltar

The last example consists of solving the problem of flow exchange through the Strait of Gibraltar. This hydraulic problem is selected because it presents a real example of two-layer shallow water flows for two major reasons. Firstly, the domain of the Strait of Gibraltar is a large-scale domain including high gradients of the bathymetry and well-defined shelf regions. Secondly, the Strait contains two water bodies with different densities, which present a challenge in the shallow water modelling. Indeed, the basic Oceanic circulation in the Strait of Gibraltar consists of an upper layer of cold, fresh surface Atlantic water (with density $\rho_1 = 1027\ kg/m^3$) and an opposite deep current of warmer and salty outflowing Mediterranean water (with density $\rho_2 = 1029\ kg/m^3$), compare for example [104]. A schematic map of the Strait of Gibraltar along with relevant locations is depicted in the left plot of Figure 5.16. The system is bounded to the north and south by the Iberian and African continental forelands, respectively, and to the west and east by the Atlantic Ocean and the Mediterranean sea. In geographical coordinates, the Strait of Gibraltar is $35^o45'$ to $36^o15'$ N latitude and $5^o15'$ to $6^o05'$ W longitude. Here, we consider a one-dimensional cross-section

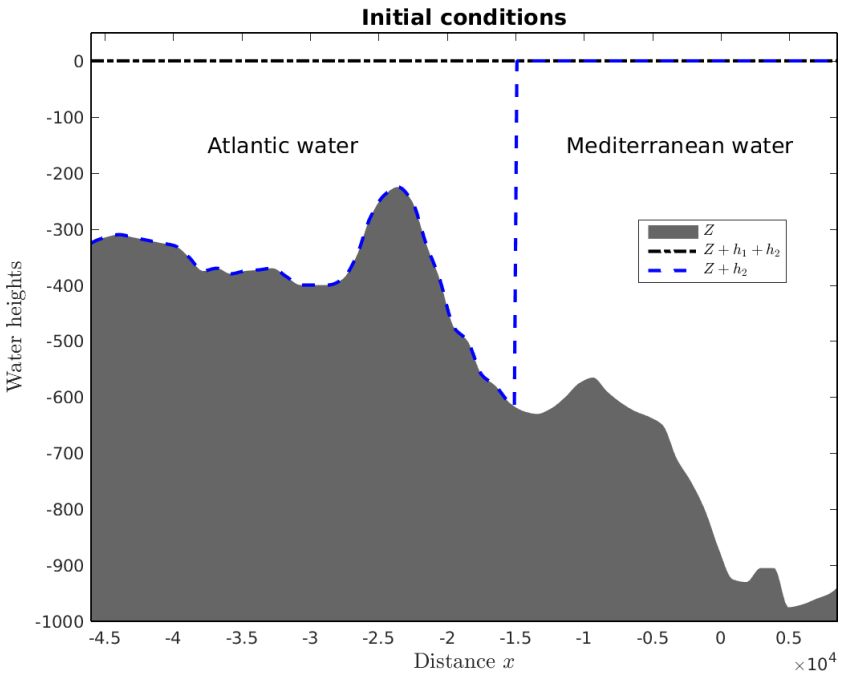

Figure 5.15: Initial conditions for the flow exchange through the Strait of Gibraltar.

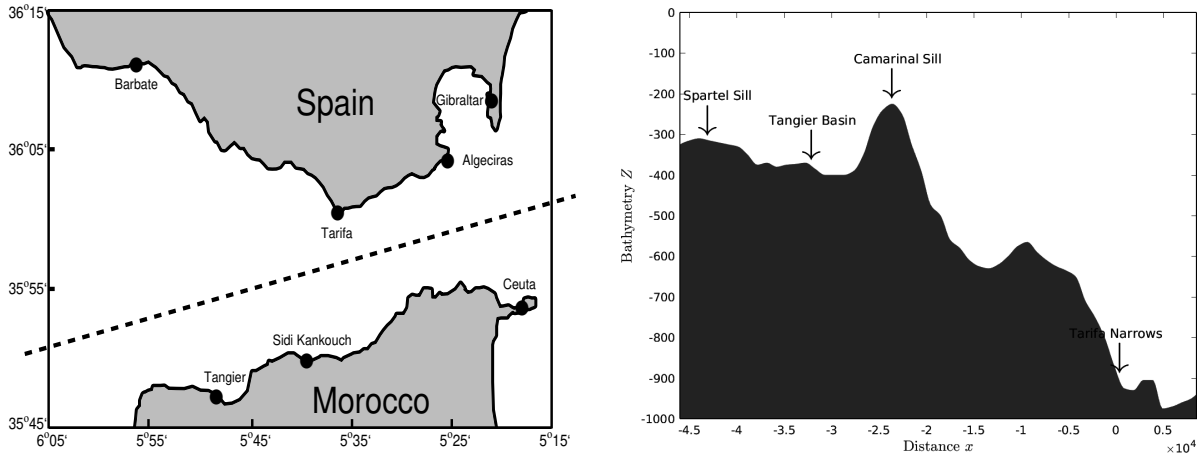

Figure 5.16: Schematic map of the Strait of Gibraltar along with relevant locations (left plot) and the bathymetry used in our simulations (right plot).

along the Strait (obtained by a longitudinal section along the dashed line in the left plot of Figure 5.16). The computational domain and the associated bathymetry are displayed in the right plot of Figure 5.16. This restricted domain has also been considered in [124, 105] among others. This hydraulic problem was experimentally studied in [51] and numerically solved in [77] using a semi-Lagrangian scheme and in [124] using a discontinuous Galerkin method. The flow parameters of this experiment are those used in [51, 77, 124]. Thus, an artificial dam is included in the Strait separating the water bodies from the Atlantic Ocean and the Mediterranean sea. On the boundaries, the ratio between the water discharges is set to 1, *i.e.*, $q_1 = -q_2$ at each boundary node. Here, the computational domain is covered with 100 control volumes and Figure 5.15 exhibits the initial water heights h_1 and h_2. The uncertainty displayed by the three numerical methods used to identify the flow in this region is evaluated.

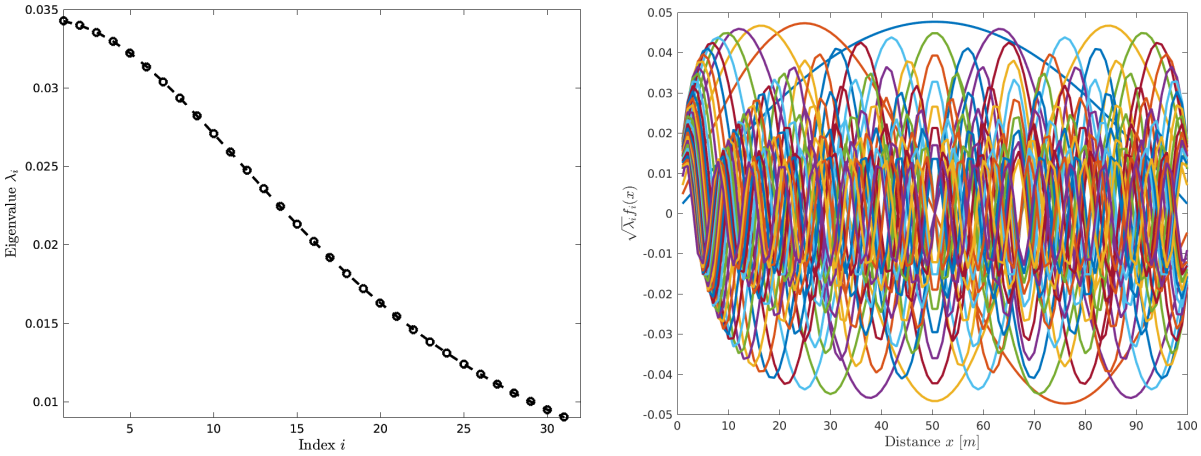

Figure 5.17: Eigenvalues (left plot) and associated eigenfunctions (right plot) used in the KL decomposition to sample the bathyemtric field over the Strait of Gibraltar using an exponential Kernel with a correlation length of 10 km.

Table 5.5: Best polynomial degree along with the LOO error for the POD mode in the hydraulic states using different numerical schemes for the problem of flow exchange through the Strait of Gibraltar.

	FVC	Lax-Friedrich's	Rusanov
Optimal polynomial degree (h_1)	3	3	3
Optimal polynomial degree (h_2)	3	3	3
Optimal polynomial degree (u_1)	3	3	3
Optimal polynomial degree (u_2)	3	3	3
LOO error (h_1)	3.2×10^{-6}	2.9×10^{-6}	3.1×10^{-6}
LOO error (h_2)	2.6×10^{-5}	2.1×10^{-5}	2.3×10^{-5}
LOO error (u_1)	1.9×10^{-7}	1.5×10^{-7}	1.5×10^{-7}
LOO error (u_2)	2.1×10^{-7}	1.7×10^{-5}	1.75×10^{-7}

The aim is to quantify the uncertainty generated by an error in the reconstruction of the Strait bathymetry using the three different numerical methods. First, a KL decomposition is carried out in order to represent the stochastic aspect of the bathymetric field. The spatial correlation matrix was supposed to have an exponential Kernel as in [261] and the correlation length is set to a value of 10 km. Figure 5.17 displays the results of this decomposition. It is evident that the stochastic dimension of this hydraulic problem is very high as more than 30 modes are needed for the LOO error to be under the threshold error of 10^{-2}. This is mainly attributed to the size of the physical domain used in the modelling of flow exchange through the Strait of Gibraltar.

Following the methodology discussed in Section 5.3, the fields of water height and velocity are decomposed using a POD. Then, the uncertainty is supposed to be described by the eigenvalues of the POD approach. For the considered hydraulic conditions and given the threshold used in the POD, only one mode is enough to represent correctly the uncertainty. Again, the considered variance in the bathymetry has been selected reasonably small in order to maintain

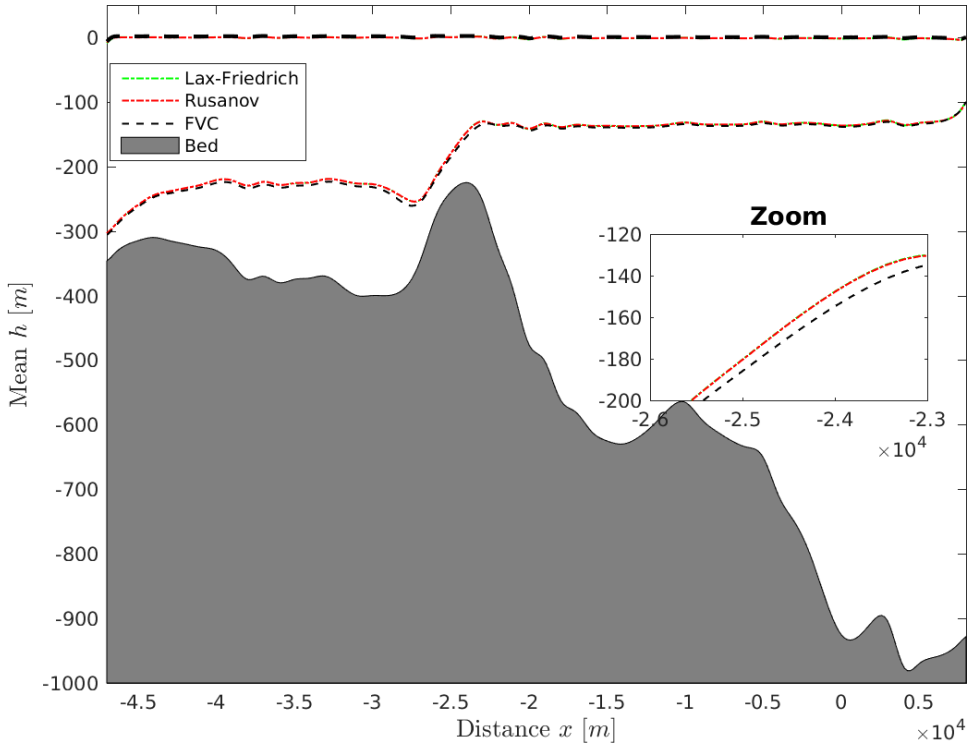

Figure 5.18: Mean hydraulics for the problem of flow exchange through the Strait of Gibraltar.

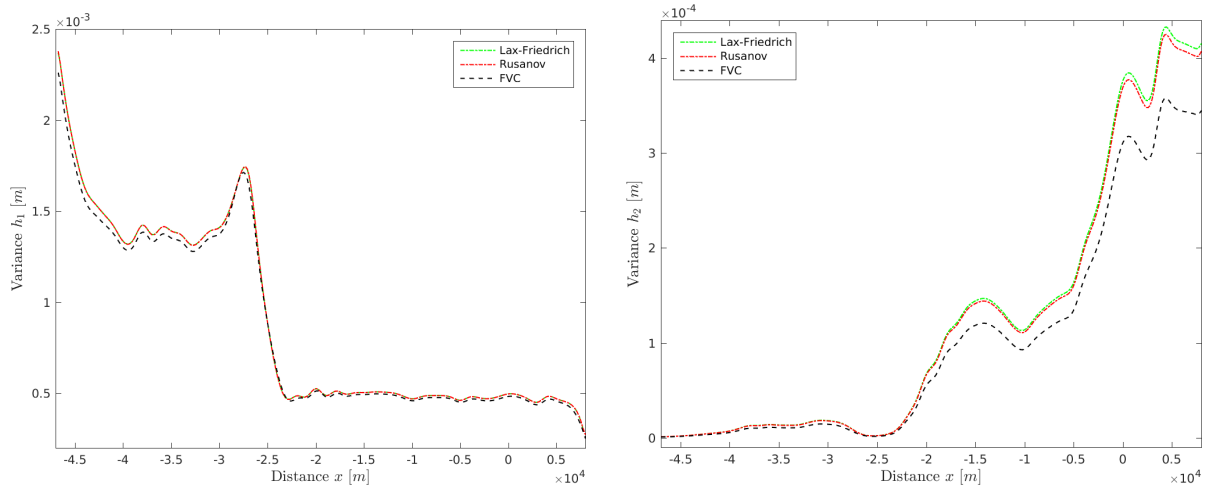

Figure 5.19: Variance in water height h_1 (left plot) and h_2 (right plot) for the problem of flow exchange through the Strait of Gibraltar.

the stability of the numerical schemes. Table 5.5 describes the assessment of the PCE for this mode in all the three numerical methods used in this study. Overall, a polynomial degree of 3 is able to correctly resolve the uncertainty with an error estimated to be less than 10^{-5} for the four fields considered in a two-layer shallow water model and for the three numerical methods considered for its numerical simulations.

Figure 5.18 represents the mean fields of the water free-surface h_1 and the water interface h_2 obtained at the steady-state time. As can be seen, the Mediterranean water moves downstream and exits the Strait resulting in the formation of strong and weak shocks. Under actual flow conditions, it is clear that a hydraulic jump is detected in the water interface near the Camarinal

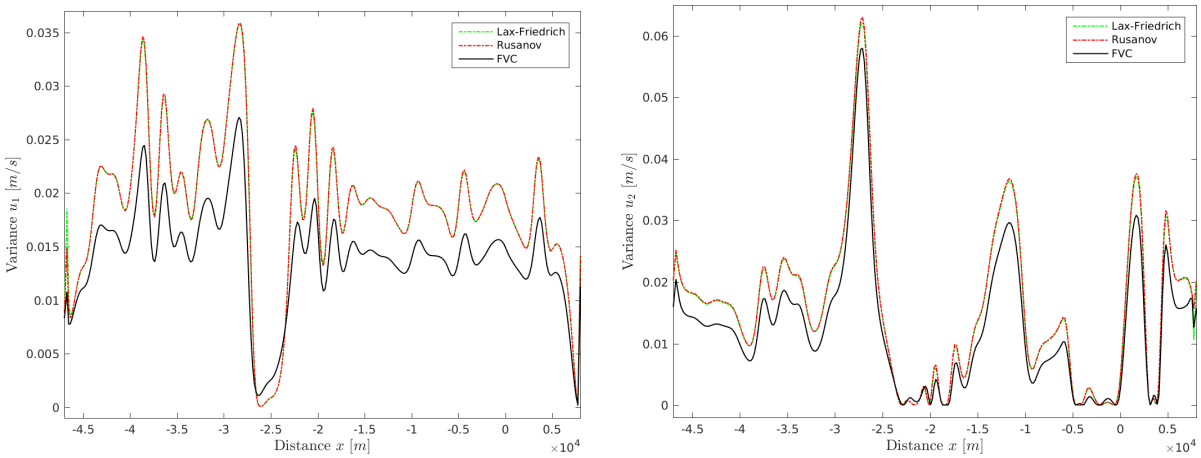

Figure 5.20: Variance in water velocity u_1 (left plot) and u_2 (right plot) for the problem of flow exchange through the Strait of Gibraltar.

Sill. The exchange discharge predicted by this method is $q_1 = -q_2 = 0.856\ sv$. There is an excellent agreement between the numerical results obtained by the considered methods and those from previous studies reported in [51, 77, 124]. It is worth remarking that the exact solutions to these examples are not available, but the computed solutions using the proposed methods seem to converge to the physically relevant solutions in all selected test cases. The numerical methods used in this case capture the shock accurately and do not diffuse the fronts or exhibits oscillations near the steep gradients in the computational domain. Overall, there is a good convergence between the results of the three numerical methods considered for this exchange flow problem. This agreement is also observed in the mean velocity field of the upper layer for the three numerical methods. However, for the water interface, there is a slight difference between the mean fields obtained using the FVC method and those obtained using the other considered numerical methods for this flow problem. These discrepancies are also observed in the variance fields, see Figure 5.19 and Figure 5.20. Hence, the FVC method being numerically more accurate, it displays less uncertainty than the diffusive methods. This case example demonstrates that when the physical hydraulics is very complex, the use of a highly accurate numerical method is necessary and the uncertainty quantified by this method is expected to be well predicted.

5.6 Conclusions

In the current study, the uncertainty quantification in a class of finite volume methods for free-surface flows has been examined. The models consist of both single-layer and two-layer shallow water equations with stochastic bathymetry and Manning roughness coefficients. This methodology allows to overcome many known challenges in the uncertainty quantification for computational hydraulics and it combines: (i) a Karhunen-Loève decomposition to sample stochastic processes independently of the required number of control volumes in the mesh to achieve reasonable accuracy, (ii) a sparse polynomial chaos expansion to overcome the well known problem of curse of dimensionality risen by the Karhunen-Loève decomposition at a reasonable computational cost, and (iii) a proper orthogonal decomposition for hydraulic states to increase further the efficiency of the proposed method. In order to reduce the number of samples required for the uncertainty quantification in these methods, the proper orthogonal

decomposition method is combined with the polynomial chaos expansions for efficient resolution of complex hydraulic problems with large numbers of random variables. Numerical results are presented for dam-break problems for single-layer models and for exchange flows for two-layer models including the problem of flow exchange through the Strait of Gibraltar. It has been shown that the uncertainty in the hydraulic calculations is very sensitive to both the mathematical model and the numerical methods selected for their approximations. Indeed, many works have been devoted in the literature to develop advanced numerical methods to improve the accuracy of the models to meet with the required physical hydraulics. However, the cost of this accuracy lies on the poor quantification of uncertainty in the hydraulic models. In addition, the simulation time has also been highlighted to be a subject of uncertainty such that the uncertainty tends to increase with the simulation time. Therefore, the numerical method should carefully be chosen and according to the hydraulic problem under consideration.

Efforts on correcting the bathymetric fields would be very relevant to reduce the uncertainty of such models. In the case of two-layer shallow water flows such as flow through the Strait of Gibraltar, highly accurate finite volume schemes are shown to be the best numerical tools to quantify uncertainties in their involved parameters. Although, we have studied only the case of one-dimensional problems in hydraulics, the extension to two-dimensional problems would be an encouraging next step and requires an in-depth study on finite volume methods for solving stochastic shallow water equations in unstructured meshes. In the present work, the impact of the stochasticity either in the Manning coefficient and/or in the bed bathymetry on the uncertainty in the computed hydraulic states has been assessed. The obtained results demonstrate that the hydraulic states are more sensitive to the uncertain bathymetry than the Manning coefficient. Therefore, efforts on correcting the bathymetric fields would be more relevant than the friction coefficients to reduce the uncertainty. In case of two-layer shallow water flows such as flow through the Strait of Gibraltar, highly accurate finite volume schemes are shown to be the best numerical tools to quantify uncertainties in their involved parameters. The obtained results demonstrated that in some hydraulic applications, highly accurate numerical method yields an increase in its uncertainty and makes it very demanding to use in an operational manner with measured data from the field. This method can be extended to two-dimensional shallow water flows directly and with no major corrections to the prescribed procedure.

Chapter 6

Efficient quantification of uncertainties in multi-layer Shallow Water Flows with Mass Exchange

Modelling water flows at places such as Mediterranean sea is of utmost importance, especially at the Strait of Gibraltar. At this place, an exchange between a denser water from the Atlantic Ocean and a fresher water from the Mediterranean sea occurs. Moreover, under the impact of the topography and wind forces, the hydrodynamics can be very complex [139]. Therefore, monitoring activities such as maritime transportations, management of pollution spills [106] and fishery [85] could be very challenging. Numerical modelling of such hydrodynamics would require the use of the full three-dimensional Navier-Stokes equations. As many studies reported, the flow is mainly driven by the baroclinic modes of variability. The transport and the occurrence of some eddies and small scale surface waves are driven by the longitudinal gradient of pressure, temperature and density. These hydraulic features can not be captured using the standard shallow water equations. However, with the introduction of multi-layer shallow water equations, the use of computationally efficient numerical models is possible. This class of multi-layer shallow water equations avoid the computationally demanding methods needed to solve the three-dimensional Navier-Stokes equations, but at the same time they provide stratified flow velocities since the pressure distribution is still assumed to be hydrostatic. In the current study, the free-surface flow problem is approximated as a layered system made of multiple shallow water systems of different water heights but coupled through mass-exchange terms between the embedded layers. Recently, multi-layer shallow water equations have been subject of various research studies [87, 81, 124] and have been used for modelling a variety of free-surface flows where water flows interact with the bed geometry and wind stresses. While general efforts have been concentrated to present efficient numerical tools that allow to solve the deterministic problem, to the best of our knowledge, uncertainty quantification of these models have not been considered. In the present work, we consider these methods to model the exchange flow occurring at Strait of Gibraltar and quantify the uncertainty of the numerical response. Especially that many heterogeneous observational data are available at this Strait based on GPS, radar, remote sensing and in-situ measurements [139, 126, 111]. Furthermore, it has already been established that monitoring this area using numerical models coupled with altimetry observations could be very effective using data assimilation methods [64].

When using numerical algorithms such as data assimilation, the forecast of the model is predicted based on a reduced dynamic model uncertainty. Therefore, uncertainty is ubiquitous to

the results of these simulations for different reasons, see for example [201]. One of the major source of uncertainty especially in hydraulic computations comes from calibration [253, 146]. In fact, friction coefficient is a proxy that represents the hydraulic energy dissipation. This occurs in a molecular scale. Therefore, in fluid dynamic computations, it is generally estimated using empirical equations with some coefficients to be estimated. Moreover, the use of multi-layer shallow water equations introduces a viscosity coefficient which model the numerous exchange of informations between layers. This coefficient is purely used for modelling purposes and in practice, these parameters are estimated by means of calibration (or inverse problem) where data for a specific event are used, see for example [142, 214, 127]. Indeed, exact estimations are not possible for all ranges of variation in hydraulics for which modelling uncertainties is required. Many studies showed that uncertainty in the estimation of the mentioned parameters can lead to high uncertainty in the hydraulic states for some flow configuration [208, 80, 46, 113]. Furthermore there is also a natural variability due to the imperfect description of boundary conditions which lead to stochastic uncertainties [203]. This has been demonstrated in the case of hydraulic simulations over unknown topography [72]. For instance, the description of the Strait topography could not be known everywhere. This lack of information due to measurement limitations could lead to uncertain hydraulic simulation, as reported by [60]. With the high availability of remote sensing data, the possibility to reduce the uncertainty of hydraulic simulation propagated from uncertain bathymetry is now possible [261, 22].

One major problem when tackling uncertainty quantification (UQ) with hydraulic computations is the *curse of dimensionality*. The topography of the Strait, the river or the lake is often presented as a stochastic process regarding its space dependency. Moreover, the computed results for the water velocity and water height also depend on the space and time. Therefore, using classical methods for uncertainty quantification could be very time consuming. Note that in uncertainty quantification, it is very common to use surrogate models also known as meta-models or response surface. Their purpose is to mimic the behavior of the true model while being less time consuming. Such methodology was successfully used in the context of hydraulic computations using polynomial chaos expansion [80] or Kriging [208]. However, these studies in [80, 208] have considered only single value parameters (random variables) such as Manning Coefficient to be responsible for uncertainty in the model simulation, see for example [108] among others. The bathymetry, given its space dependency, has rarely been considered for an uncertainty quantification problem. In fact one need to reduce the dimensionality of the field before using any surrogate model in [99, 166] as the problem of dimensionality could be very challenging when using surrogate models. This is mainly the reason why only few works have been dedicated to quantify its uncertainty [122]. In the present work we consider a Karhunen-Loéve decomposition in order to reduce the dimensionality of the bathymetry. This method relies on a spectral decomposition of the spatial correlation matrix of the bathymetry to approximate the real stochastic process in the mean-square sense. Another advantage of this method, resides in the fact that it is very easy to sample once the decomposition is achieved. This method has been widely used in the context of random process, see [212] for a review. Reducing the space of the input variables makes it very easy to build surrogate models. In the present work, we consider the polynomial chaos expansion, given its success rate for quantifying the uncertainty in hydraulic simulations, see [108, 78, 180]. Furthermore, in order to reduce the dimensionality of the output results (water height and velocity in each layer) we use Proper Orthogonal Decomposition (POD). This method avoids building a single surrogate model for each numerical component of the vector. Instead, a spectral decomposition is carried out and

we suppose that the eigenvalues yield the uncertainty that ought to be propagated. Therefore, the surrogate model is built only on the eigenvalues. Such methods have been successfully used in uncertainty quantification since they allow to reduce the output dimension and yield some high accuracy given the uncertainty quantification, see for example [197, 79].

In the present study, we evaluate the uncertainty of the hydraulic states such as the water height and the water velocity as responses from the bathymetric forces including bed topography, Manning coefficient, wind friction and viscosity between layers. The uncertainty is quantified for numerical solution of the multi-layer shallow water equations over three different test cases. The first case related to the dam-break problem over a flat bed. The aim of this case is to assess the surrogate model for uncertainty quantification and compare between the results in uncertainty over three numerical methods. The second example considers a wind driven circulation in a bounded lake. The purpose of this case is to assess the impact of the number of layers in the multi-layer model on the uncertainty. Finally the last case study the uncertainty quantification in the real case of Strait of Gibraltar. The purpose here is to assess the UQ methodology over a real complex case. Moreover, as the sensitivity analysis of the uncertainty towards each parameter is performed, especially in locations where data measurements are available. The rest of this paper is organized as follows. The equations for multi-layer shallow water flows are presented in Section 6.1. The formulation of the finite volume modified method of characteristics for the numerical solution of multi-layer models is also presented in this section. The general methodology used to address the uncertainty quantification problem is described in section 6.3. Section 6.4 is devoted to numerical results for several test examples for free-surface water flows over stochastic topography. Our new approach is shown to enjoy the expected accuracy as well as the robustness. Section 6.5 contains concluding remarks.

6.1 Multi-layer shallow water equations for free-surface water flows

In the current work we consider M layers of water bodies bounded vertically by a fixed bottom topography and a free-surface as illustrated in Figure 6.1. Based on the vertical P_0 discretization of the horizontal velocity, the equations for three-dimensional hydrostatic incompressible Navier-Stokes equations with free-surface yield the so-called multi-layer shallow water equations, see [15, 14] for detailed derivations of these equations. The governing equations are similar to the single-layer shallow water equations with additional terms for exchanging momentum between the layers formulated as

$$\begin{aligned} \frac{\partial H}{\partial t} + \sum_{\alpha=1}^{M} \frac{\partial}{\partial x}\left(l_\alpha H u_\alpha\right) &= 0, \\ \frac{\partial}{\partial t}\left(l_\alpha H u_\alpha\right) + \frac{\partial}{\partial x}\left(l_\alpha H u_\alpha^2 + \frac{1}{2} g l_\alpha H^2\right) &= -g l_\alpha H \frac{\partial z}{\partial x} + \mathcal{S}_\alpha^u + \mathcal{S}_\alpha^\mu + \mathcal{S}_\alpha^b + \mathcal{S}_\alpha^w, \end{aligned} \tag{6.1}$$

where $z(x)$ is the bed topography, $u_\alpha(t,x)$ the local water velocity for the αth layer, g the gravitational acceleration, $H(t,x)$ the water height of the whole flow system and l_α denotes the relative size of the αth layer with

$$l_\alpha > 0, \qquad \sum_{\alpha=1}^{M} l_\alpha = 1.$$

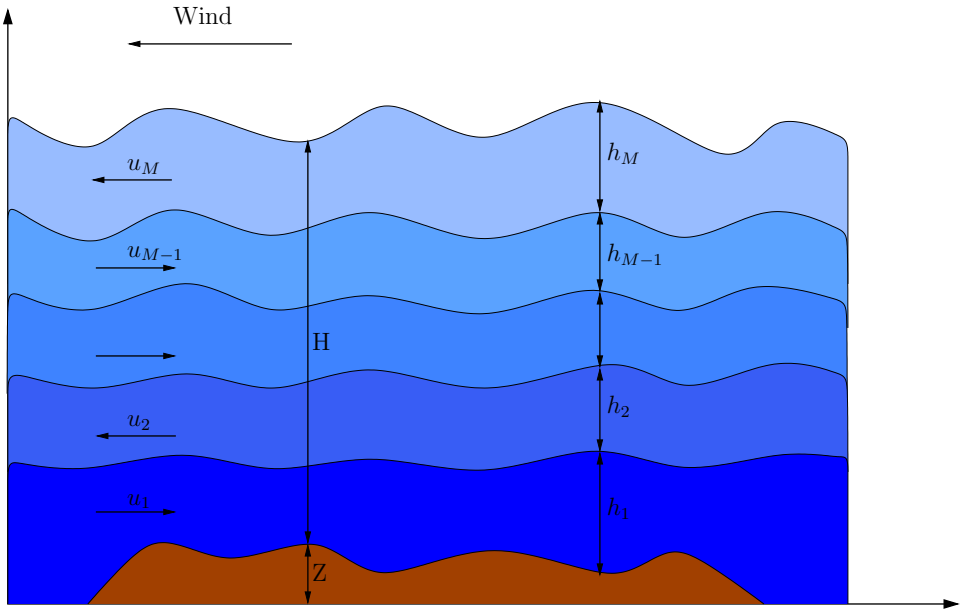

Figure 6.1: Illustration of the multi-layer shallow water system.

The water height $h_\alpha(t,x)$ of the αth layer is defined as a fraction of the total water height as

$$h_\alpha = l_\alpha H, \qquad \alpha = 1,\ldots,M.$$

In (6.1), the source term $\mathcal{S}_\alpha^u$ is related to the momentum exchanges between the layers which is defined through the vertical P_0 discretization of the flow as

$$\mathcal{S}_\alpha^u = u_{\alpha+1/2}G_{\alpha+1/2} - u_{\alpha-1/2}G_{\alpha-1/2}, \tag{6.2}$$

with the mass exchange terms $G_{\alpha-1/2}$ and $G_{\alpha+1/2}$ are calculated by

$$G_{\alpha-1/2} = \begin{cases} 0, & \text{if} \quad \alpha = 1, \\ \displaystyle\sum_{\beta=1}^{\alpha}\left(\frac{\partial\left(h_\beta u_\beta\right)}{\partial x} - l_\beta \sum_{\gamma=1}^{M}\frac{\partial\left(h_\gamma u_\gamma\right)}{\partial x}\right), & \text{if} \quad \alpha = 2,3\ldots,M, \end{cases} \tag{6.3}$$

$$G_{\alpha+1/2} = \begin{cases} \displaystyle\sum_{\beta=1}^{\alpha}\left(\frac{\partial\left(h_\beta u_\beta\right)}{\partial x} - l_\beta \sum_{\gamma=1}^{M}\frac{\partial\left(h_\gamma u_\gamma\right)}{\partial x}\right), & \text{if} \quad \alpha = 1,2,\ldots,M-1, \\ 0, & \text{if} \quad \alpha = M, \end{cases} \tag{6.4}$$

and the interface velocities $u_{\alpha-1/2}$ and $u_{\alpha+1/2}$ are evaluated using an upwind procedure following the sign of the mass exchange terms (6.3) and (6.4) as

$$u_{\alpha-1/2} = \begin{cases} u_{\alpha-1}, & \text{if} \quad G_{\alpha-1/2} \geq 0, \\ u_\alpha, & \text{if} \quad G_{\alpha-1/2} < 0. \end{cases} \qquad u_{\alpha+1/2} = \begin{cases} u_\alpha, & \text{if} \quad G_{\alpha+1/2} \geq 0, \\ u_{\alpha+1}, & \text{if} \quad G_{\alpha+1/2} < 0. \end{cases} \tag{6.5}$$

The vertical kinematic eddy viscosity terms $\mathcal{S}_\alpha^\mu$ in (6.1) account for the friction between the neighboring layers as

$$\mathcal{S}_\alpha^\mu = \begin{cases} 2\nu \dfrac{u_2 - u_1}{(l_2 + l_1)\, H}, & \text{if} \quad \alpha = 1, \\ 2\nu \dfrac{u_{\alpha+1} - u_\alpha}{(l_{\alpha+1} + l_\alpha)\, H} - 2\nu \dfrac{u_\alpha - u_{\alpha-1}}{(l_\alpha + l_{\alpha-1})\, H}, & \text{if} \quad \alpha = 2, 3, \ldots, M-1, \\ -2\nu \dfrac{u_M - u_{M-1}}{(l_M + l_{M-1})\, H}, & \text{if} \quad \alpha = M, \end{cases} \tag{6.6}$$

where ν is the eddy viscosity. The external friction terms $\mathcal{S}_\alpha^b$ and $\mathcal{S}_\alpha^w$ in (6.1) are defined by

$$\mathcal{S}_\alpha^b = \begin{cases} -g n_b^2 \dfrac{u_1 \, |u_1|}{H^{1/3}}, & \text{if} \quad \alpha = 1, \\ 0, & \text{if} \quad \alpha = 2, 3, \ldots, M, \end{cases} \qquad \mathcal{S}_\alpha^w = \begin{cases} 0, & \text{if} \quad \alpha = 1, 2, \ldots, M-1, \\ \sigma_s^2 \rho_a \dfrac{w \, |w|}{H}, & \text{if} \quad \alpha = M, \end{cases} \tag{6.7}$$

with n_b is the Manning roughness coefficient at the bed, w the wind velocity at 10 m above the water surface, σ_s^2 the wind stress coefficient and ρ_a the air density. Note that the internal friction term $\mathcal{S}_\alpha^\mu$ models the friction between neighboring layers in (6.1), the bed-friction forcing term $\mathcal{S}_\alpha^b$ is acting only on the lower layer, and the wind-driven forcing term $\mathcal{S}_\alpha^w$ is acting only on the upper layer. For simplicity in the presentation, the multi-layer shallow water equations (6.1) are reformulated in a compact vector form as

$$\frac{\partial \mathbf{W}}{\partial t} + \frac{\partial \mathbf{F}(\mathbf{W})}{\partial x} = \mathbf{Q}(\mathbf{W}) + \mathbf{R}(\mathbf{W}), \tag{6.8}$$

where $\mathbf{W}$ is the vector of conserved variables, $\mathbf{F}$ the vector of flux functions, $\mathbf{Q}$ and $\mathbf{R}$ are the vectors of source terms

$$\mathbf{W} = \begin{pmatrix} H \\ Hu_1 \\ Hu_2 \\ \vdots \\ Hu_M \end{pmatrix}, \qquad \mathbf{F}(\mathbf{W}) = \begin{pmatrix} \displaystyle\sum_{\alpha=1}^{M} l_\alpha H u_\alpha \\ Hu_1^2 + \dfrac{1}{2} g H^2 \\ Hu_2^2 + \dfrac{1}{2} g H^2 \\ \vdots \\ Hu_M^2 + \dfrac{1}{2} g H^2 \end{pmatrix}, \qquad \mathbf{Q}(\mathbf{W}) = \begin{pmatrix} 0 \\ -gH \dfrac{\partial z}{\partial x} \\ -gH \dfrac{\partial z}{\partial x} \\ \vdots \\ -gH \dfrac{\partial z}{\partial x} \end{pmatrix},$$

$$\mathbf{R}(\mathbf{W}) = \begin{pmatrix} 0 \\ \frac{1}{l_1}\left(u_{3/2}G_{3/2} - gn_b^2\frac{u_1\,|u_1|}{H^{1/3}} + 2\nu\frac{u_2-u_1}{(l_2+l_1)\,H}\right) \\ \frac{1}{l_2}\left(u_{5/2}G_{5/2} - u_{3/2}G_{3/2} + 2\nu\frac{u_3-u_2}{(l_3+l_2)\,H} - 2\nu\frac{u_2-u_1}{(l_2+l_1)\,H}\right) \\ \vdots \\ \frac{1}{l_{M-1}}\left(u_{M-1/2}G_{M-1/2} - u_{M-3/2}G_{M-3/2} + 2\nu\frac{u_M-u_{M-1}}{(l_M+l_{M-1})\,H} - 2\nu\frac{u_{M-1}-u_{M-2}}{(l_{M-1}+l_{M-2})\,H}\right) \\ \frac{1}{l_M}\left(-u_{M-1/2}G_{M-1/2} - \sigma^2\rho_a\frac{w\,|w|}{H} - 2\nu\frac{u_M-u_{M-1}}{(l_M+l_{M-1})\,H}\right) \end{pmatrix}.$$

It should be stressed that it is not straightforward to derive the exact expressions of the $(M+1)$ eigenvalues of (6.8) and it is also not evident that the system (6.8) is hyperbolic as its associated eigenvalues may become complex. In this situation, the multi-layer shallow water equations (6.8) yield the so-called Kelvin-Helmholtz instability at the interface separating the water layers. In the current study, the asymptotic estimation of these eigenvalues reported in [15] is used to adjust the timestep size in the numerical simulations. Thus, we suppose that all the velocities u_α are closed to the mean velocity u and a first-order approximation of the two barotropic eigenvalues gives

$$\lambda_{ext}^{\pm} = u_m \pm \sqrt{g\sum_{\alpha=1}^{M} h_\alpha} + \mathcal{O}\left(|u_\beta - u|^2\right)_{\beta=1,\dots,M}, \qquad u_m = \frac{\sum_{\alpha=1}^{M} h_\alpha u_\alpha}{\sum_{\alpha=1}^{M} h_\alpha}, \tag{6.9}$$

and a zeroth-order approximation of the $2(M-1)$ barotropic eigenvalues associated with $(M-1)$ interfaces gives

$$\lambda_{int}^{\pm,\alpha+\frac{1}{2}} = u \pm \sqrt{\frac{1}{2}g\sum_{\alpha=1}^{M} h_\alpha} + \mathcal{O}\left(|u_\beta - u|\right)_{\beta=1,\dots,M}, \qquad \alpha = 1, 2, \dots, M-1. \tag{6.10}$$

Notice that the eigenvalues (6.9)-(6.10) are approximations for eigenvalues of the original system using the water heights h_α instead of the total height H. This results in a system of $2M$ equations for which each layer has two eigenvalues.

6.2 A fast and accurate finite volume method

The lack of explicit analytical expressions of the eigenvalues and eigenvectors for the multi-layer shallow water model (6.8) renders Riemann-solver finite volume methods inappropriate for solving these equations. These methods include the Roe, HLL, HLLC schemes and other Godunov methods from computational fluids dynamics, see [205, 90, 178]. In the current study,

we propose a second-order Finite Volume Characteristics (FVC) method which does not require the calculation of the eigenvalues for the multi-layer system and the selection of time steps is carried out using the asymptotic approximations (6.9)-(6.10). For the spatial discretization of (6.8), we discretize the spatial domain into control volumes $[x_{i-1/2}, x_{i+1/2}]$ with uniform size $\Delta x = x_{i+1/2} - x_{i-1/2}$, $x_{i-1/2} = i\Delta x$ and $x_i = (i + 1/2)\Delta x$ is the center of the control volume. Integrating the equation (6.8) with respect to space over the control volume $[x_{i-1/2}, x_{i+1/2}]$, we obtain the following semi-discrete equations

$$\frac{d\mathbf{W}_i}{dt} + \frac{\mathcal{F}_{i+1/2} - \mathcal{F}_{i-1/2}}{\Delta x} = \mathbf{Q}(\mathbf{W}_i) + \mathbf{R}(\mathbf{W}_i), \tag{6.11}$$

where $\mathbf{W}_i(t)$ is the space average of the solution $\mathbf{W}$ in the control volume $[x_{i-1/2}, x_{i+1/2}]$ at time t, *i.e.*,

$$\mathbf{W}_i(t) = \frac{1}{\Delta x} \int_{x_{i-1/2}}^{x_{i+1/2}} \mathbf{W}(t, x)\, dx,$$

and $\mathcal{F}_{i\pm1/2} = \mathbf{F}(\mathbf{W}_{i\pm1/2})$ are the numerical fluxes at $x = x_{i\pm1/2}$ and time t. Here, the time integration of (6.11) is performed using a second-order splitting method studied in [27]. Thus, to integrate the equations (6.8) in time we divide the time interval into N sub-intervals $[t_n, t_{n+1}]$ with length $\Delta t = t_{n+1} - t_n$ for $n = 0, 1, \ldots, N$. We also use the notation W^n to denote the value of a generic function W at time t_n. The considered operator splitting method consists of three stages given by:

Stage 1:

$$\begin{aligned} \frac{\partial \mathbf{W}_i^*}{\partial t} &= \mathbf{R}(\mathbf{W}_i^*), \qquad t \in (t_n, t_n], \\ \mathbf{W}_i^*(t_n) &= \mathbf{W}_i(t_n). \end{aligned} \tag{6.12}$$

Stage 2:

$$\begin{aligned} \frac{\partial \mathbf{W}_i^{**}}{\partial t} + \frac{\partial \mathbf{F}(\mathbf{W}_i^{**})}{\partial x} &= \mathbf{Q}(\mathbf{W}_i^{**}), \qquad t \in (t_n, t_{n+1}], \\ \mathbf{W}_i^{**}(t_n) &= \mathbf{W}_i^*(t_n). \end{aligned} \tag{6.13}$$

Stage 3:

$$\begin{aligned} \frac{\partial \mathbf{W}_i^{***}}{\partial t} &= \mathbf{R}(\mathbf{W}_i^{***}), \qquad t \in (t_n, t_{n+1}], \\ \mathbf{W}_i^{***}(t_n) &= \mathbf{W}_i^{**}(t_{n+1}). \end{aligned} \tag{6.14}$$

The time integration is complete once a time stepping scheme is applied to the above three stages. It is clear that the nonlinear terms are dealt with in the first and third stages, whereas only linear terms are accounted for in the second stage of the splitting. To avoid solution of linear systems of algebraic equations associated with implicit time stepping, we consider only explicit time integration methods for the stages (6.12)-(6.14). To this end, we use the explicit third-order Runge-Kutta method studied in [9]. Hence, the procedure to advance the solution of an ordinary differential equation of the structure (6.12) from the time t_n to the next time t_{n+1} can be carried out as

$$\begin{aligned} \mathcal{W}_i^{(1)} &= \mathbf{W}_i^n + \Delta t \mathbf{R}(\mathbf{W}_i^n), \\ \mathcal{W}_i^{(2)} &= \frac{3}{4}\mathbf{W}_i^n + \frac{1}{4}\mathcal{W}_i^{(1)} + \frac{1}{4}\Delta t \mathbf{R}(\mathcal{W}_i^{(1)}), \\ \mathbf{W}_i^{n+1} &= \frac{1}{3}\mathbf{W}_i^n + \frac{2}{3}\mathcal{W}_i^{(2)} + \frac{2}{3}\Delta t \mathbf{R}(\mathcal{W}_i^{(2)}), \end{aligned} \tag{6.15}$$

where we have dropped the asterisk of the variables in (6.12) for ease of notation. Note that the Runge-Kutta method (6.15) has been widely used for time integration of hyperbolic systems of conservation laws mainly because it can be interpreted as a convex combination of first-order Euler steps which exhibits strong stability properties. As a consequence, the Runge-Kutta method (6.15) is TVD, third-order accurate in time, and stable under the usual Courant-Friedrichs-Lewy (CFL) condition involving the asymptotic eigenvalues (6.9)-(6.10). The spatial discretization (6.11) is complete when a reconstruction of the numerical fluxes $\mathcal{F}_{i\pm1/2}$ and source terms $\mathbf{Q}(\mathbf{W}_i)$ and $\mathbf{R}(\mathbf{W}_i)$ are chosen. In general, the reconstruction of the numerical fluxes requires a solution of Riemann problems at the interfaces $x_{i\pm1/2}$. From a computational viewpoint, this procedure is very demanding and may restrict the application of the method for which Riemann solutions are not available. On the other hands, Riemann-solver free finite volume methods such as the canonical Lax-Friedrichs and Rusanov schemes can also be used in (6.11). For the Lax-Friedrichs method, the numerical fluxes $\mathcal{F}_{i+1/2}$ in (6.11) are defined by

$$\mathcal{F}^n_{i+1/2} = \frac{1}{2}\left(\mathbf{F}(\mathbf{W}^n_{i+1}) + \mathbf{F}(\mathbf{W}^n_i)\right) + \frac{\Delta x}{2\Delta t}\left(\mathbf{W}^n_i - \mathbf{W}^n_{i+1}\right). \tag{6.16}$$

For the Rusanov method, the numerical fluxes $\mathcal{F}_{i+1/2}$ in (6.11) are

$$\mathcal{F}^n_{i+1/2} = \frac{1}{2}\left(\mathbf{F}(\mathbf{W}^n_{i+1}) + \mathbf{F}(\mathbf{W}^n_i)\right) + \frac{\lambda}{2}\left(\mathbf{W}^n_i - \mathbf{W}^n_{i+1}\right), \tag{6.17}$$

where λ is the Rusanov speed defined by

$$\lambda = \max_{1\leq\alpha\leq M-1}\left(\left|\lambda^+_{ext}\right|, \left|\lambda^-_{ext}\right|, \left|\lambda^{+,\alpha+\frac{1}{2}}_{int}\right|, \left|\lambda^{-,\alpha+\frac{1}{2}}_{int}\right|\right), \tag{6.18}$$

with $\lambda^{\pm}_{ext}$ and $\lambda^{\pm,\alpha+\frac{1}{2}}_{int}$ are the approximated eigenvalues in (6.9) and (6.10), respectively.

6.2.1 Discretization of the flux gradients

Our objective in the present work is to present a class of Finite Volume Characteristics (FVC) method that is simple, easy to implement, and accurately solves the equations (6.8) without relying on Riemann problem solvers or complicated techniques for well-balancing the discretizations of the gradient fluxes and the source terms. This objective is achieved by reformulating the multi-layer system in an advective form and integrating the obtained system along the characteristics defined by the advection velocity. To reconstruct the numerical fluxes $\mathcal{F}^n_{i\pm1/2}$ in (6.11), we consider the method of characteristics applied to an advective version of the system (6.1). In practice, the advective form of the multi-layer shallow water equations (6.8) is built such that the non-conservative variables are transported with a velocity field associated with each layer. Here, the multi-layer shallow water equations (6.8), without accounting for the source term $\mathbf{R}(\mathbf{W})$, are reformulated in an advective form as

$$\begin{aligned}
\frac{\partial H}{\partial t} + \left(\sum_{\alpha=1}^{M} l_\alpha u_\alpha\right)\frac{\partial H}{\partial x} &= -\sum_{\alpha=1}^{M} l_\alpha H \frac{\partial u_\alpha}{\partial x}, \\
\frac{\partial q_\alpha}{\partial t} + u_\alpha\frac{\partial q_\alpha}{\partial x} &= -q_\alpha\frac{\partial u_\alpha}{\partial x} - gH\frac{\partial}{\partial x}\left(H+z\right), \qquad \alpha = 1, 2\ldots, M,
\end{aligned} \tag{6.19}$$

which can be rearranged in a compact form as

$$\frac{\partial U_\alpha}{\partial t} + \mathcal{U}_\alpha\frac{\partial U_\alpha}{\partial x} = S_\alpha\left(\mathbf{U}\right), \qquad \alpha = 0, 1, \ldots, M, \tag{6.20}$$

where $q_\alpha = Hu_\alpha$ is the water discharge, $\mathbf{U} = (U_0, U_1, \ldots, U_M)^T$, $\mathbf{S}(\mathbf{U}) = (S_0, S_1, \ldots, S_M)^T$ with

$$\mathbf{U} = \begin{pmatrix} H \\ q_1 \\ q_2 \\ \vdots \\ q_M \end{pmatrix}, \qquad \mathbf{S}(\mathbf{U}) = \begin{pmatrix} -\sum_{\alpha=1}^{M} l_\alpha H \dfrac{\partial u_\alpha}{\partial x} \\ -Hu_1 \dfrac{\partial u_1}{\partial x} - gH \dfrac{\partial}{\partial x}(H+z) \\ -Hu_2 \dfrac{\partial u_2}{\partial x} - gH \dfrac{\partial}{\partial x}(H+z) \\ \vdots \\ -Hu_M \dfrac{\partial u_M}{\partial x} - gH \dfrac{\partial}{\partial x}(H+z) \end{pmatrix},$$

and the advection velocity $\mathcal{U}_\alpha$ is defined as

$$\mathcal{U}_\alpha = \begin{cases} \displaystyle\sum_{\beta=1}^{M} l_\beta u_\beta, & \text{if} \quad \alpha = 0, \\ \\ u_\alpha, & \text{if} \quad \alpha = 1, 2, \ldots, M. \end{cases} \tag{6.21}$$

Note that the case with $\alpha = 0$ does not refer to any layer in the system but to the global mass equation. It is only used here to formulate the compact advective form (6.20) for the whole system. The fundamental idea of the method of characteristics is to impose a regular grid at the new time level and to backtrack the flow trajectories to the previous time level. At the old time level, the quantities that are needed are evaluated by interpolation from their known values on a regular grid. For more discussions we refer the reader to [234, 213] among others. Thus, the characteristic curves associated with the equation (6.20) are solutions of the initial-value problems

$$\begin{aligned} \frac{dX_{\alpha,i+1/2}(\tau)}{d\tau} &= \mathcal{U}_{\alpha,i+1/2}\Big(\tau, X_{\alpha,i+1/2}(\tau)\Big), \quad \tau \in [t_n, t_{n+1}], \\ X_{\alpha,i+1/2}(t_{n+1}) &= x_{i+1/2}, \qquad \alpha = 0, 1, \ldots, M. \end{aligned} \tag{6.22}$$

Note that $X_{\alpha,i+1/2}(\tau)$ are the departure points at time τ of a particle that will arrive at the gridpoint $x_{i+1/2}$ in time t_{n+1}. The method of characteristics does not follow the flow particles forward in time, as the Lagrangian schemes do, instead it traces backward the position at time t_n of particles that will reach the points of a fixed mesh at time t_{n+1}. By doing so, the method avoids the grid distortion difficulties that the conventional Lagrangian schemes have, see for instance [234, 196] and further references are therein. In our simulations we used the third-order Runge-Kutta method (6.15) for the solution of the initial-value problems (6.22). In general $X_{\alpha,i+1/2}(t_n)$ will not coincide with the spatial position of a gridpoint. Hence, once the characteristic curves $X_{\alpha,i+1/2}(t_n)$ are accurately calculated, a solution at the cell interface $x_{i+1/2}$ is reconstructed as

$$\mathbf{U}^{n+1}_{\alpha,i+1/2} = \mathbf{U}_\alpha\left(t_{n+1}, x_{i+1/2}\right) = \widetilde{\mathbf{U}}_\alpha\left(t_n, X_{\alpha,i+1/2}(t_n)\right), \tag{6.23}$$

where $\widetilde{\mathbf{U}}_\alpha\left(t_n, X_{\alpha,i+1/2}(t_n)\right)$ is the solution at the characteristic foot computed by interpolation from the gridpoints of the control volume where the departure point resides *i.e.*

$$\widetilde{\mathbf{U}}_\alpha\left(t_n, X_{\alpha,i+1/2}(t_n)\right) = \mathcal{P}\Big(\mathbf{U}_\alpha\left(t_n, X_{\alpha,i+1/2}(t_n)\right)\Big), \tag{6.24}$$

where $\mathcal{P}$ represents an interpolating polynomial. For instance, a Lagrange-based interpolation polynomials can be formulated as

$$\mathcal{P}\Big(\mathbf{U}_j\left(t_n, X_{\alpha,i+1/2}(t_n)\right)\Big) = \sum_k \mathcal{L}_k(X_{\alpha,i+1/2})\mathbf{U}^n_{\alpha,k}, \tag{6.25}$$

with $\mathcal{L}_k$ are the Lagrange polynomials given by

$$\mathcal{L}_k(x) = \prod_{k'\neq k} \frac{x - x_{k'}}{x_k - x_{k'}}.$$

Note that other interpolation procedures such as Spline or Hermite interpolation methods or interpolation techniques based on radial basis functions can also be applied in (6.24). It is worth mentioning that the proposed finite volume method is fully conservative by construction and the non-conservative system (6.19) is used only to compute the intermediate states for the numerical fluxes in (6.11).

6.2.2 Discretization of the source terms

Applied to the equations (6.20), the characteristic solutions are given by

$$\begin{aligned}
H^n_{i+1/2} &= \widetilde{H}^n_{i+1/2} - \frac{\Delta t}{\Delta x}\widetilde{H}^n_{i+1/2}\sum_{\alpha=1}^{M} l_\alpha\left(u^n_{\alpha,i+1} - u^n_{\alpha,i}\right),\\
q^n_{\alpha,i+1/2} &= \widetilde{q}^n_{\alpha,i+1/2} - \frac{\Delta t}{\Delta x}\left(\widetilde{q}^n_{\alpha,i+1/2}\left(u^n_{\alpha,i+1} - u^n_{\alpha,i}\right) + g\widetilde{H}^n_{i+1/2}\left((H^n_{i+1} + z^n_{i+1}) - (H^n_i + z^n_i)\right)\right),
\end{aligned}$$

where

$$\widetilde{H}^n_{i+1/2} = H\left(t_n, X_{0,i+1/2}(t_n)\right), \qquad \widetilde{q}^n_{\alpha,i+1/2} = q_\alpha\left(t_n, X_{\alpha,i+1/2}(t_n)\right),$$

are the solutions at the characteristic foot computed by interpolation from the gridpoints of the control volume where the departure points $X_{\alpha,i+1/2}(t_n)$ belong. The numerical fluxes $\mathcal{F}_{i\pm1/2}$ in (6.11) are calculated using the intermediate states $\mathbf{W}^n_{i\pm1/2}$ recovered accordingly from the characteristic solutions $\mathbf{U}^n_{j,i\pm1/2}$ in (6.23). Hence, the corrector stage in the FVC method reduces to

$$\begin{aligned}
H^{n+1}_i &= H^n_i - \frac{\Delta t}{\Delta x}\sum_{\alpha=1}^{M}\left((l_\alpha H u_\alpha)^n_{i+1/2} - (l_\alpha H u_\alpha)^n_{i-1/2}\right),\\
q^{n+1}_{\alpha,i} &= q^n_{\alpha,i} - \frac{\Delta t}{\Delta x}\left(\left(Hu^2_\alpha + \frac{1}{2}gH^2\right)^n_{i+1/2} - \left(Hu^2_\alpha + \frac{1}{2}gH^2\right)^n_{i-1/2}\right) - \frac{\Delta t}{\Delta x}g\widehat{H}^n_i\left(z^n_{i+1} - z^n_{i-1}\right),
\end{aligned} \tag{6.26}$$

In our FVC method, the reconstruction of the term $\widehat{H}^n_i$ in (6.26) is carried out such that the discretization of the source terms is well balanced with the discretization of flux gradients using the concept of C-property [30]. Here, a numerical scheme is said to satisfy the C-property for the equations (6.8) if the condition

$$z + H^n = C, \qquad u^n_\alpha = 0, \qquad \alpha = 1, 2, \ldots, M, \tag{6.27}$$

holds for stationary flows at rest. In (6.27), C is a positive constant. Therefore, the treatment of source terms in (6.26) is reconstructed such that the condition (6.27) is preserved at the discrete level.
Let us assume a stationary flow at rest, $u_\alpha = 0$, $\alpha = 1, 2, \ldots, M$, and a linear interpolation procedure is used in the FVC method. Thus, the system (6.8) reduces to

$$\frac{\partial}{\partial t}\begin{pmatrix} H \\ 0 \end{pmatrix} + \frac{\partial}{\partial x}\begin{pmatrix} 0 \\ \frac{1}{2}gH^2 \end{pmatrix} = \begin{pmatrix} 0 \\ -gH\frac{\partial z}{\partial x} \end{pmatrix}. \tag{6.28}$$

Applied to the system (6.28), the stage (6.26) computes

$$\begin{aligned} H^n_{i+1/2} &= \frac{H^n_i + H^n_{i+1}}{2}, \\ u^n_{\alpha,i+1/2} &= 0, \qquad \alpha = 1, \ldots, M, \end{aligned} \tag{6.29}$$

while the stage (6.26) updates the solution as

$$\begin{aligned} H^{n+1}_i &= H^n_i, \\ q^{n+1}_{\alpha,i} &= q^n_{\alpha,i} - \frac{1}{2}\frac{\Delta t}{\Delta x} g\left(\left(H^n_{i+1/2}\right)^2 - \left(H^n_{i-1/2}\right)^2\right) - \Delta t g\left(H\frac{\partial z}{\partial x}\right)^n_i, \end{aligned} \tag{6.30}$$

To obtain stationary solutions $H^{n+1}_i = H^n_i$, the sum of discretized flux gradient and source term in (6.30) should be equal to zero *i.e.*,

$$\frac{1}{2\Delta x}\left(\left(H^n_{i+1/2}\right)^2 - \left(H^n_{i-1/2}\right)^2\right) = -\left(H\frac{\partial z}{\partial x}\right)^n_i, \tag{6.31}$$

Using $H^n_{i+1/2} = \dfrac{H^n_i + H^n_{i+1}}{2}$, the condition (6.31) is equivalent to

$$\frac{1}{8\Delta x}\left(H^n_{i+1} + 2H^n_i + H^n_{i-1}\right)\left(H^n_{i+1} - H^n_{i-1}\right) = -\left(H\frac{\partial z}{\partial x}\right)^n_i, \tag{6.32}$$

Since for stationary solutions $H^n_{i+1} - H^n_{i-1} = Z_{i+1} - Z_{i-1}$, the equations (6.32) become

$$\left(H\frac{\partial z}{\partial x}\right)^n_i = \frac{H^n_{i+1/2} + H^n_{i-1/2}}{2}\frac{z_{i+1} - z_{i-1}}{2\Delta x}, \tag{6.33}$$

Hence, if the source term $\widehat{H}^n_i$ in the predictor stage (6.26) is discretized as

$$\widehat{H}^n_i = \frac{1}{4}\left(H^n_{i+1} + 2H^n_i + H^n_{i-1}\right), \tag{6.34}$$

then the proposed FVC method satisfies the C-property. A detailed analysis of convergence and stability has been presented in [28] for nonlinear scalar problems. Notice that this property is achieved by assuming a linear interpolation procedure in the predictor stage of the FVC method. However, a well-balanced discretization of flux gradients and source terms for a quadratic or cubic interpolation procedures can be carried out using similar techniques. In summary, the implementation of FVC method to solve the multi-layer shallow water equations (6.8) is carried out following the steps in Algorithm 6.1.

Algorithm 6.1 FVC method solving the multi-layer shallow water equations.

Given the solution $\left(H_i^n, q_{\alpha,i}^n\right)$ at time t_n, we compute the solution $\left(H_i^{n+1}, q_{\alpha,i}^{n+1}\right)$ at the next time level t_{n+1} via:

1: Perform the first step of the time splitting in (6.12) to compute the solutions H_i^* and $q_{\alpha,i}^*$, $\alpha = 1, 2, \ldots, M$.
2: Compute the departure points $X_{\alpha,i+1/2}(t_n)$, with $\alpha = 0, 1, \ldots, M$ by solving (6.22).
3: Compute the approximations

$$\widetilde{H}_{i+1/2}^n = H\left(t_n, X_{0,i+1/2}(t_n)\right) \quad \text{and} \quad \widetilde{q}_{\alpha,i+1/2}^n = q_\alpha\left(t_n, X_{\alpha,i+1/2}(t_n)\right), \qquad \alpha = 1, \ldots, M$$

employing an interpolation procedure.
4: Evaluate the intermediate states $H_{i+1/2}^n$ and $q_{\alpha,i+1/2}^n$ from the predictor stage (6.26).
5: Update the solutions H_i^{n+1} and $q_{\alpha,i}^{n+1}$ using the corrector stage (6.26).

6.3 Uncertainty quantification methods

In general, the purpose of uncertainty quantification is to identify the main sources of uncertainty in a physical model (*e.g.* parameters, external forcing, boundary conditions, initial conditions), and to quantify their impact on the quantities of interest simulated by the numerical model (prognostic variables, probability of exceeding the threshold). This allows to associate every forecast with a level of confidence since the accuracy of a simulation significantly depends on the quantity and the quality of the input data. Therefore, to better understand the results of numerical simulations it is necessary to take into account these uncertainties in the simulations. In addition, a problem of uncertainty quantification is a problem which aims at estimating uncertainty on the outputs of a numerical simulation according to the uncertainties on knowledge of its input parameters. Because of the random nature of uncertainty, the probabilistic approach to deal with a problem of uncertainty quantification is to consider the uncertain data of the model as random variables or random processes, and to reconsider the real deterministic numerical model as a stochastic model. This section presents the methods used in the current study for uncertainty quantification. First, the methods of generating different independent realizations of the bathymetric field are presented. Therefore, the classical method of Polynomial Chaos Expansion (PCE) is used as a surrogate tools to alleviate the computational cost. Finally, as the hydraulic state is also considered as stochastic process, we suggest to reduce the dimension of the problem using the Proper Orthogonal Decomposition (POD) and to compute a PCE only for the associated nonphysical variables.

6.3.1 Karhunen-Loève expansion for stochastic process

A stochastic process is defined by the means of an indexation set X, E is a measurable space and $(\Omega, \mathcal{F}, \mathcal{P})$ a σ-algebra representing the probability space [249]. The stochastic process $\mathbf{z}$ is then defined as a collection $\{\mathbf{z}_x, x \in X\}$ which the random values are in the state space E and described statistically by the probabilistic space $(\Omega, \mathcal{F}, \mathcal{P})$

$$\mathbf{z}_x : \Omega \longrightarrow E.$$

Consequently, one is able to define a realization $\omega \in \Omega$ for a stochastic process as

$$\mathbf{z}(\omega) : \begin{array}{ccc} X & \longrightarrow & E \\ x & \longmapsto & \mathbf{z}_x(\omega) \end{array}$$

The Karhunen-Loève expansion (KL) allows to model a random process based on a spectral decomposition of its spatial covariance matrix $\mathcal{C}(x, x')$, see for example [128, 160]. Note that, by construction the covariance function is real, symmetric and positive definite. Consequently, the set of eigenfunctions form a complete orthogonal basis for the space in which the process belongs. Hence, a stochastic process can be defined as

$$\boldsymbol{z}(x, \boldsymbol{\omega}) = \overline{\boldsymbol{z}}(x) + \sum_{i=0}^{\infty} \omega_i l_i \phi_i(x), \tag{6.35}$$

where x is the curvilinear abscissa, $\overline{\boldsymbol{z}}$ the mean of the random process, $\boldsymbol{\omega} = \{\omega_1, \dots, \omega_\infty\}$ a set of independent random variables, l_i $(i = 0, 1, \dots)$ the set of the eigenvalues of the covariance function, and $\phi_i(x)$ $(i = 0, 1, \dots)$ the set of the eigenfunctions. In practice and for computational reasons, the equation (6.35) is truncated at a certain degree d. The choice of this latter is often determined by a threshold ϵ from which the eigenvalues could be neglected *i.e.*

$$\frac{\sum_{i=0}^{d} l_i}{\sum_{i=0}^{\infty} l_i} > 1 - \epsilon.$$

Thus, the expansion (6.35) is replaced by

$$\mathbf{z}(x, \boldsymbol{\omega}) = \overline{\mathbf{z}}(x) + \sum_{i=0}^{d} \omega_i l_i \phi_i(x). \tag{6.36}$$

It should be stressed that the major limitation of the KL decomposition is the *a priori* knowledge of the covariance matrix. In the literature, this parameter is estimated empirically and therefore could be subject to uncertainty itself. This uncertainty is not considered in the present work and the reader may be referred to [222] for more discussions on this topic. This expansion is commonly used to model the uncertainty of a stochastic input parameter for two reasons: firstly the mean-square error of the finite representation (6.36) is minimized such that the equation (6.35) converges following the ℓ_2-norm. The second reason is related to the generation of random samples. In fact, making a realization of $\boldsymbol{z}(x, \boldsymbol{\omega})$ amounts to randomly draw the different ω_i following a defined probability density function. Those parameters are assumed to be independent random variables. Therefore, the KL decomposition offers a good representation of the input parameters when the covariance is known. In our study, the covariance matrix $\mathcal{C}(x, x')$ is supposed to be exponential. Indeed, authors in [261] showed that the uncertainty in the description of the bathymetric field followed this spatial correlation function. Thus, the correlation matrix is defined as

$$\mathcal{C}(x, x') = \sigma^2 \exp\left(-\frac{|x - x'|}{\theta}\right), \tag{6.37}$$

where σ and θ are the hyper-parameters of the covariance function with σ is the standard deviation of the process and θ the correlation length. Note that, calculating the eigenvalues and eigenvectors is well known by the Fredholm problem. There exits many algorithms that aim to solve this latter given a well defined matrix, see for example [133] for more details. Once, l_i and $\phi_i(x)$ are known, the KL expansion is obtained in a straightforward manner. Therefore, the bathymetry could be written as described in (6.36) and could be sampled in order to consider its uncertainty in the hydraulic computations.

6.3.2 Polynomial chaos expansions

The PCE has been intensively used as a surrogate model in the context of uncertainty quantification, see [108, 80] among others. It aims to reproduce the global behavior of the considered numerical models. Supposing that the input parameters of this model are represented by M independent random variables $\boldsymbol{\zeta} = \{\zeta_1, \zeta_2, \ldots, \zeta_M\}$ with finite variance well defined in a probabilistic space, the response $\mathbf{U}$ of this model is also random. Note that $\mathbf{U}$ is a vector-valued response as it represents the spatial variability of the hydraulic states. Considering that the expectation $\mathbb{E}[\|\mathbf{U}\|^2]$ is finite, the behavior of $\mathbf{U}$ could be reproducible following a polynomial decomposition namely the PCE [219] as

$$\mathbf{U}(x, \boldsymbol{\zeta}) = \sum_{i \in \mathbb{N}} \alpha_i(x) \Psi_i(\boldsymbol{\zeta}), \tag{6.38}$$

where Ψ_i is the multivariate polynomials that form the basis and chosen in such way they are orthonormal with respect to the associated probability density function of $\boldsymbol{\zeta}$, *i.e.* $\mathbb{E}[\Psi_i(\boldsymbol{\zeta})\Psi_j(\boldsymbol{\zeta})] = \delta_{ij}$ where δ_{ij} is the Kronecker symbol, compare for example [248, 252]. In (6.38), α_i are the unknown spectral coefficients of the decomposition to be determined. Again, the sum in (6.38) is truncated to a finite series as

$$\mathbf{U}(x, \boldsymbol{\zeta}) \approx \sum_{i \in \mathcal{I}} \alpha_i(x) \Psi_i(\boldsymbol{\zeta}), \tag{6.39}$$

where $\mathcal{I} \subset \mathbb{N}$ is the finite set of indices. The determination of a PCE is therefore conditioned by the estimation of the spectral coefficients α_i. There are many methods used in the literature to achieve this step and we refer to [251, 252, 144] for a review on these methodologies. In the current work, only the regression method is used and this choice comes from the fact that these methods coupled with compressed sensing techniques are advantageous when the stochastic dimension of the problem M is high (which is more likely to be the case here after the use of the KL decomposition). The regression method is based on solving a least-square (LS) minimization problem in some ℓ_2-norm to estimate the coefficients α_i, see for instance [65, 33]. In practice, we begin by defining an error $\boldsymbol{\epsilon}$ as the distance between the model and the PCE for a finite set of randomly sampled input variables of size N_{ls} as

$$\boldsymbol{\epsilon} = \left\| \mathbf{U}(x, \boldsymbol{\Xi}) - \sum_{i \in \mathbb{N}} \alpha_i(x) \Psi(\boldsymbol{\Xi}) \right\|_2 \equiv \boldsymbol{\mathcal{W}} - \boldsymbol{\alpha}^\top \boldsymbol{\Psi}, \tag{6.40}$$

where $\boldsymbol{\Xi} = [\boldsymbol{\zeta}^{(1)}, \ldots, \boldsymbol{\zeta}^{(N_{ls})}]^\top$ is the set of considered realizations for the stochastic input variables $\boldsymbol{\zeta}$ and $\boldsymbol{\mathcal{W}} = [\mathbf{U}^{(1)}, \ldots, \mathbf{U}^{(N_{ls})}]^\top$ the vector of associated model outputs. We also define $\boldsymbol{\alpha} = [\alpha_0, \ldots, \alpha_{N_{PC}-1}]^\top$ as the vector of the $N_{PC} = Card(\mathcal{I})$ unknown coefficients and $\boldsymbol{\Psi}$ is the matrix of size $N_{PC} \times N_{ls}$ assembling the values of all orthonormal polynomials at the stochastic input realizations values $\boldsymbol{\Psi}_{ik} = \Psi_i(\boldsymbol{\zeta}^{(k)})$, with $i = 0, 1, \ldots, N_{PC-1}$ and $k = 1, 2, \ldots, N_{ls}$. Following the ordinary least-square (6.40), the estimation of the set of coefficients $\boldsymbol{\alpha}$ is equivalent to minimize the following function

$$\mathrm{J}(\boldsymbol{\alpha}) = \boldsymbol{\epsilon}^\top \boldsymbol{\epsilon} = \left(\boldsymbol{\mathcal{W}} - \boldsymbol{\alpha}^\top \boldsymbol{\Psi}\right)^\top \left(\boldsymbol{\mathcal{W}} - \boldsymbol{\alpha}^\top \boldsymbol{\Psi}\right), \tag{6.41}$$

which leads to a standard well-known linear algebraic solution as

$$\boldsymbol{\alpha} = (\boldsymbol{\Psi}^\top \boldsymbol{\Psi})^{-1} \boldsymbol{\Psi}^\top \boldsymbol{\mathcal{W}}. \tag{6.42}$$

Here, the input space exploration is fulfilled using a Monte Carlo sampling-based approach [39, 80]. It is worth mentioning that the number of coefficients N_{PC} needed is directly affected by the stochastic dimension M as well as the polynomial degree p. As a consequence, the Monte Carlo size N_{ls} will also increase significantly with M and p. This is a classical problem of PCE also known as *the curse of dimensionality*. The adaptive Least Angle Regression (LAR) method [48] has been introduced and used to overcome this specific problem [39]. This method, introduced in the context of compressed sensing, has made it possible to give the best polynomial representation given a fixed budget of finite simulations. It will be used in the present work as it has been demonstrated to be very efficient in this framework. The idea behind this method is to select with an iterative manner an optimal sparse basis among the original one and then to compute a limited number of coefficients using a standard regression method. In the context of PCE, a hybrid LAR method is used. The method consists on using LAR to evaluate the best set of predictors among the full basis elements with the help of a cross-validation method. These coefficients are estimated using the classical least square method, see [39] for more details. The infinite expansion (6.38) describing PCE converges with respect to the standard ℓ_2-norm known by the mean-squared convergence, see for example [251]. However, due to the errors of truncation and spectral coefficient estimation, the accuracy of this expansion must be evaluated in the same error norm. There are many different error metrics that allow to assess the accuracy of the PCE, see [80, 251] among others. In the present work, all the PCEs are assessed using the Leave-one-out (*LOO*) error. This method avoids integrating the model over another set of validation samples and therefore the computational cost is optimized. It has been introduced in this context with the introduction of sparse PCE [33] and the *LOO* technique required the formulation of several surrogates [75, 39]. Each surrogate model is built excluding one point out of the input sample and the accuracy of the surrogate model is then quantified at this particular point. Following this theory, the error ϵ_{LOO} is defined by

$$\epsilon_{LOO} = \frac{\sum_{k=1}^{N_{ls}} \left(\mathbf{U}^{(k)} - \mathbf{U}^{(-k)}\right)^2}{\sum_{k=1}^{N_{ls}} \left(\mathbf{U}^{(k)} - \overline{\mathbf{U}}\right)^2}, \tag{6.43}$$

where $\overline{\mathbf{U}}$ denotes the sample-averaged model simulations and $\mathbf{U}^{(-k)}$ stands for the evaluation of the PCE at $\boldsymbol{\zeta}^{(k)}$ when the surrogate has been built using an experimental design in which $\boldsymbol{\zeta}^{(k)}$ was excluded. In the present work, the determination of the optimal polynomial degree is performed using an iterative method. Thus, a PCE is computed for different degrees varying from 1 to 20 and the optimal degree is determined based on the value of the corresponding ϵ_{LOO}. For the same value of a given error, the lowest value of the degree is retained.

Note that, when dealing with numerical models with spatial or temporal dependence, the classical way used in numerical simulations is to discretize the physical domain and resolve the governing equations for each control volume. This procedure leads to multiple decompositions to ensure the numerical convergence. As a result, uncertainty quantification becomes computationally very demanding not only because of the stochastic dimensions but also because of the spatial or temporal dimensions of the output variables. For these reasons, many methods have been introduced in the literature in order to reduce the dimensionality of the output vector, see for instance [197, 41, 63, 40]. Among all these different techniques, the POD has proven to be efficient in the context of physical fields with rapid variability as in hydraulics [197].

Algorithm 6.2 The implementation of the stochastic POD procedure.

1: Define the covariance matrix (6.45).
2: Expand the matrix $\mathbf{C}$ using an SVD algorithm to determine λ_i and $\phi_i(x)$.
3: Retain only the first k eigenvalues and eigenvectors in the expansion using the condition (6.44).
4: Reconstruct the stochastic solutions $\mathbf{U}(x, \boldsymbol{\zeta})$ using (6.44).

6.3.3 Stochastic proper orthogonal decomposition

The proper orthogonal decomposition (POD) is a well-established technique that allows a high-dimensional system to be approached by a low-dimensional one, compare [68] among others. This method consists in determining a basis of orthogonal eigenvalues representative of the simulated physics. The eigenvectors are obtained by solving the integral of Fredholm problem whereas, the kernel of this integral is constructed from a set of simulations constructed using a set of experiments. The interesting property of this representation lies in the fact that the eigenfunctions associated with the problem are optimal in the sense of the energetic representation (as described later) which makes it possible to use them to construct a reduced representation of physics. Notice that the POD is used in uncertainty quantifications to reduce the size of a random vector at the output of the model. The uncertainty is therefore carried out over each direction defined by the eigenvectors $\phi_i(x)$. The idea is based on projecting the solution $\mathbf{U}$ of the model into a finite and orthonormal basis $\{\phi_i, i \in \mathcal{I}_{POD}\}$, where $\mathcal{I}_{POD}$ is a discrete finite set of indices. Thus, the process $\mathbf{U}(x, \boldsymbol{\zeta})$ is decomposed as

$$\mathbf{U}(x, \boldsymbol{\zeta}) = \sum_{i \in \mathcal{I}_{POD}} \widehat{\lambda}_i(\boldsymbol{\zeta}) \phi_i(x). \tag{6.44}$$

The estimation of $\{\phi_i,\ i \in \mathcal{I}_{POD}\}$ is performed by decomposing the covariance matrix as

$$\mathbf{C} = \frac{1}{N_{ls}} \mathbf{U}\mathbf{U}^\top. \tag{6.45}$$

Indeed, the literature is rich of techniques that aim to decompose a covariance matrix. One of the most known methods is the Singular Value Decomposition (SVD) algorithm [74]. Hence, we define a POD-truncated error ϵ such as only the most k invaluable eigenvectors are retained as

$$\frac{\sum_{i=0}^{k} \lambda_i}{\sum_{i=0}^{N_{ls}} \lambda_i} > 1 - \epsilon, \tag{6.46}$$

where $\widehat{\lambda}_i$ is the mean value of $\lambda_i(\boldsymbol{\zeta})$. In summary, the stochastic POD procedure can be implemented using the steps described in Algorithm 6.2. It is worth remarking that the selection of the convergence criterion ϵ is problem dependent. The selection criterion of ϵ for test examples in the present investigation is discussed in Section 6.4 where numerical examples are described.

Once the stochastic POD is reconstructed, the eigenvalues are considered as stochastic independent variables (since the eigenvectors form a basis). This means that we can define a PCE

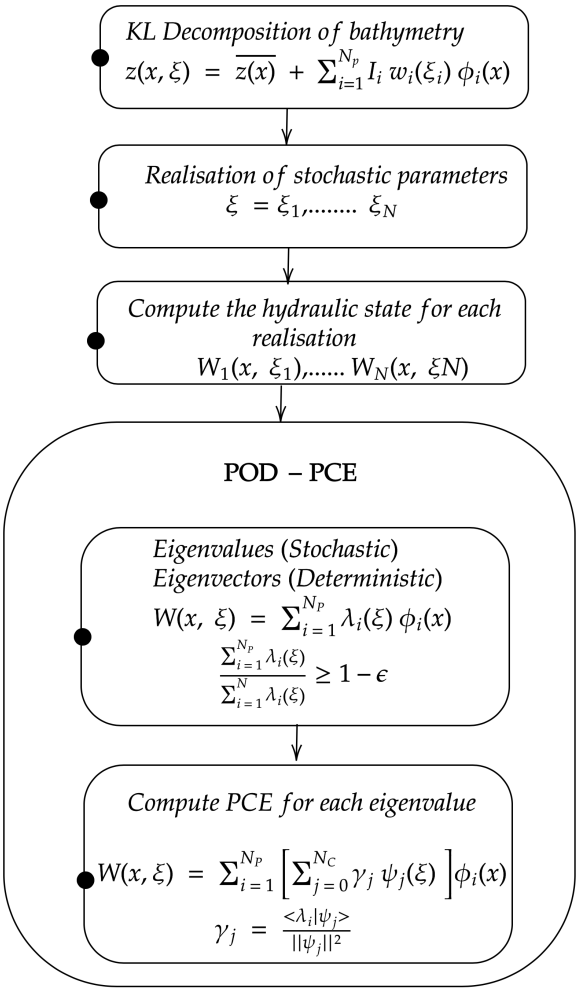

Figure 6.2: Schematic representation of the difference between flowcharts for the classical PCE based surrogate model and the POD-PCE based surrogate model.

for each eigenvalue following the same manner as described in the previous section on polynomial chaos expansions leaving the spatial dependence described by the eigenvectors $\phi_i(x)$ as

$$\lambda_i(\boldsymbol{\zeta}) = \sum_{j=0}^{N_{PC}} \gamma_j \Psi_j(\boldsymbol{\zeta}), \tag{6.47}$$

where γ_j are the corresponding spectral coefficients. Hence, using (6.47), the equation (6.39) reduces to

$$\mathbf{U}(x,\boldsymbol{\zeta}) = \sum_{i \in \mathcal{I}_{POD}} \left(\sum_{j=0}^{N_{PC}} \gamma_j \Psi_j(\boldsymbol{\zeta}) \right) \phi_i(x). \tag{6.48}$$

Figure 6.2 summarizes both algorithms that we consider in the present work for quantification of uncertainties in multi-layer shallow water flows. Note that the classical way to deal with a problem of uncertainty quantification using the PCE is performed when a decomposition is achieved for each node in the computational mesh. This method is illustrated by steps 1, 2 and 3 in Figure 6.2. However, as mentioned before, one method to alleviate the spatial distribution is to make a first reduction using the POD. This latter will help to separate the

spatial dependence from the stochastic one as the stochasticity is included in the associated eigenvalues. Once the POD is carried out, only few eigenmodes are retained enabling to make less PCE than its conventional counterpart. This algorithm follows steps 1, 2, 4 and 5 in Figure 6.2.

6.4 Numerical results and examples

In this section we present numerical results for several test problems of shallow water flows using multi-layer shallow water equations over flat and non-flat beds. The main goal of this section is to illustrate the numerical performance of the techniques described above for the uncertainty quantification in multi-layer shallow water flows. In our simulations, the Courant number is set to $Cr = 0.85$ and the time stepsize Δt is adjusted at each time step according to the CFL stability condition as

$$\Delta t = Cr \frac{\Delta x}{\max\limits_{1\leq\alpha\leq M-1}\left(\left|\lambda^{+}_{ext}\right|, \left|\lambda^{-}_{ext}\right|, \left|\lambda^{+,\alpha+\frac{1}{2}}_{int}\right|, \left|\lambda^{-,\alpha+\frac{1}{2}}_{int}\right|\right)},$$

where $\lambda^{\pm}_{ext}$ and $\lambda^{\pm,\alpha+\frac{1}{2}}_{int}$ are the approximated eigenvalues in (6.9) and (6.10), respectively. In all the computations reported herein, the total water height H and the total number of layers M are given whereas, the water height h_α at each αth layer is equidistantly calculated as

$$h_\alpha = l_\alpha H, \qquad \text{with} \qquad l_\alpha = \frac{1}{M}, \qquad \alpha = 1, 2, \ldots, M.$$

We also present the two-dimensional velocity fields for the considered examples using the post-processing procedure described in [12, 81]. Here, the vertical velocity v is computed using the divergence-free condition from the incompressible Navier-Stokes equations as

$$\frac{\partial u}{\partial x} + \frac{\partial v}{\partial z} = 0. \tag{6.49}$$

To compute the vertical velocity v, we integrate the equation (6.49) for each layer assuming non-penetration boundary conditions at the bottom, see [12, 81] for more details on this procedure. In this section we also compare the results obtained using the proposed FVC scheme to those obtained using the well-established Lax-Friedrichs method and the Kinetic method investigated in [12].

6.4.1 Dam-break problem over a flat bed

For this test example, the uncertainty quantification is performed for a dam-break flow problem over a stochastic flat bed. The channel is 100 m long and subject to the following initial conditions

$$H(0,x) = \begin{cases} 2, & \text{if} \quad x \leq 0, \\ 1, & \text{if} \quad x > 0, \end{cases} \qquad\qquad u_\alpha(0,x) = 0.$$

At initial time $t = 0$, the dam breaks and the flow problem consists of a shock wave propagating downstream and a rarefaction wave propagating upstream. In this example, the water density $\rho = 1000\ kg/m^3$, the gravitational acceleration $g = 9.81\ m/s^2$, the viscosity term

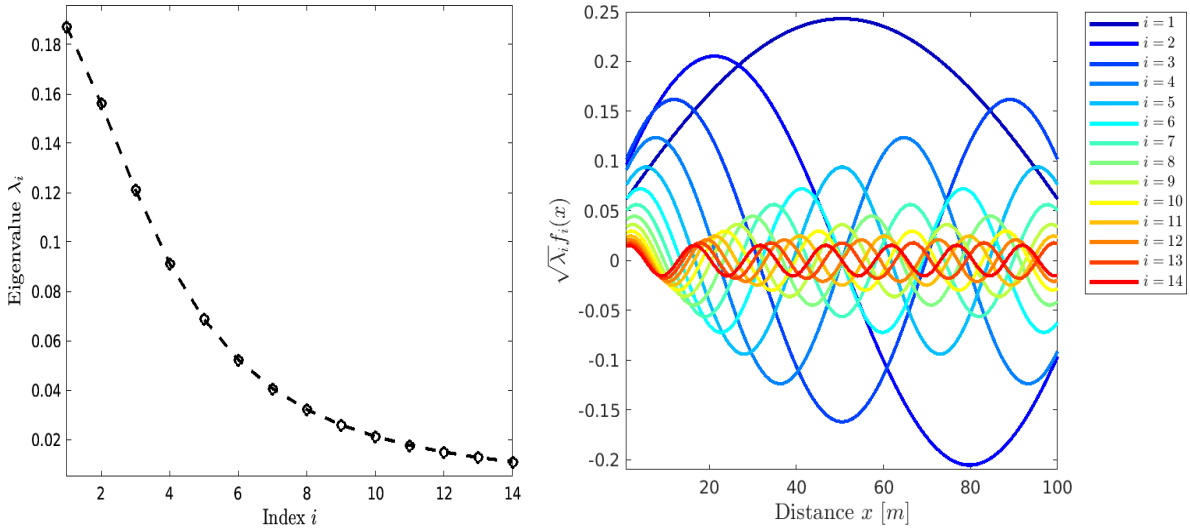

Figure 6.3: Eigenvalues (left plot) and the associated eigenfunctions (right plot) of the correlation matrix in the KL decomposition for the dam-break problem over a flat bed.

$\nu = 0.013$, number of samples = 1000, the Manning coefficient of friction $n_b = 0.05\ s/m^{1/3}$, using 100 gridpoints in simulation time $t = 6\ s$. We suppose that the bathymetry field is a Gaussian process that could be expanded following the KL decomposition and the coefficient of variation is fixed to 30%. The aim here is to quantify the uncertainty on the water height and the vertical mean velocity using the considered numerical methods namely, the FVC, the Kinetic and the Lax-Friedrich schemes.

Figure 6.3 presents the eigenvalues and eigenvectors obtained for the bathymetry process. This latter is supposed to be a Gaussian process described with an exponential spatial autocorrelation function. Given a value of threshold $\epsilon = 10^{-2}$, 14 eigenvalues are required to correctly sample the bathymetric field. In other words, the stochastic dimension of this problem is 16 (14 representing the bathymetry, one for the friction coefficient and one for the viscosity parameter). For each of the three numerical methods tested in this study, a 1000 Monte-Carlo simulations are run while the POD is then used to reduce the output space. In this case, different modes are retained to correctly represent the water height and the water velocity fields. An iterative procedure is used to determine the best polynomial degree along with the LOO error that is used to assess the robustness of the considered PCE. In order to futher assess the quality of the surrogate model, its performance is compared to a full Monte Carlo simulations fulfilled with a design of experiment with a size set at 100000.

Table 6.1 summarizes the results obtained for the first and second POD modes. It is evident that a polynomial of degree 3 is enough to correctly reproduce the uncertainty translated from errors in the bathymetry for the three considered finite volume methods. For both output fields (water height or water velocity), the LOO error varies from 10^{-12} to 10^{-7} which makes the surrogate model very reliable for uncertainty quantification in this class of dam-break problems. Note that the LOO error reflects the accuracy of the polynomial chaos expansion to estimate the uncertainty expressed by each mode. Therefore, it should not be mistaken with the accuracy of the surrogate model (polynomial chaos expansion with a proper orthogonal decomposition) to estimate the physical values. For this purpose, accuracy of the surrogate model is assessed using the full Monte Carlo simulations. As each physical component has a

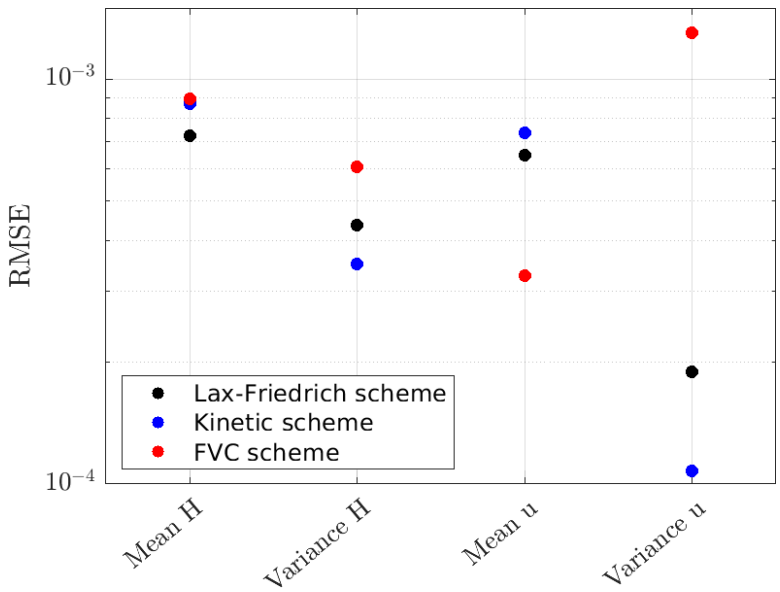

Figure 6.4: RMSE in the variance and the mean fields using the Lax-Friedrichs, Kinetic and FVC schemes for the water height and the mean velocity for the dam-break problem over a flat bed.

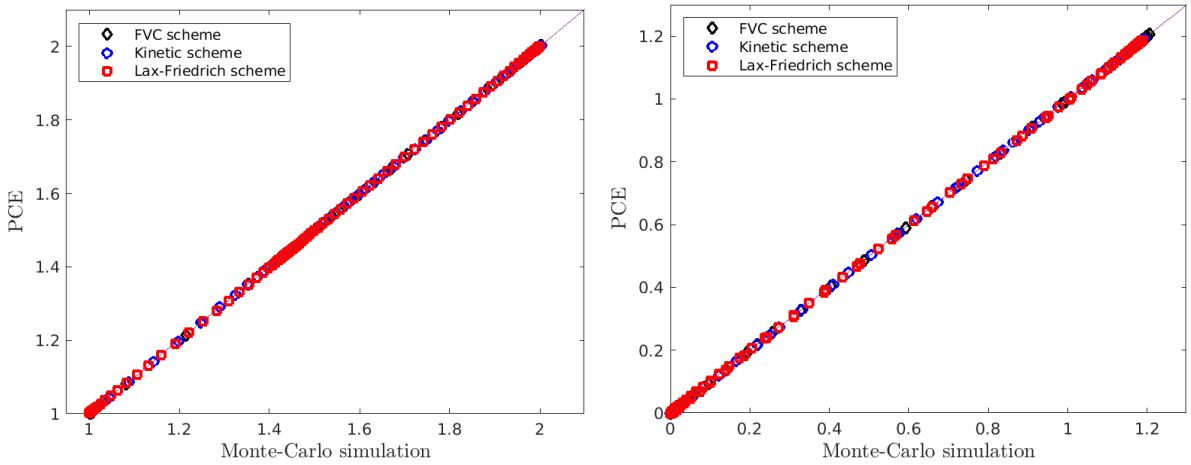

Figure 6.5: The QQ-plot between the Monte Carlo simulations and the surrogate model for the estimation of the mean for the water height(left plot) and the velocity (right plot) for the dam-break problem over a flat bed.

Table 6.1: Best polynomial degrees with LOO errors for the POD modes in the water height and mean velocity using different numerical schemes for the dam-break problem over a flat bed.

	Error and polynomial degree for water height H		
	Lax-Friedrich scheme	Kinetic scheme	FVC scheme
Number of modes	5	6	6
Error (M1)	5.764E-10	4.768E-10	2.354E-7
Error (M2)	6.684E-10	1.674E-10	2.369E-7
Error (M3)	6.442E-10	3.186E-10	2.528E-7
Error (M4)	5.456E-9	3.750E-10	3.816E-7
Error (M5)	7.562E-9	5.300E-10	4.468E-7
Error (M6)	———	9.590E-10	1.557E-7
Polynomial (M1)	3	3	3
Polynomial (M2)	3	3	3
Polynomial (M3)	3	3	3
Polynomial (M4)	3	3	3
Polynomial (M5)	3	3	3
Polynomial (M6)	———	3	3

	Error and polynomial degree for water mean velocity u		
	Lax-Friedrich scheme	Kinetic scheme	FVC scheme
Number of modes	8	7	7
Error (M1)	1.705E-5	2.961E-5	1.621E-5
Error (M2)	8.588E-8	7.389E-8	4.110E-6
Error (M3)	1.995E-8	9.500E-8	9.001E-6
Error (M4)	2.736E-6	5.583E-6	7.860E-6
Error (M5)	4.047E-7	8.670E-8	1.111E-6
Error (M6)	4.276E-6	6.949E-6	1.339E-5
Error (M7)	1.080E-6	6.779E-7	2.960E-5
Error (M8)	1.145E-6	———	———
Polynomial (M1)	3	3	3
Polynomial (M2)	2	2	3
Polynomial (M3)	3	3	3
Polynomial (M4)	2	3	3
Polynomial (M5)	3	2	3
Polynomial (M6)	3	3	3
Polynomial (M7)	2	3	3
Polynomial (M8)	2	———	———

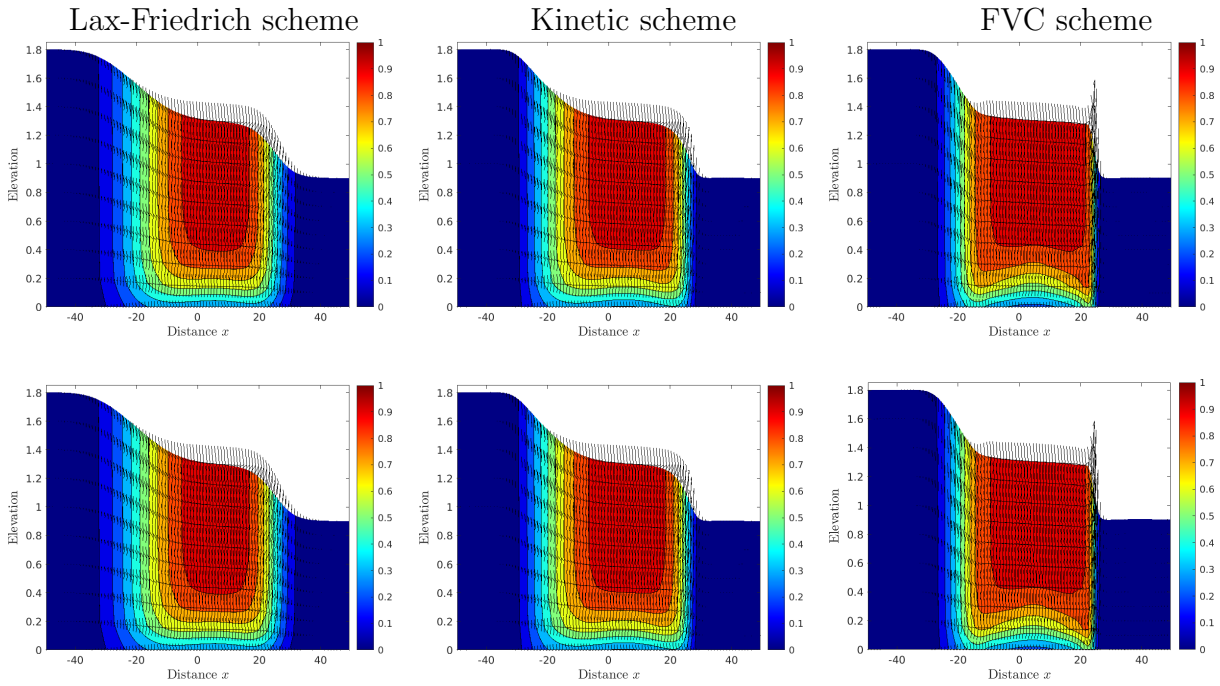

Figure 6.6: Deterministic flow fields (first row) and stochastic mean flow fields (second row) for the dam-break problem over a flat bed using Lax-Friedrich scheme (first column), Kinetic scheme (second column) and FVC scheme (third column).

spatial dependency, the Root Mean Square Error (RMSE) is estimated for the water height, the averaged velocity and for the mean and the variance fields using the three considered numerical models. The obtained results are reported in Figure 6.4 and it is clear that the RMSE value varies from 10^{-4} to 10^{-3} confirming the fact that the surrogate model has a good accuracy to estimate the first and second statistical moments. Furthermore, a QQ-plot displaying the results from the surrogate model against the Monte Carlo simulations is illustrated in Figure 6.5 for the water height and the averaged velocity. As it can be seen from this figure, all points of the domain are located in the first bisector of the QQ-plot which means that there is a good agreement between the results from the proposed model and the surrogate model. Hence, the surrogate model requiring 100 times few simulations than the Monte Carlo simulations is able to provide accurate results for uncertainty quantification in this dam-break problem. In addition, the proper orthogonal decomposition allowed to reduce the dimensionality of the problem to only 8 modes for the velocity and 6 modes for the water height.

Next, we turn our attention to the estimation of the first- and second-order moments using the surrogate model. The objective here is to present a comparison between the uncertainty displayed by each of the considered finite volume methods. First, we compare in Figure 6.6 the mean field and the deterministic solutions obtained at time $t = 6\ s$ using the considered numerical schemes. There are no significant changes between the deterministic solutions and the mean fields. The only differences observed are those already known from the differences between the finite volume methods for solving this class of problems. We also report in Figure 6.7 the mean solution of the water height along with its Confidence Interval (CI) that we define by taking the stochastic mean and adding and removing one standard deviation. As it can be seen from these results, the mean fields highlight some well-established results on the accuracy of the numerical methods such that the numerical diffusion is more pronounced for the

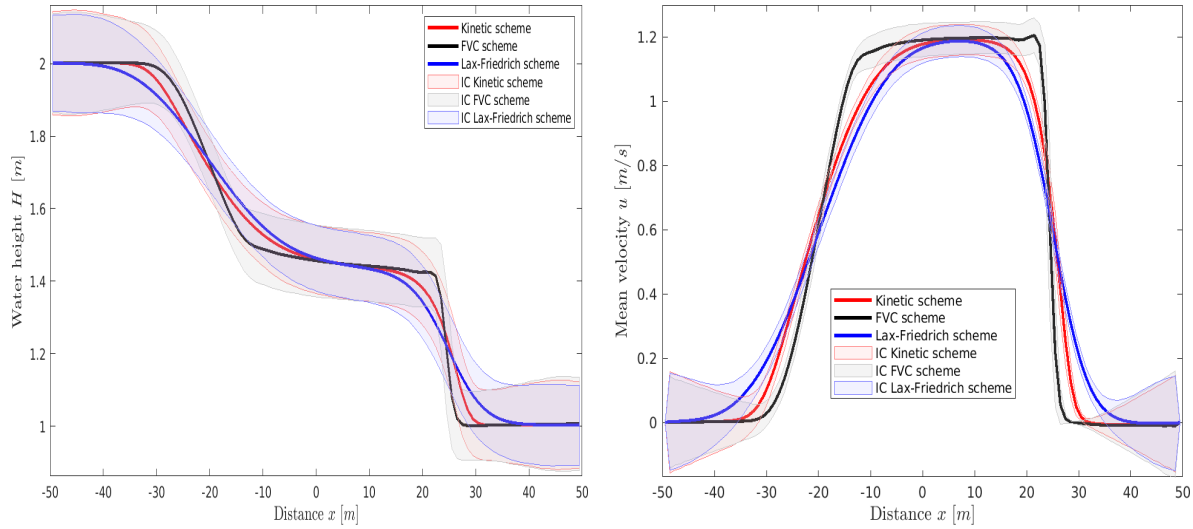

Figure 6.7: Mean solutions for water height (left plot) and mean velocity (right plot) for the dam-break problem over a flat bed.

Lax-Friedrichs method than for the FVC method. However, these methods do not display the same uncertainty for this test problem. In fact, the interval of confidence follows the physical feature of each variable namely, the water height and the water velocity. One can also notice that the FVC method displays less uncertainty than the other methods, especially around the shock area. For this reason, in the following we will consider only this method to solve the multi-layer shallow water equations.

6.4.2 Wind-driven recirculation flow over a flat bed

In this example we consider a class of wind-driven recirculation flow problems in closed domains. It should be pointed out that these recirculation features of the water flow can not be captured using the conventional single-layer shallow water equations. Hence, the present test is served as a prototype to verify the performance of multi-layer shallow water flows to reproduce such phenomena. In this example the multi-layer system is solved in a closed domain of 16 m long filled at 2 m with flat bottom topography. The water flow enters the lake from the left boundary with a speed of $w = 20\ m/s$ and flows towards the left exit of the lake. At later time, due to the wind effects, the water flow changes the direction pointing towards the right coast of the lake. The flow parameters are: viscosity coefficient $\nu = 0.1$ friction coefficient $n_b = 0.00001\ s/m^{1/3}$, wind stress coefficient $\sigma_s^2 = 0.0015$, water density $\rho = 1000\ kg/m^3$, air density $\rho_a = 1200\ kg/m^3$ and gravitational acceleration $g = 9.81\ m/s^2$, the simulation time for all the results presented in this example is $t = 20\ s$, using 17 control volumes. The aim of this test example is to study the effects of the accounted uncertainty for the bathymetry, the bed friction and the viscosity on the hydraulic states. We also investigate the impact of the number of layers used to capture the physical features on the uncertainty of the different physical variables. As in the previous example, the KL decomposition is used to sample the bathymetric field and the associated eigenvalues and eigenvectors are shown in Figure 6.8. The bathymetry process is supposed to be a Gaussian process described with 14 independent normal distributed random variables. In addition to these variables, we add the three other random variables representing the bed friction, the viscosity between layers and the wind stress. Three different numbers of layers

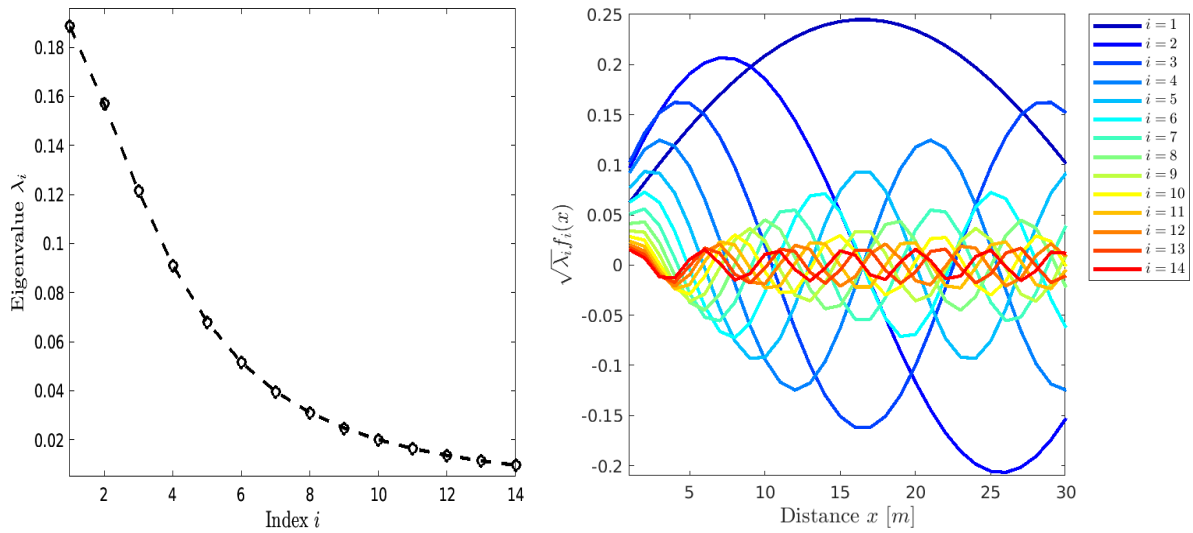

Figure 6.8: Eigenvalues (left plot) and associated eigenfunctions (right plot) of the correlation matrix in the KL decomposition for the wind-driven recirculation flow problem over a flat bed.

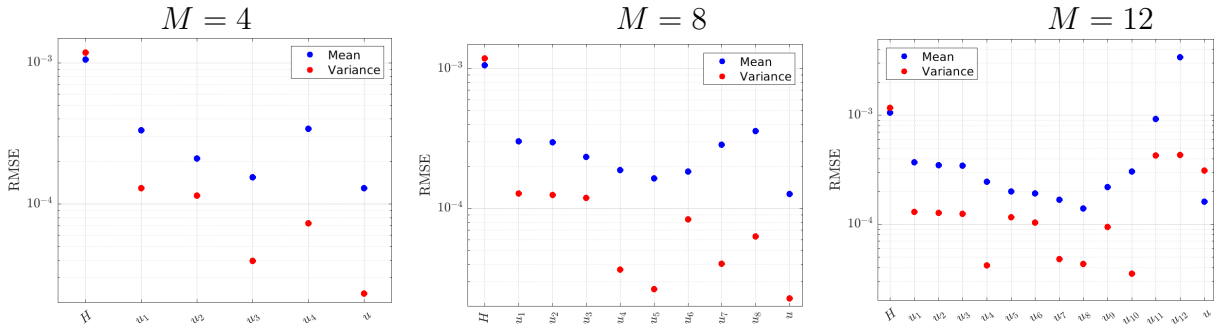

Figure 6.9: RMSE in the variance and the mean fields using 4, 8 and 12 layers for the wind-driven recirculation flow problem over a flat bed.

$M = 4$, 8 and 12 are used in this example.

In our computations, the surrogate model is built using 1000 forward simulations of the numerical model. Then, only few representative modes are selected using the proper orthogonal decomposition where the corresponding eigenvalues are supposed to contain the uncertainty displayed by the model. The PCE are therefore built using these eigenvalues. Table 6.2 summarizes the steps needed for building the surrogate model to quantify the uncertainty of both the water height and velocity. For this case, results demonstrate that only 5 modes are needed to accurately estimate the physical variability *i.e.*, only 5 polynomial representations are needed instead of the 100 polynomials corresponding the number of control volumes used in the FVC scheme. Results in Table 6.2 also demonstrate that the LOO error for this problem is very low suggesting that the polynomial chaos expansion has accurately assessed the uncertainty given by each mode. In addition, Table 6.2 suggests that a polynomial degree equal 3 is sufficient for all the eigenvalues of the POD. For the average velocity field, results for the POD ensure that, given the physical variability of the system and in order to have accurate proper decomposition, 30 modes are needed *i.e.*, 30 polynomial chaos expansions are needed to accurately assess the uncertainty. Yet, this number is smaller compared to the number needed without using the POD (in this case 100 expansions are needed corresponding to the number

Table 6.2: Best polynomial degrees with LOO errors for the POD modes in the water height and mean velocity using different numbers of layers for the wind-driven recirculation flow problem over a flat bed.

	Error and polynomial degree for water height H		
	$M = 4$	$M = 8$	$M = 12$
Number of modes	5	5	5
Error (M1)	1.365E-06	1.267E-06	1.251E-06
Error (M2)	9.059E-08	8.113E-08	8.06E-08
Error (M3)	4.012E-08	3.783E-08	3.739E-08
Error (M4)	5.095E-08	4.595E-08	4.263E-08
Error (M5)	3.596E-08	3.297E-08	3.154E-08
Polynomial (M1 - M5)	3	3	3

	Error and polynomial degree for water mean velocity u		
	$M = 4$	$M = 8$	$M = 12$
Number of modes	30	30	30
Error (M1)	8.018E-06	7.453E-06	8.064E-06
Error (M2)	1.820E-05	1.870E-05	1.844E-05
Error (M3)	9.717E-05	8.930E-05	9.236E-05
Error (M4)	5.629E-05	5.156E-05	4.688E-05
Error (M5)	6.351E-05	5.950E-05	5.767E-05
Error (M6)	6.104E-05	5.735E-05	5.886E-05
Error (M7)	6.566E-05	6.5180E-05	6.497E-05
Error (M8)	6.397E-05	6.865E-05	6.628E-05
Error (M9)	7.209E-05	6.528E-05	6.198E-05
Error (M10)	8.240E-05	8.059E-05	6.966E-05
Error (M11)	9.463E-05	8.461E-05	8.699E-05
Error (M12)	11.430E-05	11.06E-05	10.62E-05
Error (M13)	14.760E-05	13.96E-05	13.86E-05
Error (M14)	20.08E-05	21.20E-05	22.08E-05
Error (M15)	19.81E-05	20.24E-05	20.47E-05
Error (M16)	66.30E-05	65.33E-05	64.24E-05
Error (M17)	70.64E-05	66.91E-05	71.38E-05
Error (M18)	81.25E-05	75.44E-05	77.41E-05
Error (M19)	73.52E-05	72.42E-05	69.00E-05
Error (M20)	74.24E-05	82.57E-05	75.28E-05
Error (M21)	73.12E-05	73.59E-05	70.81E-05
Error (M22)	66.04E-05	67.76E-05	81.09E-05
Error (M23)	82.39E-05	82.39E-05	80.61E-05
Error (M24)	82.42E-05	82.78E-05	84.72E-05
Error (M25)	72.63E-05	75.82E-05	77.95E-05
Error (M26)	82.13E-05	77.52E-05	86.38E-05
Error (M27)	86.96E-05	86.36E-05	84.49E-05
Error (M28)	86.34E-05	85.27E-05	92.65E-05
Error (M29)	86.12E-05	87.62E-05	91.32E-05
Error (M30)	88.28E-05	88.33E-05	90.98E-05
Polynomial (M1 - M30)	3	3	3

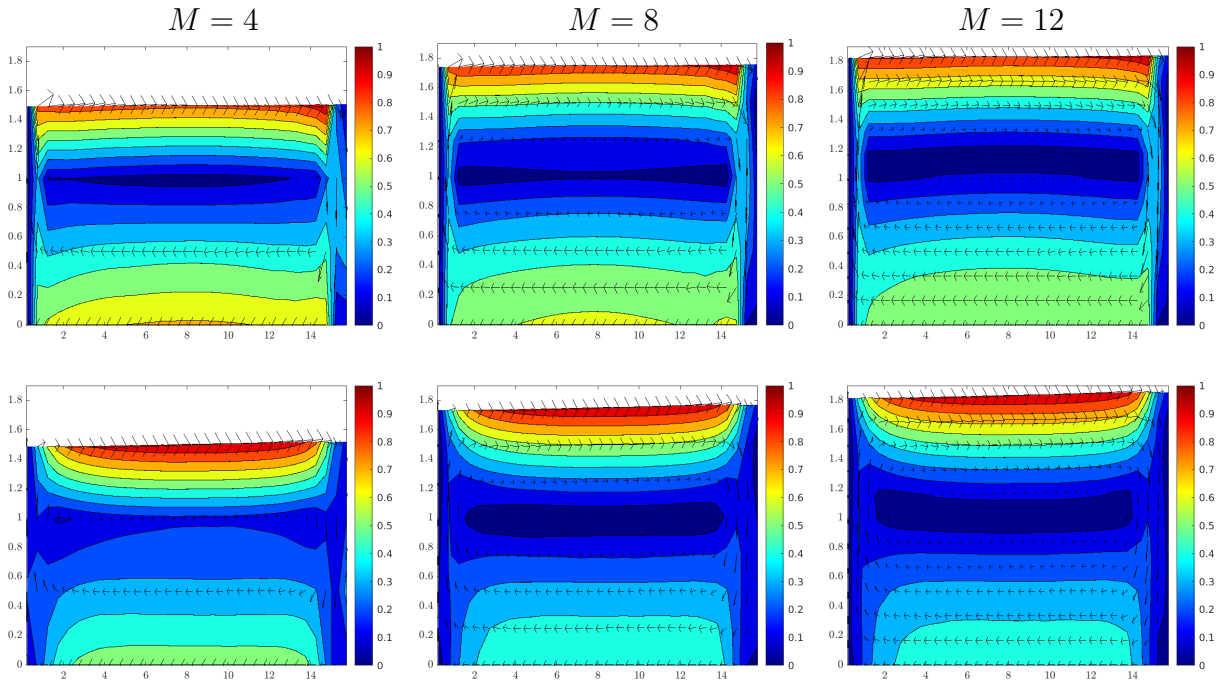

Figure 6.10: Deterministic flow fields (first row) and stochastic mean flow fields (second row) for the wind-driven recirculation flow problem over a flat bed using $M = 4$ (first column), $M = 8$ (second column) $M = 12$ (third column).

of control volumes). Again, as suggested by the results for the velocity in Table 6.2, the PCE computed over the eigenvalues converge with respect to the LOO error as all the errors are below 10^{-5}. Note that, although the errors in Table 6.2 confirm that the PCE converges, it is necessary to assess the accuracy of the whole surrogate model as the POD is expected to add some uncertainties on the surrogate model. For this purpose, an assessment of the accuracy of the surrogate model is performed in comparison with the Monte Carlo simulations using 100000 samples. We use the RMSE to quantify the errors in the estimation of the variance and the mean solutions. Figure 6.9 depicts the obtained results for all the considered cases. Notice that the RMSE errors are also estimated for velocities of all the layers. It is clear that values of the errors are below the LOO errors estimated previously. However, the RMSE errors are below 10^{-3} for all considered cases which makes the use of the surrogate model very reliable to quantify the uncertainty generated by the multi-layer shallow water equations for this flow problem. Figure 6.10 exhibits the velocity fields obtained using the considered numbers of layers. As can be seen, a central recirculation has been generated in the flow domain and an increase of the number of layers in the one-dimensional model yields a consistent convergence to the velocity profile obtained using the three-dimensional Navier-Stokes equations, compare for example [12, 81]. These results are a clear indication that it is possible to efficiently resolve the vertical variation in the water velocity using the one-dimensional shallow water equations without need to the three-dimensional Navier-Stokes equations. Furthermore, the mean solution computed by the surrogate model shows some differences compared to the deterministic solutions for this example. This is mainly due to the nonlinearities associated with the multi-layer shallow model equations. In order to investigate further the impact of these nonlinearities, ranges of uncertainty in the water height and averaged water velocity are included in Figure 6.11. One can see that all the three numbers of layers yield the same behavior in both the estimated water height and the averaged velocity. Note that there is a little

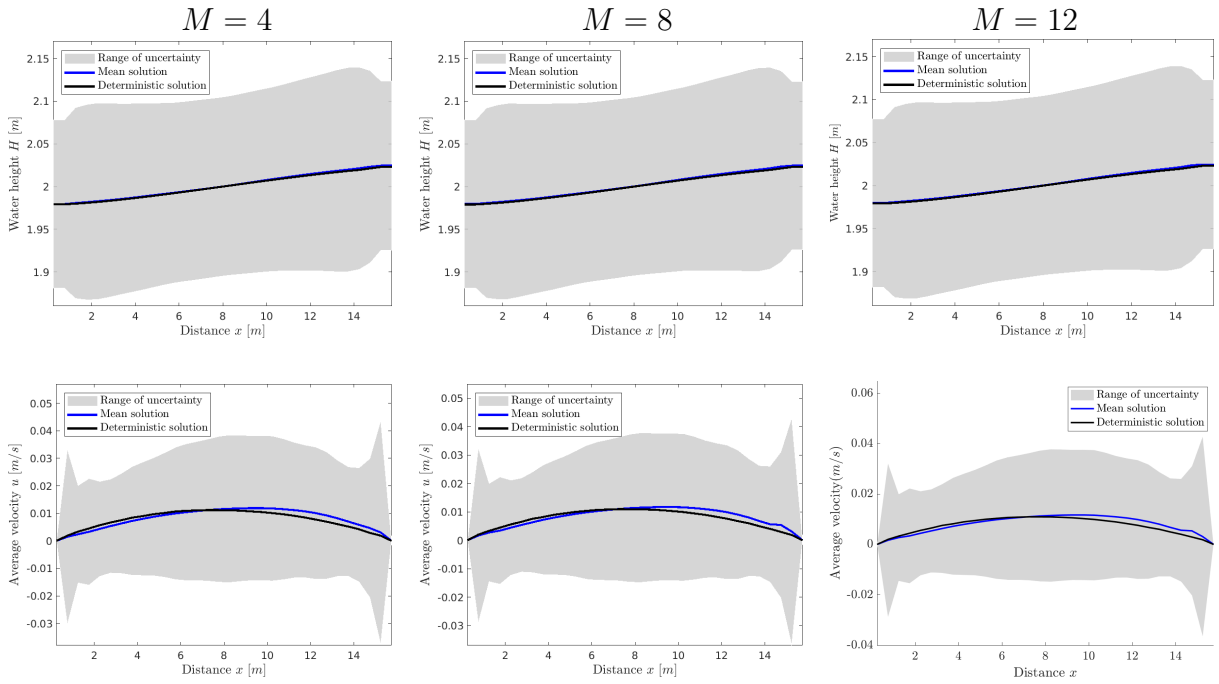

Figure 6.11: Uncertainty ranges for water height (first row) and mean velocity (second row) along with deterministic solutions for the wind-driven recirculation flow problem over a flat bed.

difference noticed between the stochastic and deterministic solutions in the averaged velocity profile. This suggests that the discrepancies observed in Figure 6.10 are generated from the velocity between layers. Moreover, One can also assess that the stochastic parameters considered in this recirculation flow problem are responsible for up to 5% in the uncertainty in the outputs.

6.4.3 Multi-layer free-surface flows in the Strait of Gibraltar

Our final test problem consists of a flow recirculation in the Strait of Gibraltar using the multi-layer shallow water equations with mass exchange. Note that this flow problem presents a realistic practical test of multi-layer shallow water flows for two major reasons. Firstly, the domain of the Strait of Gibraltar is relatively large including high gradients of the bathymetry and well-defined shelf regions. Secondly, the Strait is deep and contains two water bodies with different densities, which present a challenge in the shallow water modelling. Indeed, the basic Oceanic circulation in the Strait of Gibraltar consists of an upper layer of cold, fresh surface Atlantic water and an opposite deep current of warmer, salty outflowing Mediterranean water, compare for example [7, 104, 143]. A schematic map of the Strait of Gibraltar along with relevant locations is depicted in the left plot of Figure 6.12. The system is bounded to the north and south by the Iberian and African continental forelands, respectively, and to the west and east by the Atlantic ocean and the Mediterranean sea. In geographical coordinates, the Strait is $35^o45'$ to $36^o15'$ N latitude and $5^o15'$ to $6^o05'$ W longitude. Here, we consider a one-dimensional cross section along the Strait (obtained by a longitudinal section along the dashed line in the left plot of Figure 6.12). The computational domain and the associated bathymetry are displayed in the right plot of Figure 6.12. This restricted domain has also been considered in [55, 57, 164] among others. In this example the multi-layer system is solved in a

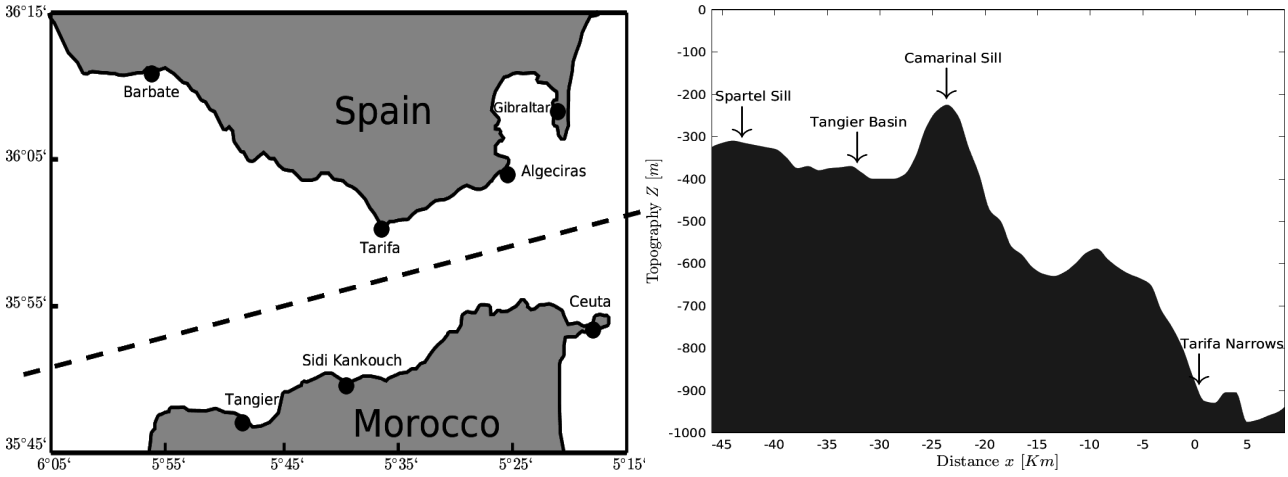

Figure 6.12: Schematic map of the Strait of Gibraltar along with relevant locations (left plot) and the bathymetry used for the one-dimensional simulations in the present study (right plot).

closed domain filled at 2 m of water with a wind speed of $w = 15\ m/s$ and flows towards the right exit of the lake. The flow parameters are: viscosity coefficient $\nu = 0.02$, friction coefficient $n_b = 0.07\ s/m^{1/3}$, wind stress coefficient $\sigma_s^2 = 0.0015$, water density $\rho = 1000\ kg/m^3$, air density $\rho_a = 1200\ kg/m^3$ and gravitational acceleration $g = 9.81\ m/s^2$, the simulation time for all the results presented in this example is $t = 50\ s$ using 50 uniform finite volume mesh. The purpose here is to quantify the uncertainty of hydraulic modelling using multi-layer shallow water equations. This step is very important if one wants to monitor the hydraulics linked activities such as maritime transport and fishery among others. In addition, one of the purposes of this study is to perform a sensitivity analysis for free-surface flows in the Strait of Gibraltar. This will help to prioritize the modelling parameters based on their contribution to the uncertainty of the hydraulic states. This will also identify the parameters that should be controlled once the model is used in an operational framework.

As in the previous examples, we construct our meta-model for all the physical variables (water height, averaged water velocity and the velocity for each layer). We begin by assessing the quality of the surrogate model compared to the Monte-Carlo simulations using 100000 evaluations of the model. We recall here that in order to reduce the dimensionality of the problem and to avoid the problem of reducing the number of control volumes which will impact the numerical accuracy, we use the proper orthogonal decomposition. Thus, the polynomial chaos expansion is computed over the eigenvalues of the decomposition. This would allow to have less number of decompositions than the original problem which consists on computing a decomposition for each variable at each control volume. The obtained results for the best polynomial degree and LOO errors for the POD modes in the water height and velocity using the FVC scheme are presented in Table 6.3. First, one can see that for a fixed value of the truncation error, the POD does not yield the same number of orthogonal functions. For example, the water height needs only 3 modes whereas, the averaged water velocity needs 15 modes. It should be stressed that this is a considerable reduction in the dimension of the output. Moreover, using the LAR method in order to build the polynomial expansion over the eigenvalues, Table 6.3 also reveals that polynomials of degree 2 to 3 are enough to correctly capture the uncertainty generated in the eigenvalues. the LOO error estimated for each mode demonstrates that the uncertainty of these modes are well captured by the considered polynomials with an error varying from 10^{-7} to 10^{-10}.

Table 6.3: Best polynomial degree with LOO errors for the POD modes in the water height and velocity using the FVC scheme for the flow recirculation in the Strait of Gibraltar.

	Water height	Mean water velocity
Number of modes	3	15
LOO error (M1)	6.169E-10	5.804E-08
LOO error (M2)	4.989E-09	1.320E-06
LOO error (M3)	1.588E-09	1.464E-07
LOO error (M4)	———	5.142E-08
LOO error (M5)	———	1.015E-07
LOO error (M6)	———	9.949E-08
LOO error (M7)	———	3.199E-07
LOO error (M8)	———	6.806E-07
LOO error (M9)	———	3.357E-07
LOO error (M10)	———	1.868E-07
LOO error (M11)	———	7.066E-07
LOO error (M12)	———	7.829E-07
LOO error (M13)	———	1.520E-06
LOO error (M14)	———	1.957E-06
LOO error (M15)	———	3.466E-07
Polynomial (M1)	3	3
Polynomial (M2)	3	3
Polynomial (M3)	2	3
Polynomial (M4-M11)	———	3
Polynomial (M12)	———	2
Polynomial (M13-M15)	———	3

It should be pointed out that in general assessing the accuracy of the PCE over the eigenvalues of the POD does not guarantee the convergence of the surrogate model. For this reason, the accuracy of the proposed surrogate model is compared to a very demanding Monte-Carlo simulations composed of 100000 forward simulations. Then, the RMSE is estimated for all physical variables of the hydraulic states for the estimation of the mean and variance solutions. The obtained results for this case are reported in Figure 6.13 and as for the previous case, the surrogate model allows to correctly quantify the uncertainty for all the physical parameters as the error is less than 10^{-3} in both the mean and variance solutions. Since the Monte Carlo simulations have been performed, we also assess the ability of the surrogate model to estimate the whole Probability Density Function (PDF) at the locations where data measurements are often collected for hydraulics namely, Camarinal Sill, Tangier Basin and Tarifa Narrows as shown in Figure 6.12. This comparison is shown in Figure 6.14 where the estimation of the whole PDF at these locations using Monte Carlo simulation are compared to those obtained

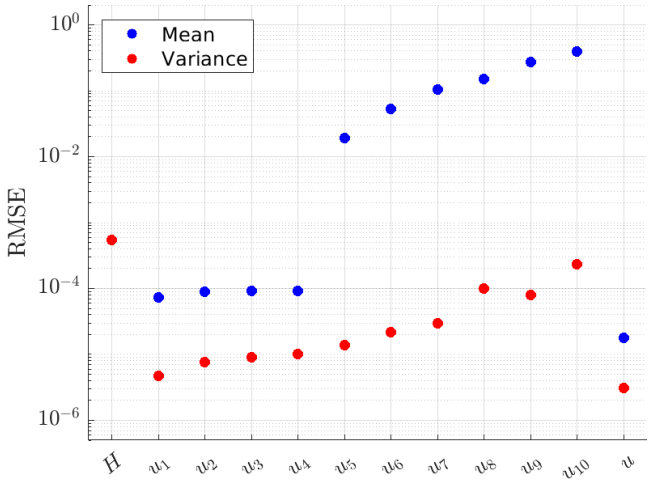

Figure 6.13: RMSE in different physical variables computed by the model for the flow recirculation in the Strait of Gibraltar.

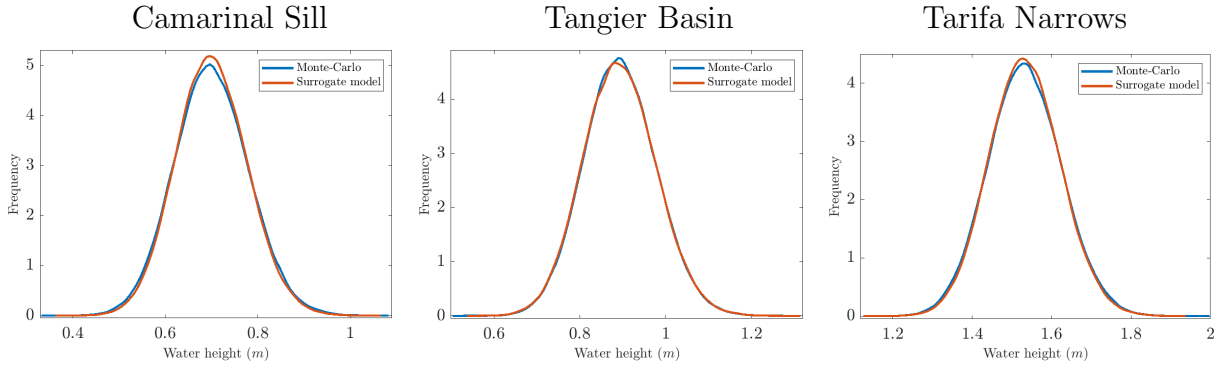

Figure 6.14: Probability density functions obtained at three different locations using the surrogate model and the Monte-Carlo for the flow recirculation in the Strait of Gibraltar.

suing the surrogate model. It is clear that the results demonstrate that generally there is a good estimation of the probability density function using the tools presented in this study.
A comparison between the deterministic and stochastic approaches is also carried our for this flow problem. In Figure 6.15 we compare the deterministic and stochastic mean solutions obtained for the flow fields. It is clear that the computed results exhibit slight differences especially in the downstream of the Strait. This is resulting from the nonlinearities of the exchange terms appearing in the multi-layer shallow water equations. Next, the uncertainty ranges of the hydraulic states are displayed in Figure 6.16. The obtained results show that the uncertainty ranges especially in the water height could not be negligible. The velocity profiles have also been tracked at the three locations where data is regularly collected. The uncertainty ranges in these velocity profiles are very narrow compared to the uncertainty in the water heights. Moreover, the same figure also illustrates the uncertainty range for the averaged water velocity. Although there is huge physical variability in this parameter, which can explain the need for high number of POD model, see Table 6.3, the uncertainty range is very narrow. These results demonstrate that the uncertainty in the bathymetry, the viscosity and the friction coefficients impact mostly the water height.
Finally, sensitivity analysis is carried out for this recirculation flow problem in the Strait of Gibraltar. Since, the water height is the parameter impacted the most from the stochasticity

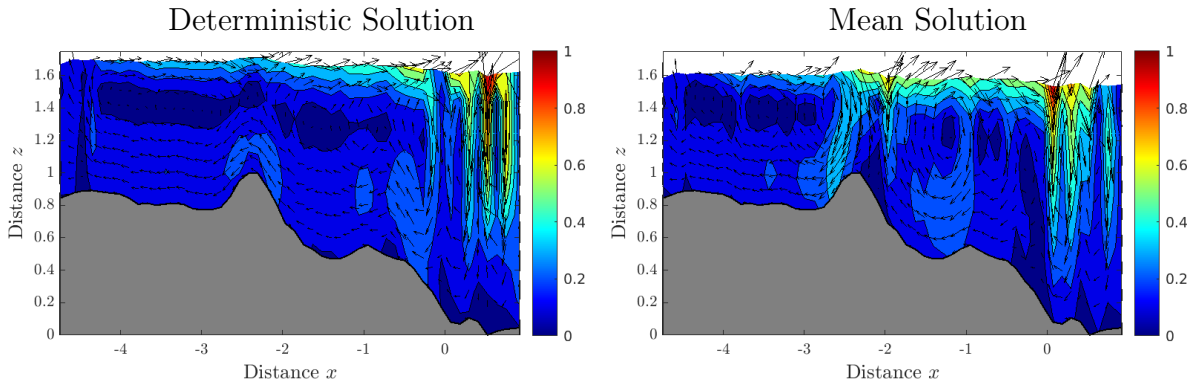

Figure 6.15: Deterministic and mean solutions of the velocity fields for the flow recirculation in the Strait of Gibraltar.

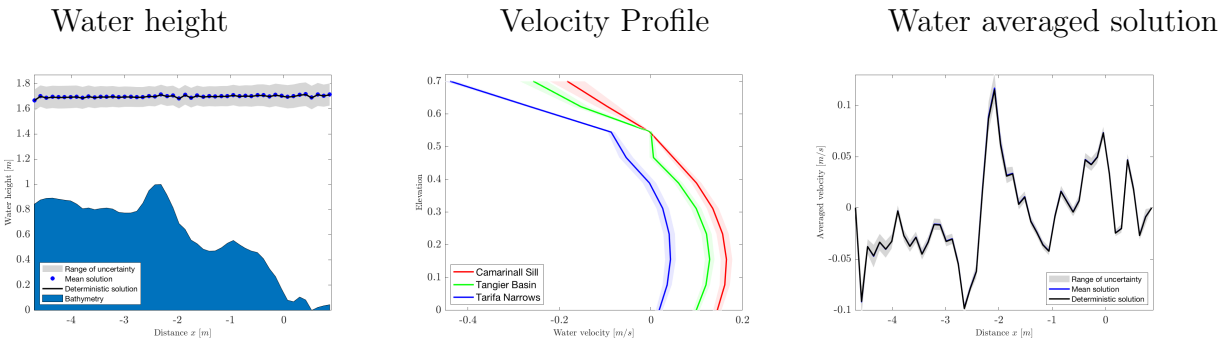

Figure 6.16: Uncertainty range in the water level (left plot), velocity profiles (middle plot) and averaged water velocity (right plot) for the flow recirculation in the Strait of Gibraltar.

considered in this study, the sensitivity analysis is carried out over this parameter. Note that the KL decomposition allows to sample the bathymetric field by introducing 16 random variables. Therefore, we assessed first a total Sobol index for these 16 random variables to which we add the Manning coefficient, the viscosity parameter and the wind friction coefficients. Furthermore, the sensitivity analysis is carried only at the three measurement locations and the obtained results are presented in Figure 6.17. First the result show that there are no differences between the first and total order, suggesting that the interaction between the random variables is negligible. Next at all considered locations, only random variables of the KL decomposition have high values. This suggests that the simulations of the water height are very sensitive to barthymetry. Finally one can see that reducing the uncertainty could be achieved with monitoring only four or three modes at most of the KL decomposition.

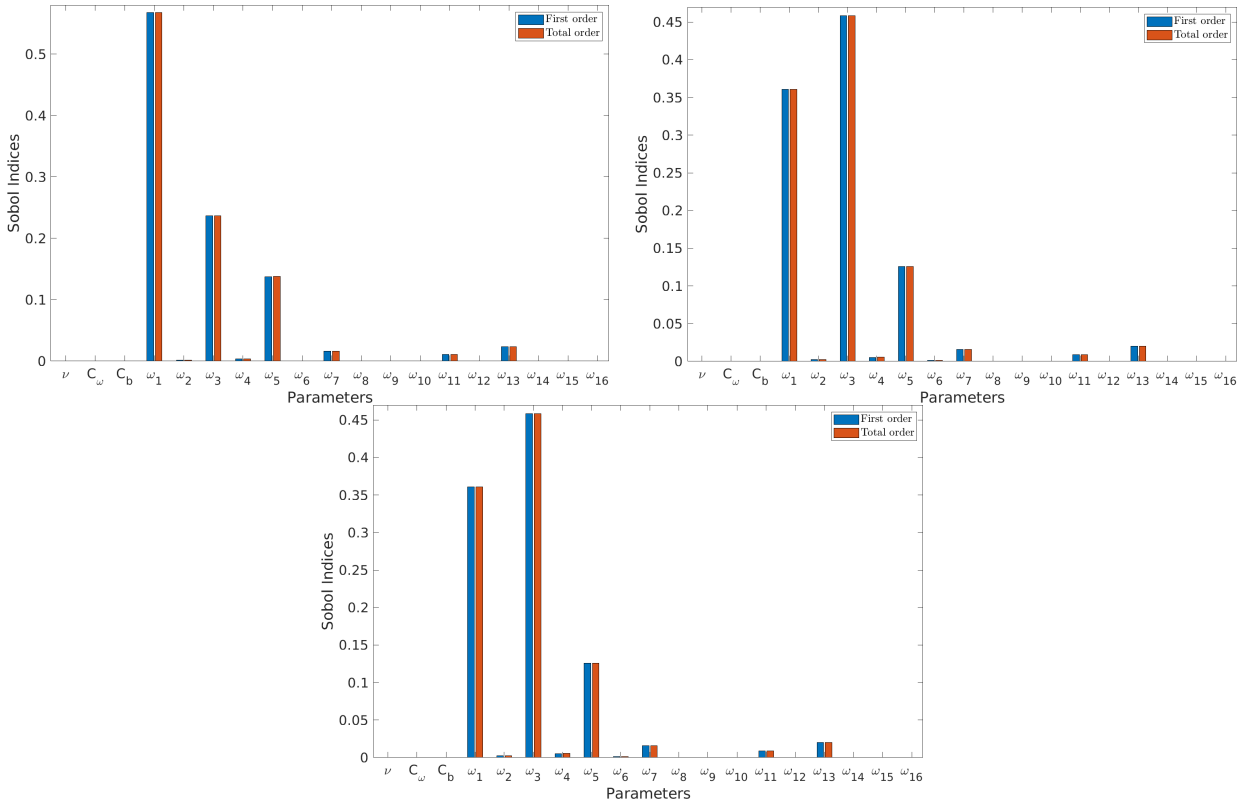

Figure 6.17: Sensitivity analysis using the Sobol indices at three locations in the Strait where data are measured periodically for Camarill, Tangier basin and Tarifa Narrow, respectively.

6.5 Conclusions

A surrogate model has been investigated in the present study for the propagation and quantification of the uncertainty in hydraulic modelling. The flow in such cases has usually many complex features making the classical shallow water equations not suitable for this type of hydraulic problems. In general, one has to consider the full three-dimensional Navier-Stokes equations which require a considerable computational cost to be numerically solved. However, the multi-layer shallow water models have proven their efficiency to replace the full three-dimensional Navier-Stokes equations while preserving the numerical flexibility given by the shallow water system and therefore could be considered to model the oceanic recirculation. While several previous studies demonstrated the numerical performance of the multi-layer shallow water models to accurately capture the complex pattern existing in the oceanic recirculation, to the best of our knowledge the problem of uncertainty quantification has been investigated for the first time. The implementation of surrogate models is a common practice for uncertainty quantification in computational fluid dynamics. The numerical model needs to be run several times, which increases the computational cost. Through the use of the surrogate models, the required numerous evaluation could be performed easily in a reasonable time. The literature has reported many surrogate models that are used in the context of uncertainty quantification. The choice of one or another is generally done based on numerical experiences. Usually when possible the robustness of theses models is assessed with comparison to the well established Monte-Carlo simulations given its statistical properties. In the present work, we choose to used polynomial chaos expansion based on the previous results of this model in the hydraulic computations. Furthermore, the spatial dimension of different quantities of interest

(water height and velocity) are reduced thanks to a proper orthogonal decomposition. The results are presented for three application cases: a dam-break problem, a wind driven circulation over a lake, and the real case of Strait of Gibraltar.
In the first case, we performed uncertainty quantification for a dam break problem. We assumed that the uncertainty of the simulations resulted from stochastic bed, friction coefficient, viscosity between layers and the wind friction terms. Moreover, the highlight was put here on the numerical schemes used to solve the multi-layer shallow water equations. We used three different numerical schemes, namely the Kinetic, the Lax-Friedrich and a finite volume characteristics method. The results demonstrated that the surrogate model performed well when compared to the Monte-Carlo simulations. The RMSE reaches an order of magnitude up to 10^{-3} for the estimation of the mean and the variance solutions using all the considered numerical methods. The results also demonstrated a good agreement in the simulation of the physical patterns in the mean field. Finally, we concluded that the numerical schemes do not display the same level of uncertainties. In the second, we performed uncertainty quantification for a wind driven circulation problem. As for the previous case, the stochastic parameters considered here include the bathymetry, the friction term, the viscosity between layers and the wind friction terms. The results showed a good agreement between the surrogate model and the Monte-Carlo simulations. The RMSE has an order of magnitude ranging from 10^{-4} to 10^{-3}. Moreover, we compared the results of the uncertainty for different number of layers in the model. We concluded that the uncertainty in the model is not much affected by the number of layers. However, one should be aware that the number of layers could affect the physical modelling which can yield modelling errors.
Finally, we applied our methodology to the real case of a flow recirculation in the Strait of Gibraltar. This place knows consistent economical activities over the time including fishery, transport and tourism among others. Therefore, it is important to monitor the flow in the Strait of Gibraltar. First the surrogate model is compared to Monte-Carlo simulations. Results demonstrated the good agreement represented by a value of RMSE ranging from 10^{-5} to 10^{-3}. Moreover, as three stations exist in this area, we evaluated the ability of the surrogate models to compute the probability density function. The results were compared with a probability density function computed with Monte-Carlo simulations. The results prove that the surrogate model perform very well for this flow problem. Finally, we were interested in a sensitivity analysis in these location. This could be a good indicator of what are the physical variables that one should monitor using either data assimilation or Bayesian inference in order to reduce the uncertainty of the numerical model. Results showed that the bathymetry is the main driver of uncertainty in the considered three locations.

Chapter 7

A developed optimization technique for reconstruction of topography in dam-break flows

Modelling dam-break flows over non-flat beds requires an accurate representation of the topography which is the main source of uncertainty in the model [66]. Therefore, developing robust and accurate techniques for reconstructing topography in this class of problems would reduce the uncertainty in the flow system [231]. In many hydraulic applications, experimental techniques have been widely used to measure the bed topography. In practice, experimental work in hydraulics may be very demanding in both time and cost. On the other hand, computational hydraulics have been served as an alternative for laboratory and field experiments. Unlike the forward problem, the inverse problem is used to identify the bed parameters from the given experimental data [271]. In this case, the shallow water equations used for modelling the hydraulics need to be rearranged in a way that the model parameters can be evaluated from measured data. However, this approach is not always possible and it suffers from stability restrictions [98]. In the present work, an adaptive optimal control technique to numerically identify the underlying bed topography from a given set of free-surface observation data is proposed. In this approach, a minimization function is defined to iteratively determine the model parameters. The proposed technique can be interpreted as a fractional-stage scheme. In the first stage the forward problem is solved to determine the measurable parameters from known data. In the second stage, the adaptive control Ensemble Kalman Filter is implemented to combine the optimality of observation data in order to obtain the accurate estimation of the topography. The main features of this method are on one hand, the ability to solve for different complex geometries with no need for any rearrangements in the original model to rewrite it in an explicit form. On the other hand, its achievement of strong stability for simulations of flows in different regimes containing shocks or discontinuities over any geometry. Numerical results are presented for a dam-break flow problem over non-flat bed using different solvers for the shallow water equations. The robustness of the proposed method is investigated using different numbers of loops, sensitivity parameters, initial samples, location of observations. The obtained results demonstrate high reliability and accuracy of the proposed techniques.

Bed topography is of paramout importance for the study of fluvial hydraulics, flood prediction and river flow monitoring [122]. It is therefore important to develop fast, easy to implement and cost effective methods to determine underwater river topography. Over the past few decades, extensive research has been performed to accurately predict and describe the environmental processes associated with geophysical flows. This includes monitoring river flow, predicting

floods with their potential risk of creating natural disasters and predicting Tsunami run-up [254]. Bed topography identification in open channel is of paramout importance for the study of the respective flows. In the former, the knowledge of the channel bed topography is required for modelling the hydrodynamics of open channel flows, fluvial hydraulics, flood propagation, and river flow monitorning. Indeed, flow models based on the shallow water approximation require prior information on the channel bed topography to accurately capture the flow features. While in the latter, usable bedrock topographic information is very important for flow modellers to accurately predict the flow characteristics. Experimental techniques to understand the bed topography are usually used but are mostly time consuming, and sometimes not possible due to geometrical restrictions. However, the measurement of free-surface elevation is relatively easy. Alternative to experimental techniques, it is therefore important to develop fast, easy to implement, and cost-effective numerical methods.

Bed topography has a crucial impact on many hydraulic applications which are widely modeled using the well-established shallow water equations. These models require prior information on the bed topography to be solvable and consequently resolve the flow features in the problem under study. Experimental measurements have been used in many hydraulic applications to reconstruct bathyemtry in free-surface flows. However, this may be limited with time, cost and also geographical restrictions which need to be replaced with fast, easy to implement and cost effective computational techniques [179]. In recent years, many research studies have been carried out to accurately describe and predict geophysical flows. This includes predicting floods, monitoring river flows, and predicting tsunami waves, see for example [123, 91, 168]. Accurate numerical modeling of this class of free-surface flows and predicting flood inundation all depends on the accurate representation of the bed topography. Authors in [34] have investigated the quality of the bathymetric airbone LiDAR survey. Information about the river bed geometry from top view has also investigated in [267]. In a slightly different context, authors in [221] have studied the inverse problem of reconstructing the topography from known data at the free-surface. On the other hand, there have been significant developments in experimental techniques to measure river bathymetry and flow depths. For instance, the interferometric Synthetic Aperture Radar (SAR) digital photogrammetry has been described in [24]. However, most experimental techniques to identify the bed elevation are expensive and time consuming, see for example [161, 3].

From a numerical view point, there are mainly two different approaches for bed reconstruction in hydraulics namely, the direct approach and the optimization-based approach. The direct approach of the inverse problem is not a common way in the literature. In this method, the governing equations of the forward problem are used in the model rearrangement. In practice, the process depends on the determination of observable parameters in the analysis of the forward problem. However, this approach is not always possible and it is restricted to some inverse problems. For example, authors in [23, 240] have implemented this approach to determine the bed elevation from known data in open channel and Glacier flows. The optimization-based approach is well known for solving this type of inverse problems in computational hydraulics. In this approach, a minimization function is formulated and used to iteratively determine the model parameters. This iterative procedure has been implemented in [263, 95, 130] to determine the topography and the bed roughness for several hydraulic problems.

In the current study the aim is to tackle problems of bed reconstruction in shallow water flows using adaptive control Ensemble Kalman Filter (EnKF). The reconstruction is carried out

based on given observation data at the free-surface for the water depth. The main focus is on dam-break problems over non-flat beds for which the topography required reconstruction. The governing equations consist of the conservation system of shallow water equations accounting for bathymetric effects. The purpose is to examine the performance of the optimal control method for different solvers of the direct problem. Computational results are presented for various tests on a dam-break problem over non-flat topography. The sensitivity of the method on different inputs including the initial guess and the uncertainty of observations is also examined. Numerical results presented in this study demonstrate high resolution of the proposed method and confirm its capability to provide highly accurate solutions for bed reconstruction in shallow water flows.

This chapter is structured as follows: Modelling dam-break problems is discussed in section 7.1. This section introduces the shallow water equations and the finite volume schemes used for the numerical solution. Section 7.2 presents the proposed adaptive control Ensemble Kalman Filter (EnKF) for bed reconstruction. This section includes an overview of the EnKF in data assimilation and the implementation of the method for bed reconstruction in dam-break problems. Numerical results are discussed in section 7.3. Numerical results for a wide range of input parameters are presented. Section 7.4 contains concluding remarks.

7.1 Modelling dam-break flows over non-flat beds

The well-established shallow water equations are considered in this study to model dam-break flows over non-flat beds. These equations can be derived by depth-averaging the incompressible Navier-Stokes equations and neglecting the vertical acceleration of water particles while the pressure is assumed hydrostatic, see [225] among others. In one space dimension, the shallow water equations read

$$\begin{aligned} \frac{\partial h}{\partial t} + \frac{\partial (hu)}{\partial x} &= 0, \\ \frac{\partial (hu)}{\partial t} + \frac{\partial}{\partial x}\left(hu^2 + \frac{1}{2}gh^2\right) &= -gh\frac{\partial B}{\partial x} - gh\tau_f, \end{aligned} \tag{7.1}$$

where t is the time variable, x the space coordinate, $h(x,t)$ the water depth, $u(x,t)$ the water velocity, g the gravitational constant and $B(x)$ the bed topography. In (7.1), τ_f is the friction slope term which models effects of the bottom friction as

$$\tau_f = M_b^2 \frac{u\,|u|}{h^{1/3}}, \tag{7.2}$$

where M_b is the Manning roughness coefficient on the bed. To be consistent with a dam-break problem, the equations (7.1) are equipped with the following initial condition

$$h(0,x) = \begin{cases} h_l, & x \le x_0, \\ \\ h_r, & x > x_0 \end{cases} \tag{7.3}$$

where x_0 is the location of the dam, h_l and h_r are the water heights at upstream and downstream of the dam. The equations (7.1)-(7.3) have been widely used in the literature to simulate dam-break problems, see for example [94, 26].

For simplicity in the representation, the equations (7.1) are reformulated in a conservative form as

$$\frac{\partial \mathbf{W}}{\partial t} + \frac{\partial \mathbf{F}(\mathbf{W})}{\partial x} = \mathbf{Q}(\mathbf{W}) + \mathbf{S}(\mathbf{W}), \tag{7.4}$$

where

$$\mathbf{W} = \begin{pmatrix} h \\ hu \end{pmatrix}, \qquad \mathbf{F}(\mathbf{W}) = \begin{pmatrix} hu \\ hu^2 + \frac{1}{2}gh^2 \end{pmatrix},$$

$$\mathbf{Q}(\mathbf{W}) = \begin{pmatrix} 0 \\ -gh\dfrac{\partial B}{\partial x} \end{pmatrix}, \qquad \mathbf{S}(\mathbf{W}) = \begin{pmatrix} 0 \\ -gM_b^2 \dfrac{u\,|u|}{h^{\frac{1}{3}}} \end{pmatrix}.$$

It is also well known that the system (7.1) is strictly hyperbolic with real and distinct eigenvalues given as

$$\lambda_1 = u - \sqrt{gh}, \qquad \lambda_2 = u + \sqrt{gh}. \tag{7.5}$$

Notice that the equations (7.1)-(7.3) have to be solved in a time interval and spatial domain equipped with given boundary conditions.

Numerical solution of the shallow water equations (7.1) has been subject of many research studies and several numerical methods have been developed for their accurate and efficient solutions. In the current work, four finite volume numerical solvers for hyperbolic systems of conservation laws were implemented. To deal with source terms in (7.1), a splitting operator was implemented for which the differential source terms $\mathbf{Q}(\mathbf{W})$ and the non-differential source term $\mathbf{S}(\mathbf{W})$ are solved in two stages. Hence, the time interval was divided into subintervals $[t_n, t_{n+1}]$ with uniform size Δt and $t_n = n\Delta t$. Using the notation $\mathbf{W}^n(x) = \mathbf{W}(x, t_n)$ to denote the discrete solution at time t_n. Thus, given the solution $\mathbf{W}^n$ at time t_n, the solution $\mathbf{W}^{n+1}$ at next time level t_{n+1} is obtained using the following two-stage splitting procedure:

Step 1: Solve for $\widetilde{\mathbf{W}}$

$$\frac{\widetilde{\mathbf{W}} - \mathbf{W}^n}{\Delta t_n} + \frac{\partial \mathbf{F}(\mathbf{W}^n)}{\partial x} = \mathbf{Q}\left(\mathbf{W}^n\right). \tag{7.6}$$

Step 2: Solve for $\mathbf{W}^{n+1}$

$$\frac{\mathbf{W}^{n+1} - \widetilde{\mathbf{W}}}{\Delta t_n} = \mathbf{S}\left(\widetilde{\mathbf{W}}\right). \tag{7.7}$$

For the space discretization, the domain was discretized into control volumes $\left[x_{i-\frac{1}{2}}, x_{i+\frac{1}{2}}\right]$ with uniform length Δx for simplicity only. Using the notation $\mathbf{W}_i^n$ to denote the space-averaged of $\mathbf{W} = \mathbf{W}(t, x)$ in the cell $\left[x_{i-\frac{1}{2}}, x_{i+\frac{1}{2}}\right]$ at time t_n, and $\mathbf{W}_{i+\frac{1}{2}}$ is the intermediate solution at $x_{i+\frac{1}{2}}$ at time t as

$$\mathbf{W}_i(t) = \frac{1}{\Delta x}\int_{x_{i-\frac{1}{2}}}^{x_{i+\frac{1}{2}}} \mathbf{W}(t, x)\, dx, \quad \mathbf{W}_{i+\frac{1}{2}} = \mathbf{W}\left(t, x_{i+\frac{1}{2}}\right).$$

Integrating the system (7.6) over the control domain $\left[x_{i-\frac{1}{2}}, x_{i+\frac{1}{2}}\right]$, one obtains the following fully discrete system

$$\mathbf{W}_i^{n+1} = \mathbf{W}_i - \frac{\Delta t}{\Delta x}\left(\mathbf{F}_{i+\frac{1}{2}}^n - \mathbf{F}_{i-\frac{1}{2}}^n\right) + \Delta t \mathbf{Q}_i^n, \tag{7.8}$$

where $\mathbf{F}^n_{i\pm\frac{1}{2}} = \mathbf{F}\left(\mathbf{W}^n_{i\pm\frac{1}{2}}\right)$ are the numerical fluxes at $x = x_{i\pm\frac{1}{2}}$ and time $t = t_n$ whereas, $\mathbf{Q}^n_i$ is a consistent discretization of the source term $\mathbf{Q}$ in (7.6). Note that the spatial discretization (7.8) is complete when the numerical fluxes $\mathbf{F}_{i\pm1/2}$ and the source term $\mathbf{Q}_i$ are reconstructed. Generally, this step can be carried out using any finite volume method developed in the literature for solving hyperbolic systems of conservation laws. In the present study, the following finite volume reconstructions are considered:

- Lax-Friedrich scheme [243]:

$$\mathbf{F}^n_{i+\frac{1}{2}} = \frac{1}{2}\left(\mathbf{F}\left(\mathbf{W}^n_{i+1}\right) + \mathbf{F}\left(\mathbf{W}^n_i\right)\right) + \frac{\Delta x}{2\Delta t}\left(\mathbf{W}^n_i - \mathbf{W}^n_{i+1}\right). \tag{7.9}$$

- Rusanov scheme [45]:

$$\mathbf{F}^n_{i+\frac{1}{2}} = \frac{1}{2}\left(\mathbf{F}\left(\mathbf{W}^n_{i+1}\right) + \mathbf{F}\left(\mathbf{W}^n_i\right)\right) + \frac{1}{2}\lambda\left(\mathbf{W}^n_i - \mathbf{W}^n_{i+1}\right), \tag{7.10}$$

  where $\lambda = \max\left(\lambda^n_1, \lambda^n_2\right)$ is the Rusanov speed with λ_1 and λ_2 are the two eigenvalues associated with the system defined in (7.5).

- Roe scheme [205]:

$$\mathbf{F}^n_{i+\frac{1}{2}} = \frac{1}{2}\left(\mathbf{F}(\mathbf{W}^n_{i+1}) + \mathbf{F}(\mathbf{W}^n_i)\right) + \frac{1}{2}\mathbf{A}\left(\widehat{\mathbf{W}}^n_{i+\frac{1}{2}}\right)\left(\mathbf{W}^n_i - \mathbf{W}^n_{i+1}\right), \tag{7.11}$$

  where $\widehat{\mathbf{W}}^n_{i+\frac{1}{2}}$ is the averaged state calculated as

$$\widehat{\mathbf{W}}^n_{i+\frac{1}{2}} = \begin{pmatrix} \dfrac{h^n_i + h^n_{i+1}}{2} \\ \dfrac{\sqrt{h^n_i}u^n_i + \sqrt{h^n_{i+1}}u^n_{i+1}}{\sqrt{h^n_i + h^n_{i+1}}} \end{pmatrix}, \tag{7.12}$$

  and $\mathbf{A}$ is the Roe matrix defined as $\mathbf{A} = \mathbf{R}\mathbf{\Lambda}\mathbf{R}^{-1}$ with

$$\mathbf{R} = \begin{pmatrix} 1 & 1 \\ \widehat{\lambda}_1 & \widehat{\lambda}_2 \end{pmatrix}, \qquad \mathbf{\Lambda} = \begin{pmatrix} \widehat{\lambda}_1 & 0 \\ 0 & \widehat{\lambda}_2 \end{pmatrix},$$

  where $\widehat{\lambda}_1$ and $\widehat{\lambda}_2$ are the two eigenvalues associated with the system defined in (7.5) evaluated at the Roe state (7.12).

- FVC scheme [28]: To reconstruct the numerical fluxes using the Finite Volume Characteristics (FVC) method, the equations (7.1) are first reformulated in an advective form as

$$\begin{aligned} \frac{\partial h}{\partial t} + u\frac{\partial h}{\partial x} &= -h\frac{\partial u}{\partial x}, \\ \frac{\partial u}{\partial t} + u\frac{\partial u}{\partial x} &= -gh\frac{\partial}{\partial x}\left(h + B\right). \end{aligned} \tag{7.13}$$

Then, using the method of characteristics to compute the solutions of (7.13) at the interfaces $x_{i\pm\frac{1}{2}}$. Thus, the associated characteristic curves $X_{i+\frac{1}{2}}(\tau)$ are computed as solutions of the initial-value problem

$$\begin{aligned} \frac{dX_{i+\frac{1}{2}}(\tau)}{d\tau} &= u\Big(\tau, X_{i+\frac{1}{2}}(\tau)\Big), \quad \tau \in [t_n, t_{n+1}], \\ X_{i+\frac{1}{2}}(t_{n+1}) &= x_{i+\frac{1}{2}}. \end{aligned} \tag{7.14}$$

To solve the ordinary differential equations (7.14) a second-order explicit Runge-Kutta method was used, see [28] for more details.

The numerical fluxes in the FVC scheme are obtained by integrating the advective equations (7.13) along the characteristics in the time interval $[t_n, t_n + \Delta t]$. Thus, assume an accurate approximation of the characteristics curves $X_{i+\frac{1}{2}}(t_n)$ is made, the intermediate solutions are obtained from (7.13) as

$$\begin{aligned} h^n_{i+\frac{1}{2}} &= \widetilde{h}^n_{i+\frac{1}{2}} - \frac{\Delta t}{\Delta x}\widetilde{h}^n_{i+\frac{1}{2}}\left(u^n_{i+1} - u^n_i\right), \\ u^n_{i+\frac{1}{2}} &= \widetilde{u}^n_{i+\frac{1}{2}} - g\frac{\Delta t}{\Delta x}\left((h^n + B)_{i+1} - (h^n + B)_i\right), \end{aligned} \tag{7.15}$$

where

$$\widetilde{h}^n_{i+\frac{1}{2}} = h\left(t_n, X_{i+\frac{1}{2}}(t_n)\right), \quad \widetilde{u}^n_{i+\frac{1}{2}} = u\left(t_n, X_{i+\frac{1}{2}}(t_n)\right),$$

are solutions at the departure points $X_{i+\frac{1}{2}}(t_n)$ computed by a cubic Lagrange interpolation from the gridpoints of the control volume where the departure point $X_{i+\frac{1}{2}}(t_n)$ belongs. Hence, the numerical fluxes for the FVC scheme are defined by

$$\mathbf{F}^n_{i+\frac{1}{2}} = \begin{pmatrix} h^n_{i+\frac{1}{2}} u^n_{i+\frac{1}{2}} \\ \\ h^n_{i+\frac{1}{2}}\left(u^n_{i+\frac{1}{2}}\right)^2 + \frac{1}{2}g\left(h^n_{i+\frac{1}{2}}\right)^2 \end{pmatrix}, \tag{7.16}$$

where $h^n_{i+\frac{1}{2}}$ and $u^n_{i+\frac{1}{2}}$ are intermediate solutions approximated in (7.15).

For the approximation of the source term in (7.8), we use the well-balanced discreization discussed in [28]. Hence, the discretization of the source term $\mathbf{Q}_i$ is carried out as

$$gh\frac{\partial B}{\partial x} \approx g\frac{h_{i+1} + 2h_i + h_{i-1}}{4}\frac{B_{i+1} - B_{i-1}}{2\triangle x}. \tag{7.17}$$

Note that, using this discretization of the source term, the scheme (7.8) satisfies the well-known C-property [28]. It should be stressed that other numerical solvers for the shallow water equations (7.1) can also be used in the present study without major conceptual modifications.

7.2 Optimal control method for reconstruction of topography

In this section, numerical tools used for the optimal control reconstruction of topography in dam-break flows are presented. In general, Data Assimilation (DA) aims at combining field

observations with different model inputs in order to reduce the uncertainty of a numerical model and improve its predictability in an optimal manner, see [172] among others. For hydraulics, a numerical model relies on mathematical description of the dynamic whereas, observation produces more accurate description of the actual state of the flow. Despite producing different outputs, the resulting uncertainty produced by the DA is below the uncertainties of both the numerical model and the observational data. Although the DA has been initially used for weather forecasting, different research topics have adopted this tool for operational purposes. In hydraulics, the DA is still emerging compared to other geophysical fields, see for example [175, 20] and further references are therein. Technically the DA aims at controlling the value of the model parametrization responsible for the largest amount of uncertainty. The optimality of this control is achieved due to the information given by the observations. Here, the cost function can be formulated as

$$J(x) = \frac{1}{2} \|x - x_B\|_{\mathbf{B}} + \frac{1}{2} \|y - \mathcal{H}(x_B)\|_{\mathbf{O}} , \tag{7.18}$$

where x_b is a prior knowledge (initial guess, back ground value) of the parameter which is usually referred to as the background, y the set of observation data at the hydrostatic state (either water depth or water speed), and $\mathcal{H}$ the observation operator. Since the DA takes into account the uncertainties, both norms $\|\cdot\|_{\mathbf{B}}$ and $\|\cdot\|_{\mathbf{O}}$ are defined within the uncertainty region of the background and the observation, respectively, as explained in the next section in more detailes. It should also be noted that the observation is not necessarily of the same nature as the parameter x and for example, the bathymetry may need correction using observations of the water level. In this case, the observation operator reduces to a linear interpolation operator. However, in most cases of hydraulic applications, this operator is highly nonlinear. The main objective of the DA is to minimize the cost function $J(x)$ under the constraints given by the uncertainties on the observation and the background. In general, equation (7.18) does not have an exact solution. However, a statistical estimation of the optimal parameter that minimizes the function $J(x)$ can be achieved using some inference methods such as filtering. When the uncertainties expressed around the parameter and the observation are supposed to follow a Gaussian probability distribution, the filtering could be carried out using the Kalman filter, compare [218].

7.2.1 Ensemble Kalman Filter

For the assumption of Gaussian uncertainties, estimating the probability distribution reduces to evaluating the mean and the covariance matrices. Thus, optimizing the functional (7.18) yields to find the main parameter x and its covariance matrix. In this framework, the background and the observation are fully defined by their covariance matrices $\mathbf{B}$ and $\mathbf{O}$, respectively. The Kalman Filter (KF) is a sequential DA algorithm which is able to reproduce these solutions under the assumption given above. This means that the KF provides an updated optimal solution for (7.18) whenever an observation is available. For this reason, this algorithm is classically divided into two steps: (i) the forecast stage and (ii) the analysis stage. During the first one, the model is dynamically moving forward in time with the background information until an observation is available. The analysis stage is then achieved by correcting the value of the background such that

$$x_a = x_b + \mathbf{K} (y - \mathbf{H}x) , \tag{7.19}$$

where x_a is the analysed value (the corrected value) of the parameter and $\mathbf{K}$ is the so-called Kalamn gain matrix defined by

$$\mathbf{K} = \mathbf{B}\mathbf{H}^\top \left(\mathbf{H}\mathbf{B}\mathbf{H}^\top + \mathbf{O}\right)^{-1}. \tag{7.20}$$

Algorithm 7.1 Proposed algorithm for bed reconstructions.

Require:

$Tend$: The final time for the simulation.

1: Perform a first simulation in order to generate the observation data.
2: Generate a set of bathymetric fields around the background value.
3: **while** $t < Tend$ **do**
4: Run the Ensemble of simulation.
5: Compute the Kalman Filter gain using a stochastic step as:

$$\mathbf{B}\mathbf{H}^\top = \frac{1}{N}\left(B - \overline{B}\right)\left(h - \overline{h}\right)^\top, \quad \mathbf{H}\mathbf{B}\mathbf{H}^\top = \frac{1}{N}\left(h - \overline{h}\right)\left(h - \overline{h}\right)^\top.$$

6: Compute the analysis state.
7: **end while**

As mentioned before, the KF is not only able to give the mean value but also the uncertainties modelled here in its covariance matrix

$$\mathbf{A} = (\mathbb{I} - \mathbf{K}\mathbf{H})\,\mathbf{B}, \tag{7.21}$$

where $\mathbb{I}$ is the identity matrix. Note that, in most hydraulic applications, the governing equations describing the physics are highly nonlinear such as the shallow water equation (7.1). Consequently, the KF can not be used because the operator $\mathcal{H}$ is nonlinear. One interesting way to overcome this drawback is to use the Ensemble Kalman Filter (EnKF).
In practice, the EnKF relies on the stochastic approach in order to overcome the problem of nonlinearity in the classical KF, see for instance [86]. Here, instead of considering the whole distribution for modelling the uncertainty of the parameter under study, one uses a set of sample $x_B = \left(x_b^{(1)}, \ldots, x_b^{(N)}\right)$ based on the distribution (Ensemble). Indeed, using Monte-Carlo simulations of the model, it is possible to stochastically estimate the different matrices forming the Kalman gain matrix such that

$$\mathbf{B} = \frac{1}{N-1}\left(x_b - \bar{x}_b\right)\left(x_b - \bar{x}_b\right)^\top, \tag{7.22}$$

where $\bar{x}_b$ denotes the mean value of x_b. Therefore, the covariance functions can be approximated using statistical averages of the solution ensemble.

7.2.2 Twin Experiment

In the present study a twin experiment is used to assess the quality of the DA algorithm. This is a well known methodology used when the access to real data is not possible, see [220] among others. The experiment consists on using a simulation with a supposed true value of the bathyemtry. The hydraulic state resulting from this simulation will be used as the observation. Then, using another value of the bathymetry (referred to by the background),

the EnKF will be applied. The analysis obtained by the proposed algorithm will be compared to the bathymetry which allows to obtain the hydraulic state of the observation. The EnKF is based on a stochastic approach such that the background value of the bathymetry will be perturbed. Hence, using an ensemble of bathymetric fields, a set of hydraulic state equations can be obtained. It is worth mentioning that the perturbation in this case follows a normal law with a mean value set to the background value and a fixed coefficient of variation. As in this case the covariance matrix has been implemented to be exponentially distributed. In order to have a good estimation of the reconstruction, the algorithm is performed several times. The iteration procedure is used here and for each test example the number of loops used will be mentioned. In summary, the proposed algorithm can be carried out using the steps described in Algorithm 7.1. In all our simulations, the coefficient of variation is set to 20% unless stated otherwise. Furthermore, the Root Mean Square (RMS) error is used to quantify the accuracy and performance of the proposed algorithm.

7.3 Numerical results

In this section numerical results for a dam-break problem over a non-flat bed are presented. The main goals of this test example are to illustrate the numerical performance of the techniques described above and to verify numerically their capability to reconstruct the correct topography using different initial guesses. Here, the system (7.1)-(7.3) is solved in a 30 m long channel with the upstream and downstream water heights $h_l = 1\ m$ and $h_r = 0.5\ m$, respectively. The dam is located at $x_0 = 15\ m$, the gravitational acceleration $g = 9.81 m/s^2$, the Manning coefficient $M_b = 0.03\ s/m^{1/3}$ and the computational domain is discretized into 100 control volumes with $\Delta x = 0.3\ m$. In all computations reported herein, the Courant number is set to $Cr = 0.75$ and the time stepsize Δt is adjusted at each time step according to the Courant-Friedrichs-Lewy condition

$$\Delta t = Cr \frac{\Delta x}{\max\left(|\lambda_1^n|, |\lambda_2^n|\right)}, \tag{7.23}$$

where λ_1 and λ_2 are the eigenvalues given by (7.5). The first step is solving the forward problem for a total time of $t = 2\ s$ over a known bed defined by a hump as

$$B(x) = \frac{1}{5} \exp\left(-\frac{(x-14)^2}{20}\right),$$

and store the water height at given locations to be used later as observational data in the Twin experiment. Examining the performance of the proposed method by changing (i) initial bed guesses, (ii) number and locations of observations, and (iii) finite volume schemes solving the shallow water equations.

7.3.1 Sensitivity on background values

The effects of the initial guess used for the bed function (background) on the accuracy of the reconstructed bed (analysis) are examined. The purpose here is to identify the ability of the EnKF to reconstruct the barthymetric field using different values for the background. In this

example, the following functions are implemented for the background bathymetry

$$\begin{aligned} B_1(x) &= 0, \\ B_2(x) &= \frac{1}{10}\exp\left(-\frac{(x-10)^2}{20}\right), \\ B_3(x) &= \frac{1}{5}, \\ B_4(x) &= \frac{1}{5}\exp\left(-\frac{(x-5)^2}{10}\right) + \frac{1}{5}\exp\left(-\frac{(x-25)^2}{10}\right). \end{aligned} \tag{7.24}$$

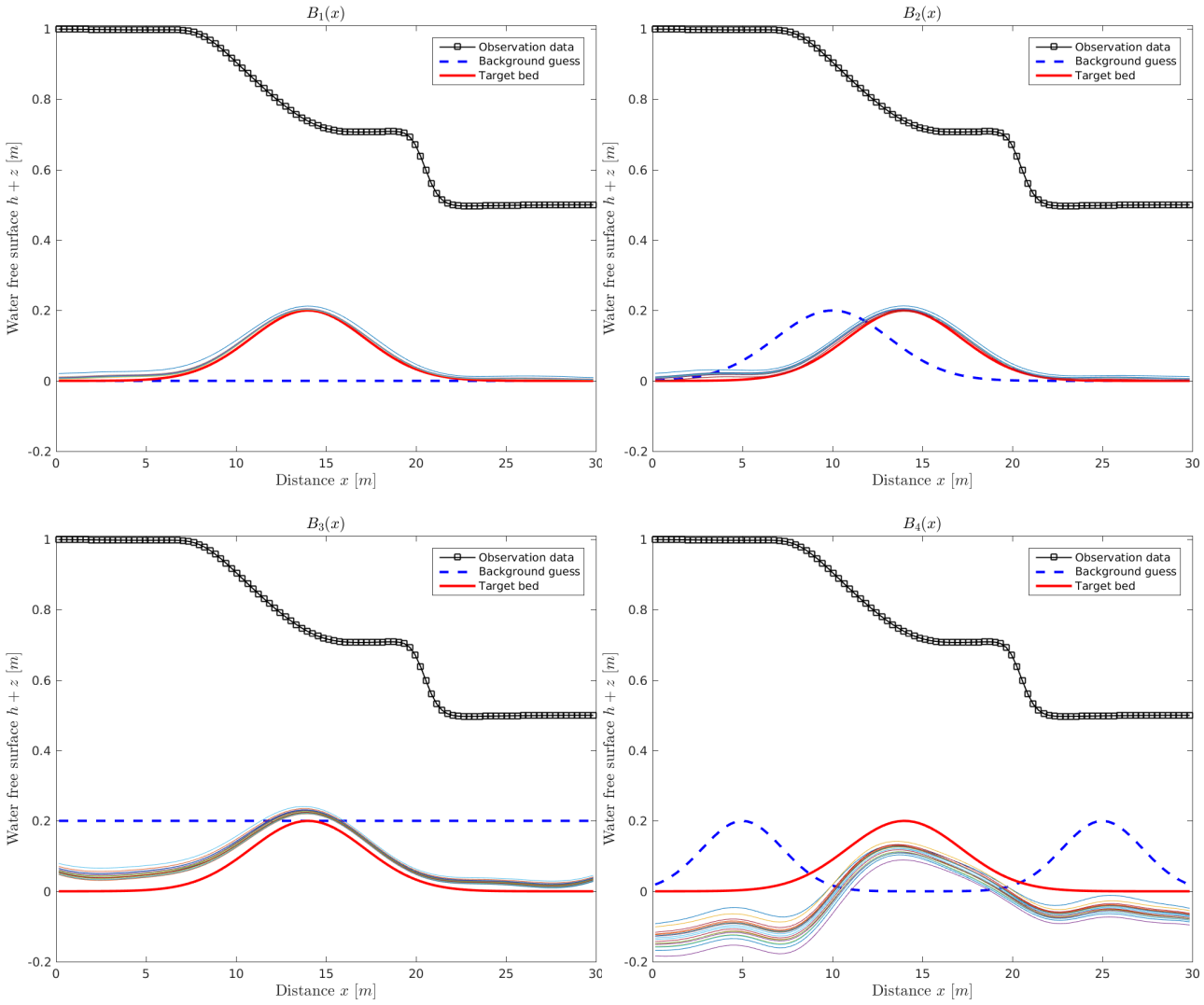

Figure 7.1: Results for the bed reconstruction using different initial bed functions.

In this example, the bed function $B_1(x)$ has been implemented to solve the forward problem and save the observation data at the water surface. Four bed functions $B_1(x), B_2(x), B_3(x)$ and $B_4(x)$ as a background guess have been choosen. The EnKF algorithm is run for each of background value defined in (7.24) using an Ensemble size of 200 simulations. Here, as numerical solver for the direct problem the Roe scheme has been implemented. The obtained numerical results for the expected bed are shown in Figure 7.1. In this Figure the observational

Table 7.1: RMS errors for the bed reconstruction using different initial bed functions.

Bed function	RMS error
$B_1(x)$	0.008075
$B_2(x)$	0.009475
$B_3(x)$	0.03158
$B_4(x)$	0.07210

data, the initial guess and the target bed for each run have been presented. As expected for a dam-break problem, at time $t = 0$ the dam collapses and the flow problem consists of a shock wave travelling downstream and a rarefaction wave travelling upstream. These features are well captured by this method in the results shown in Figure 7.1. In order to assess the quality of the DA algorithm for each of background used, the RMS error is computed for each experiment. Table 7.1 represents the value of the RMS error for the four bed functions in (7.24).

It is clear from the results shown in Figure 7.1 and Table 7.1 that the bed reconstruction is impacted by the value of the background used in the simulations. Indeed, using $B_1(x)$ and $B_2(x)$ as background valued in the optimal control method produces better results than those obtained using $B_3(x)$ and $B_4(x)$. This mainly due to the fact that the selected background values $B_1(x)$ and $B_2(x)$ are close to the target bed. As suggested by the value of RMS error, the correction gained one order of magnitude just by getting as close as possible to the target solution. It should be pointed out that this is one of the major difficulties when dealing with DA to reconstruct the bathymetry in hydraulics. This problem has also been reported in other studies, see for example [187]. This confirms that numerical tools can not replace *in-situ* experiments and field works carried out by hydraulic engineers remain an essential stage for bed reconstructions. In fact, using field measurements, the background value used for the bathymetry can be very close to the target bed which would help DA algorithms to gain accuracy. The proposed method performs well for this test example and the target bed can be accurately reconstructed without requiring complicated tools.

7.3.2 Sensitivity on finite volume schemes

In addition to the background value used in the method, selection of numerical schemes for shallow water equations constitutes an important key in DA algorithms. It is therefore important to assess the ability of such tool to correctly reconstruct the bathymetric field. Generally, there are two main key parameters that should be kept in mind when using a model with a stochastic-based algorithm like the EnKF namely, the choice of the numerical model and the uncertainty propagation in this model. In this section the impact of these two proprieties on the bathymetry reconstruction was evaluated. On the other hand the impact of the four finite volume schemes considered in this study on the reconstruction of topography in dam-break flows was assessed as well. The same parameters as in the previous run have been considered and then solving the forward problem Lax-Friedrich's, Rusanov, Roe, and FVC scheme at final time of $t = 2\ s$. A set of 100 observations of the water height uniformly distributed in the computational domain is used for the bed reconstruction. As initial guess for the bed, the background value $B_2(x)$ defined in (7.24) was used. In this simulations for this run, 100 samples and 20 iterations are used in the EnKF algorithm.

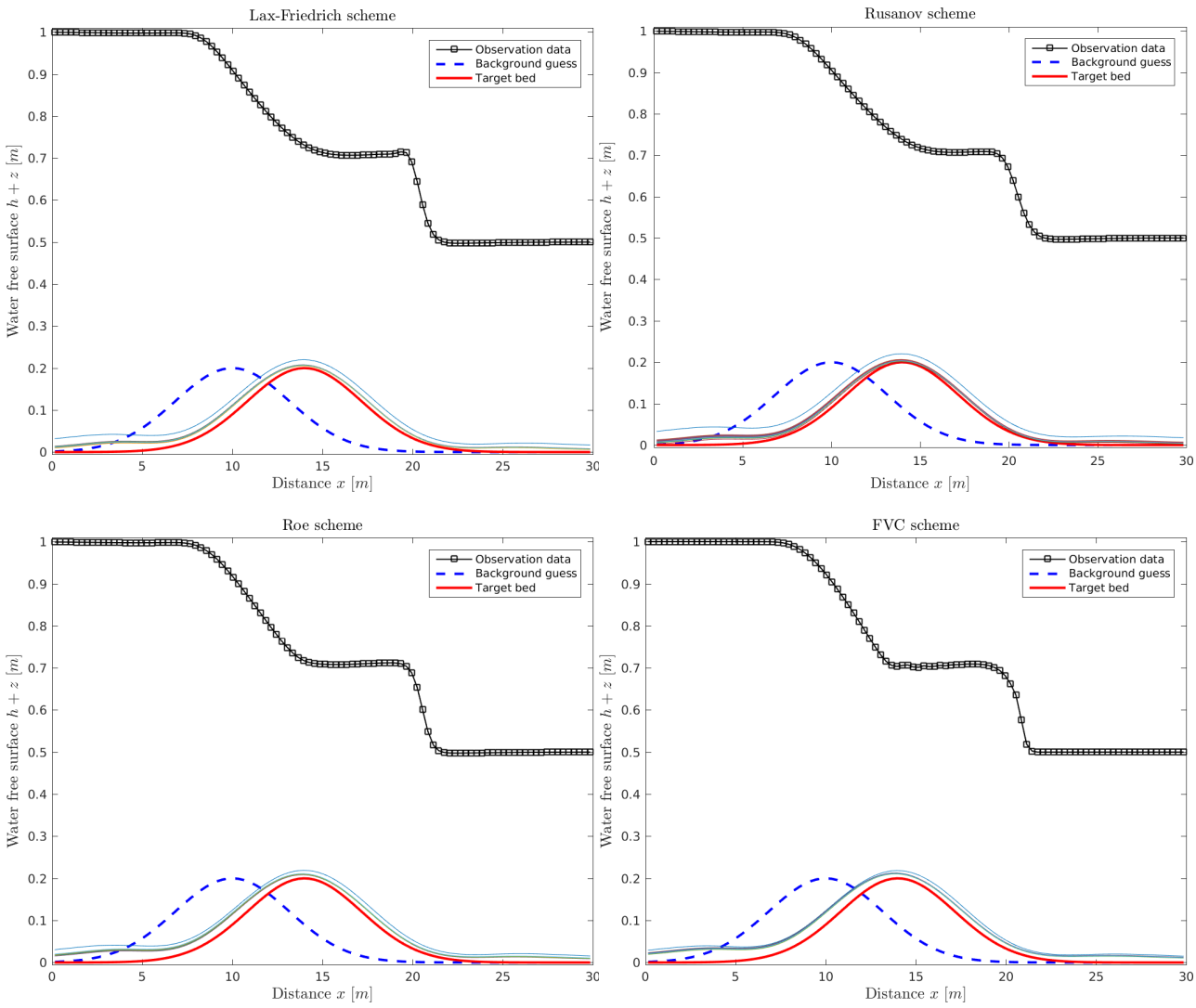

Figure 7.2: Results for the bed reconstruction using different finite volume schemes.

Figure 7.2 presents the obtained results for bed reconstruction using the four considered finite volume schemes. The evolution of RMS errors for these schemes at each iteration is illustrated in Figure 7.3. The results reveal that the EnKF does not show the same trends for these finite volume schemes. Indeed, the EnKF is based on a stochastic method such that the uncertainty is propagated into the model and the matrix which constitutes the Kalman Gain Matrix will be different depending on the numerical method used. The results shown in Figure 7.3 for the RMS errors confirm that the Roe and FVC schemes are more consistent than the Lax-Friedrich and Rusanov schemes. The numerical diffusion generated by Lax-Friedrich and Rusanov schemes could explain these differences whereas, the Roe and FVC schemes have proven to be very flexible to catch strong nonlinearity and discontinuities in the shallow water equations. Note that the main advantage of high accurate finite volume schemes lies on the fact that they can converge easily when used in algorithms like EnKF. However, the associated uncertainties may increase in the simulations which leads to poor reconstruction in the DA algorithm. On the other hand, using low accurate schemes, the numerical dissipation makes the DA algorithm very hard to converge, but they could easily lead to satisfying corrections.

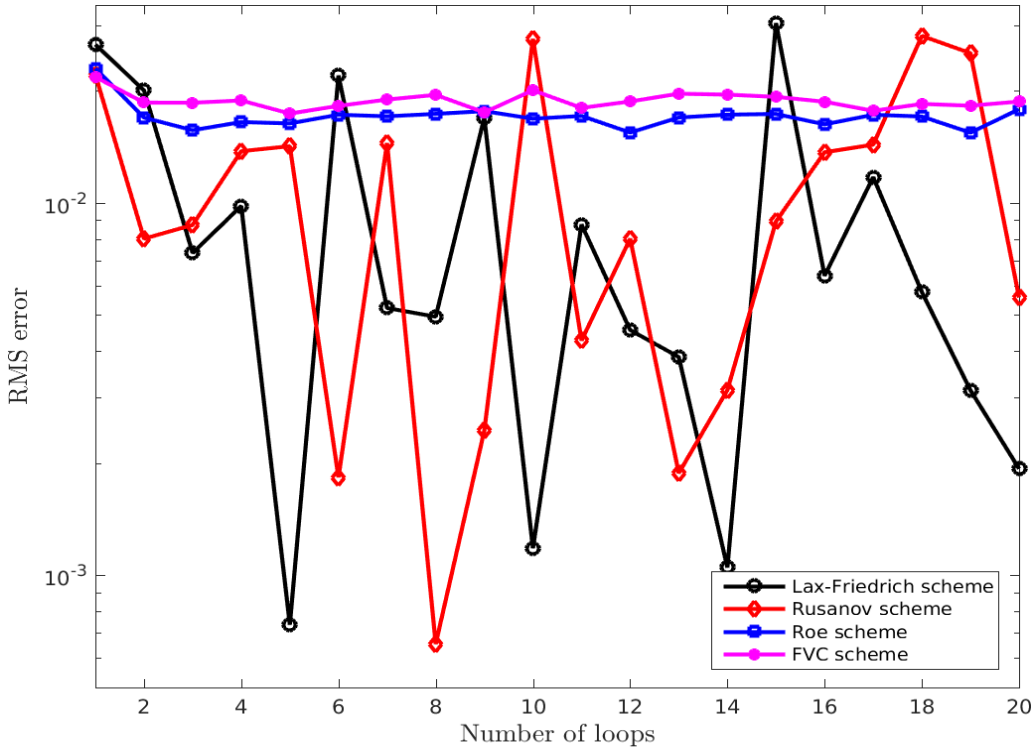

Figure 7.3: RMS errors for the bed reconstruction using different finite volume schemes.

7.3.3 Sensitivity on uncertainty in the background value

The next step is to check the impact of the uncertainty on the background and its effect on the bed reconstruction. In this test, the EnKF algorithm is running using three different uncertainty assumptions on the bed. It should be stressed that the well-established numerical methods for shallow water flows have been considered only the deterministic problems. The solutions are then admitted without paying attention to the uncertainty that are ubiquitous to any numerical model. Note that the classical way to assess the uncertainty of a numerical model is to reconsider it as a stochastic input. This means that the model parameters, boundary and initial conditions have to be seen as random parameters and/or processes. In this run, the same parameters are considered and flow conditions as in the previous case but an uncertainty in the bed was introduced. Three different levels of uncertainty are applied in this test with the coefficient of variation in the bed $CV_b = 7\%$, 11% and 16%.
The bed reconstruction results obtained using different levels of uncertainty are presented in Figure 7.4. On the other hand the RMS errors corresponding to these levels of uncertainty were depicted in Figure 7.5. As it can be seen in these Figures, increasing the value of the background uncertainty may help to achieve good level of correction. In fact, when using a Bayes theorem-based algorithm one should keep in mind that the selection of the parameters to be inferred has to be large enough in order to contain the uncertainty of the observation. This problem has been discussed in the literature, see [162] among others.

The correction obtained using the EnKF changes by applying iteratively the algorithm several times. As consequence, the quality of the reconstructed bed is impacted by the number of iterations used. Table 7.2 demonstrates the effect of changing the number of iterations at two different times $t = 1\ s$ and $t = 2\ s$. Clearly, the DA is impacted by the assimilation

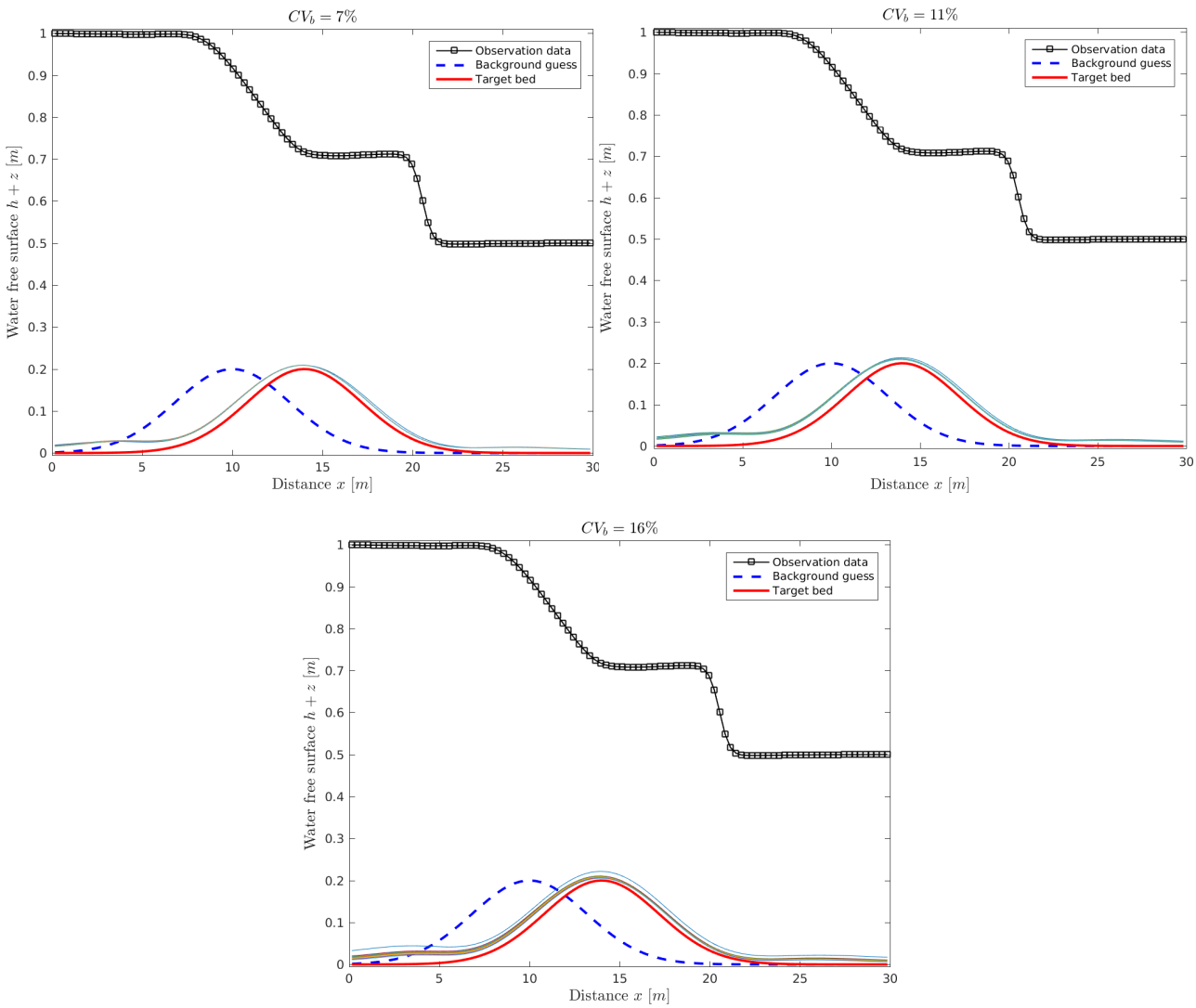

Figure 7.4: Results for the bed reconstruction using different uncertainties in the background value.

window that the quality of the correction with the DA dependants on the physical time used in the simulations. Results included in Table 7.2 gives a clear idea on the impact of these two parameters on the correction of the bathyemtry in dam-break flows.

As observed in the obtained results, the quality of the reconstruction does not improve with iterations when using an assimilation window at time $t = 1\ s$. This is due to the fact that the hydraulic has not been developed enough and all the information are still locked. Note that, this expected results if the well-known Best Linear Unbiased Estimator (BLUE) is employed. However, for the assimilation window at time $t = 2\ s$, the quality of the bed reconstruction improves considerably with the number of iterations. Moreover, the quality of the bed reconstruction is improved in this case compared to the the first case at $t = 1\ s$. Thus, these results emphasis the importance of considering a time-based algorithm such as the EnKF rather than a time-independent one such as the BLUE. It is also evident from the presented results that the assimilation is closely linked to the hydrodynamic. Hence, using the stochastic approach, one should make sure that the hydrodynamic has been developed enough to ensure a better correction. However, it is important to point out that the simulation time will also impact the

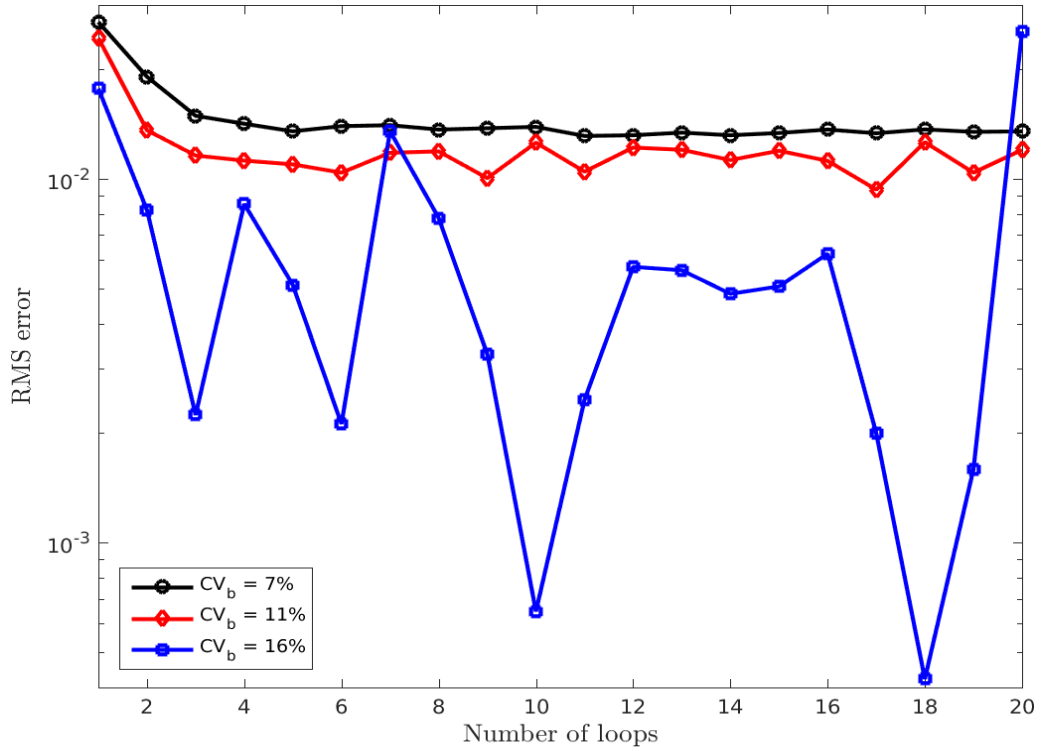

Figure 7.5: RMS errors for the bed reconstruction using different uncertainties in the background value.

Table 7.2: Evolution of RMS errors for the bed reconstruction using different uncertainties in the background value for different number of loops at time $t = 1\ s$ and $t = 2\ s$.

	RMS error	
Number of iteration	$t = 1\ s$	$t = 2\ s$
5	0.0382	0.01274
10	0.03391	0.01014
15	0.03601	0.009825
20	0.03666	0.009815
25	0.03754	0.009737
30	0.03733	0.009459
35	0.03764	0.009001
40	0.03724	0.009263
45	0.03693	0.008525
50	0.03654	0.009812

uncertainty propagation in the numerical model used in the simulations. Therefore, there is a clear trade-off related to simulation time versus the uncertainty that should be kept under consideration when using the DA for hydrodynamic models. The best use of such algorithms dictates that one should have a good length of assimilation window while paying attention to the uncertainty.

7.3.4 Sensitivity on observed data at the free-surface

Observed data is considered to be one of the most important keys in DA algorithms. Using the Twin experiment, it allows to assess the impact of the key factor on the quality of bed corrections. The level of discrepancy in these data will have a direct effect on the quality of the algorithms. Thus, in order to accurately predict the bathymetry in dam-break flows, DA algorithms should be precise and accurate with respect to the observation setting. For this purpose a dam-break problem with the same flow conditions as in the previous test is used in this run. In this section, three main parameters are investigated with regards to the observation data: (i) the number of the observation data, (ii) the location of the observation data and (iii) the uncertainty in the observation data.

First, the effects of the number of observation data used in the EnKF were assessed. This is especially important in the case where one needs to correct a space-based parameter such as the bathymetry. In this test case, different numbers of observations are used for the bed reconstruction and the obtained RMS errors for each number are presented in Table 7.3. It is clear that, as the number of iterations increases the accuracy of the reconstructed bed increases and the RMS error decreases accordingly. However, given the hydrodynamic of the dam-break under study, location of the observation data is important. This is for example what explains the difference between the run using 50 observations and the run using 25 observations. Note that the effects of the number of observation data is clearly seen on the correction in a way that more sets of observation data are available the best the correction is. From a practical point of view, this would mean that one needs to install gauges along the whole flow channel to collect measurements, which is less likely to be feasible from an economic perspective. An alternative way would be through the use of remote sensing data. However, the limitation in these techniques is associated with the uncertainty in the recorded measurements. Next, the effects of the location of observation data and the uncertainty on these data were examined.

Table 7.3: RMS errors for the bed reconstruction using different number of the observation data.

Observations	RMS error
5	0.06957
10	0.01604
20	0.009025
25	0.00739
50	0.031127
100	0.009344

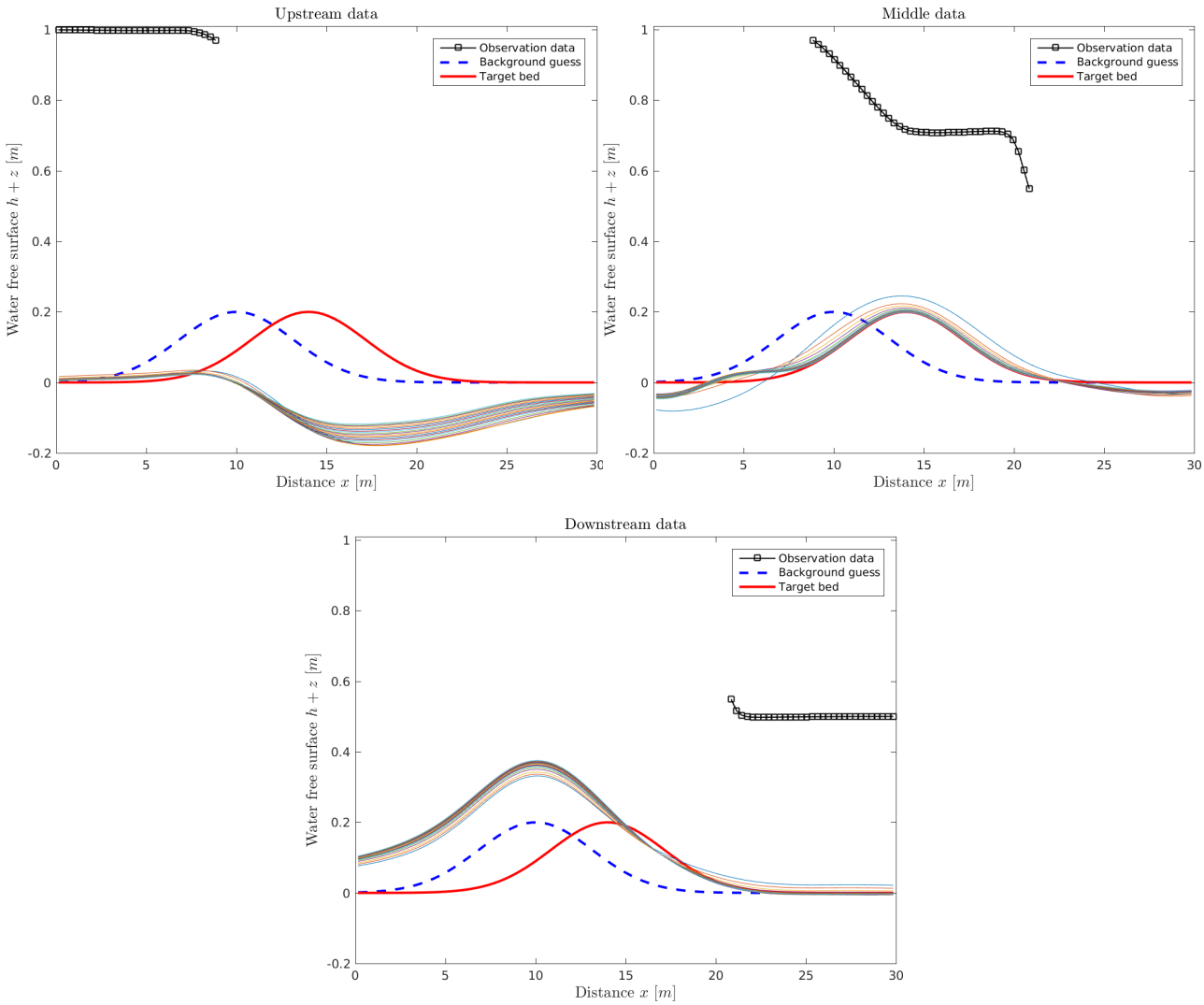

Figure 7.6: Results for the bed reconstruction using different locations of the observation data.

Table 7.4: RMS errors for the bed reconstruction using different locations of the observation data.

Location range	RMS error
1 m - 10 m	0.1038
10 m - 20 m	0.0062
20 m - 30 m	0.0814

To examine the effect of the spatial distribution of the observed data on the bed reconstruction, running the same example as before but changing the location of these data. Here, three different locations of the observation are tested along the flow channel in both downstream and upstream. More precisely, selecting observation data in the upstream region between 1 m and 10 m, in the middle region between 11 m and 20 m, and in the downstream region between 21 m and 30 m. The obtained results are illustrated in Figure 7.6 and the associated RMS errors are summarized in Table 7.4. Under the considered flow conditions, these results

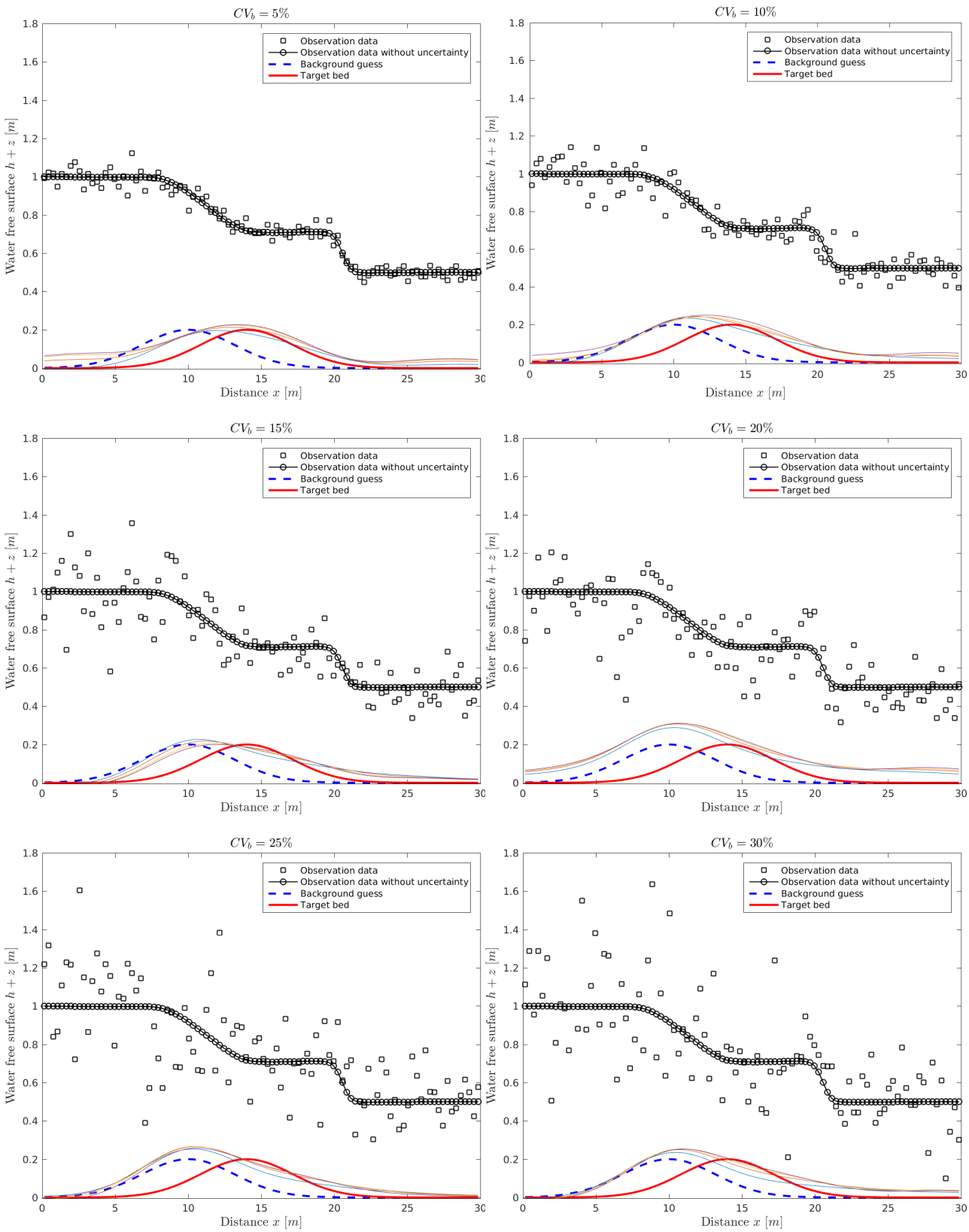

Figure 7.7: Results for the bed reconstruction using different uncertainty in the observed data.

clearly highlight the importance of the location in observations for the correction. Again, the

Table 7.5: RMS errors for the bed reconstruction using different uncertainty in the observed data.

Coefficient of variation	RMS error
0.05	0.07234
0.10	0.06092
0.15	0.04825
0.20	0.06646
0.25	0.03605
0.30	0.009845

correction is highly dependent on the hydrodynamic as it has been aforementioned. It is also evident that, when the dam-break occurs, the dynamics are mostly concentrated around the dam location. This is mainly the reason why the best bed reconstruction is obtained when the observation are around the dam location. Furthermore, when the observation data are located downstream, the EnKF produces a better correction. Needless to mention that, dealing with shallow water equations, the waves that propagates downstream and upstream do not have the same velocity. It is expected that the waves propagating downstream have more speed than the upstream ones. This explains the reason why the correction happening downstream is better than the upstream correction.

Finally, assessing the sensitivity of the EnKF on the inherited uncertainty in the observation data. This is an important feature that should be taken under consideration when dealing with reconstruction of a hydraulic field using the DA. In practice, different kind of observations would produce different measurements and each measurement is always accompanied with a range of uncertainty. In the computations reported here, six different uncertainty values with coefficient of variations $CV_b = 5\%$, $CV_b = 10\%$, $CV_b = 15\%$, $CV_b = 20\%$, $CV_b = 25\%$ and $CV_b = 30\%$ are considered. The same flow condition as those used in the previous test cases has been applied.

Figure 7.7 presents the obtained results for this run and the associated RMS errors are included in Table 7.5 for the considered coefficients of variations. As can be seen, the uncertainty on the observation data greatly impacts the correction and it can lead to big discrepancies in the required results. It is also clear from the RMS errors in Table 7.5 that, increasing the uncertainty in the observation data results in an increase in the RMS error. It is worth to mention that the DA is a trade off between the background values and the observation data used for the bed reconstruction. The quantity and quality of the background values and the observation data highly influence the algorithm outcome. Consequently, if the uncertainty of the observation data increases, one would expect more confidence on the background values. This fact is supported by the results presented in Figure 7.7 as the reconstruction hardly move from the background value.

7.4 Conclusion

A robust optimal control method for the bed reconstruction in dam-break flow problems has been implemented. The governing equations consist of the non-linear system of shallow water equations with bathymetric effects. A class of four finite volume schemes has been implemented to solve the forward problems. The optimal control methodology is based on the Ensemble Kalman Filter for the bed reconstruction. This gives a major advantage compared to the conventional direct problem methodologies based on the partial differential equations rearrangements. This can lead to complex formulations and implementations, in addition to its restrictions to simple bed topographies. This numerical approach is applicable for numerous situations related to the underwater bed reconstructions compared to experimental method. Experimental method is considered to be extremely difficult and expensive to reach for maintenance operations, so sensor failures are not uncommon. When this happen it is very difficult and takes a lot of time to repair or replace if possible. In addition to the problem of data missing and distortion until these maintenance operations carried out. The performance of the proposed method is examined using different numbers and locations of the observed data, different numbers of loops, and different initial guesses for the bed topography. We have also added stochasticity to the initial guess for the bed as well as the observed data. In all cases, the method accurately captures the expected bed confirming its ability to reconstruct the bed topography from noisy observational data. In addition, the computational results obtained for the considered test cases demonstrate the accuracy and efficiency of the proposed method. The presented results also reveal good shock resolution with high accuracy in smooth regions and without any spurious oscillations near the shock areas. Although we have restricted our simulations to the one-dimensional problems, the optimal control method investigated in the current work can be extended to free-surface flows in two space dimensions with viscous terms, Coriolis forces and over complex topography. These and further issues are subject of future investigations.

Chapter 8

Conclusions

This thesis presents a detailed study of the development and validation of an improved class of models for simulating the effect of the underground movement on the shallow water waves, which employed different coupling techniques at the interface. Likewise, an adaptive optimal control technique for bed reconstructions was implemented. Studying the effect of uncertainty in some parameters in the system showed that bed uncertainty has an enormous effect on shallow water simulation. This has been achieved by developing shallow water models to include techniques to study the full shallow water system. The resulting models have been verified as robust and less computationally demanding, achieving the goal of this thesis. This is important, as it also provides a modular platform, from which further advances can be made.

This thesis has been comprised of three major parts. The first of these seeks to resolve the modelling issues of shallow water flows over deformed beds; coupling techniques between the water free-surface and bed deformation were carefully examined. A hybrid finite element/finite volume method for solving free-surface run-up flow problems over deformable beds has been proposed; topographical deformations are the product of localized force, ensuing the propagation of waves of varying amplitude and frequency. Nonlinear, one-dimensional shallow water equations have been utilized, which incorporate friction terms for the water free-surface and two-dimensional, second-order, solid elastostatic equations for bed deformation. The hydrostatic pressure and friction forces have been implemented for the elastostatic equations whereas the deformed beds have been accounted for in the shallow water equations through the bathymetric forces. As such, the well-balanced finite volume method was applied for the shallow water system and the stabilized finite element method for linear elasticity equations. Similarly, two different methods have been offered for the transfer of information through the interface. The first one was the two-mesh procedure, which employed proper interpolation to transfer the data between the surface nodes and the control volumes, using uniform finite volume mesh distribution. In the second method, to avoid interpolation at the interface, a finite volume method, using non-uniform mesh distribution, has been chosen.

In the second part, the propagation and influence of several uncertainty parameters have been quantified in a class of numerical methods for free-surface single-layer, two-layer and multi-layer shallow water models on either flat and non-flat topographies. The uncertainty in the hydraulic states such as the water height and the water velocity as responses from the bathymetric forces (topography, Manning coefficient, wind friction and viscosity between layers) has been utilized. The free-surface profiles have been computed for different realizations of the random variables when the bed is excited, with sources whose statistics are well defined. As

numerical methods for shallow water equations, four finite volume schemes have been implemented. To reduce the required number of samples for uncertainty quantification, the proper orthogonal decomposition method has been combined with the polynomial chaos expansion, ensuring the efficient uncertainty quantification of complex hydraulic problems with a large number of random variables. The obtained results demonstrated that, in some hydraulic applications, a highly accurate numerical method yields an increase in uncertainty. On the other hand, when the complexity of the physics increases, these highly accurate numerical methods display less uncertainty compared with low accuracy methods.

In the third part, the adaptive control Ensemble Kalman Filter has been implemented to tackle the issue of bed reconstruction in shallow water flows. The main focus was on dam-break problems over non-flat beds, for which the topography required reconstruction. The reconstruction was carried out based on water depth observations data at the free-surface. The governing equations consist of the conservation system of shallow water equations, accounting for bathymetric effects. The purpose was to examine the performance of the optimal control method for different solvers of the direct problem. Computational results have been presented for various tests of a dam-break problem over non-flat topography. The sensitivity of the method on different inputs, including the initial guess and the uncertainty of observations, is also examined. Numerical results exhibit the high resolution of the proposed method and confirm its capability to provide highly accurate solutions for bed reconstruction in shallow water flows.

Solving different cases in the previous three parts encountered the problem of the wet/dry interface. To solve this issue, a new numerical model for moving wet/dry fronts in shallow water equations has been devised, using the parametrization concept and the Riemann solver; nonlinear shallow water equations were reformulated according to the speed of the wet/dry interface. The new system resolved the wet domain with a well-balanced finite volume method. A class of simple, easy, and accurate numerical methods has been developed, which overcame the moving wet/dry front encountered in shallow water flows. This finite volume scheme has been developed to such an extent that it is capable of satisfying the conservation property, resulting in numerical solutions free from spurious oscillations in significant moving wet/dry fronts. It achieved stability for simulations of slowly varying wet/dry interfaces, as well as rapidly varying wet/dry ones containing shocks. Moreover, the numerical formulation was designed so that the source terms were discretized using well- balanced techniques. These features were verified using several test examples of shallow water flows over drying areas. Results showed the high resolution of the proposed techniques and permitted the straightforward application of the method to more complex, physically-based shallow water flows.

For future research, the finite element/finite volume model could be further developed to include erosion and deposition effects, allowing for sediment transport and morphodynamics in the shallow water flows. The work conducted in this thesis has been mainly focused on the elastic deformation in bed topography and it can be extended to study the effect of nonlinear plasticity in bed deformation and the strong interaction of water flows on soft beds. For real-time simulations, these coupling techniques can be extended to study the three-dimensional cases. The second area of development could be assessing uncertainty quantification for parameters in two-dimensional shallow water flows, in addition to studying the impact of uncertainty in the force magnitudes and frequencies affecting the underground bed and its results in the shallow water waves. Developing new optimal control techniques for bed reconstructions, such as Genetics algorithms and neural networks, might be the third area of development. This

is important in order to fully investigate the potential of the propsed techniques for future implementations.

Bibliography

[1] A. Abdollahi and H. Mason. Tsunami-induced pore water pressure response of unsaturated soil beds: Numerical formulation and experiments. *Computers and Geotechnics*, 110:19–27, 2019.

[2] V. Aizinger and C. Dawson. A discontinuous Galerkin method for two dimensional flow and transport in shallow water. *Water resources*, 25:67–84, 2005.

[3] A. Akanbi and N. Katapoda. Model for flood propagation on initially dry land. *J. of Hydraulic energy*, 114:689–706, 1988.

[4] F. Alcrdo and P. Garcia. Flux difference splitting for 1D open channel flow equations. *Int. J. Numer. Meth. Fluids*, 14:1009–1018, 1992.

[5] F. Alcrdo and P. Garcia. A high resolution Godunov type scheme in finite volume for the 2D shallow water equations. *Int. Numerical methods fluids*, 16:10–17, 1993.

[6] S. Aliabadi, M. Akhbar, and R. Patel. Hybrid finite element/volume method for shallow water eqution. *International Journal for numerical methods in Engineering*, 83:1719–1738, 2010.

[7] J. Almazán, H. Bryden, T. Kinder, and G. Parrilla. *Seminario Sobre la Oceanografía Física del Estrecho de Gibraltar*. SECEG, Madrid, 1988.

[8] D. Ambrosi. Approximation of shallow water equations by Roe's Riemann solver. *Journal of hydrology*, 20:157–168, 1995.

[9] S. Amiri, N. Talebbeydokhti, and A. Baghlani. A two-dimensional well-balanced numerical model for shallow water equations. *Scientia Irancia*, 20:97–107, 2013.

[10] G. Aronica, B. Hankin, and K. Beven. Uncertainty and equifinality in calibrating distributed roughness coefficients in a flood propagation model with limited data. *Advances in water resources*, 22:349–365, 1998.

[11] C. Arvanitis and A. Delis. Behavior of finite volume schemes for hyperbolic conservation laws on adaptive redistributed spatial grids. *SIAM journal on scientific computing*, 28:1927–1956, 2006.

[12] E. Audusse. A multilayer Saint-Venant system: Derivation and numerical validation. *Discrete and Continuous Dynamical Systems, Ser. B.*, 5:189–214, 2005.

[13] E. Audusse, F. Bouchut, M. Bristeau, R. Klein, and B. Perthame. A fast and stable well-balanced scheme with hydrostatic reconstruction for shallow water flows. *SIAM Journal on Scientific Computing*, 25:2050–2065, 2004.

[14] E. Audusse, M. Bristeau, M. Pelanti, and J. Sainte-Marie. Approximation of the hydrostatic Navier-Stokes system for density stratified flows by a multilayer model: Kinetic interpretation and numerical solution. *J. Comp. Physics.*, 230:3453–3478, 2011.

[15] E. Audusse, M. Bristeau, B. Perthame, and J. Sainte-Marie. A multilayer Saint-Venant system with mass exchanges for shallow water flows. derivation and numerical validation. *M2AN Math. Model. Numer. Anal.*, 45:169–200, 2011.

[16] C. Baladron, A. Javier, L. Calavia, C. Belen, S. Antonio, and H. Luis. Performance study of the application of artificial neural networks to the completion and prediction of data retrieved by underwater sensors. *Sensors*, 12:1468–1481, 2012.

[17] M. Banner and W. Peirson. Wave breaking onset and strength for two-dimensional deep-water wave groups. *Journal of fluid mechanics*, 585:93–115, 2007.

[18] A. Bareza, R. Donat, and A. Matinez. A numerical treatment of wet/dry zones in well-balanced hybrid schemes for shallow water flow. *Applied numerical mathematics*, 62:264–277, 2012.

[19] S. Barman, D. Johnson, and S. Bhuvaneswari. Application of the shallow water equation to real flooding case. *International journal of advanced science and technology*, 29:1169–1174, 2020.

[20] S. Barthélémy, S. Ricci, O. Pannekoucke, O. Thual, and P. Malaterre. Emulation of an Ensemble Kalman Filter algorithm on a flood wave propagation model. *Hydrology and Earth System Sciences Discussions*, 10:6963–7001, 2013.

[21] P. Bates and M. Horritt. Modelling wetting and drying processes in hydraulic models. *Applications in environmental hydraulics*, 2:7–15, 2005.

[22] N. Baudry and S. Calmant. 3D modelling of seamount topography from satellite altimetry. *Geophysical Research Letters*, 18:1143–1146, 1991.

[23] C. Beffa and R. Connell. Two dimensional flood plain flow: Model description. *Journal of hydrologic engineering*, 6:397–405, 2001.

[24] L. Bellemare, J. Dumas, and G. Dhatt. A finite element model of estuarian and river flows with moving boundaries. *Adv. Water resources*, 13:158–168, 1990.

[25] K. Benjamin and R. David. A direct simulation method for particle-Fluid systems. *Journal of engineering computation*, 21:151–168, 2004.

[26] F. Benkhaldoun, S. Sari, and M. Seaid. A flux-limiter method for dam-break flows over erodible sediment beds. *Applied Mathematical Modelling*, 36:4847–4861, 2012.

[27] F. Benkhaldoun, S. Sari, and M. Seaid. A simple multi-layer finite volume solver for density-driven shallow water flows. *Mathematics and computers in simulations*, 99:170–189, 2014.

[28] F. Benkhaldoun and M. Seaid. A simple finite volume method for the shallow water equations. *J. Comp. Applied Math*, 234:58–72, 2010.

[29] C. Bermm, N. Goseberg, I. Schlurmann, and I. Nistor. Long wave flow interaction with a single square structure on a sloping beach. *J. Mar. Sci. Eng*, 821:821–844, 2015.

[30] A. Bermudez and M. Vázquez-Cendón. Upwind methods for hyperbolic conservation laws with source terms. *Computers & Fluids*, 23:1049–1071, 1994.

[31] M. Bermúdez, C. Neal, P. Bates, G. Coxon, J. Freer, L. Cea, and J. Puertas. Quantifying local rainfall dynamics and uncertain boundary conditions into a nested regional-local flood modeling system. *Water Resources Research*, 53:2770–2785, 2017.

[32] P. Bernardara, E. de Rocquigny, N. Goutal, A. Arnaud, and G. Passoni. Uncertainty analysis in flood hazard assessment: hydrological and hydraulic calibration. *Canadian Journal of Civil Engineering*, 37:968–979, 2010.

[33] M. Berveiller, B. Sudret, and M. Lemaire. Stochastic finite element: a non intrusive approach by regression. *European Journal of Computational Mechanics/Revue Européenne de Mécanique Numérique*, 15:81–92, 2006.

[34] G. Berz. Flood disasters: Lessons from the past worries for the future. *Water and marine time engineering*, 142:1–10, 2000.

[35] S. Bi, J. Zhou, Y. Liu, and L. Song. A finite volume method for modeling shallow water with wet/dry fronts on adaptive cartesian grids. *Mathematical problems in engineering volumes*, 20:321–331, 2014.

[36] A. Blanzo. Evaluation of methods for numerical simulations of wetting and drying in shallow water flow models. *Coastal engineering*, 34:83–107, 1998.

[37] G. Blatman. *Chaos polynomial creux et adaptatif pour la propagation d'incertitudes et l'analyse de sensibilité*. PhD thesis, 2009.

[38] G. Blatman and B. Sudret. An adaptive algorithm to build up sparse polynomial chaos expansions for stochastic finite element analysis. *Probabilistic Engineering Mechanics*, 25:183–197, 2010.

[39] G. Blatman and B. Sudret. Adaptative sparse polynomial chaos expansion based on Least Angle Regression. *Journal of Computational Physics*, 230:2345–2367, 2011.

[40] G. Blatman and B. Sudret. Principal component analysis and least angle regression in spectral stochastic finite element analysis. In *Proc. 11th Int. Conf. on Applications of Stat. and Prob. in Civil Engineering (ICASP11), Zurich, Switzerland*, 2011.

[41] G. Blatman and B. Sudret. *Sparse polynomial chaos expansions of vector-valued response quantities*. CRC Press/Balkema, 2013.

[42] G. Blatman and B. Surdret. An adaptive algorithm to build up sparse polynomial Chaos expansion for stochastic finite element analysis. *Probabilistic engineering mechatronics*, 25:183–197, 2010.

[43] A. Bollermann, G. Chen, A. Kurganov, and S. Noelle. A well-balanced reconstruction of wet/dry fronts for the shallow water equations. *J Sci Comput*, 56:267–290, 2013.

[44] A. Bollermann, S. Noelle, and M. Lukácová-Medvidová. Finite volume evolution Galerkin methods for the shallow water equations with dry beds. *Communications in Computational Physics*, 10:371–404, 2001.

[45] F. Bouchut. *Nonlinear Stability of Finite Volume Methods for Hyperbolic Conservation Laws and Well-Balanced Schemes for Sources*. Birkhäuser, Basel, 2004.

[46] S. Bozzi, G. Passoni, P. Bernardara, N. Goutal, and A. Arnaud. Roughness and discharge uncertainty in 1D water level calculations. *Environmental Modeling & Assessment*, 20:343–353, 2015.

[47] S. Bradford and B. Sandres. Finite-volume for shallow water flooding of arbitrary topography. *Journal of hydraulic engineering*, 128:289–292, 2002.

[48] E. Bradley, H. Trevor, J. Iain, and T. Robert. Least angle regression. *The Annals of Statistics*, 32:407–499, 2004.

[49] M. Brocchini and N. Dodd. Nonlinear shallow water equations modeling for coastal engineering. *J. Waterw. Port, Coastal, Ocean Eng*, 134:104–120, 2008.

[50] P. Brufall, M. Vazques-Cendon, and P.Garcia Navarro. A numerical model for the flooding and drying of irregular domains. *International Journal of numerical methods in fluids*, 39:247–275, 2002.

[51] H. Bryden, J. Candela, and T. Kinder. Exchange through the strait of Gibraltar. *Progress in Oceanography*, 33:201–248, 1994.

[52] J. Calle, P. Devloo, and S. Gomes. Stabilized discontinuous Galerkin method for hyperbolic equations. *Computer methods in applied mechanics and engineering*, 194:1861–1874, 2005.

[53] M. Carpenter, O. Gottlib, and S. Abaebanel. The stability of numerical boundary treatment for compact high-order finite difference schemes. *Journal of computational physics*, 108:275–295, 1993.

[54] C. Castro, E. Taro, and M. Kaser. ADER scheme on unstructured meshes for shallow water simulation of Tsunami waves. *Geophysical Journal international*, 189:1505–1520, 2012.

[55] M. Castro, T. Chacón, E. Nieto, and C. Parés. On well-balanced finite volume methods for nonconservative nonhomogeneous hyperbolic systems. *SIAM J. Sci. Comput.*, 29:1093–1126, 2007.

[56] M. Castro, A. Ferrero, J. Garcia, J. Vida, J. Marcia, C. Pres, and M. Elena. The numerical treatment of wet/dry fronts in shallow flows: Application to one-layer and two-layer systems. *Mathematical and computer modeling*, 42:536–545, 2005.

[57] M. Castro, J. Macías, and C. Parés. A Q-scheme for a class of systems of coupled conservation laws with source term, .application to a two-layer 1D shallow water system. *M2AN Math. Model. Numer. Anal.*, 35:107–127, 2001.

[58] L. Cea and J. French. Bathymetric error estimation for the calibration and validation of estuarine hydrodynamic models. *Estuarine, coastal and shelf science*, 100:124–132, 2012.

[59] O. Ceyhun and A. Yalcin. A remote sensing of water depths in shallow water via artificial neural networks. *Estuar. Coast. Shelf. Sci.*, 89:89–96, 2010.

[60] E. Chávarri, A. Crave, M. Bonnet, J. Da Silva, and J. Guyot. Hydrodynamic modelling of the amazon river: Factors of uncertainty. *Journal of South American Earth Sciences*, 44:94–103, 2013.

[61] C. Chen, C. Shen, C. Chen, and M. Cheng. Stability analysis of an oceanic structure using the Lyapunov method. *Engineering Computations*, 27:186–204, 2010.

[62] A. Chertock, S. Cui, A. Kurganov, and T. Wu. Well-balanced positivity preserving central-upwind scheme for the shallow water systems with friction terms. *International Journal for numerical methods in fluids*, 78:355–383, 2015.

[63] M. Chevreuil and A. Nouy. Model order reduction based on proper generalized decomposition for the propagation of uncertainties in structural dynamics. *International Journal for Numerical Methods in Engineering*, 89:241–268, 2012.

[64] M. Chin, C. Haza, and J. Mariano. A reduced-order information filter for multilayer shallow-water models: profiling and assimilation of sea surface height. *Journal of Atmospheric and Oceanic Technology*, 19:517–533, 2002.

[65] S. Choi, R. Grandhi, R. Canfield, and C. Pettit. Polynomial Chaos expansion with Latin Hypercube Sampling for estimating response variability. *AIAA journal*, 42:1191–1198, 2004.

[66] W. CL and W. Chau. A flood forecasting neural network model with genetic algorithms. *Internationsl Journal of Environment and pollution*, 28:261–273, 2006.

[67] B. Cockburn and C. Shu. Runge-kutta discontinuous Galerkin method for convection dominated problems. *Journal of scientific computing*, 16:173–261, 2001.

[68] R. Crisovan, D. Torlo, R. Abgrall, and S. Tokareva. Model order reduction for parametrized nonlinear hyperbolic problems as an application to uncertainty quantification. *Journal of Computational and Applied Mathematics*, 348:466–489, 2019.

[69] C. Cristo, M. Greco, M. Iervolino, R. Martino, and A. Vacca. A remark on finite volume method for 2D shallow water equations over irregular bottom topography. *Journal of hydraulic research*, 2:536–545, 2020.

[70] A. de Saint-Venant. Théorie du mouvement non permanent des eaux, avec application aux crues des riviére at á l'introduction des warées dans leurs lits. *Comptes Rendus des séances de l'Académie des Sciences*, 73:237–240, 1871.

[71] P. Dellar. Non-hydrodynamic modes and a priori construction of shallow water lattice Boltzmann equations. *Phys. Rev. Estate. Nonlin. Soft Matters Phys*, 65:1–12, 2002.

[72] S. Dey, S. Saksena, and V. Merwade. Assessing the effect of different bathymetric models on hydraulic simulation of rivers in data sparse regions. *Journal of Hydrology*, 575:838–851, 2019.

[73] U. Drahne, N. Goseberg, S. Vater, N. Beisiegel, and J. Behrans. An experimental and numerical study of long wave run-up on a plane beach. *Journal of marine science and engineering*, 4:1–23, 2016.

[74] Z. Drmac. A posteriori computation of the singular vectors in a preconditioned Jacobi SVD algorithm. *IMA journal of numerical analysis*, 19:191–213, 1999.

[75] S. Dubreuil, M. Berveiller, F. Petitjean, and M. Salan. Construction of bootstrap confidence intervals on sensitivity indices computed by polynomial chaos expansion. *Reliability Engineering and System Safety*, 121:263–275, 2014.

[76] G. Duplis and J. Goel. Finite element with high degree of regularity. *Numerical methods in engineering*, 2:563–577, 1970.

[77] M. El-Amrani and M. Seaid. An essentially non-oscillatory semi-lagrangian method for tidal flow simulations. *International Journal for Numerical Methods in Engineering*, 81:805–834, 2010.

[78] N. El Moçayd. La décomposition en polynômes du chaos pour lámélioration de lássimilation de données ensembliste en hydraulique fluviale. *PhD Université de Toulouse, INP*, 2017.

[79] N. El Moçayd, S. Mohamed, D. Ouazar, and M. Seaid. Stochastic model reduction for polynomial chaos expansion of acoustic waves using proper orthogonal decomposition. *Reliability Engineering & System Safety*, 195:106–733, 2020.

[80] N. El Moçayd, S. Ricci, N. Goutal, M. Rochoux, S. Boyaval, C. Goeury, D. Lucor, and O. Thual. Polynomial surrogates for open-channel flows in random steady state. *Environmental Modeling & Assessment*, 13:1–23, 2017.

[81] A. Emmanuel, F. Benkhaldoun, S. Sari, M. Seaid, and P. Tassi. A fast finite volume solver for multi-layered shallow water flows with mass exchange. *Journal of Computational Physics*, 272:23–45, 2014.

[82] A. Ern, S. Piperno, and K. Djade. A well-balanced Runge-Kutta discontinuous Galerkin method for the shallow water equations with flooding and drying. *Int. J. Numer. Methods Fluids*, 58:1–25, 2008.

[83] C. Escalante, T. Luna, and M. Castro. Non-hydrostatic pressure shallow flows: GPU implementation using finite volume and finite difference scheme. *International Journal for Computer-aided Engineering and Software*, 338:631–659, 2018.

[84] M. Esray, O. Lakkis, and P. Townsend. A Saint-Venant shallow water model for overland flows with perception and recharge. *Numerical analysis*, 1:1–26, 2017.

[85] R. Esteban, P. Verborgh, P. Gauffier, J. Gimnez, C. Guinet, and R. de Stephanis. Dynamics of killer whale, bluefin tuna and human fisheries in the Strait of Gibraltar. *Biological Conservation*, 194:31–38, 2016.

[86] G. Evensen. The Ensemble Kalman Filter: Theoretical formulation and practical implementation. *Ocean Dynamics*, 53:343–367, 2003.

[87] D. Farmer and L. Armi. Maximal two-layer exchange over a sill and through a combination of a sill and contraction with barotropic flow. *J. Fluid Mech.*, 164:53–76, 1986.

[88] Y. Feng and D. Peric. A time adaptive space-time finite element method for incompressible Lagrangian flows with free-surfaces computational issues. *Computer methods in applied mechanics and engineering*, 190:499–518, 2000.

[89] Y. Feng and D. Peric. A specially adaptive linear-space -time finite element solution procedure for incompressible flows with moving domains. *International Journal for numerical methods in fluids*, 43:1099–1106, 2003.

[90] F. Franzini and S. Soares-Franzao. Efficiency and accuracy of lateralized HLL and HLLS and augmunted Roes's scheme with energy balance for river flows in irregular channels. *Applied mathematical modelling*, 4:7427–7446, 2016.

[91] M. Le Gal, D. Violeau, R. Ata, and X. Wang. Shallow water numerical models for the 1947 gisborne and 2011 Tohoku-Oki tsunamis with kinematic seismic generation. *Coastal Engineering*, 139:1–15, 2018.

[92] J. Gallardo, C. Parés, and M. Castro. On a well-balanced high-order finite volume scheme for shallow water equations with topography and dry areas. *Journal of Computational Physics*, 227:574–601, 2007.

[93] F. Gao, D. Jeng, and H. Sekiguchi. Numerical study on the interaction between non-linear wave, buried pipeline and non-homogeneous porous seabed. *Computers and Geotechnics*, 30:535–547, 2003.

[94] P. Garcia-Navarro, A. Fras, and I. Villanueva. Dam-break flow simulation: some results for one-dimensional models of real cases. *Journal of Hydrology*, 216:227–247, 1999.

[95] B. Gatmiri. A simplified finite element analysis of wave-induced effective stress and pore pressure in permeable sea beds. *Geotechnique*, 40:15–30, 1990.

[96] L. Ge, K. Cheung, and H. Marcelo. Stochastic solution for uncertainty propagation in nonlinear shallow-water equations. *Journal of hydraulic engineering*, 134:1732–1743, 2008.

[97] I. Gejadze and P. Malaterre. Discharge estimation under uncertainty using variational methods with application to the full Saint-Venant hydraulic network model. *International Journal for Numerical Methods in Fluids*, 83:405–430, 2017.

[98] A. Gessesse, M. Sellier, E. Houten, and G. Smart. Reconstruction of river bed topography from free surface data using a direct numerical approach in one-dimensional shallow water flow. *Inverse problems*, 27:1–12, 2011.

[99] R. Ghanem, D. Higdon, and H. Owhadi. *Handbook of uncertainty quantification*, volume 6. Springer, 2017.

[100] A. Al Ghosoun, M. Herty, and M. Seaid. A new numerical treatment of moving wet/dry fronts in dam-break flows. *Journal of Applied Mathematics and Computing*, 59:489–516, 2019.

[101] B. Ginting and R. Mundani. Comparison of shallow water solvers: Applications for dam-break and Tsunami cases with reordering strategy for efficient vectorization on modern hardware. *Water*, 11:1–31, 2019.

[102] X. Giraldo, S. Heshaven, and T. Warburton. Nodal high-order discontinuous Galerkin methods for the spherical shallow water equations. *J. Comput. Phys*, 231:7898–8008, 2012.

[103] P. Glaister. Approximate Riemann solutions of the shallow water equations. *Hydraulic Research*, 26:293–306, 1988.

[104] F. Gómez. The role of the exchanges through the Strait of Gibraltar on the budget of elements in western mediterranean sea: Consequences of humain-induced modifications. *Marine Pollution Bulletin.*, 46:685–694, 2003.

[105] C. González, E. Reyes, Ó. Álvarez, A. Izquierdo, M. Bruno, and R. Mañanes. Surface currents and transport processes in the strait of Gibraltar: Implications for modeling and management of pollutant spills. *Ocean & Coastal Management*, 179:104–869, 2019.

[106] C. Gonzlez, E. Reyes, A. Izquierdo, M. Bruno, and R. Maanes. Surface currents and transport processes in the Strait of Gibraltar: Implications for modeling and management of pollutant spills. *Ocean & Coastal Management*, 179:104–869, 2019.

[107] N. Goseberg. A laboratory perspective of long wave generation. In *Proceedings of the international offshore and polar engineering conference*, pages 54–60, June 2012.

[108] N. Goutal, C. Goeury, R. Ata, S. Ricci, N. El Mocayd, M. Rochoux, H. Oubanas, I. Gejadze, and P. Malaterre. Uncertainty quantification for river flow simulation applied to a real test case: The garonne valley. In *Advances in Hydroinformatics*, pages 169–187. Springer, 2018.

[109] S. Grilli and P. Guyenne. A fully non-linear model for three-dimensional overturning waves over an arbitrary bottom. *J. Fluid Mech*, 35:829–867, 2001.

[110] T. Grillis, C. Harris, T. Tajalibakhsh, T. Kirby, T. Shi, F. Masterlark, and C. Kyriakopiulos. Numerical simulation of the 2011 Tohoku tsunami: Comparison with field observations and sensitivity to model parameters. In *Proceedings of the 22nd offshore and polar Engng. Conf. (ISOPE12)*, pages 32–46, June 2012.

[111] J. Gmez-Enri, C. Gonzlez, M. Passaro, S. Vignudelli, O. lvarez, P. Cipollini, R. Maanes, M. Bruno, M. Lpez-Carmona, and A. Izquierdo. Wind-induced cross-strait sea level variability in the Strait of Gibraltar from coastal altimetry and in-situ measurements. *Remote Sensing of Environment*, 221:596–608, 2019.

[112] J. Habert. *Prévisions des crues en temps réel sur le bassin de la Marne: Assimilation in situ pour la correction du modèle hydraulique mono-dimensionnel Mascaret.* PhD thesis, 2016.

[113] J. Hall, S. Tarantola, P. Bates, and M. Horritt. Distributed sensitivity analysis of flood inundation model calibration. *Journal of Hydraulic Engineering*, 131:117–126, 2005.

[114] L. Hammack. A note on tsunami: Their generation and propagation in an ocean of uniform depth. *Journal of fluid mechanics*, 60:769–800, 1973.

[115] S. Hargarten and J. Robl. Modeling rapid mass movements using the shallow water equations. *Natural hazards and earth system sciences*, 2:6775–6809, 2019.

[116] C. Heining and N. Aksel. Bottom reconstruction in thin flow over topography. *Phys. Fluids*, 21:592–605, 2009.

[117] K. Hogrefe, D. Wright, and E. Hochberg. Derivation and integration of shallow-water bethymetry: Implications for coastal terrain modelling and subsequent analysis. *Marine Geodesy*, 1:299–317, 2008.

[118] G. Holland. An analytical model of the wind and pressure profiles in Hurricanes. *Monthly Weather Review*, 108:2212–1218, 1980.

[119] K. Holz and G. Nitsche. Tidal wave analysis for estuaries with intertidal flats. *Finite element in water resources*, 5:113–115, 1980.

[120] L. Hong, F. Hong, W. Guo, and B. Li. Efficient communication scheduling for underwater sensor networks. *Sensors*, 11:2920–2938, 2011.

[121] M. Horritt. Evaluating wetting and drying algorithms for finite element models of shallow water flows. *International Journal of numerical methods in engineering*, 55:835–851, 2002.

[122] M. Horritt. Stochastic modelling of 1-D shallow water flows over uncertain topography. *Journal of Computational Physics*, 180:327–338, 2002.

[123] A. Humberto, E. Schubert, and F. Sanders. Two-dimensional, high-resolution modeling of urban dam-break flooding: A case study of Baldwin Hills, California. *Advances in Water Resources*, 32:1323–1335, 2009.

[124] N. Izem, M. Seaid, and M. Wakrim. A discontinuous Galerkin method for two-layer shallow water equations. *Mathematics and Computers in Simulation*, 120:12–23, 2016.

[125] S. Jonkman, H. Voortman, W. Klerk, and S. Vuren. Development in the management of flood defenses and hydraulic infrastructure in the Netherland. *Structure and Infrastructure engineering*, 14:895–910, 2018.

[126] G. Jord, A. Sanchez-Roman, and D. Gomis. Reconstruction of transports through the Strait of Gibraltar from limited observations. *Climate Dynamics*, 48:851–865, 2017.

[127] W. Junna and Z. Zhonglong. Evaluating riparian vegetation roughness computation methods integrated within HEC-RAS. *Journal of Hydraulic Engineering*, 145:401–421, 2019.

[128] K. Karhunen. Zur spektraltheorie stochastischer prozesse. *Ann. Acad. Sci. Fennicae, AI*, 34, 1946.

[129] M. Karim, G. Roby, M. Ismail, and M. Meah. A shallow water model for computing tsunami along the west coast of Peninsular Malysia and Thailand using boundary-fitted curvilinear grids. *Science of Tsunami hazards*, 26:1–21, 2007.

[130] R. Karim, T. Nogami, and G. Wang. Analysis of transient response of saturated porous elastic soil under cyclic loading using element free Galerkin method. *International Journal of Solids and Structures*, 39:6011–6033, 2002.

[131] N. Kato. Seismic cycle on a strike-slip fault with rate-and state-dependent strength in an elastic layer overlying a viscoelastic half-space. *Earth planets space*, 54:1077–1083, 2002.

[132] M. Kawahara, H. Hirano, K. Tsbota, and K. Inagaki. Selective lumping finite element method for shallow water flow. *International journal for numerical methods in fluids*, 2:89–112, 1982.

[133] A. Kendall. A survey of numerical methods for the solution of Fredholm integral equations of the second kind. 1976.

[134] G. Kesserwani, S. Lee, M. Ribinato, and J. Shucksmith. Experimental and numerical validation of shallow water flows around a surcharging manhole. In *Proceedings of the international conference on case Histories in Geotechnical engineering*, pages 145–154, September 2015.

[135] G. Kesserwani and Q. Liang. Locally limited and fully conserved RKDG2 shallow water solutions with wetting and drying. *J. Sci. Comput*, 50:120–144, 2012.

[136] G. Kirstetter, J. Hu, O. Delestre, F. Darboux, P. Lagree, S. Popinet, J. Fullana, and C. Josserand. Modeling rain-driven overland flow empirical versus analytical friction terms in the shallow water approximation. *Journal of Hydrology*, 536:1–9, 2016.

[137] R. Klausen and N. Risebro. Stability of conservation laws with discontinuous coefficients. *Journal of differential equations*, 157:41–60, 1999.

[138] A. Koukouselis, K. Chatzioannou, E. Mistakidis, and V. Katsardi. Development of an equivalent static method for the approximation of the dynamic response of offshore structures. *Engineering Computations*, 36:1121–1141, 2019.

[139] A. Koulali, D. Ouazar, A. Tahayt, R. King, P. Vernant, R. Reilinger, S. McClusky, T. Mourabit, M. Davila, and N Amraoui. New GPS constraints on active deformation along the Africa–Iberia plate boundary. *Earth and Planetary Science Letters*, 308:211–217, 2011.

[140] A. Kreuzhuber, Z. Horvath, S. Noelle, G. Bloschi, and J. Waser. A fast second-order shallow water scheme on two-dimensional structured grids over abrupt topography. *Advances in water resources*, 127:89–108, 2019.

[141] V. Laborie, S. Ricci, M. Lozzo, N. Goutal, Y. Audouin, and P. Sergent. Quantifying forcing uncertainties in the hydrodynamics of the Gironde estuary. *Computational Geosciences*, 4:1–22, 2019.

[142] A. Lacasta, M. Morales-Hernndez, J. Burguete, P. Brufau, and P. Garca-Navarro. Calibration of the 1D shallow water equations: a comparison of Monte Carlo and gradient-based optimization methods. *Journal of Hydroinformatics*, 19:282–298, 2017.

[143] J. Lafuente, J. Almazán, F. Catillejo, A. Khribeche, and A. Hakimi. Sea level in the Strait of Gibraltar: Tides. *Int. Hydrogr. Rev. LXVII.*, 1:111–130, 1990.

[144] O. Le Maître and O. Knio. *Spectral methods for uncertainty quantification: with applications to computational fluid dynamics*. Springer Science & Business Media, 2010.

[145] O. Le Maıtre, M. Reagan, H. Najm, R. Ghanem, and O. Knio. A stochastic projection method for fluid flow: Ii. Random process. *Journal of computational Physics*, 181:9–44, 2002.

[146] G. Lee, W. Kim, H. Oh, D. Youn, and H. Kim. Review of statistical model calibration and validation—from the perspective of uncertainty structures. *Structural and Multidisciplinary Optimization*, 60:1619–1644, 2019.

[147] H. Lee. Implicit discontinuous Galerkin scheme for shallow water equations. *Journal of mathematical science and technology*, 33:3301–3310, 2019.

[148] C. Legleiter and P. Kyriakidis. Spatial prediction of river channel topography. *Earth. Surf. Process. Land*, 14:841–867, 2000.

[149] R. LeVeque. *Numerical Methods for Conservation Laws*. Lectures in Mathematics, ETH Zürich, 1992.

[150] R. LeVeque. Balancing source terms and flux gradients in high-resolution Godunov methods: the quasi-steady wave-propagation algorithm. *Journal of Computational Physics*, 146:346–365, 1998.

[151] R. LeVeque. *Finite volume methods for hyperbolic problems*. Cambridge Texts in Applied Mathematics. Cambridge University Press, 2002.

[152] P. Li, W. Don, and Z. Ghao. High order well-balanced finite difference WENO interpolation based schemes for shallow water equations. *Computers and fluids*, 201:104–117, 2020.

[153] X. Li and H. Castaneda. Damage evolution of coasted steel pipe under cathodic-protection in soil. *Anti-Corrosion methods and materials*, 64:118–126, 2017.

[154] Y. Li and F. Raichlen. Non-breaking and breaking solitary wave run-up. *J. Fluid Mech*, 456:295–318, 2002.

[155] Q. Liang and A. Borthwick. Adaptive quadtree simulation of shallow flows with wet-dry fronts complex topography. *Computers and fluids*, 38:221–234, 2009.

[156] Q. Liang and F. Marche. Numerical resolution of well-balanced shallow water equations with complex source terms. *Advances in water resources*, 32:873–884, 2009.

[157] C. Linares, M. Asunicon, M. Castro, S. Mishra, and J. Sukys. Multi-level Montecarlo finite volume method for shallow water equations with uncertain parameters applied to landslides generated tsunamis. *Applied mathematical modelling*, 39:7211–7226, 2015.

[158] H. Liu, J. Zhang, and S. Shafiai. A second order treatment to the wet dry interface of shallow water. *Journal of Hydrology*, 536:514–523, 2016.

[159] H. Liu, J. Zhou, and R. Burrows. Lattice Boltzmann model for shallow water flows in curved and meandering channel. *International journal to Comput fluid dynamics*, 23:209–220, 2015.

[160] M. Loève. Elementary probability theory. In *Probability Theory I*, pages 1–52. Springer, 1977.

[161] Y. Loukili and A. Soulaimani. Numerical tracking of shallow water waves by the unstructured finite volume WAF approximation. *International Journal of computational methods in engineering science and mechanics*, 8:1–14, 2007.

[162] F. Lu, M. Morzfeld, X. Tu, and A. Chorin. Limitations of Polynomial Chaos Expansions in the bayesian solution of inverse problems. *Journal of Computational Physics*, 282:138–147, 2015.

[163] P. Lynett, T. Renwu, and P. Liu. Modelling wave run-up with depth integrated equations. *Coastal engineering*, 46:89–107, 2002.

[164] J. Macías, C. Parés, and M. Castro. Improvement and genralization of a finite element shallow water solver to multi-layer systems. *Int. J. Numer. Methods Fluids.*, 31:1037–1059, 1999.

[165] P. Madsen, H. Bingham, and H. Liu. A new Boussinesq method for fully nonlinear waves from shallow to deep water. *J. Fluid Mech*, 462:1–30, 2002.

[166] A. Marrel, N. Saint-Geours, and M. Lozzo. Sensitivity analysis of spatial and/or temporal phenomena. *Handbook of Uncertainty Quantification*, 1:1–31, 2016.

[167] R. Martines and J. Leandro. Wetting and drying numerical treatments for the Roe Riemann solver. *Journal of hydraulic research*, 1:1–14, 2017.

[168] S. Martínez-Aranda, J. Murillo, and P. García-Navarro. A 1D numerical model for the simulation of unsteady and highly erosive flows in rivers. *Computers & Fluids*, 181:8–34, 2019.

[169] N. Matskevich and L. Chubarov. Exact solution to shallow water equations for a water oscillation problem in an idealized basin and their use in verifying some numerical algorithms. *Numerical analysis and application*, 12:1169–1174, 2019.

[170] B. Merz and A. Thieken. Separating natural and epistemic uncertainty in flood frequency analysis. *Journal of Hydrology*, 309:114–132, 2005.

[171] K. Mevellie and P. Matsuv. Distribution of breaking waves at the ocean surface. *Nature*, 417:58–63, 2002.

[172] G. Michael and P. Malanotte-Rizzoli. Data Assimilation in metrology and oceanography. *Advances in Geophysics*, 33:141–266, 1991.

[173] H. Mingham and C. Causon. Numerical simulation of wave overtopping of coastal structures using the non-linear shallow water equations. *Coast. Eng*, 13:41–433, 2000.

[174] S. Mishra, C. Schwab, and J. Sukys. Multi level Monte Carlo finite volume methods for shallow water equations with uncertain topography in multi-dimensions. *SIAM. J. Sci. Comput*, 36:761–754, 2012.

[175] N. El Moçayd. *La décomposition en polynôme du chaos pour l'amélioration de l'assimilation de données ensembliste en hydraulique fluviale.* PhD thesis, 2017.

[176] R. Morgan, D. Morgan, and H. Finney. A predictive model for the assesment of soil erosion risk. *J. Agric. Eng. Res*, 30:245–253, 1984.

[177] S. Munier, A. Polebistki, C. Brown, G. Belaud, and D. Lettenmaier. SWOT data assimilation for operational reservoir management on the upper Niger river basin. *Water Resources Research*, 51:554–575, 2015.

[178] J. Murillo and P. Garcia-Navarro. Augmented versions of the HLL and HLLC Riemann solvers including sourc terms in one and two dimensions for the shallow flow applications. *Journal of computational physics*, 231:6861–6906, 2012.

[179] V. Murino and A. Trucco. A geometrical approach to the surface-fitting problem in underwater three-dimensional acoustic images. *Meas. Sci. Technol*, 10:1135–1141, 1999.

[180] M. Navarro, P. Le Maître, I. Hoteit, L. George, T. Mandli, and M. Knio. Surrogate-based parameter inference in debris flow model. *Computational Geosciences*, 22:1447–1463, 2018.

[181] I. Navon. Finite element simulation of the shallow water equations model on a limited area domain. *Applied mathematical modelling*, 3:337–348, 1979.

[182] T. Nguyen, B. Hofland, V. Chinch, and M. Stive. Wave overtopping discharge for very gently sloping for shores. *Water*, 12:1–18, 2020.

[183] I. Nikolos and A. Delis. An structured node-centered finite volume scheme for shallow water flows with wet/dry fronts over complex topography. *Computer methods in applied mechanics and engineering*, 155:49–72, 1998.

[184] S. Noelle, N. Pankratz, G. Puppo, and J. Natvig. Well-balanced finite volume schemes of arbitrary order of accuracy for shallow water flows. *Journal of Computational Physics*, 213:474–499, 2006.

[185] J. Noorzaei, M. Viladkar, and P. Godbole. Nonlinear soil-structure interaction in plane frames. *Engineering computations*, 11:303–316, 1994.

[186] A. Nouy and O. Le Maıtre. Generalized spectral decomposition for stochastic nonlinear problems. *Journal of Computational Physics*, 228:202–235, 2009.

[187] H. Oubanas, I. Gejadze, P. Malaterre, and F. Mercier. River discharge estimation from synthetic SWOT-type observations using variational data assimilation and the full Saint-Venant hydraulic model. *Journal of hydrology*, 559:638–647, 2018.

[188] O. Pannekoucke, L. Berre, and G. Desroziers. Background-error correlation length-scale estimates and their sampling statistics. *Quarterly Journal of the Royal Meteorological Society*, 134:497–508, 2008.

[189] F. Pappenberger and J. Beven. Ignorance is bliss: Or seven reasons not to use uncertainty analysis. *Water Resources Research*, 42:22–29, 2006.

[190] F. Pappenberger, K. Beven, M. Horritt, and S. Blazkova. Uncertainty in the calibration of effective roughness parameters in HEC-RAS using inundation and downstream level observations. *Journal of Hydrology*, 302:46–69, 2005.

[191] F. Pappenberger, P. Matgen, K. Beven, J. Henry, and L. Pfister. Influence of uncertain boundary conditions and model structure on flood inundation predictions. *Advances in water resources*, 29:1430–1449, 2006.

[192] Y. Peng, J. Zhou, and R. Burrows. Modeling solute transport in shallow water with the Lattice Boltzmann method. *Computers and fluids*, 50:181–188, 2011.

[193] R. Perianez and J. April. Modeling tsunami propagation in Iberia-Africa plate boundary: historical events. regional exposure and the case study of the former Gulf of Tartosses. *Journal of marines system*, 23:1–12, 2012.

[194] H. Poulos and E. Davis. *Elastic solutions for soil and rock mechanics*. The University of Sydney, Australia, 1991.

[195] S. Pudjaprasetya and A. Ribal. Numerical solution of Saint Venant equation to study floods in rivers. *Coastal Engineering*, 56:747–758, 2009.

[196] J. Pudykiewicz and A. Staniforth. Some properties and computive performance of the Semi-Lagrangian method of Robert in the solution of advection-diffusion equation. *Atmosphere-Ocean*, 22:283–308, 1984.

[197] M. Raisee, D. Kumar, and C. Lacor. A non-intrusive model reduction approach for polynomial chaos expansion using proper orthogonal decomposition. *International Journal for Numerical Methods in Engineering*, 103:293–312, 2015.

[198] K. Ramadan, H. Hassan, and S. Hanna. Modeling of tsunami generation and propagation by a spreading curvilinear seismic faulting in linearized shallow-water wave theory. *Applied mathematical modelling*, 35:61–79, 2011.

[199] C. Rasmussen and C. Williams. Gaussian processes for machine learning, Ser. adaptive computation and machine learning. *Cambridge, MA, USA: MIT Press*, 38:715–719, 2006.

[200] B. Reddy and M. Kussner. Some low-order quadrilateral elements based on novel integration rules. *Engineering computations*, 15:700–720, 1998.

[201] J. Refsgaard, J. van der Sluijs, A. Højberg, and P. Vanrolleghem. Uncertainty in the environmental modelling process–a framework and guidance. *Environmental modelling & software*, 22:1543–1556, 2007.

[202] R. Reid and D. Bodline. Numerical model for storm surges in Galveston Bay. *Americal society of civil engineering*, 94:33–57, 1968.

[203] M. Ricchiuto, P. Marco Congedo, and I. Argiris. *Runup and uncertainty quantification: Sensitivity analysis via ANOVA decomposition*. PhD thesis, INRIA, 2014.

[204] L. Richardson. The approximate arithmetical solution by finite difference of physical problems. *Trans. R. Soc*, A210:307–357, 1910.

[205] P. Roe. Approximate Riemann solvers, parameter vectors, and difference schemes. *Journal of Computational Physics*, 43:357–372, 1981.

[206] J. Rossmanith. A wave propagation method for hyperbolic systems on the sphere. *Journal of computational physics*, 212:629–658, 2006.

[207] D. Roux, A. Staniforth, and C. Lin. Finite elements for shallow water equations ocean models. *Monthly weather review*, 126:72–89, 1998.

[208] P. Roy, N. El Moçayd, S. Ricci, J. Jouhaud, N. Goutal, M. De Lozzo, and M. Rochoux. Comparison of polynomial chaos and Gaussian process surrogates for uncertainty quantification and correlation estimation of spatially distributed open-channel steady flows. *Stochastic Environmental Research and Risk Assessment*, 3:1–19, 2017.

[209] R. Salmon. The Lattice Boltzmann solutions of the three-dimensional planetary geostrophic equations. *J. Mar. Res*, 57:847–884, 1999.

[210] J. Sampson, A. Easton, and M. Singh. Moving boundary shallow water flow above parabolic bottom topography. *ANZIAM*, 47:73–87, 2006.

[211] A. Schaffer, A. Madsen, and A. Deigaard. A Boussinesq model for waves breaking in shallow water. *Coast Engineering*, 20:536–545, 1993.

[212] C. Schwab. Karhunen–Loève approximation of random fields by generalized fast multipole methods. *Journal of Computational Physics*, 217:100–122, 2006.

[213] M. Seaid. Semi-Lagrangian integration schemes for viscous incompressible flows. *Comp. Methods in App. Math.*, 4:392–409, 2002.

[214] M. Shamkhi and Z. Attab. Estimation of Manning's roughness coefficient for Tigris river by using HEC-RAS model. *Wasit Journal of Engineering Sciences*, 6:90–97, 2018.

[215] R. Sharma and A. Kumar. Case histories of earthern dam failure. *International conference on case Histories in Geotechnical Engineering*, pages 1–7, 2014.

[216] J. Shaw, G. Kesserwani, and P. Pettersson. Probabilistic Godunov-type hydrodynamic modelling under multiple uncertainties: Robust wavelet-based formulations. *Advances in Water Resources*, 5:103–526, 2020.

[217] A. Sielecki and G. Wurtele. The numerical integration of the nonlinear shallow water equations with sloping boundaries. *J. Phys*, 6:219–236, 1970.

[218] J. Simon, J. Jeffrey, and K. Uhlmann. New extension of the Kalman Filter to nonlinear systems. In Ivan Kadar, editor, *Signal Processing, Sensor Fusion, and Target Recognition VI*, volume 3068, pages 182 – 193. International Society for Optics and Photonics, SPIE, 1997.

[219] C. Soize and R. Ghanem. Physical systems with random uncertainties: Chaos representations with arbitrary probability measure. *SIAM Journal on Scientific Computing*, 26:395–410, 2004.

[220] Y. Spitz, J. Moisan, M. Abbott, and J. Richman. Data Assimilation and a pelagic ecosystem model: parameterization using time series observations. *Journal of Marine Systems*, 16:51–68, 1998.

[221] C. Sqsulli. Semi implicit finite difference methods for the two-dimensional shallow water equations. *J. Comput. Phys*, 86:56–74, 1990.

[222] I. Sraj, O. Le Maître, O. Knio, and I. Hoteit. Coordinate transformation and polynomial chaos for the bayesian inference of a Gaussian process with parametrized prior covariance function. *Computer Methods in Applied Mechanics and Engineering*, 298:205–228, 2016.

[223] P. Sraj, I.and Le Maître, M. Knio, and I. Hoteit. Coordinate transformation and polynomial chaos for the bayesian inference of a Gaussian process with parametrized prior covariance function. *Computer Methods in Applied Mechanics and Engineering*, 298:205–228, 2016.

[224] R. Stanislow and E. Penlinovosky. Run-up of dispersive and breaking waves on beaches. *Oceanologia*, 43:61–97, 2001.

[225] J. Stoker. *Water Waves*. Interscience Publishers, Inc., New York, 1986.

[226] G. Strang. On the construction and the comparison of difference schemes. *SIAM J. Numer. Anal*, 5:506–517, 1968.

[227] Y. Sun, S. Chen, and Y. Yang. The families of nonconforming mixed finite elements for linear elasticity on simplex grids. *Applied mathematics and computation*, 358:348–362, 2019.

[228] H. Swart and J. Zimmerman. Morphodynamics of tidal intel systems. *Fluid Mech*, 41:203–229, 2009.

[229] E. Synolakis. The runup of solitary waves. *Journal of fluid mechanics*, 185:523–545, 1987.

[230] E. Synolakis and L. Kong. Run-up measurements of the december 2014 indian ocean tsunami. *Earthq. Spectra*, 22:67–91, 2006.

[231] B. Tang and W. Hsieh. Coupling neural network to dynamical systems via variational data assimilation. *Monthly Weather Review*, 131:1855–1870, 2001.

[232] G. Tchamen and R. Kahawita. Modelling wetting and drying effects over complex topography. *Hydrological processes*, 12:1151–1182, 1998.

[233] C. Temperton and A. Staniforth. An efficient two-time-level Galerkin characterestics semi-implicit integration scheme. *Quart. J. Roy. Meteor. Soc*, 113:1025–1039, 1987.

[234] C. Temperton and A. Staniforth. An efficient two-time-level semi-Lagrangian semi-implicit integration scheme. *Quart. J. Roy. Meteor. Soc.*, 113:1025–1039, 1987.

[235] S. Thomas. A finite element model for the analysis of wave induced stresses, displacements and pore pressures in an unsaturated seabed I: theory. *Computers and Geotechnics*, 8:1–38, 1989.

[236] Y. Thorimbert, J. Latt, and B. Chopard. Coupling of Lattice Boltzmann shallow water model with Lattice-Boltzmann free-surface model. *Journal of computational science*, 33:1–10, 2019.

[237] V. Titov and E. Synolakis. Numerical modeling of tidal wave runup. *Coastal ocean engineering*, 124:157–171, 1998.

[238] E. Toro. *Shock-capturing methods for free-surface shallow flows*. Wiley, 2002.

[239] R. Touma. Well-balanced central schemes for systems of shallow water equations with wet and dry states. *Applied mathematical modelling*, 5:1–17, 2015.

[240] Y. Tsui and C. Helfrich. Wave-induced pore pressure in submerged sand layer. *Journal of geotechnical engineering*, 109:603–618, 1983.

[241] S. Voit. Tsunamis. *Fluid Mech*, 19:217–236, 1987.

[242] J. Von-Neumann and R. Richtmyer. A method for the numerical calculation of hydrodynaic shocks. *Journal of applied physics*, 21:232–237, 1950.

[243] C. Vreugdenhil. *Numerical Method for Shallow Water Flow*. Kluwer Academic, Dordsecht, 1994.

[244] D. Vu and T. Phan. Solving two-dimensional Saint-Venant equation by using cellular neural network. In *Proceedings of the 7th Asian control conference*, pages 1258–1263, August 2009.

[245] D. Wang, B. Bienen, M. Nazem, Y. Tian, J. Zheng, T. Pucker, and M. Randolph. Large deformation finite element analysis in geotechnical engineering. *Computers and Geotechnics*, 65:104–114, 2015.

[246] A. Wasantha. Calibration of riverbed roughness. *Journal of Hydraulic Engineering*, 121:664–671, 1995.

[247] P. Wetahettiga, K. Vaagsaether, and B. Lie. A solution method for one-dimensional shallow water equations using flux limiter centered scheme for open Venturi channels. *The journal of computational multiphase flows*, 4:212–223, 2018.

[248] N. Wiener. The homogeneous chaos. *American Journal of Mathematics*, 60:897–936, 1938.

[249] D. Williams. *Diffusions, Markov processes, and martingales. Vol. 1, Foundations*. Wiley, 1979.

[250] Y. Xing and C. Shu. High order finite difference WENO schemes with the exact conservation property for the shallow water equations. *J. Comp. Physics*, 208:3206–227, 2005.

[251] D. Xiu. *Numerical methods for stochastic computations: a spectral method approach*. Princeton university press, 2010.

[252] D. Xiu and G. Karniadakis. The Wiener–Askey polynomial chaos for stochastic differential equations. *SIAM journal on scientific computing*, 24:619–644, 2002.

[253] T. Xu, J. Valocchi, M. Ye, F. Liang, and F. Lin. Bayesian calibration of groundwater models with input data uncertainty. *Water Resources Research*, 53:3224–3245, 2017.

[254] R. Yahia-Djouadi, D. Hernane-Boukari, and D. Teniou. A study of the inverse of a free surface problem. *Abstr. Appl. Anal*, 2:159–171, 2005.

[255] Y. Yamazaki, Z. Kowalik, and K. Cheung. Depth integrated non-hydrostatic model for wave breaking and run-up. *International Journal for numerical methods in fluids*, 61:473–497, 2009.

[256] S. Yim, D. Cox, and M. Park. Experimrntal and computational activities at the Oregon state university needs tsunami facility. *Science of Tsunami hazards*, 28:1–16, 2009.

[257] L. Yinerg. A coupled Lattice Boltzmann model for advection and anistropic dispersion problem in shallow water. *Advances in water Resources*, 50:181–193, 2008.

[258] G. Ying and F. Raichlen. Non-breaking and breaking solitary wave run-up. *Journal of Energy*, 114:689–706, 1988.

[259] X. Ying and A. Wang. Upwind conservation scheme for the Saint Venant equations. *J. Hydraul. Eng*, 130:977–987, 2004.

[260] Y. Ying and Y. Wang. Improved implementation of the HLL approximate Riemann solver for one dimensional open channel flows. *Journal of Hydraulic Research*, 46:21–34, 2008.

[261] Y. Yoon, M. Durand, C. Merry, E. Clark, K. Andreadis, and D. Alsdorf. Estimating river bathymetry from data assimilation of synthetic SWOT measurements. *Journal of hydrology*, 464:363–375, 2012.

[262] K. Zen and H. Yamazaki. Mechanism of wave-induced liquefaction and densification in seabed. *Soils and foundations*, 30:90–104, 1990.

[263] K. Zen and H. Yamazaki. Oscillatory pore pressure and liquefaction in seabed induced by ocean waves. *Soils and foundations*, 30:147–161, 1990.

[264] J. Zhang, J. Zhou, S. Bi, Q. Li, and Y. Fan. A well-balanced numerical scheme for shallow water simulation on adaptive grids. *Journal of physics*, 495:1–10, 2014.

[265] M. Zhang and W. Wu. A two dimensional hydrodynamic and sediment transport model for dam break based on finite volume method with quadtree grid. *Applied Ocean Research*, 33:297–308, 2011.

[266] S. Zhang and D. Jennifer. 1D finite volume model of unsteady flow over mobile bed. *Journal of hydrology*, 405:57–68, 2011.

[267] X. Zhang, W. Long, H. Xie, J. Zhu, and J. Wang. Numerical simulations of flood inudation processes. *Water and marine time engineering*, 142:1–10, 2000.

[268] Y. Zhang and Y. Pei. Well-balanced finite volume scheme for shallow water flooding and drying over arbitrary topography. *Engineering applications of computational fluid mechanics*, 2:1994–2006, 1997.

[269] X. Zhihua. Numerical study of breaking waves by a two-phase flow model. *International Journal for numerical methods in fluids*, 1:53–67, 2011.

[270] F. Zhou, G. Chen, Y. Huang, and H. Feng. An adaptive moving finite volume scheme for modeling flood inundation over dry and complex topography. *Water Resources Research*, 49:1914–1928, 2013.

[271] Q. Zhu, J. Bai, and X. Yang. A multi-fault diagnosis method for sensor systems based on principle component analysis. *Sensors*, 10:241–253, 2010.

[272] Q. Zhu, A. Cao, W. Zaifend, J. Song, and C. Shengli. Damage evolution of coasted steel pipe under cathodic-protection in soil. *Anti-Corrosion methods and materials*, 58:234–237, 2011.

[273] K. Zti, B. Huat, J. Noorzaei, M. Jaafar, and G. Sew. A review of basic soil constitutive models for geotechnical application. *Journal of geotechnical engineering*, 69:201–120, 2009.